Metal Strong Damped Lyman Alpha Systems And Their Context With The Local Group

by

Trystyn Andrew Munro Berg
B.Sc., University of Victoria, 2012

A Thesis Submitted in Partial Fulfillment of the
Requirements for the Degree of

MASTER OF SCIENCE

in the Department of Physics and Astronomy

Metal Strong Damped Lyman Alpha Systems And Their Context With The Local Group

by

Trystyn Andrew Munro Berg
B.Sc., University of Victoria, 2012

Supervisory Committee

Dr. S. Ellison, Supervisor
(Department of Physics and Astronomy)

Dr. K. Venn, Departmental Member
(Department of Physics and Astronomy)

Dr. L. Simard, Departmental Member
(Department of Physics and Astronomy)

Supervisory Committee

Dr. S. Ellison, Supervisor
(Department of Physics and Astronomy)

Dr. K. Venn, Departmental Member
(Department of Physics and Astronomy)

Dr. L. Simard, Departmental Member
(Department of Physics and Astronomy)

ABSTRACT

Damped Lyman α systems (DLAs) are useful probes of the chemical enrichment of the universe as they provide accurate abundance measurements of many chemical species. Using a sample of 30 DLAs (with large metal column densities) observed with the High Resolution Echelle Spectrometer on the Keck I telescope, the abundances of several elements (i.e. iron, zinc, chromium, silicon, sulphur, phosphorus, manganese, and boron) are derived and presented. A comparison is drawn between the abundances from these metal-rich DLAs with literature samples encompassing the largest compilation of high resolution observations of other DLAs, and stars from the Milky Way and its satellite galaxies to understand the astrophysical nature of DLAs.

Furthermore, the first ever extragalactic study of boron is presented. Using the sample of 30 metal-rich DLAs, two 3σ detections and one near detection (2.97σ) were found. From the comparison of [B/O] and, for the first time, [B/S], with studies in the Milky Way, there appears to be an excess of boron relative to its parent nucleus (oxygen) in these three DLA systems, suggesting that there may be a higher cosmic ray flux in DLAs than in the Milky Way.

Contents

List of Tables

List of Figures

ACKNOWLEDGEMENTS

I would like to thank:

Sara Ellison for being an excellent supervisor by providing me with the resources and opportunities necessary both to complete this thesis and support my research interests.

Kim Venn for her mentorship since Astro 250 and all her help in developing my understanding of stellar abundance measurements.

J. Xavier Prochaska for providing the amazing data in this thesis, and his wisdom in writing the boron paper.

Luc Simard for participating on the committee.

Falk Herwig, Marco Pignatari, and Christian Ritter for their insightful discussions on the nucleosynthetic origin of the elements.

Friends and family all of which have supported me through my education.

Do. Or do not. There is no try.
Yoda (Star Wars Ep. V)

For Larry, Fiona, and Heather.

Chapter 1

Damped Lyman Alpha Systems

1.1 Chemical Evolution of the Universe

The universe is full of galaxies, and these galaxies are full of gas and stars. The chemical relation between stars and the gas play an important role in the evolution of the galaxy. Stars form within the cold, neutral gas of galaxies, and throughout their lifetime burn hydrogen and other elements. The end products of stellar nucleosynthesis are then recycled back into the gas of the galaxy through stellar winds and supernovae which in turn will form the next generations of stars (e.g. Burbidge et al., 1957). The constituents of the galaxy are then passed on to future galaxies; either through a merger and accretion of material into a bigger galaxy, or gas emitted back into the intergalactic medium through winds and outflows. A cartoon of all the overlapping processes is shown in Figure 1.1. Nevertheless, this *chemical evolution* of the universe traces many aspects of astrophysics, and by studying the abundances of these elements one can understand how the universe has evolved.

1.1.1 Big Bang Nucleosynthesis

In the Big Bang model of the universe, the initial temperatures and densities could keep all matter and photons in a state of thermal equilibrium (Hayashi, 1950). As the universe expanded adiabatically, the temperature of this cosmic soup cooled down, *freezing-out* the fundamental building blocks of matter (e.g. protons, neutrons, neutrinos) out of equilibrium with their antiparticles and photons. This freeze-out occurs in an order of decreasing rest mass, starting with protons (939 MeV), neutrinos (1.29MeV), and finally electrons (511 keV); occurring all within the first second after

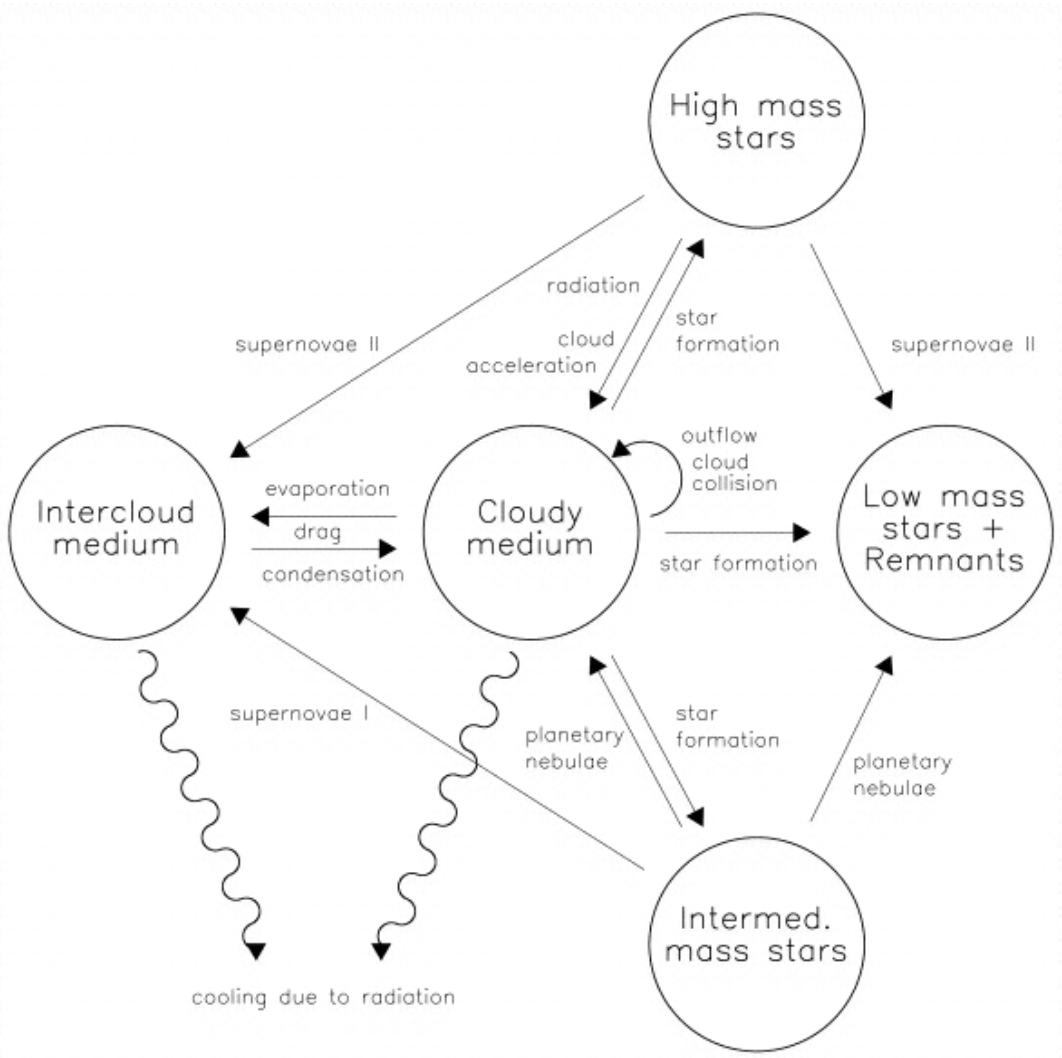

Figure 1.1 A cartoon summarising all the processes involved in the transfer of matter and energy in a galaxy (taken from Samland et al., 1997). The study of chemical evolution as a whole implies the study of many different astrophysical processes within a galaxy.

the beginning of the universe (Pagel, 2009).

The amount of baryons available for Big Bang nucleosynthesis hinges on the baryon-photon ratio (typically denoted η). Upon electron-positron freeze-out, the neutrinos emitted from the electron-positron annihilations interact with photons through the transfer of entropy to the photons (Pagel, 2009). Once the positrons are exhausted and no more neutrinos are emitted, the total number of photons and baryons is conserved, fixing η. By measuring the baryon density of the universe and knowing the temperature of the universe during Big Bang nucleosynthesis, η can be determined by measuring the overall abundances of the primordial elements produced in the Big Bang (Pagel, 2009). In addition, the ratio of protons and neutrons plays an important role in the subsequent nucleosynthesis of the elements as the number of neutrons limits the amount of heavy elements that can form. As neutrinos freeze out (denoted by the end of the lepton era), protons and neutrons are no longer in equilibrium. With the decrease in temperature, the proton-neutron ratio freezes out at ~ 5 (Pagel, 2009).

To form any elements heavier than hydrogen, nuclei require the capture of neutrons. However, free neutrons have a half life of ~ 900 s (Willis, 2011), and must be locked up in the heavy elements before decaying. The only mechanism available to lock up the neutrons into nuclei is through the production of deuterium. However, deuterium is easily photodissociated at the temperatures in which the lepton era ends. Therefore, the universe needs to expand sufficiently for the temperature to drop below 2.2 MeV and prevent deuterium photodissociation (Pagel, 2009). The decay of neutrons and cooling of the universe compete in deuterium formation, restricting the amount of helium and other heavier elements that can form. Once the universe has cooled to about 80KeV, there is insufficient energy to continue producing the heavier elements, effectively halting Big Bang nucleosynthesis. Figure 1.2 shows a summary of the production yields of all the Big Bang nucleosynthesis species; showing that the production of nuclei heavier than deuterium clearly depend on the amount of deuterium with time. The total abundance (in summary) is $\sim 75\%$ hydrogen, $\sim 25\%$ helium, and trace amount of lithium and beryllium (Pagel, 2009).

1.1.2 Stellar Nucleosynthesis

Once the primordial material funnels into dark matter halos, the primordial gas cools to densities high enough to overcome thermal pressure that resists collapse. The collapse of this gas forms the first stars. In general, stars support themselves from

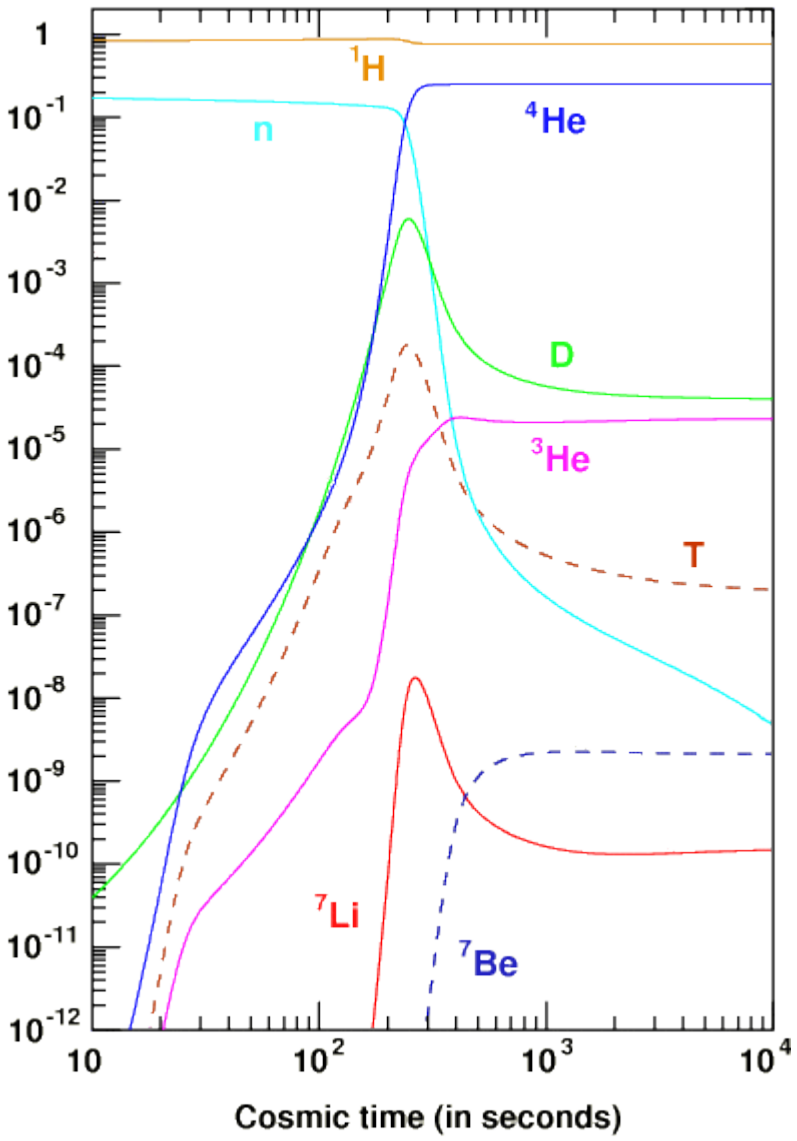

Figure 1.2 Yields (in terms of mass) of the primordial species from Big Bang nucleosynthesis as a function of time. The dependence on the amount of deuterium is clearly shown by the sudden increase in all heavier species after sufficient deuterium has formed ($\sim$ 250 s). Taken from `http://www.einstein-online.info/images/spotlights/BBN_physI/bbn_evo_en.gif`.

further gravitational collapse by the nuclear fusion (often referred to as *burning*) of material in the core. At temperatures of about 5×10^6 K, stars can convert four hydrogen nuclei into one helium nucleus through either the proton-proton (pp) chain or the CNO cycle (Burbidge et al., 1957). In brief, the pp-chain combines three hydrogen nuclei into ^{3}He, and 2 ^{3}He nuclei into ^{4}He (see Figure 1.3 for the detailed reactions of the pp-chain). The CNO cycle uses carbon, nitrogen, and oxygen as catalysts to convert hydrogen into helium (see Figure 1.4 for the reaction network). Although the pp-chain does not require the initial catalysts, it is only efficient at burning helium at a temperature $\sim 2 \times 10^7$ K, whereas the CNO cycle becomes the more favourable mechanism for producing helium at $\sim 10^8$ K (Kippenhahn & Weigert, 1994).

Following the exhaustion of hydrogen in the cores, stars continue to contract even further. If sufficiently massive cores can contract to reach temperatures of 10^8 K, helium ignites for burning. Helium burning (or the *triple alpha* process) converts helium into carbon using three helium nuclei; first by combining two helium nuclei into ^{8}Be, and then adding a third ^{4}He (e.g. Burbidge et al., 1957). However ^{8}Be is unstable at high temperatures, therefore the density and temperature of the helium-core need to be high enough such that the third helium nucleus can overcome the low cross-section of the ^{8}Be+^{4}He reaction (e.g. Carroll & Ostlie, 2006). The end result is a carbon nucleus.

Even more massive stars can undergo further contraction and burning stages using carbon (temperature of $\sim 5 \times 10^8$ K), oxygen ($\sim 10^9$ K), neon ($\sim 1.5 \times 10^9$ K), and silicon ($\sim 3 \times 10^9$ K) as fuel. Furthermore, temperatures and densities in these stars can get high enough outside the core to burn fuel in shells. This leads to a star with layers of different types of burning, and is often denoted as the onion-layer model (see Figure 1.5).

However, these onion-layered stars reach a limit to what can be burnt in the core. Silicon burning produces large amounts of nickel and iron; which cannot be further burnt as the energy resulting from the combination of two iron atoms removes energy from the core. At the end of silicon burning, the core continues to collapse as the star can no longer be supported by the temperature in the core, and the entire star collapses. This core-collapse leads to a Type II supernovae, and usually leaves a remnant neutron star or black hole. During the collapse nucleosynthesis still takes place, as a shockwave of energy rebounds off the core and passes through all the shells above it. The shockwave provides sufficient energy for all the outer shells to

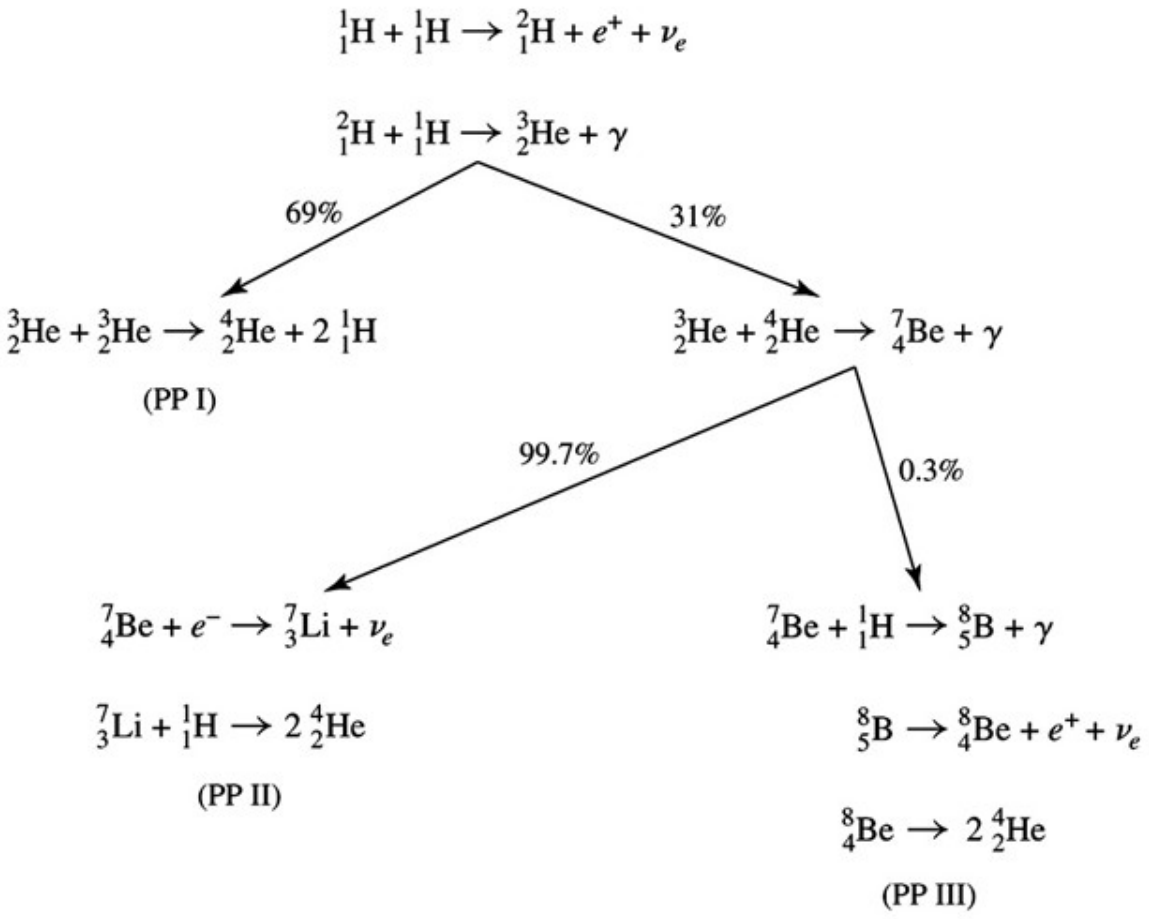

Figure 1.3 The three reaction mechanisms of the pp-chain. An estimate of the contributions of each of the three chains are shown, but are a function of the temperature of the star. Figure taken from `http://www.ap.smu.ca/~ishort/ASTR2400/pp_chain.jpg`.

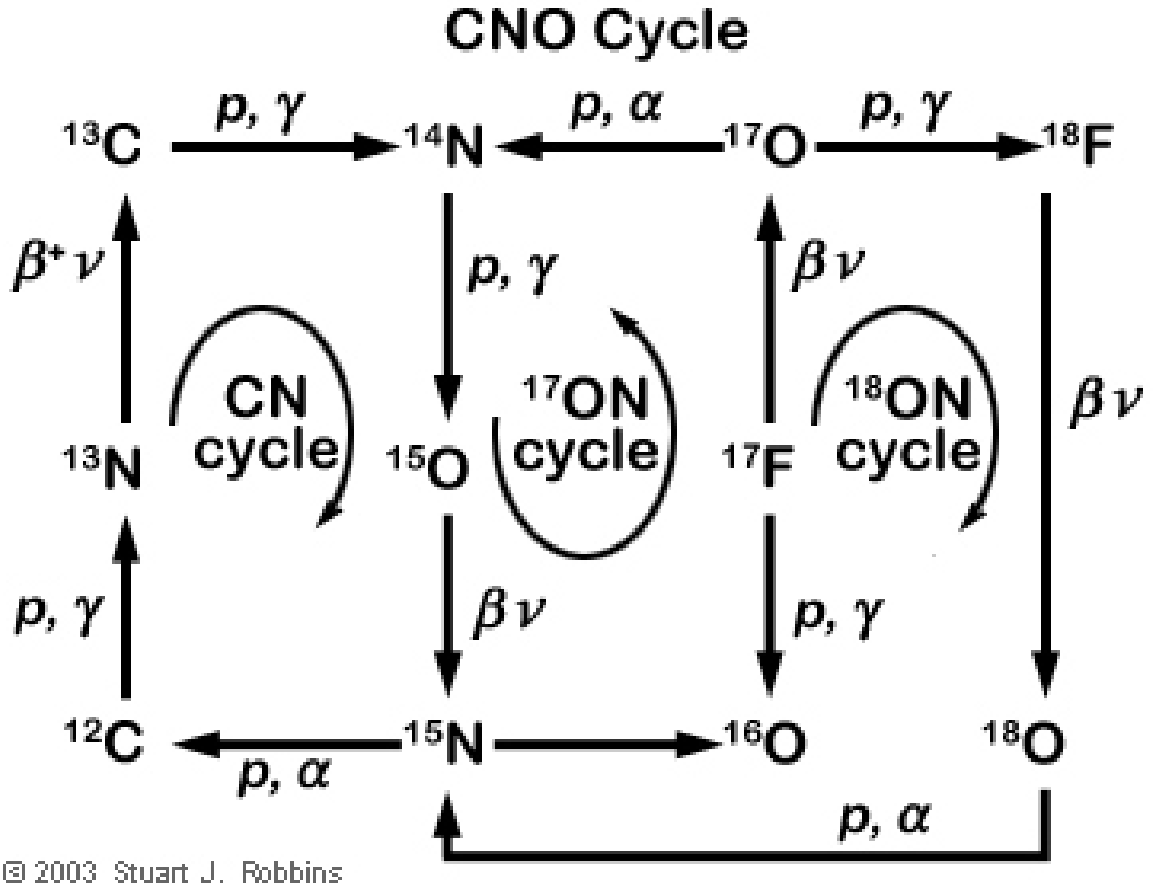

Figure 1.4 The CNO cycle mechanism. Taken from `http://jtgnew.sjrdesign.net/images/equations/cno_cycle.jpg`.

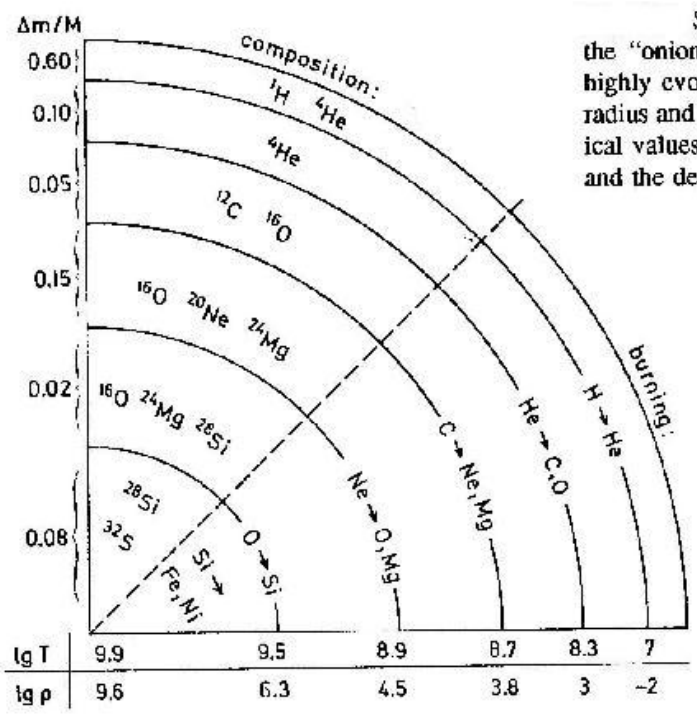

Schematic illustration (not to scale) of the "onion-skin structure" in the interior of a highly evolved massive star. Along the vertical radius and below the horizontal radius some typical values of the mass, the temperature (in K), and the density (in g cm^{-3}) are indicated

Figure 1.5 Onion-layer model of a massive star. The radial direction shows both the fraction of mass contained within the layer, as well as the temperatures and densities necessary for the various burning stages to occur. Taken from Kippenhahn & Weigert (1994).

undergo *explosive* burning, including the conversion of silicon into iron and other heavier elements.

1.1.3 Metallicity

The conversion of hydrogen and helium into heavier elements, and their dispersion into the surrounding region of the star (i.e. the *interstellar medium* or ISM) can be used as a measure of age. The more stars that evolve and explode, the more elements heavier than hydrogen or helium (typically called *metals*) are recycled into the ISM. Measuring the amount of metals within a star or gas cloud relative to the amount of hydrogen, or *metallicity* of the system, provides a clock to gauge the amount of metal enrichment. The metallicity of a system can be represented in many ways. The most common method (and the one adopted in this thesis) is to compare the number of atoms of a given element X ($n_{\rm X}$) to the number of atoms of hydrogen ($n_{\rm H}$; i.e. $\frac{n_{\rm X}}{n_{\rm H}}$[1]). As $\frac{n_{\rm X}}{n_{\rm H}}$ can range between 10^{-12} and 10^{-3} in the Sun (Asplund et al., 2009), the ratio is typically measured in logarithmic space, i.e.

$$\log({\rm X/H}) \equiv \log\frac{n_{\rm X}}{n_{\rm H}}. \tag{1.1}$$

Furthermore, log(X/H) is also made in reference to the solar abundance scale to provide a standard for comparison. This is denoted as

$$[{\rm X/H}] \equiv \log({\rm X/H}) - \log({\rm X/H})_{\odot} \tag{1.2}$$

where $({\rm X/H})_{\odot}$ is the solar abundance ratio. Typically, iron is chosen as the metallicity indicator in stars (i.e. [Fe/H]), but other elements can be used as well.

Figure 1.6 shows the evolution of the metal abundance on the surface of stars as a function of the age of the star (Timmes et al., 1995). As the surface abundance essentially represents the composition of the gas in which the star formed[2], Figure 1.6 demonstrates a monotonic relation between metallicity of a star and time. However, the relation is for a very specific set of stars, and cannot be applied to every galaxy

[1] *Column densities* (a measure of the number of atoms detected within the column that encompasses the line of sight of the observation in units of atoms cm^{-2}; denoted N(X)) can be used in place of number densities to determine the ratio of number of atoms between two species.

[2] Massive stars usually have large convective zones, bringing material up from the interior to the surface (Kippenhahn & Weigert, 1994). The up-welling of material changes the overall surface composition.

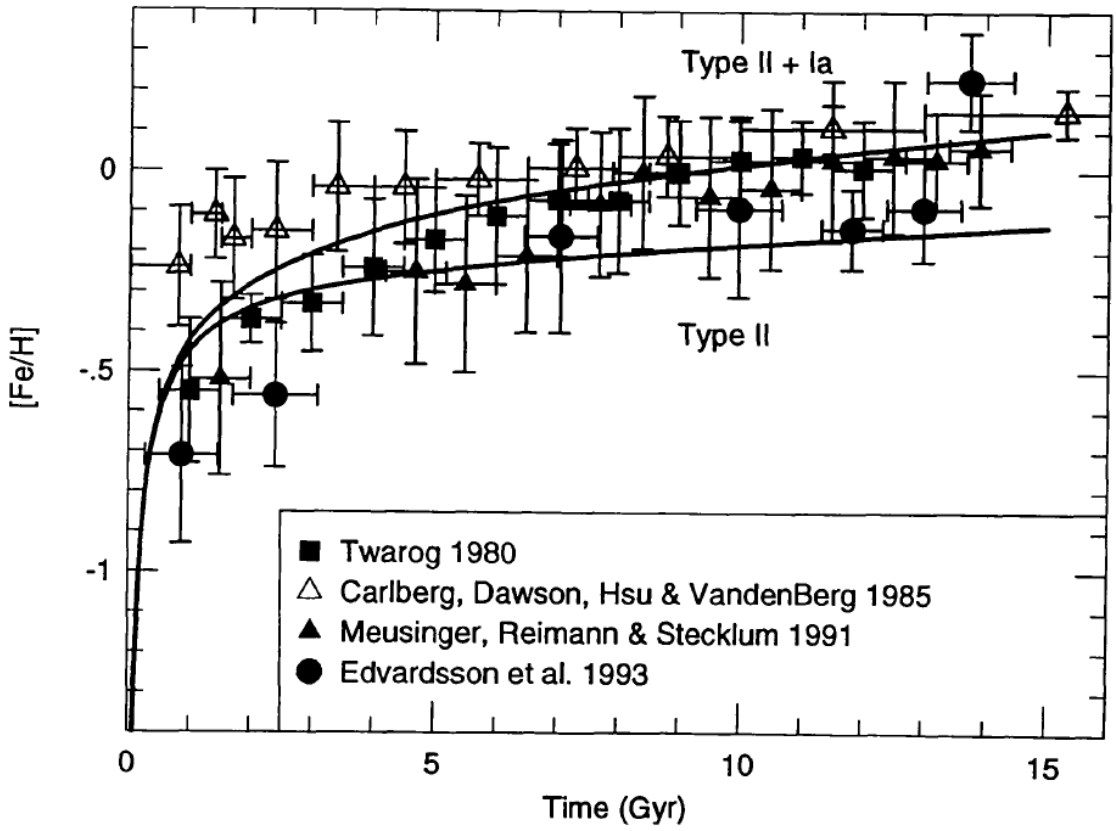

Figure 1.6 Observations (binned in time) showing the variation in metallicity ([Fe/H]) with the stellar age of solar neighbourhood stars. There is a clear monotonic relation between metallicity and stellar, age, although it is not linear. This demonstrates the idea of using metallicity as a proxy for time. Taken from Timmes et al. (1995, Figure 7).

(or region within a galaxy) as galaxies all have different masses and star formation histories.

1.1.4 Nucleosynthetic Processes and Their Chemical Signatures

A specific element typically has only one or a couple of processes associated with its nucleosynthesis. The measured abundance of any element in a star or ISM cloud can therefore hint at what processes dominated within the previous generations of stars. Although several processes can be traced through abundance determinations (such

as the amount of slow neutron capture or *s-process* material), only the two used in this thesis are highlighted; the contribution from different types of supernovae, and the amount of free neutrons.

One of the benchmarks to studying the evolution of a system is the measure of [α/Fe]. α is used to denote the *α-elements* (loosely defined as nuclei made from He nuclei; e.g. oxygen, silicon, sulphur, and magnesium), while Fe represents iron or the *iron-peak elements*[3] (e.g. iron, nickel, chromium, and zinc). In general, the most massive stars ($> 8M_{\odot}$) that explode as Type II supernovae (SNe II) dominate the production of α-elements, whereas Type Ia supernovae (SNe Ia) dominate the production of iron. Furthermore, the most massive stars are the quickest to evolve (lifetimes of $< 2 \times 10^7$ years), thus SNe II precede the lower mass binary systems responsible for SNe Ia (with lifetimes of 10^8 years; Tinsley, 1979).

Figure 1.7 shows a schematic of the expected evolution of [α/Fe] in a population (from McWilliam, 1997). The supersolar [α/Fe] 'plateau' at the lowest metallicities results only from the contributions of SNe II whereas the 'knee' at [Fe/H]~ -1 indicates when SNe Ia start to contribute iron to the system (cf. Tinsley, 1979; McWilliam, 1997; Tolstoy et al., 2009). The height of the [α/Fe] plateau and the metallicity of the knee are not fixed, and depend on the initial mass function (the number of stars of a given mass that form in a star forming cloud; IMF) and the rate of star formation (SFR; McWilliam, 1997). Increasing the number of massive stars that initially form will result in an increase in the number of α elements produced (e.g. see yields from Woosley & Weaver, 1995), driving [α/Fe] upwards (see Figure 1.7). If the star formation rate is high, the increase in the total number of stars will increase the metallicity of the system. Therefore, SNe Ia start to contribute at higher metallicities, pushing the knee in Figure 1.7 to higher metallicities. In summary, [α/Fe] provides an idea of the evolutionary history of a system, where a higher value of [α/Fe] corresponds to a system which was enriched primarily of the most massive stars.

Another tell-tale signature of the first stars evolving is the ratio of elements with odd and even atomic numbers (denoted with Z), also called the *odd-even* effect. As there are fewer metals in the first galaxies, there is a lack of extra neutrons (which come from the breaking apart of metals) to supply metals with an odd number of nuclei (Arnett, 1971). Therefore, the first generations of massive stars are thought to

[3]The term iron-peak refers to the maximum in the amount of binding energy as a function of atomic number Z; which peaks at iron and nickel. This maximum is the same reason why iron does not burn in stars as the binding energy of the next heaviest element is much less than iron itself.

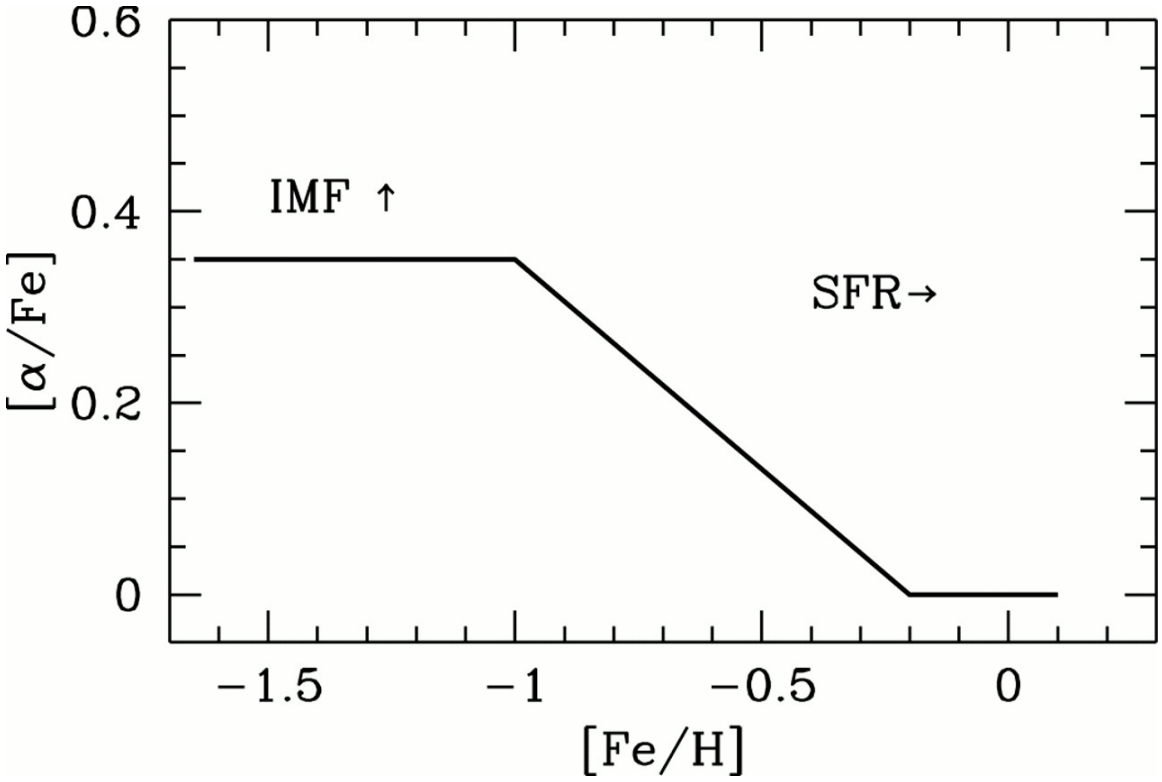

Figure 1.7 Schematic diagram showing the evolution of [α/Fe] with metallicity (Figure 1 from McWilliam, 1997). The plateau of [α/Fe] at low metallicities results from the contribution of only SNe II. The onset of SNe Ia at [Fe/H]$= -1$ decreases [α/Fe], forming the knee. The effects of making the IMF top-heavy (i.e. more massive stars) drives the plateau to higher values of [α/Fe] while higher star formation rates push the knee to higher metallicities.

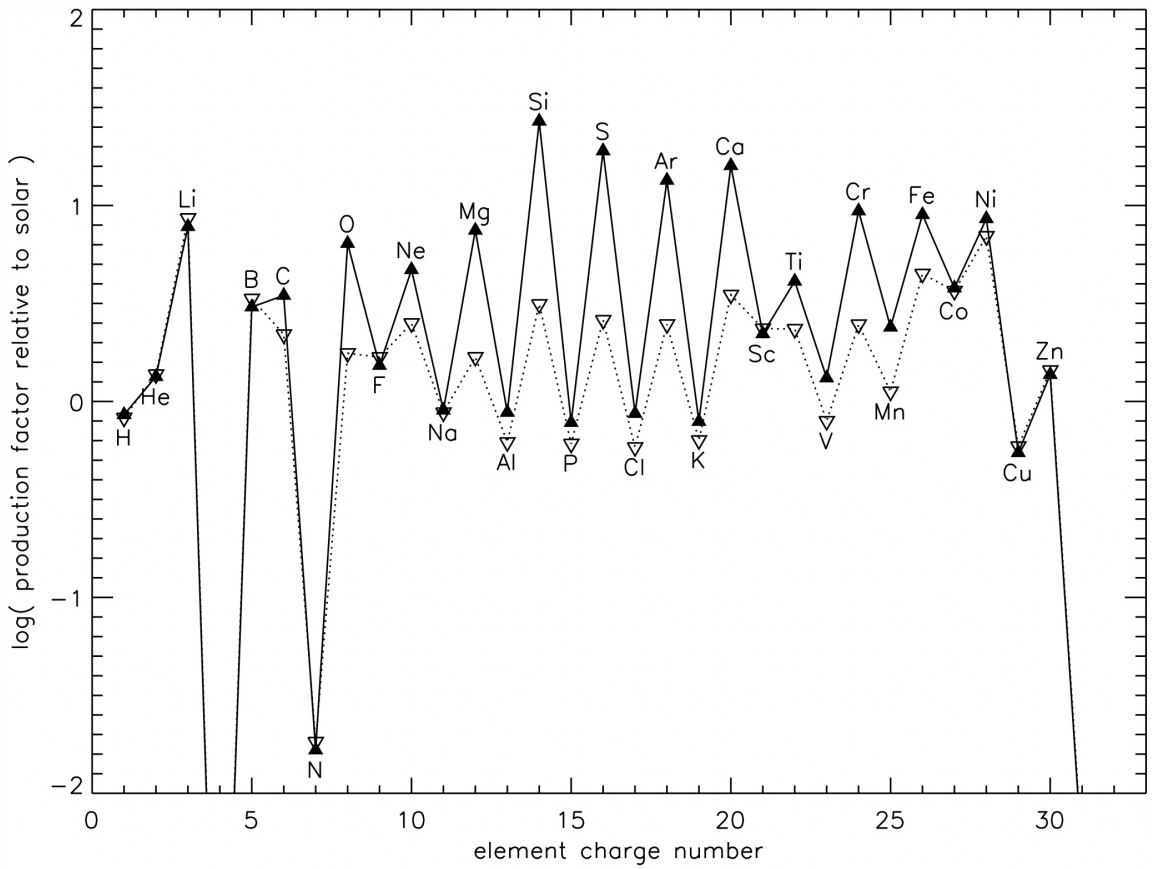

Figure 1.8 Nucleosynthetic yields as a function of Z from a metal-free star simulation (Figure 4 from Heger & Woosley, 2002). The unfilled triangles/dotted line represent the yields from 12-40 $M_{\odot}$ stars, whereas the solid triangles/lines also include 140-260 $M_{\odot}$ stars. Enhancements of the even-Z elements highlights the apparent odd-even effect. The higher mass stars show a stronger odd-even effect relative the lower mass stars.

have large enhancement in even elements with respect to the odd-Z nuclei (e.g. Heger & Woosley, 2002, see Figure 1.8). Observations of atomic ratios such as [Mn/Fe] or [P/Si] can constrain whether a system has had few generations of stars (e.g. Prochaska et al., 2003d; Caffau et al., 2011).

1.2 Milky Way Populations

Within the Milky Way itself, there are regions identified to have distinct chemical and kinematic properties (cf. McWilliam, 1997; Venn et al., 2004), i.e. the bulge, the disk,

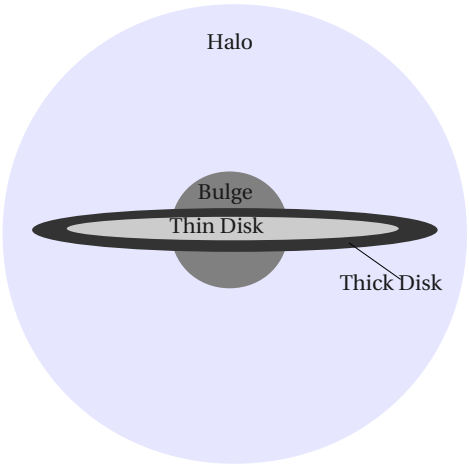

Figure 1.9 Cartoon representing the different populations of stars within the Milky Way.

and the halo (see Figure 1.9 for a schematic of the Milky Way). Overall, models that demonstrate the chemical evolution of the galaxy (e.g. van den Bergh, 1962; Schmidt, 1963; Larson, 1972; Hartwick, 1976) must match the chemistry observed in the bulge, disk, and halo (such as metallicity gradients, and [α/Fe] trends). Once in place, these models can help discern between different formation mechanisms of the Milky Way, whether it formed out of a rotating clump of gas (Eggen et al., 1962) or in multiple accretion events of smaller satellites (Searle & Zinn, 1978). The following sections describe the observed properties of each of the regions in the Milky Way system and what their chemistry implies about their formation.

1.2.1 Bulge

The Galactic bulge is believed to have formed partly from the initial collapse of gas into the Milky Way dark matter halo, and (primarily) through infalling material originating from mergers or gas transferred from the halo and disk (Wyse & Gilmore, 1992; Mo et al., 2010). As a result, the stars located within the bulge are believed to be a mix of young and old stars, ranging in metallicities between $-0.5 \lesssim$[Fe/H]$\lesssim 0.5$ (with a median metallicity near [Fe/H]~ -0.25; McWilliam & Rich, 1994; Zoccali et al., 2003; Fulbright et al., 2006). Measurements of [α/Fe] in bulge stars show

enhancements in α-elements ([α/Fe]$\sim$ 0.1$-$0.4 dex; Terndrup et al., 1995; Sadler et al., 1996), and are discrepant with all other stars within the other Galactic populations (i.e. halo and disk; see below). Although it is difficult to assess when the bulge formed (from the odd combination of high metallicities and high [α/Fe]), it is believed that the bulge formed on a rapid time scale from enriched infall material (McWilliam, 1997).

1.2.2 Disk

The disk of a galaxy refers to the rotating plane of stars embedded within gas, and is the location where the majority of stars are formed. Observations of the kinematics and metallicities of the Milky Way disk stars have revealed a bifurcation in the data (Gilmore & Reid, 1983; Edvardsson et al., 1993), where the metal-poor ($-1 \leq$[Fe/H]≤ -0.4) population of disk stars have a larger velocity dispersion (as well as a larger scale height) out of the plane of the disk ($|\mathrm{W}| \leq 40$ km s^{-1}; scale height $h \sim 1$ kpc) compared to the metal rich disk stars ($-0.8 \leq$[Fe/H]≤ 0.2; $|\mathrm{W}| \leq 20$ km s^{-1}; $h \sim 0.3$ kpc) (Edvardsson et al., 1993). This bifurcation has been suggested to be two different components of the Milky Way's disk; a *thick* and *thin* disk (respectively). The thin disk is believed to host the current star formation that produces the youngest stars in the Galaxy, and arises naturally from the infall of gas during galaxy formation. The gas collapsing into the centre of the Galactic dark matter halo loses energy through dissipation and cools down into a thin disk through the conservation of angular momentum (cf. Freeman & Bland-Hawthorn, 2002; Mo et al., 2010). After the gas settles and forms the first thin disk stars, it is believed that mergers of satellites perturbed the thin disk stars into the thick disk (Freeman & Bland-Hawthorn, 2002; Mo et al., 2010). Since the thin and thick disk have slightly different chemical properties (i.e. the thick disk stars are older, and thus have a slightly higher α-element content and lower metallicity than the younger thin disk stars), they are treated as two separate populations. Despite being two separate populations, both the thin and thick disk stars define the location of the 'knee' in the [α/Fe]-[Fe/H] plot (Figure 1.7) of the Milky Way (e.g. McWilliam, 1997).

1.2.3 Stellar Halo

Beyond the Milky Way's disk is the stellar halo, which consists of the oldest and most metal-poor stars in the galaxy (e.g. McWilliam, 1997; Freeman & Bland-Hawthorn,

2002). The halo is thought to have formed from the merger of dark matter subhalos that led to the formation of the Milky Way, leaving the stars that originally formed within these subhalos as part of the Milky Way's halo (Searle & Zinn, 1978; Freeman & Bland-Hawthorn, 2002). As stars in the halo are metal poor, they are thought to have formed before the ISM had a chance to be polluted by SNe Ia (McWilliam, 1997), thus naturally have high [α/Fe]. With the minimum metallicity of stars in the disk being [Fe/H]$\gtrsim -1.5$ (Wyse & Gilmore, 1995), a metallicity cut is often used rather than a velocity cut to determine whether a star is part of the disk or the halo (e.g. Frebel, 2010). Nevertheless, halo stars are mostly characterized by low metallicities with enhanced [α/Fe] (i.e. on the plateau in Figure 1.7, McWilliam, 1997).

1.2.4 Satellite Galaxies

Lastly, many stars have been studied outside the Milky Way in small satellite, dwarf galaxies. Dwarf galaxies all vary in their levels of star formation (Pagel, 2009), and contain varying amounts of gas (see McConnachie, 2012, for some of the satellites' properties). These dwarf galaxies are thought to be part of the buildup of mass in large galaxies through mergers in the ΛCDM paradigm, where smaller structures merge to form larger ones (Searle & Zinn, 1978). Depending on the galaxy type (e.g. dwarf spheroidals, dwarf irregulars, dwarf ellipticals), they have different amounts of gas and different star formation histories (cf. Mo et al., 2010); thus providing entirely different populations than the Milky Way has (e.g. Tolstoy et al., 2009).

To emphasize the difference in the populations, Figure 1.10 shows [α/Fe] as a function of metallicity in a variety of dwarf spheroidal galaxies (dSphs; coloured points representing different dSphs) compared to the Milky Way (grey points) from Tolstoy et al. (2009). As alluded to in Section 1.1, the height of the plateau and the metallicity location of the knee are controlled by the contribution of massive stars in the IMF and the star formation rate. In the Milky Way, [α/Fe] remains high in the halo at 0.4 dex, and decreases to solar in the thin disk. However, the transition from this plateau begins at [Fe/H]$\gtrsim -1$ (i.e. where the disk stars contribute) and corresponds to SNe Ia contribution to iron production. For each of the dwarf galaxies there appears to be not only a different metallicity where the plateau ends, but possibly even a different final [α/Fe] at solar metallicities, suggesting that the star formation histories are much different in dwarfs than in the Milky Way (e.g. Tolstoy et al., 2009).

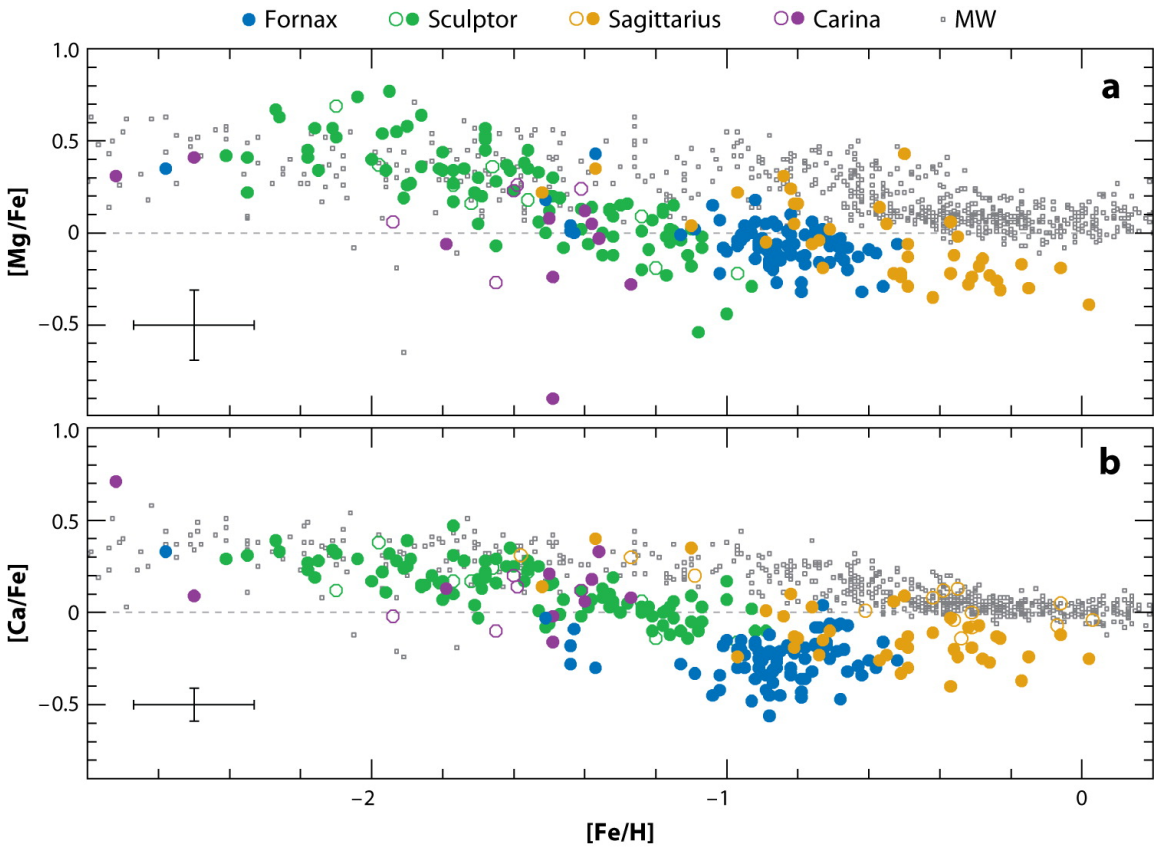

Tolstoy E, et al. 2009.
Annu. Rev. Astron. Astrophys. 47:371–425

Figure 1.10 [α/Fe] vs. [Fe/H] in the Milky Way (grey points) and dSphs (coloured points). The difference in the location of the knee for the Milky Way and dSphs suggests that dSphs have undergone a quicker burst of star formation relative to the Milky Way. Figure taken from Tolstoy et al. (2009). Filled circles represent dSph stars observed with multi-slit spectroscopy, while the unfilled circles are for observations done with a single slit.

1.3 Damped Lyman Alpha Systems

The study of chemical abundances in stars is limited to stars that are sufficiently bright enough to be studied at high resolution. Currently, these stars are limited to the Milky Way and its satellite galaxies, making it impossible to observe the detailed chemistry of stars in the early universe. Therefore, an alternative method must be sought. One possibility is observing gas in high redshift galaxies; however this gas needs to be either very bright in emission or illuminated by a bright background source and seen in absorption. The latter proves to be successful using quasars as the illuminating source. One can imagine with the large number of quasars and galaxies in the universe that it is possible for clouds of gas (whether they are merging clumps forming a galaxy, or reside within a galaxy) to serendipitously lie in front of a quasar along a sightline from Earth. These systems are called quasar absorption line systems (QALs; Figure 1.11).

There are many different categories of QALs; some detected through singly ionized magnesium absorption (MgII systems, e.g. Sargent et al., 1988; Lanzetta & Bowen, 1990; Nielsen et al., 2013) or other metal species, and others from neutral hydrogen (HI) absorption (e.g. Wolfe et al., 1986; Lanzetta et al., 1991; Wolfe et al., 1995; Ellison et al., 2001c; Prochaska & Herbert-Fort, 2004; Noterdaeme et al., 2012c). Of the HI absorption systems, there are many sub-classifications depending on the column density of HI (usually represented as N(HI), or logN(HI)). Below column densities of N(HI)$\sim 10^{17}$ atoms cm^{-2}, clouds of gas are optically thin at the Lyman limit (but can still be saturated in Lyα), and are known as Lyα forest clouds (seen in the spectrum of Figure 1.11 as 'noise' at wavelengths < 4900 Å). The next class of QALs are Lyman limit systems, ranging between 10^{17} <N(HI)$< 2 \cdot 10^{20}$. Lyman limit systems are optically thick at the Lyman limit with saturated Lyα absorption profiles.

Damped Lyman alpha systems (DLAs) are the HI absorbers with the highest column densities of neutral hydrogen. By definition, a DLA has a column density of N(HI)$\geq 2 \cdot 10^{20}$ atoms cm^{-2} (or logN(HI)$= 20.3$) (Wolfe et al., 1986). DLAs can be identified in low resolution ($\Delta\lambda \sim 5$ Å) spectra by the damped Lyman α absorption at 1215 Å in the rest frame. Due to the high column density of HI, the line is *damped* as broadening of the absorption profile's wings are dominated by the Heisenberg uncertainty principle ($\Delta E \cdot \Delta t > \hbar/2$; where ΔE represents the difference in wavelength from the expected transition) rather than thermal (or *Doppler*) broadening (e.g. Wolfe

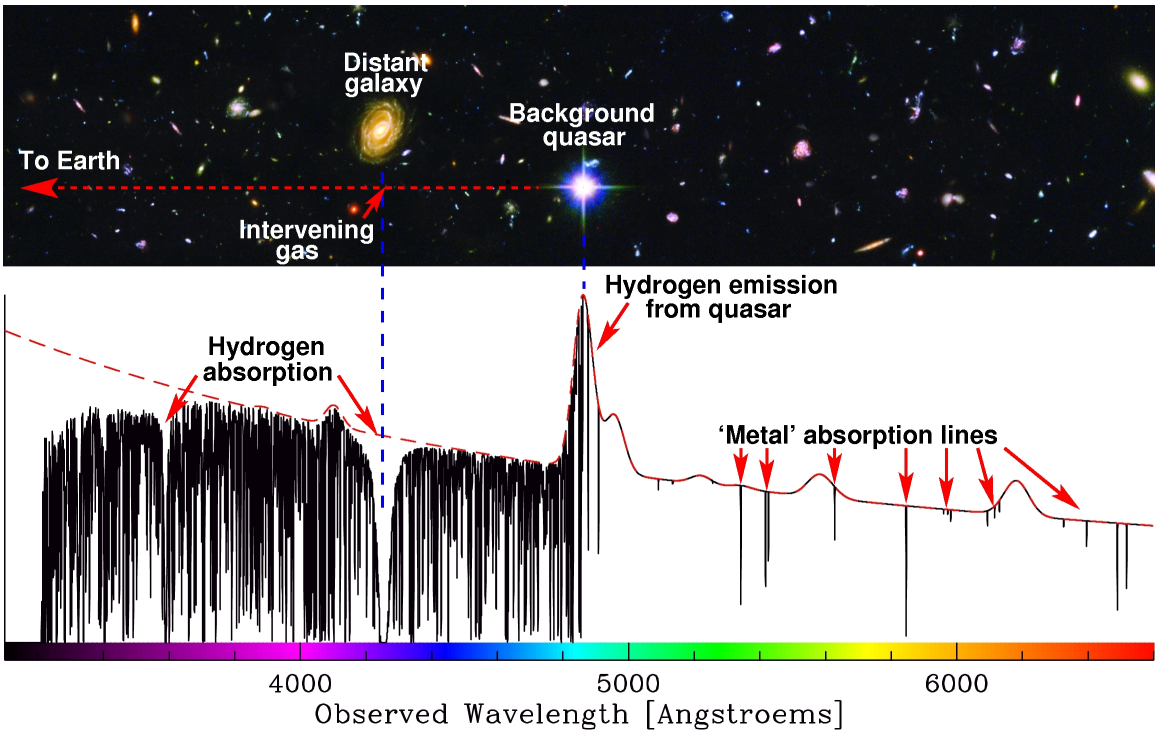

Figure 1.11 Cartoon showing a quasar absorption line system. Light from the background quasar travels through gas within a galaxy-sized object, resulting in hydrogen absorption in the observed spectrum. If strong metal absorption lines are present in the medium, they will also appear in the observed spectrum. Figure taken from `http://www.eso.org/~jliske/qsoal/qsoabs.jpg`.

et al., 2005).

Even though the minimum column density of DLAs was somewhat arbitrarily set, it corresponds to approximately the density required for a cloud of gas to be *self-shielded* to background photons with energies greater than 13.6 eV (Wolfe et al., 1986, 2005). With the outer layers of the DLA clouds absorbing all the ionizing photons from external sources such as external galaxies and quasars, the interiors of the clouds remain mostly neutral (although ionizing radiation is present from stars within the clouds). Therefore the content of DLAs is assumed to be dominated by gas in a neutral state. However, any metals within the cloud will be in the ionization state characterized by the *ionization potential* (IP) of the element in question (see Table 1.1 for a list of IPs for various elements). As photons with energies lower than 13.6 eV will penetrate the DLA, the dominant ionization state would be that with the smallest IP that is greater than 13.6 eV. As an example, neutral iron (FeI) has an IP of 7.87 eV while singly ionized iron (FeII) has an IP of 16.18 eV (see Table 1.1). As FeI would become ionized by photons with energies less than 13.6 eV, it would remain in the FeII state within the DLA cloud. However, it is possible for clouds within a DLA to be dense enough to shield neutral metals (such as FeI and SiI) from the 13.6 eV ionizing energy (D'Odorico, 2007).

Although DLAs are much fewer in number compared to Lyman limit systems (Sargent et al., 1989; Péroux et al., 2001), they dominate the neutral gas content of the universe at early redshifts (e.g. Noterdaeme et al., 2012c). This has led people to believe that DLAs are the progenitor systems of disk galaxies such as the Milky Way (Wolfe et al., 1986). However, the lack of strong evolution in DLA metallicity at low redshifts in conjunction with metallicities being significantly less than the Milky Way disk at low redshifts (Meyer & Roth, 1990; Pettini et al., 1997) has led to suggestions that DLAs could also be dwarfs. Studies of the kinematic structure of DLAs both support that either disks (Prochaska & Wolfe, 1997c) or merging dwarf galaxies (Haehnelt et al., 1998) can explain the velocity profiles of DLAs. Imaging of the galaxies responsible for DLA absorption has been successful (e.g. Chen & Lanzetta, 2003; Péroux et al., 2011; Rao et al., 2011; Fynbo et al., 2013; Krogager et al., 2013) and has shown that DLAs probe a range of different morphologies, including unstable star forming galaxies with large outflows (e.g. Fynbo et al., 2013; Kashikawa et al., 2014; Krogager et al., 2013). Overall, the combination with the large spread in metallicities, DLAs probe galaxies with a variety of star formation histories and galaxy morphologies (Lu et al., 1996a).

Table 1.1 Ionization potentials of various elements

Element	I (eV)	II (eV)	III (eV)
H	13.6	. . .	. . .
B	8.30	25.2	93.9
C	11.3	24.4	48.9
O	13.6	35.1	54.9
Al	5.99	18.8	28.4
Si	8.15	16.3	33.5
P	10.5	19.8	30.2
S	10.4	23.3	34.8
Ca	6.11	11.87	50.9
Ti	6.82	13.6	27.5
Cr	6.77	16.5	31.0
Mn	7.43	15.6	33.7
Fe	7.87	16.2	30.7
Ni	7.64	18.2	35.2
Zn	9.34	17.9	39.7

Reference–Morton (2003)

Much of the early work on metals in DLAs focused on looking at how the metal content of DLAs evolved with redshift (e.g. Meyer & Roth, 1990; Lu et al., 1996a; Pettini et al., 1997; Prochaska et al., 2003b). Combining the three decades of work on metallicity evolution of DLAs with redshift, Rafelski et al. (2012) and Rafelski et al. (2013) have shown a steady increase in metallicity with decreasing redshift (see Figure 1.12). This increase is contrasted by the nearly constant density of the HI gas present in DLAs that is available for star formation (Lanzetta et al., 1995; Wolfe et al., 1995; Prochaska & Herbert-Fort, 2004; Noterdaeme et al., 2012c)[4], suggesting that the gas is being replenished with time as DLAs evolve. Overall, DLAs present themselves as good opportunities to study the cosmic metallicity evolution (Rafelski et al., 2012, 2013), as well as the evolution of particular elements (e.g. Pettini et al., 1994, 1997; Prochaska & Wolfe, 2002).

1.4 Overview

The purpose of this thesis is to investigate the detailed chemistry of DLAs and attempt to understand their significance in both galaxy and chemical evolution within the early universe. As highlighted in this chapter, the comparison of elemental abundances derived for the local universe and in DLAs will provide a sense of the underlying stellar populations that contribute to the gas of DLAs and the evolution of galaxies.

The difficulty in such a comparison arises from the metallicity range of DLAs with respect to the different Galactic components described (i.e. the halo, disk, and satellites). As an example, Pettini et al. (1997) demonstrated that DLAs do not span the same metallicity range of the Galactic disk or the metal-poor component of the halo (see Figure 1.13). Therefore, to aid the comparison of abundances between DLAs and stars in the metal-rich (by comparison) Galactic disk, a further population of the most metal-rich DLAs needs to be used.

In order to provide a meaningful comparison with the stars in the Galactic disk and satellites, this thesis utilizes a class of DLAs with the highest metal-contents. Furthermore, the study of rare elements (such as boron) can be used to constrain very specific environmental processes. However, these rare elements are hard to detect in typical DLAs with low metal contents, but are more likely to be measured in DLAs with high metal contents (e.g. Prochaska et al., 2003d). From the abundances

[4]Although the work done by (Lanzetta et al., 1995) initially suggested a slight decrease in the amount of HI gas with decreasing redshift, especially for the higher column density systems.

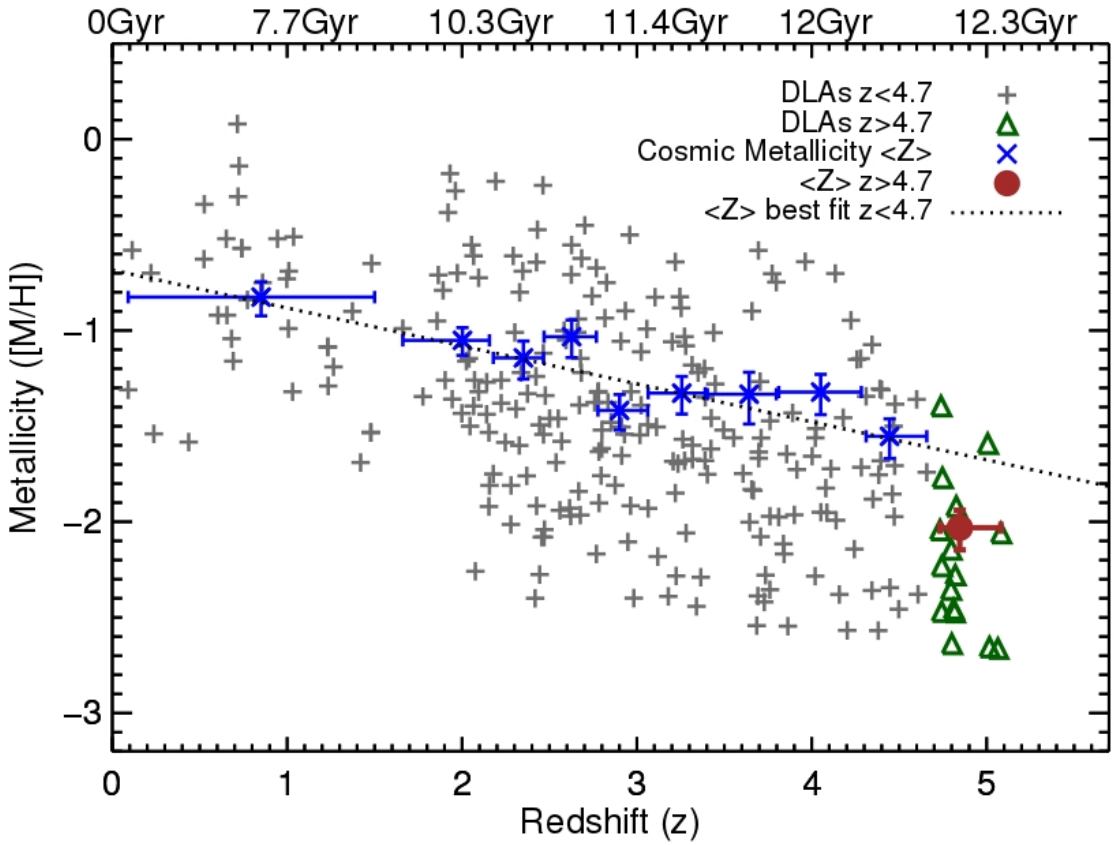

Figure 1.12 Metallicity ([M/H]) evolution of DLAs with redshift. Figure taken from Rafelski et al. (2013). Other than at redshifts higher than $z > 4.7$, there is a steady increase in metallicity with decreasing redshift.

measured in these high metal-content systems, constraints can be placed both on the chemical evolution of galaxies at high redshifts, as well as the nucleosynthetic origin of the elements.

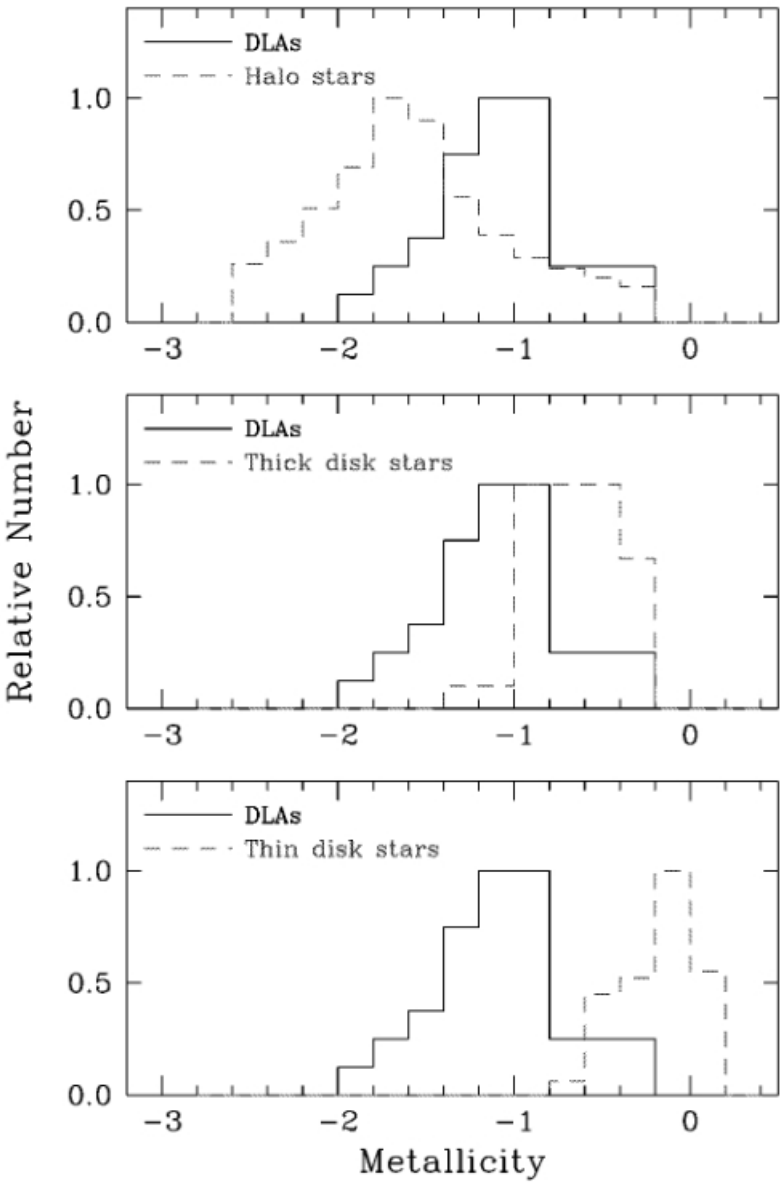

Figure 1.13 Metallicity distribution function of DLAs spanning $0 \lesssim z_{\rm abs} \lesssim 3.5$ (using [Zn/H] as metallicity indicator) in comparison with the thin disk, thick disk, and halo distributions (using [Fe/H] as the metallicity indicator; figure taken from Pettini et al., 1997). Pettini et al. (1997) demonstrated that DLAs have the most significant overlap in metallicity with Galactic halo stars, rather than the Galactic disk population.

Chapter 2

Data Compilation and Abundance Measurements

As stated in Chapter 1, the goal of this thesis is to compare the chemical abundances of the gas in high redshift galaxies, as traced through DLAs, with stars within the local population. This chapter focuses on selecting the abundances required for making comparisons of abundances from stars and DLAs. First, the largest compilation of DLA abundances from the literature is defined (Section 2.1) in order to compare with the chemical abundances of stars observed in the local populations (Section 2.2) and emphasize the necessity to probe DLAs with higher metallicity sightlines. Section 2.3 describes the observations of the main DLA sample of this thesis and presents the abundances used throughout the rest of this work. This thesis sample is then shown to bridge the gap in metal content between the stars and DLAs.

2.1 DLA High Resolution Literature Sample

To represent the chemistry of DLAs while providing a useful comparison to stars, a literature sample of DLAs is needed. The literature on DLAs spans nearly four decades of work, using many different telescopes and spectrographs. The first surveys searching for DLAs (Wolfe et al., 1986; Sargent et al., 1989; Lanzetta et al., 1991) used low resolution spectrographs to identify quasars with DLAs and measure the HI column densities to study the evolution of HI. Although DLAs and their metal contents were previously identified prior to the aforementioned large surveys (e.g. Morton et al., 1980), nucleosynthetic studies of DLAs shortly followed the large surveys (Meyer &

York, 1987; Meyer et al., 1989). The first systematic studies of metals were done by Pettini and collaborators (Pettini et al., 1990, 1994, 1997) with the Hale, William Herschel, and the Anglo-Australian telescopes. However, these studies of DLAs did not provide sufficient resolution[1] to confirm that the measured column densities were free of blending (especially with Lyα forest lines within the DLA profile) and unseen saturation in the metal line profiles.

The use of 8-10 m class telescopes by the mid-1990s furthered the studies of DLAs as fainter, higher redshift QSOs and their companion DLAs could be observed with reasonable exposure times (e.g. Storrie-Lombardi & Wolfe, 2000). With the advent of High Resolution Echelle Spectrometer (HIRES; Vogt et al., 1994) and Echellete Spectrograph and Imager (ESI; Sheinis et al., 2002) on the 10 m Keck telescopes, higher resolution observations could resolve the Lyα forest and metal lines clearly and provide more accurate abundances (although ESI still does not have the resolution to determine if lines contain saturated components). Followup surveys of the initial DLA catalogues, as well as targeting fainter background QSOs, were initiated by Prochaska and collaborators (Prochaska & Wolfe, 1996, 1997c; Prochaska et al., 2001a). This body of work has led to enormous databases of both HI column densities and metal abundances in DLAs (Prochaska et al., 2001b, 2003c; Penprase et al., 2010). The addition of the Very Large Telescope (VLT) has also opened up detailed observations of DLAs (e.g. Dessauges-Zavadsky et al., 2004, 2006; Akerman et al., 2005).

The DLA literature catalogue compiled for this work (further denoted as the *HR literature DLA sample*) contains all the DLAs which have had high-resolution observations completed. High resolution observations are necessary to ensure all the weak absorption components of the velocity profile are resolved such that: (i) line blending can be detected, and (ii) absorption features are free from saturation. Overall, high resolution observations lead to accurate abundance measurements. Typical velocities of individual clouds have a Doppler parameter of $b \sim 10$ km s^{-1} (cf. Péroux et al., 2008; Krogager et al., 2013). To resolve these clouds a resolution of $R = \frac{\lambda}{\Delta\lambda} \sim \frac{c}{b} \sim 30000$ is required. In addition, quasars are faint and require long exposures (at least 1 hour on 8-10m class telescopes; see Section 2.3) to detect weak metal lines, limiting the selection to observations completed with echelle spectrographs on the largest telescopes, i.e. Keck/ESI, Keck/HIRES, VLT/UVES (Ultraviolet and Visual Echelle Spectro-

[1]However, studies of individual sightlines were completed with high resolution echelle spectrographs on 4-m class telescopes (e.g. Carswell et al., 1987; Bergeron & Boissé, 1991; Savaglio et al., 1994; Roth & Blades, 1995; Pettini et al., 1995; Meyer et al., 1995).

graph; Dekker et al., 2000), or VLT/X-SHOOTER (Vernet et al., 2011). The HR literature sample was first assembled by Miroslava Dessauges-Zavadsky for the work in Dessauges-Zavadsky et al. (2009), and has now been updated to date in this thesis with all relevant literature since 2010.

The HR literature DLA sample (Table A.1) includes the emission and absorption redshifts of the DLAs, and the column densities of HI and several other commonly observed metals. Table 2.1 contains a list of the metal ions and transitions that are commonly measured in DLAs. There is a good representation of α elements (Mg, S, Si, Ti) and Fe-peak elements (Fe, Zn, Mn, Cr, Co, Ni) within this sample. The wavelengths and oscillator strengths[2] of the commonly observed lines are also included in Table 2.1.

Within the HR literature, there are several occasions when the same DLA has been observed and analysed by at least two different authors. All values were checked for consistency with each other by comparing the sum of the errors between two measurements with the difference in the two measured column densities. A preference was given to column densities derived with Voigt profile fitting[3], which simultaneously fits multiple transitions for multiple elements to identify the shape of the absorption profile, although the other method generally used (the Apparent Optical Depth method) provides identical abundances for clean lines to Voigt-profile fitting (Wolfe et al., 1994; Prochaska & Wolfe, 1997a; Lopez et al., 2005a). The profile fitting software only uses non-blended components as the expected absorption profile is common to all species; which effectively removes blending. Profile fitting provides a more accurate representation of the column density than summing the optical depths of the lines individually and attempting to account for blending by only selecting non-blended parts of the profile. In addition, abundances derived with HIRES or UVES are preferentially selected as they are more likely to resolve all clouds, whereas ESI or XSHOOTER may contain an unseen saturated component. All references are included in Table A.1, even if their derived column density was not adopted as the final value in the compilation. With the large number of references in this compilation, there are possible systematic errors that arise from adopting different oscillator strengths for the transition

[2]The oscillator strength is defined as the ratio of observed and theoretical equivalent widths of an absorption line. This represents the correction required if one were to assume that the electron behaves like classical oscillator. Generally, errors in the oscillator strength are not included in DLA work. However, large discrepancies in the oscillator strength may result in substantial differences in the measured column densities (e.g. see discussion in Pettini et al., 2000).

[3]E.g. VPFIT; http://www.ast.cam.ac.uk/∼rfc/vpfit.html

Table 2.1 Ions observed in the DLA HR literature sample. Each ion includes a list of the typically observed lines and the corresponding oscillator strengths.

Ion	λ (Å)	f	Ion	λ (Å)	f
OI	1302.1685	4.80×10^{-2}	MnII	2606.462	1.98×10^{-1}
OI	1355.5977	1.16×10^{-6}	MnII	2576.877	3.61×10^{-1}
NI	1134.1653	1.46×10^{-2}	MnII	2594.499	2.80×10^{-1}
NI	1134.4149	2.87×10^{-2}	FeII	1608.4511	5.77×10^{-2}
NI	1134.9803	4.16×10^{-2}	FeII	1611.2005	1.38×10^{-3}
MgI	2026.4768	1.13×10^{-1}	FeII	1901.7730	7.00×10^{-5}
MgI	2852.9642	1.83×10^{0}	FeII	2249.8768	1.82×10^{-3}
MgII	2796.352	6.16×10^{-1}	FeII	2260.7805	2.44×10^{-3}
MgII	2803.531	3.06×10^{-1}	FeII	2344.2140	1.35×10^{-1}
AlII	1670.7874	1.74×10^{0}	FeII	2374.4612	3.12×10^{-2}
AlIII	1854.7164	5.59×10^{-1}	FeII	2382.7650	3.20×10^{-1}
AlIII	1862.7895	2.78×10^{-1}	FeII	2586.6500	6.91×10^{-2}
SiII	1260.4221	1.18×10^{0}	FeII	2600.1729	2.39×10^{-1}
SiII	1304.3702	8.63×10^{-2}	CoII	1466.2120	3.10×10^{-2}
SiII	1526.7066	1.33×10^{-1}	CoII	1574.5503	2.50×10^{-2}
SiII	1808.0130	2.08×10^{-3}	CoII	1941.2852	3.40×10^{-2}
SII	1250.584	5.43×10^{-3}	CoII	2012.1664	3.68×10^{-2}
SII	1253.811	1.09×10^{-2}	NiII	1370.131	7.69×10^{-2}
SII	1259.519	1.66×10^{-2}	NiII	1709.6042	3.24×10^{-2}
TiII	1910.750	1.02×10^{-1}	NiII	1741.5531	4.27×10^{-2}
CrII	2056.2539	1.03×10^{-1}	NiII	1751.9157	2.77×10^{-2}
CrII	2062.234	7.59×10^{-2}	ZnII	2026.136	5.01×10^{-1}
CrII	2066.161	5.12×10^{-2}	ZnII	2062.664	2.46×10^{-1}

Reference–Morton (2003)

and continuum placement (specifically for HI measurements and weak lines; further discussion will be completed in Section 2.3). However, these effects were generally unnoticeable as the column densities derived between studies were consistent.

Overall, the HR literature sample contains 340 DLAs[4]. The sample is the largest compilation of high resolution data on the metal content of DLAs to date. However, there are much larger catalogues of DLAs (nearing 7000 DLAs) that have been identified in the Sloan Digital Sky Survey (SDSS; such as Noterdaeme et al., 2009, 2012c). Many of the larger catalogues contain only HI column densities and have not had any follow up high resolution observations to obtain detailed chemical composition. To demonstrate the characteristics of the HR literature sample, Figures 2.1 – 2.3 show the distribution of hydrogen column density, metallicity, and absorption redshift (respectively) for the HR literature DLAs.

It is shown in Figure 2.1 that the DLA sample spans a large range in HI column densities. However, there is a noticeable decrease in the number of DLAs as the HI column density increases, making the most HI-rich DLAs very rare. In comparison to the Noterdaeme et al. (2012c) sample of 6839 DLAs (black dashed line); the overall shape of the distributions agree (a Kolmogorov-Smirnov (KS) test reveals a 94.5% probability that the HR literature DLA sample is drawn from the Noterdaeme et al., 2012c, sample), despite the HR literature sample being at least an order of magnitude smaller than the Noterdaeme et al. (2012c) sample. Despite the agreement, Prochaska et al. (2005) demonstrated with mock spectra that the combination of the DLA search algorithm in the SDSS and the trained eye can only identify 95% of DLAs between logN(HI)= 20.3 and 20.4, leading to a slight bias towards detecting higher HI systems in these large SDSS samples.

Figure 2.2 shows the distribution of metallicity ([M/H]) in the HR literature sample. There is no standard definition of how metallicity is measured in DLAs, partially because iron (the typical metallicity indicator in stars) is easily depleted onto dust and oxygen (the metallicity indicator in HII regions) is difficult to measure (the 1302Å line is generally saturated and the 1355Å line is typically too weak to detect). Rafelski et al. (2012) defined a scheme that would determine the metallicity based on which elements were detected. They would use either sulphur, silicon, zinc, or iron (in order of decreasing preference) as their metallicity tracer (i.e. the element M in [M/H]). The justification for this scheme is that the metallicity should act as a tracer of the

[4]Six of these DLAs do not contain a measured HI column density, but are believed to be DLAs based on their high metal content.

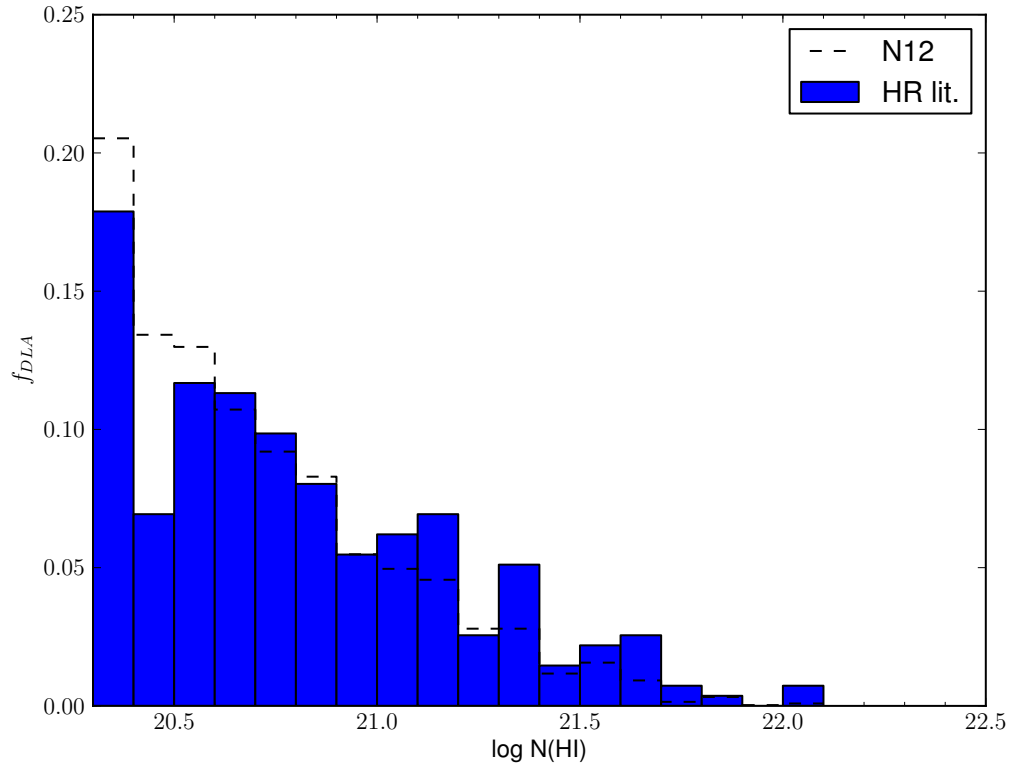

Figure 2.1 N(HI) distribution of the HR literature DLA sample. The HR literature DLA sample is represented by the blue histogram, whereas the Noterdaeme et al. (2012c) sample (N12) is shown as the dashed line. Both distributions agree, with a probability of 94.5% that the HR literature sample is drawn from the N12 sample.

mass density of heavy elements. By selecting an element to represent the mass density of all metals, one is required to choose the element which traces the star formation history (such as an α-element) and is the largest possible contributor to the mass density of the system. This element will most likely be easily measured in DLAs due to its larger column density (which is directly proportional to the mass density). It is natural to preferentially select an element such as oxygen as it is produced in the massive stars, and can act as a tracer in the youngest systems where the lower mass stars (that dominate iron production) have not started to enrich the surrounding gas.

However, certain elements are difficult to measure from a practical standpoint. For example, oxygen and carbon are difficult to measure in DLAs due to either saturated or extremely weak lines. Therefore sulphur and silicon present themselves as better candidates as they are among the most dominant α-elements in the Sun by mass (e.g. Asplund et al., 2009). As sulphur is volatile and silicon is somewhat refractory (e.g. Vladilo et al., 2011, see Section 3.1.4 for more details), a preference is given to sulphur as the metallicity tracer. If neither are present, zinc is used as it traces sulphur and oxygen well and is undepleted in DLAs (e.g. Pettini et al., 1994, see Section 3.1.2 for more details). Lastly, iron is chosen as a metallicity indicator although it is heavily depleted into dust. However, a 0.3 dex correction is added to the metallicities derived with iron to account for the α-element underabundance and dust depletion (see Rafelski et al., 2012). This scheme has been adopted in Figure 2.2.

Figure 2.2 shows the overall metallicity distributions of the HR literature sample of DLAs. Most of the DLAs tend to have a metallicity of [M/H]~ -1.5 (e.g. Prochaska et al., 2003b; Rafelski et al., 2013), but they do span a significant range in metallicity (from -3 to 0.5). However, a closer inspection of which metals are used (the different colours in Figure 2.2) shows that there is a slight bias for using certain elements for a given metallicity. Sulphur becomes the most common probe at higher metallicities resulting from the sulphur lines (which are typically located in low signal-noise ratio (SNR) regions of the spectra due to the Lyα forest) having a higher chance of detection with larger metal contents[5]. It is somewhat surprising to see zinc is the chosen metal indicator at most metallicities, considering the ZnII 2026 Å line is fairly weak and should be limited to systems with higher zinc column densities. For example, at [Zn/H]$= -2.0$ (roughly the lowest metallicity with zinc as a metallicity indicator), a

[5]As a test, the typical SNR is 5–10 in the Lyα forest at the S II λ1253 line. Assuming the DLA is at $z_{\rm abs}= 2$ with a typical absorption feature of full width half maximum 16.5 km s^{-1}, a column density of logN(S II)=14.4 (14.1) is required for a SNR of 5 (or 10). For a DLA with logN(HI)= 20.5; this corresponds to a metallicity of [S/H] ~ -1.25 (~ -1.22).

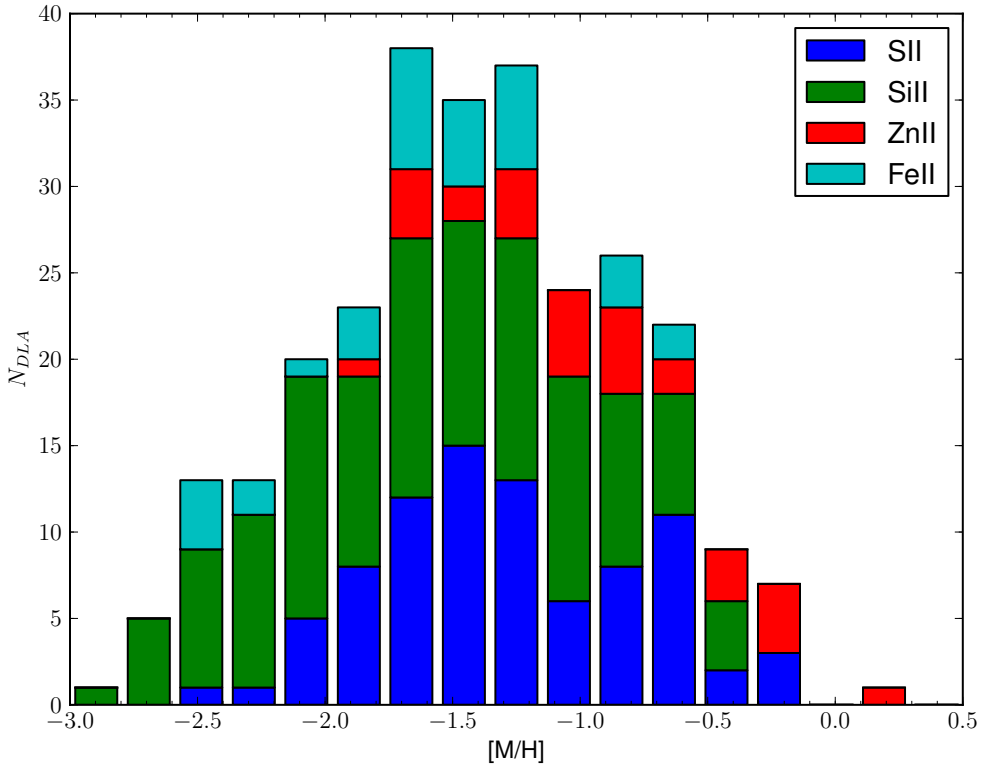

Figure 2.2 [M/H] distribution of the HR literature DLA sample. Overall, DLAs seem to have a median metallicity of [M/H]~ -1.5, although span a large range in metallicity. Sulphur is the typical metallicity indicator at higher metallicities, whereas silicon is generally used at lower metallicities. This is likely due to the ease of detecting sulphur in systems with larger column densities.

spectrum would require a SNR of ~ 47 at the Zn II 2026 line (assuming the DLA is at $z_{\rm abs}= 2$ with logN(HI)= 20.5 and a full width half maximum 16.5 km s^{-1}). In this same example DLA, the spectrum only needs to have a SNR of ~ 10 at the SII 1253 line to detect the same metallicity. Therefore, either systems with large metal columns or spectra with high SNR (or both) will have Zn as a potential metallicity indicator.

Lastly, Figure 2.3 shows the absorption redshift (z_{abs}) distribution, as well as the metallicity evolution, of the DLAs. The metallicity of each redshift bin (plotted in

red) is the HI-weighted average of all DLAs within the bin ($\langle$Z$\rangle$), i.e.

$$\langle \mathrm{Z} \rangle = \log \left(\sum_i 10^{[M/H]_i} N(\mathrm{HI})_i / \sum_i N(\mathrm{HI})_i \right). \quad (2.1)$$

The HI-weighted mean represents the average metal enrichment within each redshift bin. The error bars were derived from a bootstrap method[6]. It is clear that DLAs are chemically evolving with cosmic time. As mentioned in Section 1.3, this has been seen previously (e.g. Rafelski et al., 2012). The sudden decrease in metallicity in the highest redshift bin has been associated with the potential of probing a different galaxy population exposed to higher ionization states (Rafelski et al., 2013).

Overall, the HR literature DLA sample spans a large range in redshift and follows the HI distribution seen for the large HI-only surveys (e.g. Noterdaeme et al., 2012c). With the large range in metallicity (-3 to 0.5), the DLA HR literature sample should provide an opportunity to test whether DLAs are chemically similar to the Milky Way regimes (see Figure 1.13).

2.2 Stellar Literature

In order to understand whether DLAs have similar chemical compositions as stars at a given metallicity, a substantial representation of the various components of the Milky Way system is required. The Milky Way's thick and thin disks, halo, and its satellites (limited to dwarf spheroidal galaxies and the Large Magellanic Cloud in this work) represent the significant portion of the variations in the Galactic chemical environments. The bulge is excluded from the comparison as the stars are too metal rich ($-0.5 \lesssim$[Fe/H]$\lesssim 0.5$; cf. McWilliam, 1997) to justify a comparison with DLAs. The stellar abundance sample presented in this subsection is designed to be a representative selection of the detailed abundance studies done on the different Galactic components.

[6]The bootstrap method involves recalculating the mean several times (in this case 1000 iterations) by randomly varying each datum within the margin of error in the abundance. The standard deviation of all these calculations provides the error.

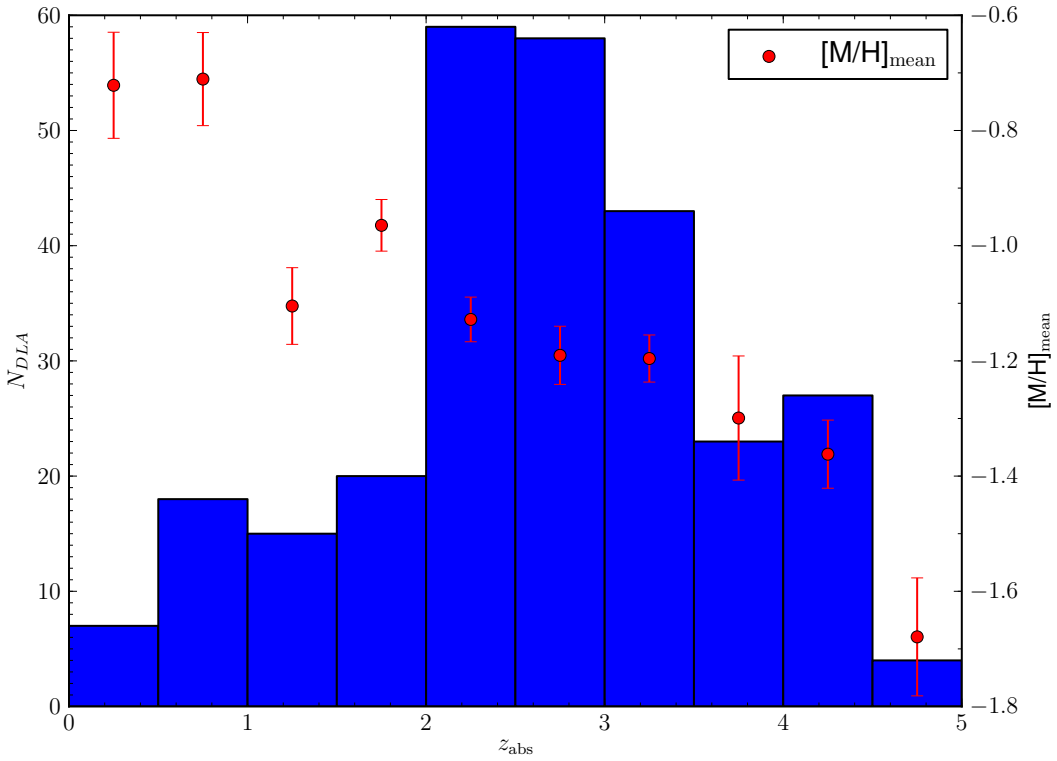

Figure 2.3 Absorption redshift (z_{abs}) distribution of the HR literature DLA sample. The entire HR literature sample spans a large range in z_{abs} (blue histogram). The error bars in the cosmic metallicity at each redshift represent the scatter in both HI and metal column densities of the DLAs within each bin. It is apparent from the decrease in mean metal content (i.e. the HI-weighted metallicity) in each bin (red points) that the DLAs are chemically evolving with cosmic time.

2.2.1 Measuring Stellar Abundances

The difficulty with assembling a large stellar catalogue is the large variety of methods to derive stellar abundances. Although abundances derived for stars are mainly influenced by the stellar atmospheric parameters adopted (i.e. effective temperature, surface gravity, and micro-turbulence); the models used and the selection of absorption lines also impacts the value of the abundance. The stellar literature sample is selected such that the highest quality data (such as high resolution [R $\gtrsim$ 10000] observations, and corrections for hyperfine splitting when applicable) are used for an accurate representation of the stellar data. However, it is impossible to select a homogeneous sample of stellar abundances derived with an identical analysis. By choosing one or two large surveys for each Galactic component, the effects of inhomogeneity between studies can be minimized within each component. This subsection highlights the differences that will result within a heterogeneous literature compilation.

The absorption lines used for measuring stellar abundances are formed in the optically thick stellar atmosphere of a star. Deriving abundances from the absorption features in stellar spectra requires a modelling of the radiative transfer of photons within the atmosphere, as well as understanding the atomic levels and ionization of the species residing within the atmosphere. Within the literature, there are a variety of different model atmosphere codes. The most commonly used codes are ATLAS (Kurucz, 1998), Model Atmospheres in Radiative and Convective Scheme (MARCS; Gustafsson et al., 1975, 2003, 2008), and MOOG (Sneden, 1973). Shetrone et al. (2003) compared using MARCS/MOOG with ATLAS/WIDTH to derive the stellar atmosphere parameters and determine the abundances (respectively). Shetrone et al. (2003) demonstrated that abundances derived for both of these methods were within $\sim$ 0.1 dex of each other, suggesting that different codes can produce slightly different results (although still within the typical errors of stellar abundances). One of the causes behind these differences is that ATLAS/WIDTH under/overestimates the neutral/singly ionized iron abundances, which in turn forces a higher surface gravity (Shetrone et al., 2003). Furthermore, using different model atmosphere inputs (e.g. effective temperature, surface gravity, etc.) within the same code can also introduce another 0.1 dex difference in the abundance, although these are typically included within the error analysis of any stellar abundance paper.

One assumption that is typically made in the models is the dimensions of the atmosphere. Generally, plane-parallel atmospheres are used, as the star's atmosphere

is generally much thinner than the radius of curvature of the star (Carroll & Ostlie, 2006). However, this is not the case for stars with thick atmospheres (i.e. giants and supergiants) as the amount of curvature grows with increasing radius; therefore a spherical model atmosphere must be adopted (e.g. Carroll & Ostlie, 2006; Heiter & Eriksson, 2006). Heiter & Eriksson (2006) compared the overall effects of adopting a spherical atmosphere over a plane-parallel model for giant stars by deriving the abundances from a grid of synthetic spectra using both plane-parallel and spherical models. By assuming a spherical model, Heiter & Eriksson (2006) found that the difference between temperature profiles is much lower, and has more variation relative to the plane-parallel model (especially with lower effective temperatures and surface gravities). The abundances in this comparison differed by up to ~ 0.4 dex in either direction, depending on the ionization state of the species or the stellar parameters adopted. In summary, Heiter & Eriksson (2006) showed that the shape of the model atmosphere adds to the spread in the abundances of giant stars in a heterogeneous sample.

Similarly, local thermodynamic equilibrium (LTE) assumptions are also assumed in stellar atmosphere models. LTE implies that the atomic level populations are described by the Saha-Boltzmann equation in thermal equilibrium. However, the radiation field from stars is generally not in thermal equilibrium, and thus the LTE assumption breaks down. LTE is a good assumption when the temperature scale height of the atmosphere is small relative to the mean free path of photons (e.g. in giant stars; Carroll & Ostlie, 2006) or for weak lines that form over a couple of layers deep within a star. For non-LTE calculations, one would need to include radiative and collisional transfer for the conditions within the atmosphere at that particular layer. However, the models take longer to run for each atomic transition, making non-LTE corrections very computationally expensive. Not only do non-LTE effects influence abundance determinations, but can also affect the stellar parameters adopted (when derived spectroscopically); compounding the net effect on the derived abundance. However non-LTE corrections are only needed for lines that form over many layers within the atmosphere, and can be avoided by selecting weak lines that form in thin regions within the atmosphere. Furthermore, the metallicity and temperature determine the strength of a line, and can influence whether non-LTE effects dominate the line formation. Although non-LTE corrections may be required for certain lines, models for some elements are just being derived (Shi et al., 2009; Bergemann & Cescutti, 2010; Mashonkina, 2013) while other still require further studies. Therefore,

correcting for non-LTE effects remains a problem in large datasets (Mashonkina, 2013).

For odd-Z elements (such as manganese, copper, and phosphorous), further corrections are needed to account for hyperfine structure splitting in the spectra. Hyperfine structure lines broaden the observed absorption line profile in the stellar spectrum on the order of tens of mÅ (e.g. Prochaska & McWilliam, 2000), which needs to be accounted for when measuring the abundance of the elements. By measuring all the split components in a laboratory and combining them using the known strengths for each component (cf. Condon & Shortley, 1935; Handrich et al., 1969), corrections can be made based on the observed equivalent width. As hyperfine splitting effects become larger with increasing equivalent width, hyperfine structure corrections can, in general, be ignored for weak lines (Prochaska & McWilliam, 2000).

In summary, stellar abundances can vary based on the choice of model atmosphere codes, stellar parameters adopted, dimensionality of the atmosphere, and absorption lines used. Although an effort can be made to choose stellar abundances where these effects are minimized (e.g. hyperfine structure corrections for manganese, using weak absorption lines, etc.), it is impossible to account for all these effects in a heterogeneous sample.

2.2.2 Galactic Component Abundances

In the following subsections, the relevant papers used to acquire the stellar abundances for each Galactic component are summarized (in order of increasing metallicity). For the elements studied in Chapter 3 (i.e. silicon, sulphur, chromium, manganese, phosphorous, iron, and zinc), non-LTE effects are ignored as the recent work by Shi et al. (2009), Bergemann & Cescutti (2010), and Mashonkina et al. (2011) are just starting to provide non-LTE atomic models for silicon, iron, and chromium (respectively). Therefore possible systematic differences between studies will only result from differences in the model atmosphere codes, dimensionality of the atmosphere, and differences between absorption lines. As all model atmosphere codes are acceptable, no preferential choice needs to be made for one code or another.

Most elements within the literature only have abundances derived for one ionization state. However, iron and titanium typically have abundances quoted for both the neutral and singly ionized states. For consistency with most of the literature selected, it was assumed (unless otherwise stated) that neutral iron and titanium

(FeI and TiI) abundances represent the total iron and titanium abundances in these systems. All abundances have been converted to the Asplund et al. (2009) solar scale, unless otherwise stated.

Stellar Halo

The sample of halo stars are chosen from Venn et al. (2004, 80 stars) and Frebel (2010, 867 stars). Both samples are literature compilations, although the Venn et al. (2004) sample has been identified based on the kinematics of the stars whereas Frebel (2010) selects halo stars based on their kinematics (when present in the literature) or subsequently metallicity (i.e. metal poor stars with [Fe/H]< -1.5). Although metal-poor stars typically lie within the halo, there is no guarantee that stars in the Frebel (2010) sample could be anomalously metal-poor disk stars with metallicities lower than [Fe/H]< -1.5.

Figure 2.4 shows the metallicity distribution of the halo (blue) with respect to the DLAs (black dotted line). [Fe/H] is adopted as the metallicity indicator in the stellar sample for simplicity, although the Rafelski et al. (2012) method is still used for the DLA sample. At first glance, the halo stars are typically much more metal poor than the DLA sample. However, the Frebel (2010) sample was selected based on low metallicity stars, skewing the metallicity distribution to low metallicities. To test the effects of metallicity selection, the metallicity distribution function of the halo (in Figure 2.4) was divided into the stars from Venn et al. (2004, red dashed line) and Frebel (2010, green dashed line). The metallicity distribution of the kinematically defined sample clearly shows a nearly identical distribution as the HR DLA literature sample (agreeing with the results of Prochaska & Wolfe, 1999; Rafelski et al., 2012, both using a similar comparison to the metallicity distribution of the halo) whereas the Frebel (2010) sample tends to probe metallicities lower than the average DLA, but still spans the entire metallicity range of HR literature DLAs.

Satellites

For the comparison to DLAs, all well studied (i.e. more than 30 stars) dwarf spheroidal (dSph) galaxies with detailed chemical abundances were selected. The Large Magellanic Cloud (LMC) is also included in this sample as it is another well studied satellite galaxy. Table 2.2 shows a summary of which satellite galaxies were used, the elements available, the total number of stars (N_{stars}) within the sample, and the references.

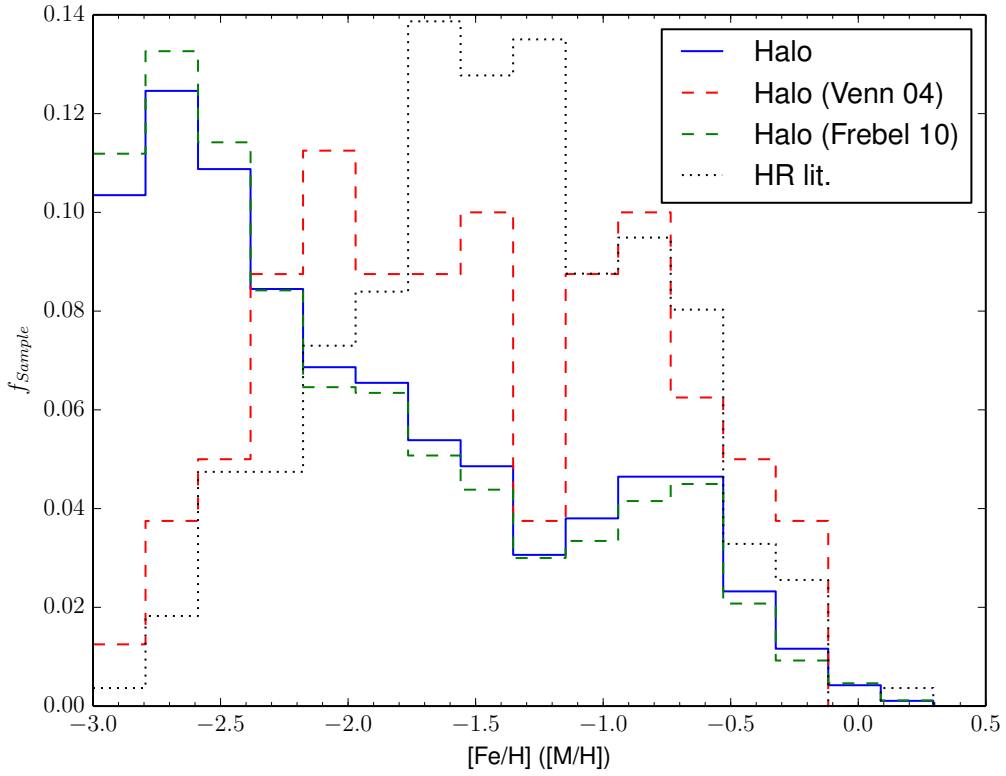

Figure 2.4 The metallicity distributions of all the stars in the Milky Way's halo sample (in blue; using [Fe/H]) and the HR literature DLA (dotted black lines; [M/H]). Although the peak metallicity of halo stars ([Fe/H]~ -2.75) is much lower than the peak metallicity of DLAs ([M/H]~ -1.5), the halo stars span the metallicity range of the HR DLA sample as well as more metal-poor environments due to the metallicity selection bias in the Frebel (2010, green dashed line) sample. However, the kinematically selected stars from Venn et al. (2004, red dashed line) show a nearly exact match in the overall distribution of DLA metallicities. It is important to note that the Frebel (2010) sample contains ~ 1000 stars, whereas the Venn et al. (2004) only contains 80 stars. Therefore the Frebel (2010) sample dominates the overall metallicity distribution when both samples are combined.

Table 2.2 Summary of satellite galaxy literature sources

Satellite	Elements	N_{stars}	Reference
Carina	O, Mg, S, Ti, Cr, Mn, Fe, Co, Ni, Zn	37	1,2,3
Fornax	O, Mg, Si, Ti, Cr, Mn, Fe, Ni, Zn	77	3,4
LMC	O, Mg, Si, Ti, Cr, Fe, Co, Ni	59	5
Sagittarius	O, Mg, Al, Si, Ti, Cr, Mn, Fe, Co, Ni, Zn	39	6,7
Sculptor	O, Mg, Ti, Cr, Mn, Fe, Co, Ni, Zn	87	2,3,8

References – (1) Venn et al. (2012); (2) Shetrone et al. (2003); (3) North et al. (2012); (4) Letarte et al. (2010); (5) Pompéia et al. (2008); (6) Sbordone et al. (2007); (7) Carretta et al. (2010); (8) Geisler et al. (2005);

Overall there are 195 stars used from the satellite galaxies. A brief summary follows for each of the relevant literature sources, including any details concerning which lines were used and whether any corrections were adopted.

- 15 red giant branch (RGB) stars in Sculptor, Fornax, Carina, and Leo I were studied by Shetrone et al. (2003) using VLT/UVES (R$\sim$ 40000). MARCS model atmospheres (Gustafsson et al., 1975) were adopted, using MOOG (Sneden, 1973, with LTE assumptions) to determine the abundances. Shetrone et al. (2003) compared their abundances to those derived from the combination of ATLAS/WIDTH combination (Kurucz, 1998), finding a difference of about 0.1 dex in the abundance per species. Hyperfine splitting corrections were adopted for Mn. Most of the oxygen abundances were derived using [OI] 6300 Å, although some required the use of [OI] 6363 Å.

- Geisler et al. (2005) observed four giant stars in Sculptor using UVES on VLT. Abundances were derived with LTE assumptions using MOOG (Sneden, 1973) with MARCS model atmospheres (Gustafsson et al., 1975). The determined Mn abundances include corrections for hyperfine splitting. All oxygen abundances were derived using the forbidden [OI] line at 6300 Å.

- 12 RGB stars in the Sagittarius dSph were observed with VLT/UVES (R$\sim$ 43000) for the stellar abundance work by Sbordone et al. (2007). 1D ATLAS model atmospheres (Kurucz, 1998) were used, assuming LTE, for deriving abundances. Hyperfine structure corrections were applied to the manganese, cobalt, and copper abundances. Oxygen abundances were derived from the [OI] 6300 Å to avoid non-LTE corrections.

- The study of the LMC by Pompéia et al. (2008) looked at 67 RGB stars with the VLT/FLAMES (R$\sim$ 24000). Abundances were derived with a MARCS 1D model atmosphere using the ATLAS code (Kurucz, 1998), assuming LTE. Hyperfine structure corrections were adopted for copper and cobalt; while the [OI] 6300Å was used to derive the oxygen abundance.

- Carretta et al. (2010) looked at 27 RGB stars in the Sagittarius dSph galaxy using VLT/FLAMES. Kurucz model atmospheres (Kurucz, 1993) were used with LTE assumptions. Oxygen abundances were derived from the [OI] 6300 Å and 6364 Å lines. Hyperfine splitting corrections were adopted for the scandium, manganese, cobalt, and copper abundances.

- A large sample of Fornax dSph stars was observed with VLT/FLAMES by Letarte et al. (2010). Abundances were derived for 81 RGB stars using spherical MARCS model atmospheres (Gustafsson et al., 2003, 2008), and include a generic correction for hyperfine splitting on europium and lanthanum.

- Venn et al. (2012) derived abundances for 9 RGB stars in the Carina dSph galaxy. Observations were completed with VLT/FLAMES and Magellan/MIKE, providing a resolution of R$\sim$ 15000. Abundances were derived using spherical MARCS model atmospheres (Gustafsson et al., 2003, 2008), with hyperfine splitting corrections included on odd-Z elements.

- North et al. (2012) compiled a list of the equivalent widths and stellar parameters from several literature sources to derive manganese in dSphs. Assuming LTE, they repeated the abundance determination under a MARCS (Gustafsson et al., 2003, 2008) spherical model (apart from Sculptor data, which used plane-parallel models), and redetermined the hyperfine splitting corrections for all the stars under the same model. They concluded that the Mn 5432 Å line is not as reliable as the others due to the differences in the behaviour of the hyperfine splitting correction resulting from the influence of non-LTE effects. Due to the homogeneity of their corrections, the Mn abundances calculated by North et al. (2012) are preferentially adopted over other literature sources in this catalogue.

Comparing the metallicity distribution of the satellite galaxies in Figure 2.5 to the DLA HR literature (dotted line) samples shows that DLAs, the LMC, and dSphs

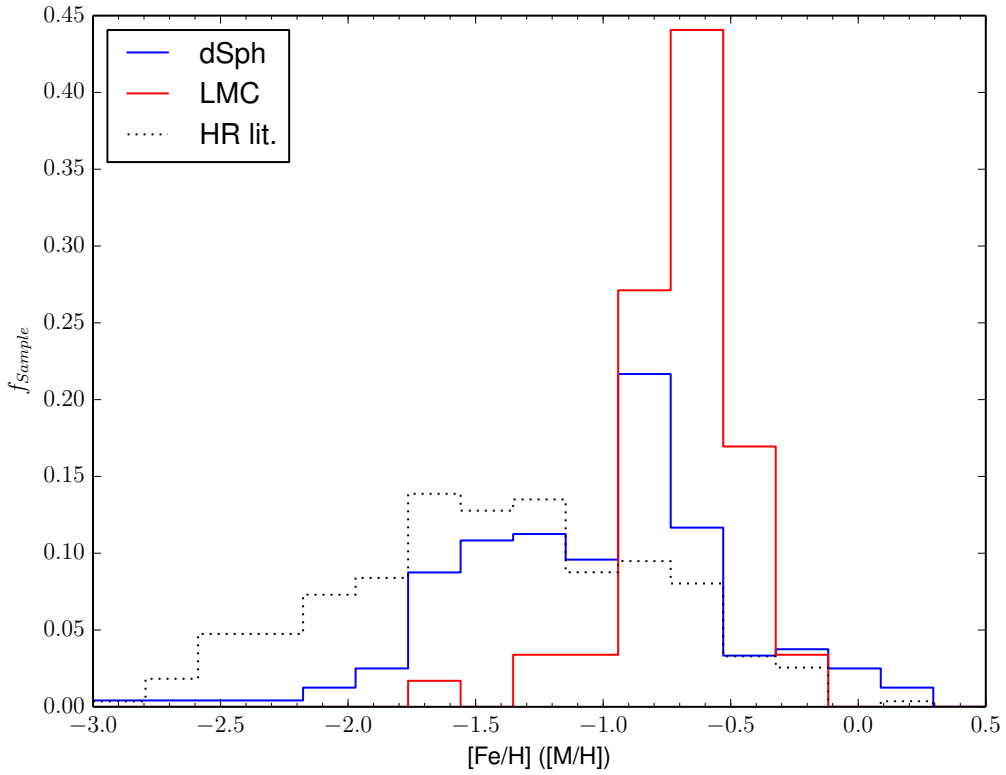

Figure 2.5 The metallicity distribution of the Milky Way's dSphs (blue; using [Fe/H]) and the LMC (red; [Fe/H]). For comparison, the HR literature DLA metallicity distribution is shown (dotted black line; [M/H]). It would appear that DLAs seem to span the same range in metallicity as dSphs and the LMC; despite having different distribution peaks.

span the same range in metallicity, with similar distributions (apart from the LMC). This supports the idea that DLAs could probe sightlines through dwarf sightlines (Pettini et al., 1994; Haehnelt et al., 1998). However, the metallicities at which the peaks of these three distributions occur do not agree with each other ([M/H]~ -1.5 for DLAs; [Fe/H]~ -1.25 for dSphs and [Fe/H]~ -0.75 for the LMC).

One question that is of interest to Figure 2.5 is how the individual dwarf systems contribute to the overall metallicity distributions of dwarfs. To demonstrate, Figure 2.6 shows the metallicity distribution for each dSph separately. It is clear that an individual dSph has a unique metallicity distribution function, with some being narrow and centered about a single metallicity (e.g. Fornax and Carina), whereas others

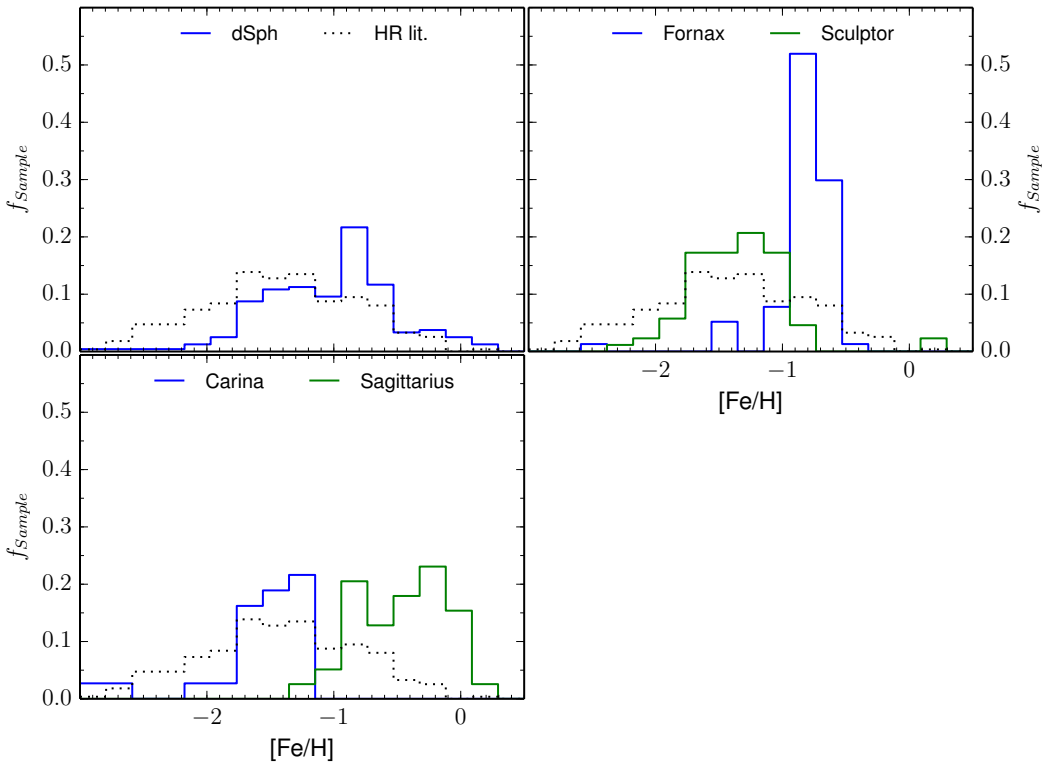

Figure 2.6 The individual metallicity distribution of each of the Milky Way's dSphs. The first panel shows the dSph distribution in Figure 2.5 for reference, whereas all subsequent panels contain individual dSphs. For comparison, the HR literature DLA metallicity distribution is shown (dotted black lines). The entire dSph metallicity distribution is made of up several, unique metallicity distribution functions, rather than all having the nearly-identical shapes.

show a much wider range in metallicity that is nearly as broad as the DLA distribution (e.g. Sagittarius, Sculptor). The difference in the metallicity distributions has been interpreted as the dSphs all having different star formation epochs and rates (cf. Tolstoy et al., 2009). As DLAs are individual sight-lines through galaxies, dSphs provide a good reference for the variation in star formation histories between galaxies.

Thin and Thick Disks

The selected thin and thick disk stellar samples consist of the data provided by Reddy et al. (2003) and Reddy et al. (2006) (respectively). In addition, the Venn et al. (2004)

compilation is included to fill the subsample with other literature sources.

Both the Reddy et al. studies look at nearby dwarf F and G stars using the 2dcoudé echelle spectrometer (R$\sim$ 60000) at the McDonald Observatory. As these stars are lower mass main sequence stars, they provide insight into the chemical composition of the ISM at the time the Milky Way first formed. What makes the Reddy et al. samples powerful is their large sample size, while using the same analysis techniques on their thin and thick disk samples to provide a relatively homogeneous sample. Reddy et al. adopt the ATLAS 9 plane-parallel model (Kurucz, 1998) with convective overshooting. LTE is assumed for deriving the abundances, however an empirical model (based on studies of stars with both OI and [OI] lines measured) is used on the OI 7771 Å line to derive non-LTE corrections. When present, the forbidden [OI] 6300Å line is preferentially used over the OI 7771 Å line as it is more reliable and does not require the non-LTE correction. Hyperfine structure effects were taken into account for the Mn and Cu lines. In Reddy et al. (2006), the probability of the stars being within the thin or thick disk, or halo is calculated; requiring a probability $> 70\%$ to determine which population the star belongs. The probability is based on the stars' kinematics being within the expected Gaussian distribution of the population and are weighted by the fraction of stars expected to be within the given population (for more details, see Reddy et al., 2006). One should note that Reddy et al. (2003) use a differential analysis for determining stellar abundances[7]. Therefore, their solar abundances are preferentially adopted over Asplund et al. (2009) only for the Reddy et al. (2003) stars.

The Venn et al. (2004) literature compilation from 14 different sources contains a total of 297 thick-disk stars and 482 thin-disk stars. These stars were identified to be in the thin or thick disk solely based on their kinematics. From their results, 33 stars that were originally classified as thin disk stars (Reddy et al., 2003) were determined by Venn et al. (2004) to reside in the thick disk. Since Reddy et al. (2006) adopts a kinematic-based classification similar to Venn et al. (2004), the Venn et al. (2004) classification is used in preference over the Reddy et al. (2003) description when applicable.

The metallicity distributions of the thin (blue line) and thick (red line) disks are shown in Figure 2.7, relative to the HR literature DLA sample (the black dotted line). Although the thin and thick disks are slightly different in their metallicity

[7]A differential analysis measures the Sun's abundances simultaneously with the stars. This removes any systematic errors between solar and stellar abundance derivations.

Table 2.3 Summary of stellar literature sample

Paper	Galactic Component	N_{stars}	Elements used in thesis
Reddy et al. (2003)	Thin Disk	181	Mg, Si, S, Cr, Mn^{H}, Fe, Zn
Shetrone et al. (2003)	Satellite	15	Mg, Si, Cr, Mn^{H}, Fe, Zn
Venn et al. (2004)	Thin Disk	301*	Mg, Fe
–	Thick Disk	121*	Mg, Fe
–	Halo	80*	Mg, Fe
Geisler et al. (2005)	Satellite	4	Mg, Si, Mn^{H}, Fe, Zn
Reddy et al. (2006)	Thick Disk	94	Mg, Si, S, Cr, Mn^{H}, Fe, Zn
Sbordone et al. (2007)	Satellite	12	Mg, Si, Cr, Mn^{H}, Fe, Zn
Pompéia et al. (2008)	Satellite	67	Mg, Si, Cr, Fe
Carretta et al. (2010)	Satellite	27	Mg, Si, Cr, Mn^{H}, Fe
Frebel (2010)	Halo	867*	Mg, Si, Cr, Mn, Fe, Zn
Letarte et al. (2010)	Satellite	81	Mg, Si, Cr, Fe, Zn
North et al. (2012)	Satellite	172	Mn^{H}, Fe
Venn et al. (2012)	Satellite	9	Mg, S, Cr, Mn^{H}, Fe, Zn

^{H} – Hyperfine stucture corrections included

* – Large literature compilation, likely containing a variety of different corrections.

distributions (as the thick disk is slightly more metal-poor than the thin disk), both are more metal rich than the literature DLA sample (in particular the thin disk). The lack of significant overlap between the two samples requires a search for much more metal-rich DLAs in order for a comparison to be made with the two disk components and high redshift galaxies.

To summarize the various papers that have been used for the stellar literature sample, Table 2.3 presents each paper with the number of stars within each component, and the elements with the abundances used in the rest of this thesis. Elements which include hyperfine structure corrections in their abundances are flagged. One should note that no non-LTE corrections have been adopted within this sample, so caution must be used for abundances derived with spectral line influenced by non-LTE effects.

2.3 Thesis Sample

Sections 2.1 and 2.2 have demonstrated that typical DLA metallicities tend to show a sufficient overlap with the dSphs and halo stars to facilitate a comparison. However,

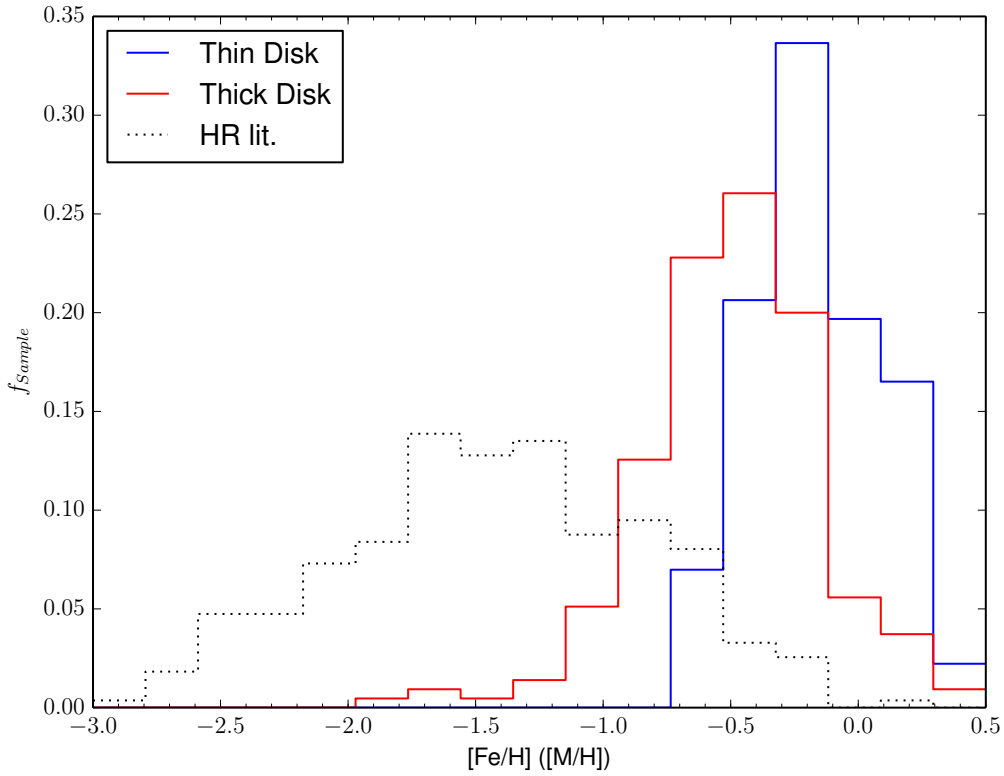

Figure 2.7 The metallicity distribution of the thin (blue; [Fe/H]) and thick (red; [Fe/H]) disk of the Milky Way. For comparison, the HR literature DLA metallicity distribution is shown (dotted black lines; [M/H]). The lack of a significant overlap in metallicity between the two disk samples and the HR literature DLAs suggests that a more metal-rich sample of DLAs is needed for a comparison.

there is very little overlap between the metallicity distributions of the literature DLAs and the disk subsamples. In order to facilitate such a comparison, a sample of thirty DLAs with large metal column densities have been identified. The first work done with these high column density systems was by Herbert-Fort et al. (2006), who defined and identified metal strong DLAs (MSDLAs) to study the high metallicity end of DLAs. By definition, MSDLAs are expected to have the highest metal content of DLAs, requiring metal column densities of logN(ZnII) $\geq$ 13.15 or logN(SiII) $\geq$ 15.95 (Herbert-Fort et al., 2006). These limits in zinc and silicon column densities were arbitrarily chosen such that weak lines from rarely detected elements (such as boron) could be observed in a typical spectrum. By searching the SDSS DLA catalogue (Prochaska & Herbert-Fort, 2004; Prochaska et al., 2005) for spectra with large metal columns (using a strong Si II 1808 as their tracer) to flag systems with strong or very strong absorption, Herbert-Fort et al. (2006) identified 435 candidate MSDLAs.

2.3.1 Observations and Data Reduction

The sample of DLAs presented in this work (henceforth called the Thesis DLA Sample) consists of thirty DLAs with relatively high abundances selected purely on the basis of their metal line strengths from the Herbert-Fort et al. (2006) catalogue[8]. The high column densities of these DLAs should overcome the small oscillator strengths of weak lines solely by having a larger number of atoms for a given metal (relative to the average DLA).

The data for this sample was taken with HIRES on the Keck I telescope over the span of 17 years by Jason Prochaska and collaborators. Table 2.4 shows a summary of the targets and observations. The *Decker* column shows which slit was selected, while the *Bin* column gives the binning of the CCD spectra during the reduction of the data. The spectra were reduced and continuum fitted (by Marcel Neeleman, J. Xavier Prochaska, and others) using the XIDL code[9]. The HIRedux software was used to reduce the spectra.

Outlining the data reduction steps, first the arcs and flats are processed, using the flats to determine the curvature of each order. The slit profile is then determined for future sky subtraction. The raw image is flatfielded, and each order is identified for future extraction. Sky subtraction takes place prior to the continuum fitting. The

[8]Since the start of the work of this thesis, data from other candidate MSDLAs from the Herbert-Fort et al. (2006) catalogue has been collected and reduced since then.

[9]http://www.ucolick.org/~xavier/IDL

continuum fit was completed order by order prior to converting the data into the final 1D spectrum. To demonstrate the quality of the final spectra, several prominent absorption lines from each sight-line are shown in Appendix A.2.

Table 2.4 Thesis Sample targets

Quasar	$z_{\rm em}$	$z_{\rm abs}$	logN(HI)	R.A.	Dec. (band)	Magnitude Time (s)	Exposure	Decker	Bin	UT Date
J0008−0958	1.95	1.76753	20.85 ± 0.15 (1)	00:08:15.3	−09:58:54.0	18.4 (r)	15029	C1	2x1	17 September 2007
J0058+0115	2.49	2.00953	21.10 ± 0.15 (1)	00:58:14.3	+01:15:30.2	17.7 (r)	14400	C1	2x1	6 October 2004
Q0201+36	2.49	2.46280	20.38 ± 0.15 (2)	02:04:55.6	+36:49:18.0	17.5 (r)	24980	C5	2x1	30 September 1994
Q0458−02	2.29	2.03950	21.65 ± 0.09 (3)	05:01:12.8	−01:59:14.2	19.0 (R)	28800	C5	2x1	31 October 1995
FJ0812+3208	2.71	2.62593	21.35 ± 0.15 (4)	08:12:40.7	+32:08:08.6	17.5 (r)	40500	C1	2x1	12 January 2008
J0927+1543	1.80	1.73113	. . .	09:27:59.8	+15:43:21.8	18.8 (r)	12800	C1	2x1	25 January 2011
J0927+5823	1.91	1.63515	20.40 ± 0.25 (2)	09:27:08.8	+58:23:19.4	18.3 (r)	21600	C1	2x1	25 January 2011
J1010+0003	1.40	1.26514	. . .	10:10:18.2	+00:03:51.3	18.1 (r)	7200	C1	2x1	15 March 2005
J1013+5615	3.61	2.28400	. . .	10:13:36.4	+56:15:36.4	18.5 (r)	3600	C1	2x1	5 January 2006
J1049−0110	2.12	1.65760	20.35 ± 0.15 (1)	10:49:15.4	−01:10:38.1	17.8 (r)	4800	C5	2x2	4 January 2006
J1056+1208	1.92	1.60954	21.45 ± 0.15 (2)	10:56:48.7	+12:08:26.8	17.9 (r)	21300	C1	2x1	6 April 2006
J1155+0530	3.48	3.32607	21.05 ± 0.10 (4)	11:55:38.6	+05:30:50.6	18.1 (r)	7200	C1	2x1	14 April 2005
J1159+0112	2.00	1.94375	21.80 ± 0.10 (5)	11:59:44.8	+01:12:07.0	17.3 (r)	25000	C1	2x1	2 March 2002
J1200+4015	3.36	3.22000	20.65 ± 0.15 (4)	12:00:39.8	+40:15:56.0	18.3 (r)	10800	B2	2x1	25 March 2008
J1249−0233	2.12	1.78085	21.45 ± 0.15 (6)	12:49:24.9	−02:33:39.7	17.7 (r)	7300	C1	2x1	3 January 2006
J1310+5424	1.93	1.80070	21.45 ± 0.15 (2)	13:10:40.2	+54:24:49.6	18.5 (r)	10800	C1	2x2	17 March 2005
J1313+1441	1.88	1.79480	. . .	13:13:41.9	+14:41:40.5	18.2 (r)	10200	C1	2x1	3 June 2006
J1417+4132	2.02	1.95090	21.45 ± 0.25 (6)	14:17:19.2	+41:32:37.0	18.4 (r)	25200	C5	2x2	16 March 2005
J1524+1030	2.06	1.94094	. . .	15:24:30.1	+10:30:32.0	18.1 (r)	9000	C1	2x1	4 July 2011
J1552+4910	2.04	1.95987	. . .	15:52:33.9	+49:10:08.3	18.0 (r)	9000	C1	2x1	3 May 2005
J1555+4800	3.30	2.39089	21.50 ± 0.15 (4)	15:55:56.9	+48:00:15.0	19.1 (r)	21600	C5	2x1	14 April 2005
J1604+3951	3.13	3.16400	21.75 ± 0.20 (4)	16:04:14.0	+39:51:21.9	18.1 (r)	10300	C1	2x1	27 April 2007
J1610+4724	3.22	2.50661	21.00 ± 0.15 (4)	16:10:09.4	+47:24:44.5	18.8 (r)	10800	C5	2x1	7 April 2006
Q1755+578	2.11	1.97110	21.40 ± 0.15 (7)	17:56:03.6	+57:48:48.0	18.3 (R)	30400	C1	2x1	9 September 2004
J2100−0641	3.14	3.09130	21.05 ± 0.15 (4)	21:00:25.0	−06:41:45.0	18.1 (r)	28000	C1	2x1	3 October 2004
J2222−0945	2.93	2.35430	20.55 ± 0.15 (4)	22:22:56.1	−09:46:36.0	18.0 (r)	10800	C1	2x1	17 August 2006
Q2230+02	2.15	1.86440	20.85 ± 0.08 (3)	22:32:35.3	+02:47:55.1	18.0 (R)	27600	C5	2x1	29 September 1997
J2241+1225	2.63	2.41800	21.15 ± 0.15 (4)	22:41:45.1	+12:25:57.1	17.9 (r)	7200	C1	2x1	17 September 2007
J2340−0053	2.09	2.05452	20.35 ± 0.15 (4)	23:40:23.7	−00:53:27.0	17.5 (r)	15000	C5	2x1	1 November 2003
Q2342+34	2.92	2.90899	21.10 ± 0.10 (8)	23:44:51.1	+34:33:46.8	19.1 (V)	7200	C5	2x1	1 November 2003

HI References – (1) Herbert-Fort et al. (2006); (2) Kaplan et al. (2010); (3) Pettini et al. (1994); (4) Prochaska & Wolfe (2009); (5) Kanekar et al. (2009); (6) Berg et al. (2013); (7) Jorgenson et al. (2006); (8) Prochaska et al. (2003c)

2.3.2 Abundances

For the majority of the absorbers in the Thesis Sample, HI column densities have been previously determined either directly from the SDSS spectra (10 DLAs, Prochaska & Wolfe, 2009), follow-up spectroscopy obtained with either Keck II/ESI (3 DLAs, Herbert-Fort et al., 2006) or MMT/BCS (4 DLAs, Kaplan et al., 2010), or were adopted from previous studies (5 DLAs). For the remaining two DLAs (with measured HI column densities), the N(HI) has been determined directly from the HIRES spectrum (by J. Xavier Prochaska). HI column densities were determined by fitting a fully damped Voigt profile to the Lyα transition using a function with the XIDL software. Six DLAs have no measured N(HI) currently available; these are lower redshift DLAs for which neither the original SDSS spectrum nor the new HIRES data cover the Lyα transition. The systems without an N(HI) measurement are still included in the sample for completeness, as ratios of elements' column densities can still provide useful information on the chemistry of the system.

All metal column densities measured for the Thesis Sample (given in Table 2.5) were obtained using the apparent optical depth method (AODM) outlined by Savage & Sembach (1991). The AODM sums the optical depth (τ) of an unsaturated absorption line (at wavelength λ, with oscillator strength f) and is converted to a column density (N) using

$$N = \frac{m_e c}{\pi e^2 f \lambda} \int \tau dv \tag{2.2}$$

where the integral of the optical depth summs over each pixel in velocity space. The limits for the optical depth integration are chosen to contain the absorption profile that is common to all other non-contaminated transitions. The AODM provides a column density across the entire sightline within the DLA, and cannot determine the individual column densities within the specific clouds which make up the DLA (which can be determined through Voigt-profile fitting). As Voigt profile fitting derives identical column densities for the entire sightline as the AODM (Wolfe et al., 1994; Prochaska & Wolfe, 1997a; Lopez et al., 2005a), there is no difference between adopting metal column densities from the AODM or Voigt profile fitting. Appendix A.3 presents the absorption profiles used and the location of the integration limits for the Thesis Sample column density measurements. For lines that were either blended or saturated (and no other *clean* transitions were available for the same species), the derived AODM column density was taken as an upper or lower limit (respectively). The errors quoted on the column densities (N_{err}) were determined from the error

spectrum using

$$N_{err} = \frac{m_e c}{\pi e^2 f \lambda} \left(\sum \left(\frac{I_{err}}{I_{spec}} \Delta v \right)^2 \right)^{0.5} \tag{2.3}$$

where I_{err} and I_{spec} are the fluxes in the error and observed spectra (respectively), and Δv is the velocity width of the pixel. The error spectrum only accounts for photon noise, and not continuum errors.

Continuum placement errors are typically negligible for strong absorption lines. As an example, Figure 2.8 shows the absorption profiles for four different absorption lines of various absorption strengths in the DLA FJ0812 + 3208. The AODM is applied to all four lines with the continuum placed at 0.99, 1.00, and 1.01 (which corresponds to $\pm \sim 50\%$ of the inverse of the signal-noise at each point; represented the grey region in Figure 2.8). $\pm \sim 50\%$ of the inverse of the signal-noise is chosen as the most extreme fits to the continuum by eye, as the continuum should be contained within noise of the spectrum. The resulting values of the column density are given in Table 2.6, along with the errors derived from the photon noise ($\log N_{err}$) and HI column density fitting ($\log N(HI)_{err}$). For the three strongest lines (FeII, NiII, and SiII), the main source of error is from the Lyα fit, and the continuum error is on the order of the photon noise. Even though the errors in the continuum and the photon noise are comparable, one should note that continuum placements used are somewhat exaggerated, thus the continuum error is most likely smaller than what is stated in Table 2.6. However, for very weak lines (e.g. BII 1362), the error from the continuum placement is as large as the HI column density error and should be considered as a notable source of error.

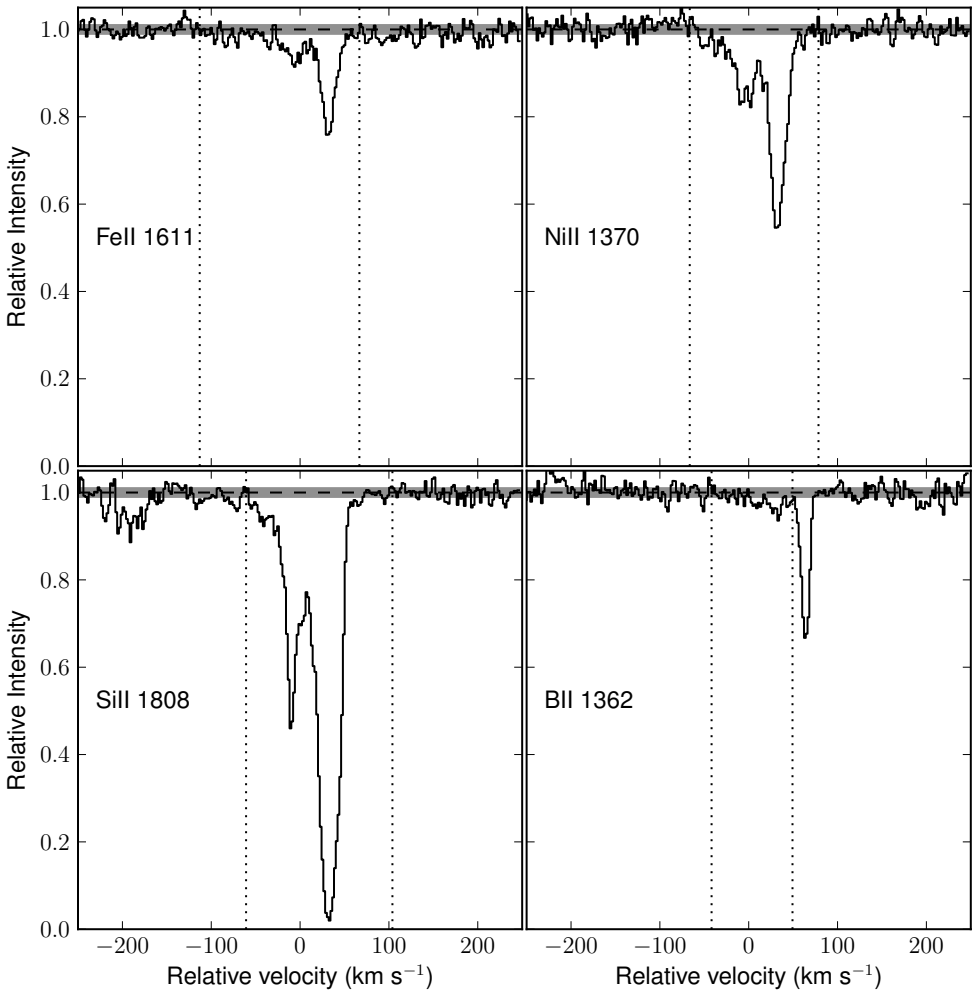

Figure 2.8 Absorption profiles of FeII 1611 (top left), NiII 1370 (top right), SiII 1808 (bottom left), and BII 1362 (bottom right). The grey region in each panel represents a variation in the continuum placement of ± 0.01 in relative flux. The dotted and dashed lines shows the AODM integration bounds for the original continuum (respectively).

Table 2.5 MSDLA Column Densities

QSO	z_{em}	z_{abs}	logN(HI)	logN(FeII)	logN(ZnII)	logN(SiII)	logN(MnII)	logN(CrII)	logN(NiII)	logN(SII)	logN(OI)
J1159+0112	2.000	1.94375	21.80 ± 0.10	15.51 ± 0.01	13.13 ± 0.01	15.98 ± 0.01	13.44 ± 0.04	13.78 ± 0.01	14.24 ± 0.01	> 15.16	< 18.00
J2241+1225	2.630	2.41800	21.15 ± 0.15	14.89 ± 0.10	...	...	13.39 ± 0.09	...	13.79 ± 0.06	14.94 ± 0.04	< 17.98
J1310+5424	1.930	1.80070	21.45 ± 0.15	15.63 ± 0.02	13.57 ± 0.01	> 16.22	...	14.00 ± 0.03	14.47 ± 0.01	> 15.97	< 18.39
Q2230+02	2.150	1.86440	20.85 ± 0.08	15.18 ± 0.02	12.82 ± 0.03	15.68 ± 0.01	...	...	14.07 ± 0.02	...	< 18.55
J1013+5615	3.610	2.28400	...	> 15.17	...	16.14 ± 0.01	...	...	...	...	...
J2222−0945	2.930	2.35430	20.55 ± 0.15	15.12 ± 0.04	...	15.56 ± 0.12	...	...	14.13 ± 0.02	15.33 ± 0.02	< 18.02
J1417+4132	2.020	1.95090	21.45 ± 0.25	15.63 ± 0.01	13.54 ± 0.01	> 16.28	...	14.04 ± 0.01	14.54 ± 0.00	...	17.98 ± 0.07
J1249−0233	2.120	1.78085	21.45 ± 0.15	< 16.60	< 13.11	...	< 13.77	13.87 ± 0.02	14.23 ± 0.01	15.50 ± 0.02	< 18.23
J1200+4015	3.360	3.22000	20.65 ± 0.15	15.39 ± 0.02	...	...	...	...	14.21 ± 0.01	15.37 ± 0.01	< 17.79
J1610+4724	3.220	2.50661	21.00 ± 0.15	15.73 ± 0.01	13.55 ± 0.01	16.16 ± 0.01	...	14.02 ± 0.01	14.62 ± 0.01	> 16.01	< 18.35
Q0201+36	2.490	2.46280	20.38 ± 0.15	15.01 ± 0.00	...	15.54 ± 0.01	...	13.29 ± 0.03	14.04 ± 0.01	...	...
J0008−0958	1.950	1.76753	20.85 ± 0.15	15.62 ± 0.02	13.32 ± 0.01	16.05 ± 0.01	< 13.44	13.92 ± 0.01	14.47 ± 0.01	15.83 ± 0.02	< 18.03
J1155+0530	3.480	3.32607	21.05 ± 0.10	15.36 ± 0.03	12.75 ± 0.04	15.95 ± 0.02	...	13.58 ± 0.04	14.18 ± 0.01	15.35 ± 0.00	< 17.66
J1056+1208	1.920	1.60954	21.45 ± 0.15	15.81 ± 0.01	13.76 ± 0.01	> 16.34	...	14.06 ± 0.01	14.61 ± 0.00	> 15.66	< 18.20
J0927+1543	1.800	1.73113	...	> 15.00	13.72 ± 0.03	15.98 ± 0.01	...	13.79 ± 0.03	14.16 ± 0.03	< 15.86	< 18.97
J1313+1441	1.880	1.79480	...	15.51 ± 0.02	13.22 ± 0.01	...	...	13.55 ± 0.03	14.18 ± 0.01	15.71 ± 0.01	< 18.19
J2100−0641	3.140	3.09130	21.05 ± 0.15	15.33 ± 0.02	< 13.20	15.89 ± 0.00	...	13.53 ± 0.01	14.23 ± 0.00	15.64 ± 0.00	< 17.71
J1604+3951	3.130	3.16400	21.75 ± 0.20	15.59 ± 0.02	13.14 ± 0.02	16.10 ± 0.01	...	...	14.30 ± 0.01	15.70 ± 0.04	< 17.69
J0927+5823	1.910	1.63515	20.40 ± 0.25	15.28 ± 0.04	13.27 ± 0.01	15.74 ± 0.01	...	13.54 ± 0.02	14.34 ± 0.01	15.79 ± 0.14	< 18.33
J0058+0115	2.490	2.00953	21.10 ± 0.15	15.19 ± 0.02	...	< 15.54	...	13.53 ± 0.02	14.09 ± 0.01	15.41 ± 0.01	< 17.89
Q2342+34	2.920	2.90899	21.10 ± 0.10	...	...	15.62 ± 0.02	...	...	13.82 ± 0.05	15.16 ± 0.01	< 17.96
J1555+4800	3.300	2.39089	21.50 ± 0.15	15.73 ± 0.02	< 13.93	> 16.52	...	14.17 ± 0.01	14.75 ± 0.01	> 15.88	< 18.42
Q0458−02	2.290	2.03950	21.65 ± 0.09	15.40 ± 0.04	13.18 ± 0.02	> 15.89	...	13.76 ± 0.01	14.20 ± 0.02	...	< 18.52
J1049−0110	2.120	1.65760	20.35 ± 0.15	15.20 ± 0.02	13.15 ± 0.02	15.78 ± 0.01	...	13.35 ± 0.03	14.10 ± 0.03	15.47 ± 0.01	< 18.11
J2340−0053	2.090	2.05452	20.35 ± 0.15	14.96 ± 0.03	...	15.23 ± 0.01	...	...	13.81 ± 0.02	14.95 ± 0.00	< 17.56
J1010+0003	1.400	1.26514	...	15.44 ± 0.02	13.02 ± 0.02	15.87 ± 0.08	13.23 ± 0.03	13.78 ± 0.02	14.20 ± 0.02	...	< 20.03
FJ0812+3208	2.710	2.62593	21.35 ± 0.15	15.06 ± 0.01	13.15 ± 0.02	15.89 ± 0.01	...	13.44 ± 0.02	13.93 ± 0.01	15.48 ± 0.02	17.69 ± 0.07
J1552+4910	2.040	1.95987	...	15.41 ± 0.02	12.96 ± 0.02	15.98 ± 0.01	13.41 ± 0.04	13.76 ± 0.02	14.24 ± 0.01	15.34 ± 0.00	< 17.96
J1524+1030	2.062	1.94094	...	15.25 ± 0.03	> 13.32	> 16.00	...	...	14.23 ± 0.02	> 15.53	< 18.05
Q1755+578	2.110	1.97110	21.40 ± 0.15	15.81 ± 0.01	< 13.82	> 16.42	< 13.55	...	14.77 ± 0.01	> 15.97	< 17.88

Table 2.6 Column density estimates based on continuum placement

Ion	logN	$\log N^{a}_{0.99}$	$\log N^{b}_{1.01}$	$\Delta\log N^{c}$	$\log N^{d}_{err}$	$\log N(HI)_{err}$
FeII 1611	15.18	15.10	15.28	0.08	0.02	0.15
NiII 1370	13.93	13.90	13.97	0.04	0.01	0.15
SiII 1808	15.89	15.87	15.93	0.03	0.01	0.15
BII 1362	11.69	11.46	11.86	0.17	0.08	0.15

[a] The column density measured from the continuum placed at a relative intensity of 0.99. [b] The column density measured from the continuum placed at a relative intensity of 1.01. [c] The largest difference in the measured column density from shifting the continuum from the original placement. [d] Error on column density from AODM analysis.

The metallicites for the Thesis Sample (along with the element used as the metallicity indicator) are tabulated in Table 2.7, following the same metallicity indicator scheme from Rafelski et al. (2012). Although the Thesis Sample DLAs were initially targeted as being potential MSDLAs, 11 of the 30 selected do not follow the MSDLA criteria defined by Herbert-Fort et al. (2006, see Table 2.7). As these systems were identified by an automated search of the Sloan Digital Sky Survey spectra, the measured column densities are not accurate as several absorption components remain unresolved in the low resolution spectra (see Section 2.1). Therefore systems that were subjectively flagged as being potential candidates may not be MSDLA by definition, but contain column densities that are still metal-rich compared to typical DLAs. As a result, the Thesis Sample contains a mixture of bonafide MSDLAs and DLAs with sufficiently large metal column densities (relative to the typical DLA) that can still provide valuable abundance information, despite not making the arbitrary column density cuts.

2.3.3 Comparison to the Literature Samples

To understand how the Thesis Sample compares to the HR literature DLAs, Figures 2.9 – 2.11 show the distributions of neutral hydrogen column density, metallicity, and absorption redshift. These distributions are compared to those produced for the HR literature DLA sample (Figures 2.1–2.3 respectively; represented by the black dashed lines). One should note that the HR literature sample *does contain* the Thesis Sample, as the Thesis Sample has been published in Berg et al. (2013) and meets all the requirements of the HR literature sample. Furthermore, the HR literature sample

Table 2.7 Metallicities of Thesis Sample

QSO	MSDLA?	[M/H] (M)
J0008−0958	Yes	-0.17 ± 0.15 (S)
J0058+0115	No	-0.84 ± 0.15 (S)
Q0201+36	No	-0.35 ± 0.15 (Si)
Q0458−02	Yes	-1.10 ± 0.10 (Zn)
FJ0812+3208	Yes	-1.02 ± 0.15 (S)
J0927+1543	Yes	. . .
J0927+5823	No	0.24 ± 0.28 (S)
J1010+0003	No	. . .
J1013+5615	Yes	. . .
J1049−0110	No	-0.03 ± 0.15 (S)
J1056+1208	Yes	-0.32 ± 0.16 (Zn)
J1155+0530	No	-0.85 ± 0.10 (S)
J1159+0112	Yes	-1.30 ± 0.11 (Zn)
J1200+4015	Yes	-0.43 ± 0.15 (S)
J1249−0233	Yes	-1.10 ± 0.16 (S)
J1310+5424	Yes	-0.51 ± 0.16 (Zn)
J1313+1441	Yes	. . .
J1417+4132	No	-0.54 ± 0.25 (Zn)
J1524+1030	Yes	. . .
J1552+4910	Yes	. . .
J1555+4800	Yes	-0.92 ± 0.20 (Fe+0.3)
J1604+3951	Yes	-1.20 ± 0.20 (S)
J1610+4724	Yes	-0.08 ± 0.16 (Zn)
Q1755+578	Yes	-0.74 ± 0.15 (Fe+0.3)
J2100−0641	Yes	-0.56 ± 0.15 (S)
J2222−0945	No	-0.37 ± 0.15 (S)
Q2230+02	No	-0.66 ± 0.09 (Zn)
J2241+1225	Yes	-1.36 ± 0.16 (S)
J2340−0053	No	-0.55 ± 0.15 (S)
Q2342+34	No	-1.08 ± 0.10 (S)

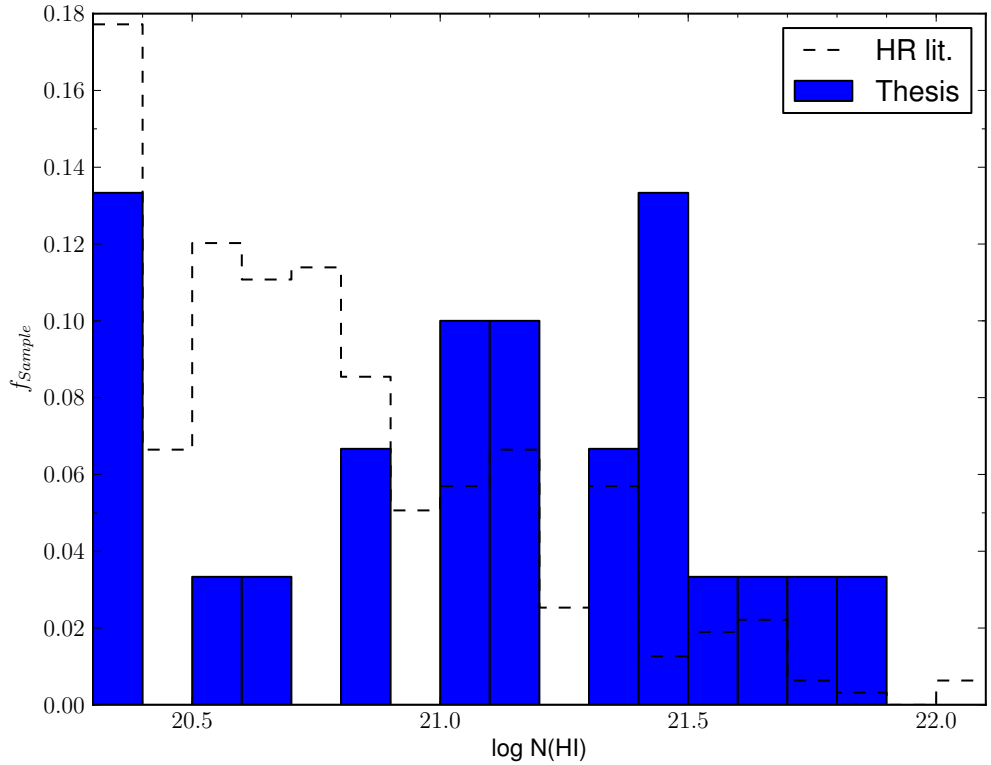

Figure 2.9 N(HI) distribution of the Thesis Sample (blue bars) compared to the HR literature DLA sample (black dashed line). Although the Thesis Sample DLAs span the entire range of N(HI) values seen in the HR literature DLAs; they are clearly biased towards high HI column densities, most having an HI column density logN(HI)$>$ 21.

already contains other MSDLAs and large metal column systems, therefore it is would be unreasonable to exclude some metal-rich systems while including others. Only the 24 DLAs in the Thesis Sample with HI measurements have metallicity measurements as it is impossible to derive a metallicity without a HI column density.

Figure 2.9 clearly shows that the neutral hydrogen column density for DLAs in the Thesis Sample spans the entire range of values as the DLAs in the HR literature sample. However the distributions are not identical. By definition of the Thesis sample, DLAs with larger column densities of metals generally have higher HI column densities. This is clearly shown by the histogram being in excess of the dashed line above neutral hydrogen column densities of log N(HI)$\sim$ 21.

Figure 2.10 shows higher than average metallicities in Thesis Sample DLAs relative to the DLA HR literature sample. Whereas the median metallicity of DLAs seems to be [M/H]~ -1.5; this metallicity is the lower limit of the Thesis Sample. The use of sulphur and zinc as metallicity indicators are preferentially selected as the Thesis Sample DLAs are more metal rich and therefore are more likely to contain detections of sulphur or zinc (see Section 2.1).

In terms of redshift (Figure 2.11), the Thesis Sample does not span the entire range that the HR literature DLA sample spans, but mostly within the redshift range of 2 to 3. The lack of large metal column DLAs at lower redshifts is partially due to selection effects. The minimum wavelength that can be measured in the Sloan Digital Sky Survey (SDSS) is 3800 Å (Adelman-McCarthy et al., 2008). If one were to look at the lines H I 1215 Å, Si II 1808 Å and Zn II 2026 Å (which are needed to determine if the system is a DLA and is metal strong), the minimum redshifts at which one could observe this DLA with SDSS would be $z_{\rm abs}$= 2.1, $z_{\rm abs}$= 1.1, and $z_{\rm abs}$= 0.9 (respectively). However, Herbert-Fort et al. (2006) only looked for systems at redshifts greater than $z_{\rm abs}$= 1.6, as ozone in the atmosphere blocks UV below 3000Å, making it impossible to get an HI measurement from the ground and confirm whether the system is a DLA.

To demonstrate that the Thesis Sample overlaps in metallicity with the Galactic disk subsamples, Figure 2.12 compares the metallicity distributions of all stellar literature subsamples along with the HR literature sample (black dotted line). It is clear that the Thesis Sample of DLAs spans the upper range of DLA metallicities, and probes the metallicity regime of the metal rich stellar component that is not well sampled by the HR literature sample. Overall, the overlap between the Thesis DLA sample and the more metal-rich stellar components of the stellar literature sample justify a comparison between the chemical evolution of a selected element for all the Milky Way populations described above.

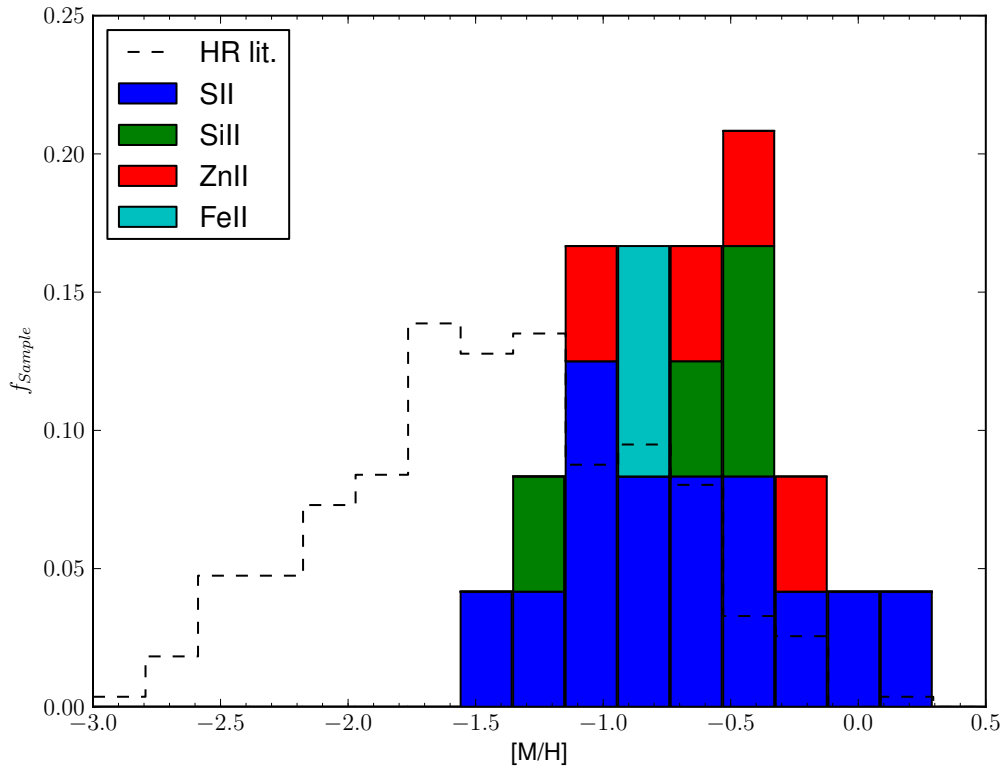

Figure 2.10 Metallicity distribution of the Thesis Sample compared to the HR literature DLA sample (black dashed line). It is clear that DLAs from the Thesis Sample probe a higher metallicity range than the HR literature DLA sample (median [M/H]~ -0.75 dex compared to ~ -1.5 dex in the HR literature sample) as expected from DLAs in the Herbert-Fort et al. (2006) sample of MSDLAs. Sulphur is the dominant metallicity tracer adopted at higher metallicities (compared to silicon in HR literature DLAs; Figure 2.2) as it is more likely detected with higher column densities in the Lyman alpha forest.

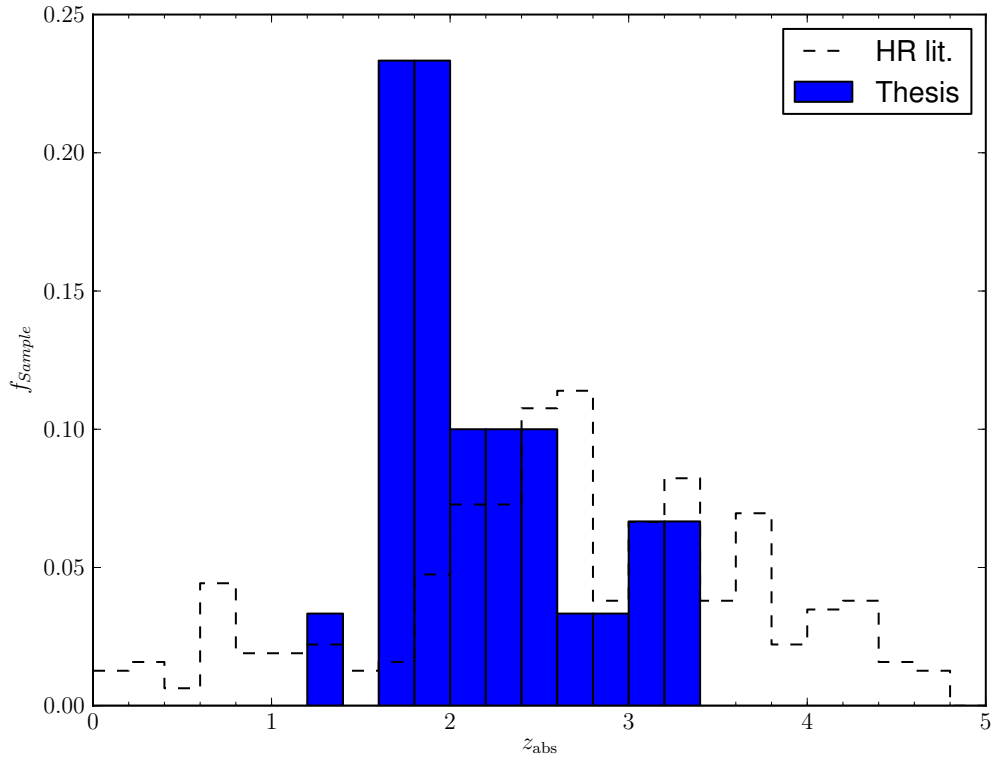

Figure 2.11 Absorption redshift distribution of the Thesis Sample compared to the HR literature DLA sample. The black-dashed lines represent the DLA HR literature distribution from Figure 2.2. The Thesis Sample DLAs are typically found at intermediate ($z_{\rm abs}\sim$ 2) redshifts as a result of selection effects from ground based, optical observations.

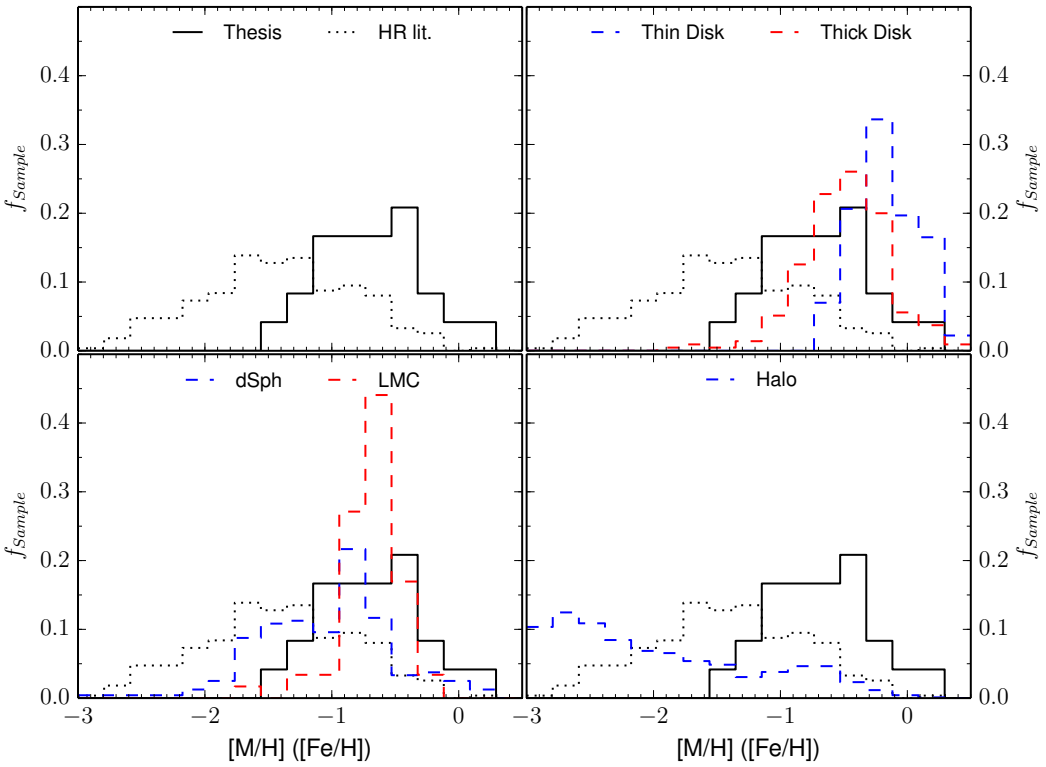

Figure 2.12 A comparison of the metallicity distributions of the Thesis Sample (black line) with the literature samples. Top left: the HR literature sample is plotted as the black dotted line. Top right: the thin and thick disk subsamples are plotted as blue and red (respectively). Bottom left: the dSphs and LMC subsamples are plotted in blue and red (respectively). Bottom right: The halo subsample is shown in blue. Overall, the Thesis Sample overlaps with the more metal-rich dSphs as well as the thin and thick disk subsamples.

Chapter 3

Chemistry Of DLAs In The Context Of The Local Group

As described in the Introduction, DLAs provide a useful tool to study the chemical evolution of the gas in high redshift galaxies. Studies of specific metals in DLAs can provide insight into the nucleosynthetic processes that occur in other galaxies, and how these processes vary from our own Galaxy.

This chapter compares the chemistry of the Thesis Sample to both the HR DLA and the stellar literature samples to motivate how the chemistry of ISM gas at high redshifts evolves relative to the stellar data. Section 3.1 presents a selection of elements (iron, zinc, sulphur, silicon, nickel, phosphorous, and manganese) and discusses the nucleosynthetic origin of each element, how the abundances are measured in stars and DLAs, the abundance patterns seen in stars, and how DLAs compare with these stellar trends. For most of these elements, such a detailed comparison is a first in over a decade (Prochaska & Wolfe, 2002), while it is the first comparison ever made for phosphorous. With the addition of DLAs from both the literature and Thesis samples, stronger constraints can be made on the nucleosynthetic trends seen in DLAs. Section 3.2 summarises what is seen in DLAs and presents what further needs to be completed in DLA-stellar comparisons.

3.1 Detailed Chemical Comparison

The comparison between stellar and DLA abundances requires an understanding of the nucleosynthetic origin of the elements in question, and the difficulties and errors

in measuring the abundances. For each of the elements below, a summary is made to this effect.

To aid the understanding of the nucleosynthetic origin of the elements, a combination of the simulation work by Woosley & Weaver (1995) and the NuGrid collaboration (Pignatari et al., 2013) will be used. For each element, a plot demonstrating the yields from stellar evolution (i.e. with respect to a Salpeter IMF; further known as a *Salpeter* plot) will be shown to describe the results from the NuGrid collaboration. As an example, Figure 3.1 shows the Salpeter plot for oxygen, displaying the ejected mass (in $M_{\odot}$) of oxygen for a simulated star of a given mass. The black dashed line reflects the mass of oxygen initially locked up in each mass bin of stars (based on a Salpeter IMF; the mass bins separated by vertical black lines) from a cloud of gas with a given metallicity (in this case one half the solar metallicity). The red line shows the mass of material processed and ejected through stellar winds from AGB stars, while the circles represent the mass released through SNe II explosions. The smaller circles represent the amount of material formed prior to the supernovae (i.e. from burning within the core and shells of the star), while the larger circles show the yields after the supernovae have taken place (i.e. explosive nucleosynthesis). The colour of the circle is the speed of the explosion (blue is slow, green is rapid) which is related to the energy of the explosion, and therefore the final stellar remnant mass of the progenitor (where a rapid explosion has more energy and produces a lower mass remnant relative to the slow explosion; see Pignatari et al., 2013). The two speeds selected by the NuGrid group represent the range in the final remnant masses expected from SNe II.

Figure 3.2 shows a cartoon representing a slice of a massive star that will undergo a supernovae to help understand which part of the star the ejected material is coming from in the Salpeter plots. Each shade represents the different structures in the star (i.e. the various burning shells, and outer envelope). The material between the top dashed line and the outer edge of the stars is the material ejected as part of the wind (including material that has been dredged up from the burning layers of the star to the surface), whereas the material between the two dashed lines represents the pre-supernovae material that will be ejected after the explosion. The remaining material below the lower dashed line will fall back onto the stellar remnant (e.g. a neutron star or black hole). The exact positions of these dashed lines are empirically driven, and can be looked up in Pignatari et al. (2013). However, the colour of the circles (i.e. green/blue) effectively represent the position (lower or higher; respectively) of

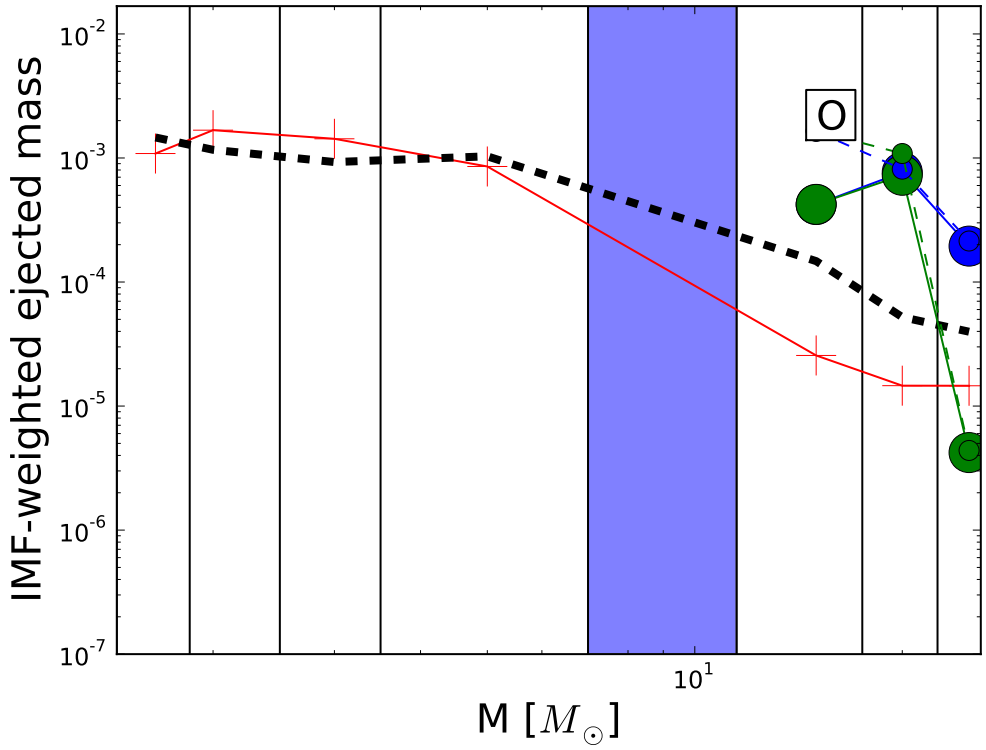

Figure 3.1 The Salpeter diagram for oxygen from the NuGrid simulations. The black dashed line represents the initial mass of oxygen in the stars based on a Salpeter IMF. The vertical black lines show the upper and lower mass limits for each mass bin. The red crosses and line represent the mass of stellar wind material that was processed and ejected by the star. The small and large circles represent the mass of oxygen in the star both before and after the supernova explosion (respectively). The colours of the circles represent whether the explosion was slow (blue) or rapid (green). Overall, the dominant source of oxygen production is in massive stars prior to the onset of supernovae explosions, as indicated by the overlap of the small and large circles. The shaded light blue region is beyond the work of this thesis, and is ignored.

the bottom black dashed line.

In all the Salpeter plots, processes that produce the elements will have relative yields *above* the black dashed line, whereas processes that consume the elements will lie *below* this line. The total amount which is produced or consumed is reflected by the difference in ejected mass between the point and the initial value. Therefore, the amount of the element produced in the evolution of the star is given by the difference between the initial value from the IMF and the small circle; while the mass produced in explosive nucleosynthesis is given as the difference between the large and smaller circle (of the same colour). Therefore, Figure 3.1 shows that massive stars ($\gtrsim 10\mathrm{M}_{\odot}$) produce oxygen during their evolution, and very little is produced during the supernovae itself. This is in agreement with other literature, as oxygen is formed during helium burning in massive stars (Clayton, 2003) and is released primarily in the Type II supernovae (Woosley & Weaver, 1995).

Although these plots provide useful information on the origin of the elements, they do not provide information on the nucleosynthesis of Type Ia supernovae. As the mechanism of the Type Ia SNe explosions remains uncertain (cf. Travaglio et al., 2004; Seitenzahl et al., 2013), the yields resulting from these explosions are not included in the NuGrid simulations. Furthermore, the simulations used in this thesis only show the yields that result from a star starting with a single metallicity (i.e. half the solar value; [Fe/H]~ -0.3), and do not necessarily represent the nucleosynthetic sites of elements in metal-poor stars (e.g. see Heger & Woosley, 2010, for further details). Therefore, although the results from the NuGrid simulations are impressive with the large nuclear networks used, they should be used in conjunction with other resources.

To provide an idea of the relative contribution of SNe Ia, Figure 3.3 shows the yields for a solar metallicity SNe Ia explosion from Travaglio et al. (2004). The figure shows that the bulk of the elements produced in SNe Ia are chromium, manganese, iron, cobalt, and nickel. However, the relative production factors (i.e. the amount produced relative to the initial composition prior to the explosion) depend on the metallicity of the star (Travaglio et al., 2004; Seitenzahl et al., 2013), as in SNe II.

A further difficulty in understanding DLA abundances is the depletion of the measured gas phase abundance into dust. The amount of dust depletion between elements is a function of the condensation temperature of the element (Figure 3.4; see Savage & Sembach, 1996), where elements with lower condensation temperatures are more *volatile* (i.e. less depleted onto dust), and elements with higher condensation temperatures are more *refractory* (i.e. more depleted onto dust). Therefore care

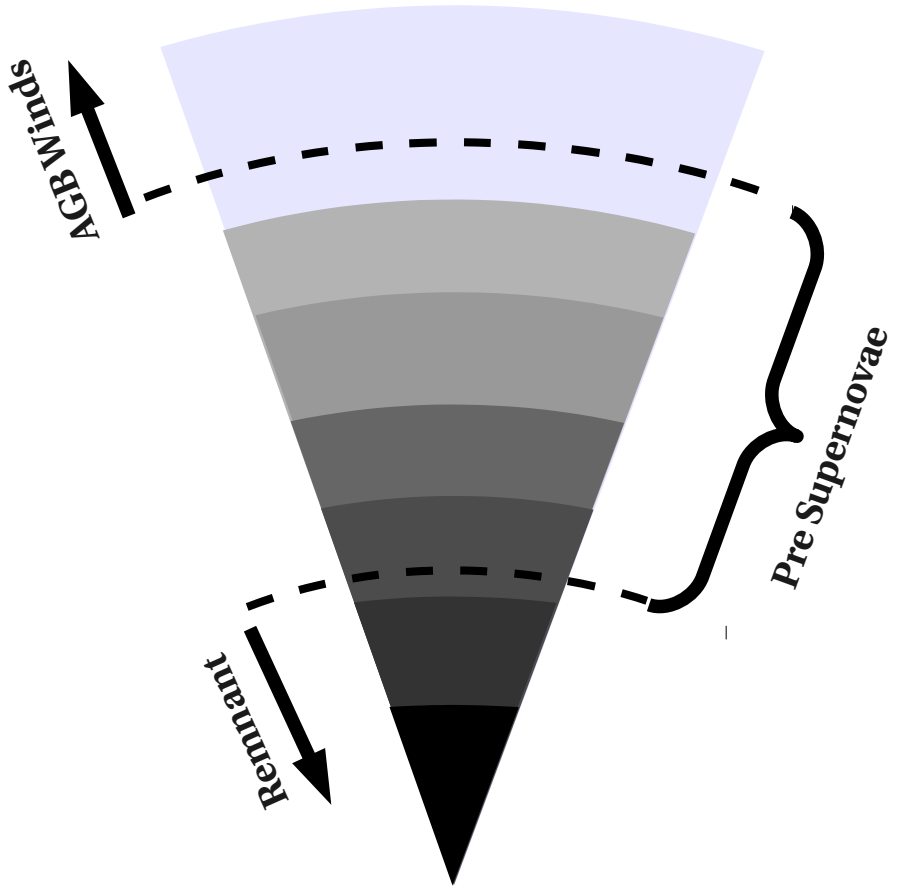

Figure 3.2 A cross-section of a star in the NuGrid simulations. The grey areas represent the structure of the star. In the simulations, the material released from winds comes from the outer atmosphere of the star (between the out edge of the star and the top dashed line). All the material that is produced in the star that is released in the supernova explosion is represented by the layers between the two dashed lines. All the remaining material below the bottom dashed line will fall back onto the remnant.

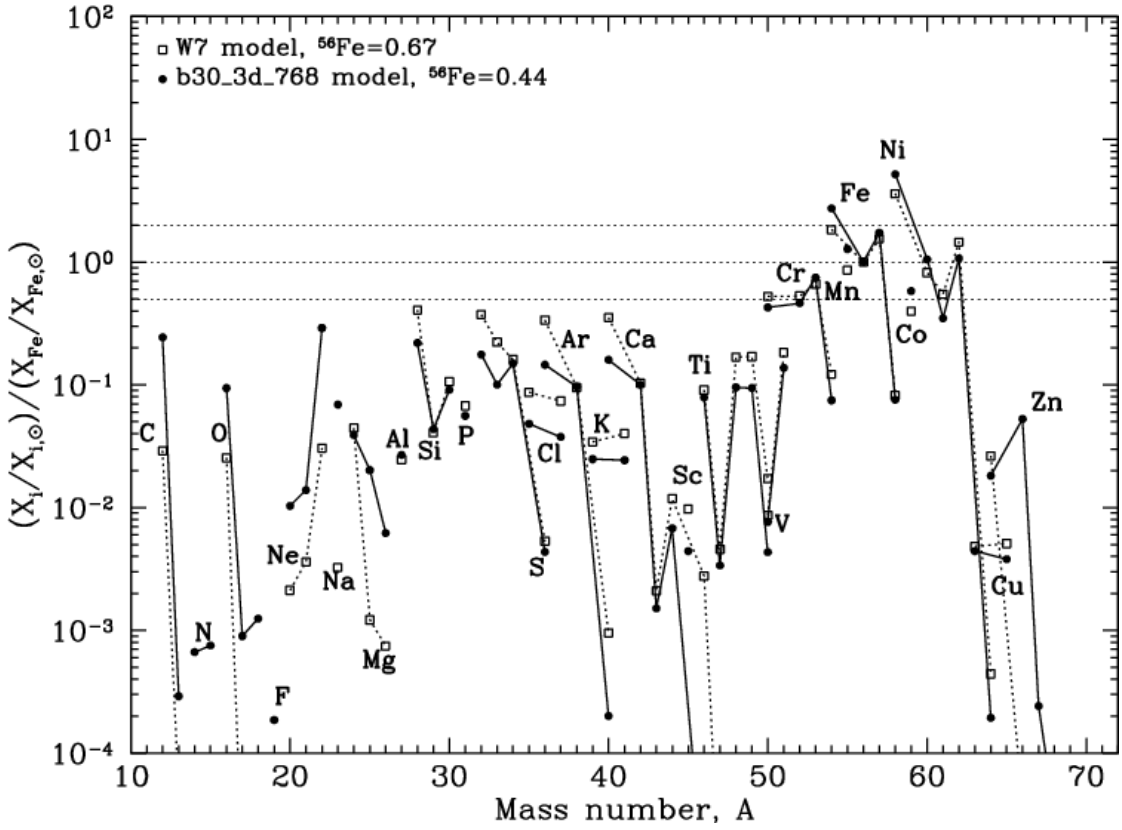

Figure 3.3 SNe Ia yields from Travaglio et al. (2004) and Thielemann et al. (2003) (circles and squares, respectively; Figure taken from Travaglio et al., 2004). The y-axis represents the yields in terms of $10^{[X/Fe]}$. The difference between the two models highlights the uncertainty in SNe Ia model yields.

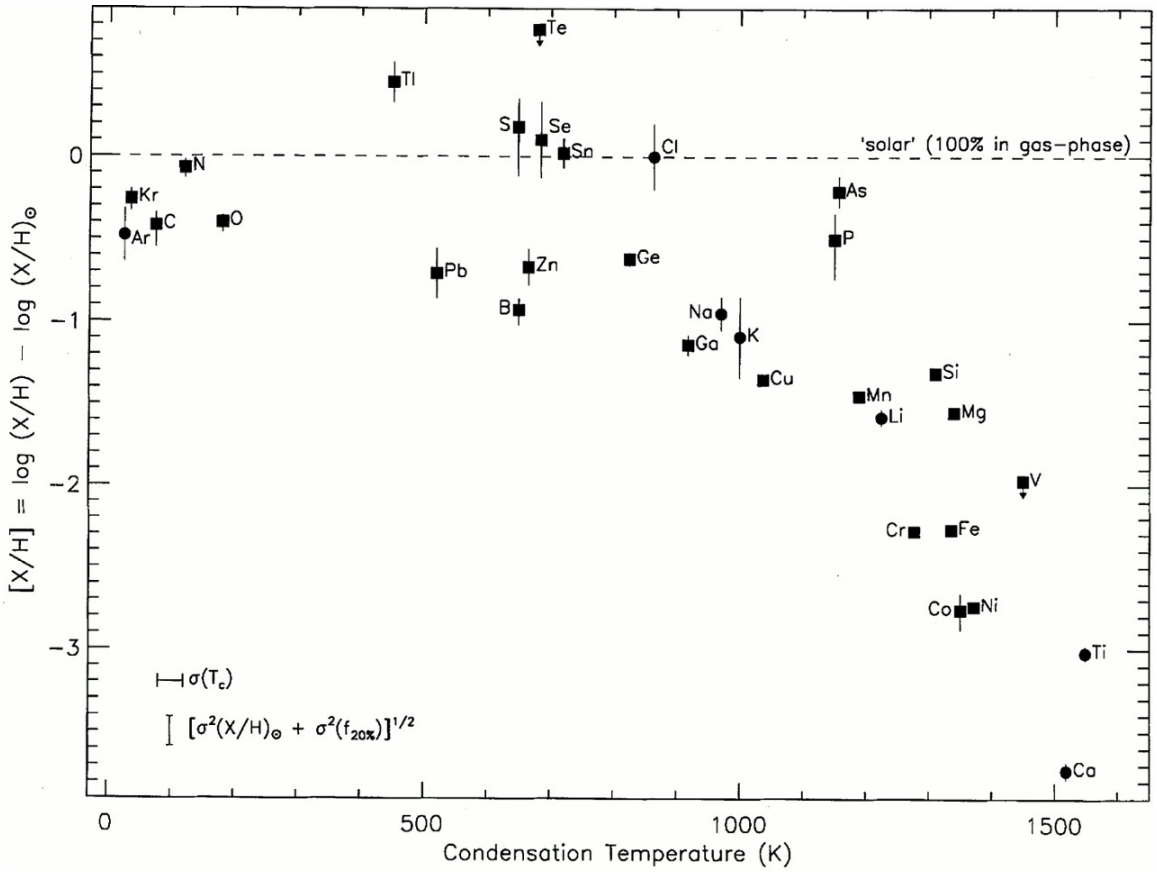

Figure 3.4 Gas phase abundance of a cool diffuse ISM cloud in Milky Way as a function of condensation temperature (Figure 4 from Savage & Sembach, 1996). This ISM gas cloud is expected to have an essentially solar abundance (i.e. [X/H]$\sim$ 0), therefore any discrepancy from the solar value is dominated by dust depletion. It is clear that elements with higher condensation temperatures are more refractory than elements with lower condensation temperatures.

must be taken when understanding the abundance trends when elements have high condensation temperatures.

The comparison of abundances in DLAs and stars is not straightforward. The stellar samples selected in Chapter 2 represent the abundances of individual stars within the different regions of the Milky Way, whereas abundances derived within a DLA represent the "average" abundance pattern of the gas seen along the line of sight through a galaxy, probing a combination of these populations. To separate the different populations out by looking at individual DLA clouds would not be effective as these clouds are show no variation in composition (e.g. Dessauges-Zavadsky et al.,

2006). However, constraints can still be placed on how the gas at high redshifts have evolved in the context of the chemical evolution of the star within the different Milky Way populations.

3.1.1 Iron

Before starting the discussion of the elements, a benchmark element is needed to study the comparison of stars and DLAs, particularly for a metallicity indicator. Iron (Fe) is the most commonly used metallicity indicator in stars as it has many absorption lines present in optical spectra of stars. In addition, it is generally the standard for deriving the model atmospheres for abundance measurements. Therefore, Fe is a good benchmark for comparison.

Fe is formed from the decay of ^{56}Ni produced in the core[1] of SNe Ia (Clayton, 2003). Fe is also produced in *α-rich freezeout*[2] in Type II supernovae. Although Fe forms in both types of supernovae, much more is produced in SNe Ia. Figure 3.5 shows the NuGrid yields for Fe. With nearly all the output falling below the initial value (black dashed line), it is generally consumed by SNe II and stellar winds, except in the lowest mass cases where supernovae explosions do produce some Fe.

Measuring Fe in stars is one of the easiest elements to study with its many absorption lines of varying oscillator strength (e.g. see Table 3 in Reddy et al., 2003). As all Fe lines must measure the same overall abundance of Fe, Fe lines are used to derive the parameters of model atmospheres. However, Mashonkina et al. (2011) suggest that some FeI lines in stars suffer from non-LTE effects; which can impact both the derivation of the surface gravity of a star, and the relative contribution of different species towards the overall abundance. Nevertheless, [Fe/H] is used as the metallicity indicator in stars due to its ease of observation.

In DLAs, Fe also has many observable absorption lines (Table 3.1). With a range in oscillator strengths, it is generally possible to measure an unsaturated Fe line to derive an abundance. However, Fe has a condensation temperature of $T_{\rm cond} = 1336$ K (Savage & Sembach, 1996), making it susceptible to dust depletion. As a result, Fe abundances in DLAs are typically underestimated (Pettini et al., 1994; Vladilo,

[1] As the binding energy per unit nucleon favours ^{56}Ni, all the material in the core is turned into ^{56}Ni in a state of *quasiequilibrium*.

[2] During the supernovae explosion, all the nuclei within the star are broken up into α-particles, freezing-them out until the energy has reduced to a point where it is favourable for the alpha particles to recombine.

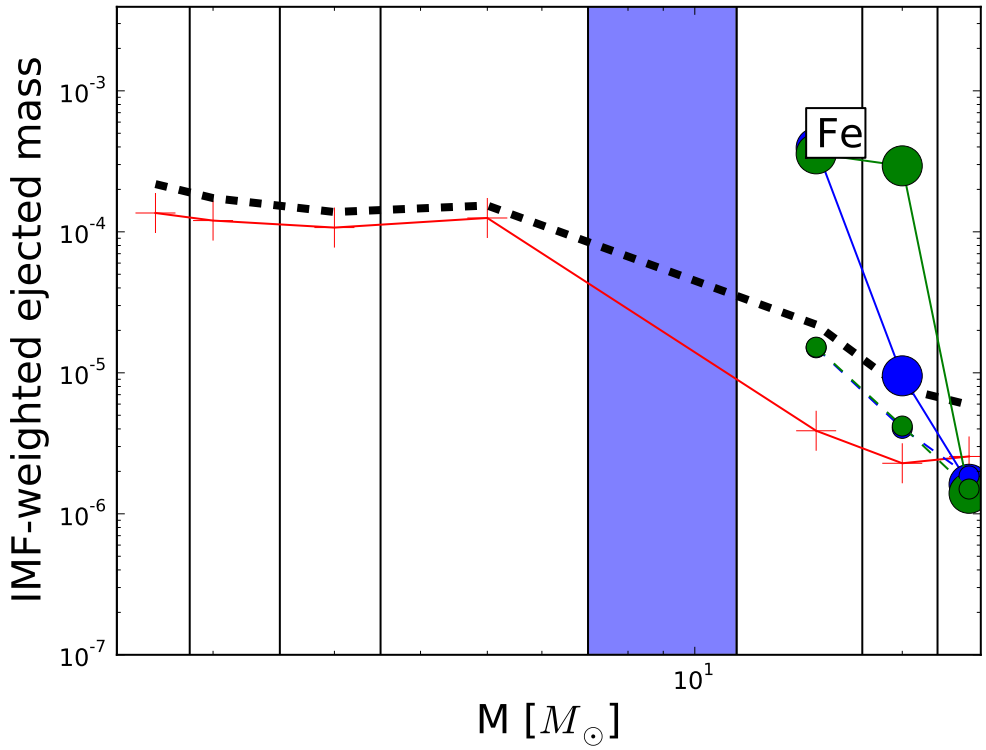

Figure 3.5 Salpeter plot for Fe from the NuGrid simulations. Symbols are the same as in Figure 3.1. The only production of Fe in their work comes from $\sim$ 30 $M_\odot$stars. Both winds and higher mass supernovae consume Fe. Although not shown, SNe Ia also contribute a significant amount of Fe (Figure 3.3).

Table 3.1 Fe lines commonly observed in DLAs

Ion	λ (Å)	f
FeII	1608.4511	5.77×10^{-2}
FeII	1611.2005	1.38×10^{-3}
FeII	1901.7730	7.00×10^{-5}
FeII	2249.8768	1.82×10^{-3}
FeII	2260.7805	2.44×10^{-3}
FeII	2344.2140	1.35×10^{-1}
FeII	2374.4612	3.12×10^{-2}
FeII	2382.7650	3.20×10^{-1}
FeII	2586.6500	6.91×10^{-2}
FeII	2600.1729	2.39×10^{-1}

Reference–Morton (2003)

2002a), and do not provide an *accurate* metallicity benchmark for the comparison to stars. For this reason, zinc is commonly used in DLAs (e.g. Pettini et al., 1994; Lu et al., 1996a; Prochaska & Wolfe, 2002).

3.1.2 Zinc

The origin of zinc (Zn) has remained somewhat of a mystery. The general picture is that Zn is produced primarily in Type II SNe (Woosley & Weaver, 1995), however it is unclear what processes actually contribute to the production of Zn. It is thought that most of the Zn is produced by a combination of the s-process and α-rich freezeout following nuclear statistical equilibrium, with very little Zn being produced by SNe Ia (Clayton, 2003). Figure 3.6 shows the predicted yields for Zn from the NuGrid simulations, showing Zn is primarily generated in explosive nucleosynthesis in $\sim 10 M_{\odot}$ stars. However, the yields are dependent on the energy of the explosion and therefore the amount of fallback, as shown by the large difference between the large green and blue circles in Figure 3.6.

Zn measurements in stars usually use one of two multiplets (further denoted as Mult.; 4722 Å and 4810 Å [Mult. 2], and 6362 Å [Mult. 6]). Chen et al. (2004) discussed the advantages and disadvantages of using these lines and concluded that, although the 6362 Å line is weaker, it is more reliable as it does not saturate near solar metallicities and does not contain blending from several weak lines in the wings. Takeda et al. (2005) tested whether the Zn and sulphur lines required non-LTE corrections by running a grid of 120 model atmospheres with and without non-LTE as-

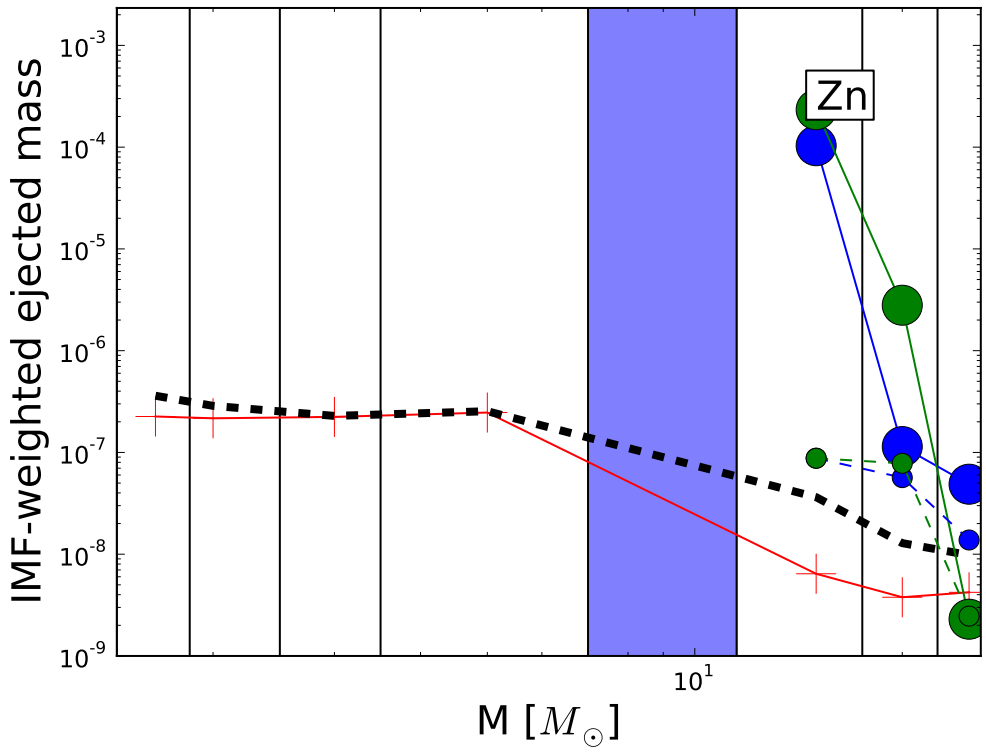

Figure 3.6 NuGrid predictions for Zn. Symbols are the same as Figure 3.1. With the large green circles being the largest contributors, $\sim 20M_\odot$ stars with little fallback are the most dominant sources of Zn production.

Table 3.2 Commonly observed Zn absorption lines in DLAs

λ (Å)	f
2026.136	5.01×10^{-1}
2062.664	2.46×10^{-1}

REFERENCE–Morton (2003)

sumptions, and determined that corrections are typically less than 0.1 dex (the 6362 Å line has nearly negligible corrections) but can be as large as 0.3 dex. Many papers (e.g. Nissen et al., 2007; Spite et al., 2011) use the non-LTE corrections from Takeda et al. (2005) by matching their stars to the model atmosphere grid and adopting the correction from the closest matching atmosphere.

Much of the stellar literature on Zn has been focused on answering the question of whether Zn traces iron over all metallicities. Part of the motivation of these studies was to determine whether using Zn in DLAs as an iron-peak tracer is valid or not. With the pioneering work on Zn done by Sneden & Crocker (1988) and Sneden et al. (1991), [Zn/Fe] appeared to be solar for disk stars between metallicities of $-3.0 \leq$[Fe/H]≤ 0.0. This had been confirmed by observations of halo stars (Nissen et al., 2004), as well as thin and thick disk stars and (Chen et al., 2004). However, with the additional observations of more metal-poor stars (Nissen et al., 2007) and the inclusion of non-LTE effects (Takeda et al., 2005), [Zn/Fe] was found to rise with decreasing metallicity after [Fe/H]≤ -1.5 (see Figure 3.7; Nissen et al., 2007). The difference in the upper and lower panels of Figure 3.7 suggests that non-LTE effects are important at $-2.5 \leq$[Fe/H]≤ -1.5, whereas the rise in [Zn/Fe] at [Fe/H]≤ -2.5 is nucleosynthetic. As a result, Zn is not a valid tracer of iron over all metallicities, however it can be used in place of iron at [Fe/H]≥ -1.5, where stars do not require non-LTE corrections.

Zn is one of the preferred metallicity indicators in DLAs. With a low condensation temperature ($T_{\rm cond}$ = 660 K; Savage & Sembach, 1996), it is considered to be undepleted into dust (Sembach et al., 1995). As early stellar studies (e.g. Sneden et al., 1991) showed that Zn tracked the iron peak elements (which are all depleted into dust); Zn became the standard iron-peak element tracer. Table 3.2 shows the two typically measured Zn lines in DLAs. Measuring Zn in DLAs is challenging as the stronger lines are often (somewhat) blended with either the Mg I 2026 or Cr II 2062 lines in low (high) resolution studies (Prochaska & Wolfe, 2002), or the DLA

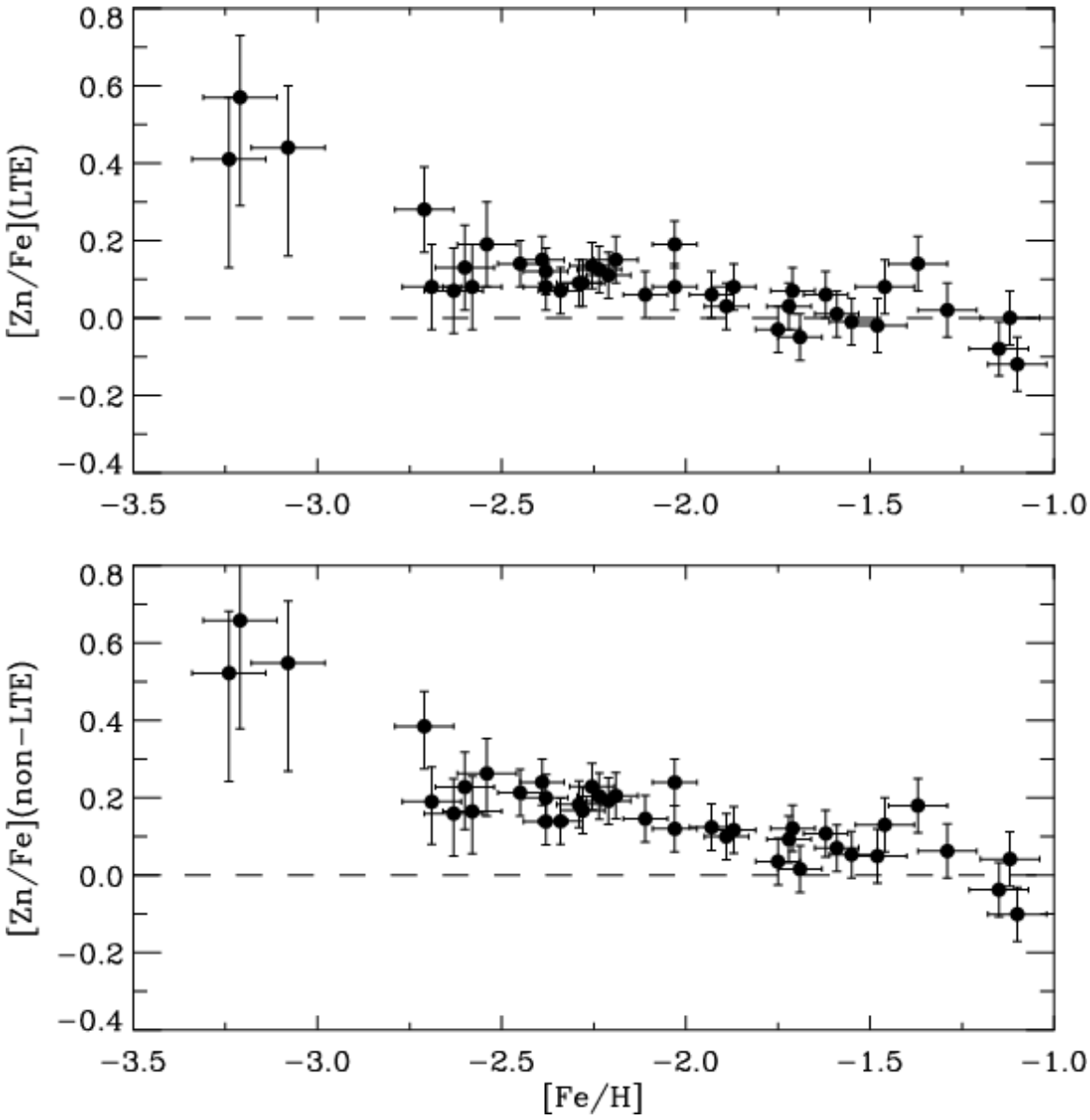

Figure 3.7 Figure from Nissen et al. (2007) showing [Zn/Fe] as a function of [Fe/H] without (upper panel) and with (lower panel) non-LTE corrections. The data includes stars from the thin and thick disk, as well as the halo. The rise at metallicities [Fe/H]≤ -1.5 indicates that Zn is not a good tracer of iron in metal poor systems.

contains a small column density of Zn[3]. Therefore accurate Zn abundance measurements are typically restricted to observations with high-resolution spectrographs to remove blending (Prochaska & Wolfe, 2002).

Studies of Zn in DLAs are usually used to assess the dust depletion in a given DLA. As Zn is somewhat volatile, it has become a standard of comparison to determine the gas–dust ratio in DLAs. Much of the early work on dust depletion focused on the [Cr/Zn] ratio (cf. Pettini et al., 1994, 1997, 2000). With Zn being relatively undepleted into dust compared to chromium, and assuming that chromium and Zn trace each other in stars (i.e. [Cr/Zn]= 0) in a DLA with no dust depletion; [Cr/Zn] would indicate what fraction of chromium was locked into dust. In Pettini et al. (1994), a threshold of [Cr/Zn]= -0.3 (i.e. 50% of chromium locked into dust) was chosen as an indicator of whether there was sufficient dust depletion in a DLA. Although this study presented a method of selecting DLAs and giving an average gas–dust ratio in DLAs, it did not provide sufficient means to correct for the dust depletion. Vladilo (2002a) and Vladilo (2002b) presented a scaling relation that would provide a dust correction based on [Fe/Zn] rather than [Cr/Zn]. The scaling law however requires two parameters are known in DLAs (the percent variations in the relative abundance in the dust from changes in either *(i)* the dust–metal ratio or *(ii)* the relative abundance of metals in the medium). However, determining these two parameters is quite challenging as it requires assumptions about how similar the ISM in these galaxies is to the ISM in the Milky Way (where these parameters can be derived empirically).

Figure 3.8 shows the trend of [Zn/Fe] in stars and DLAs with the acquired literature and Thesis samples. The increase in [Zn/Fe] in DLAs (from both the Thesis and HR literature samples) with increasing metallicity has been subject to debate, as to whether its primary origin is from dust depletion or the difference in the nucleosynthetic origin of the two species (e.g. Lu et al., 1996a; Prochaska & Wolfe, 2002). Ledoux et al. (2002a) discussed the uncertainty, arguing that if [Zn/Fe] can be as high as +0.2 dex in the thick disk ([Fe/H]~ -0.5; see Prochaska et al., 2000), any DLA with [Zn/Fe]> 0.2 dex must be influenced by dust depletion. It is still difficult to determine whether Zn is behaving more like an α-element or and iron-peak element (where [Zn/Fe] would effectively be solar). Rafelski et al. (2012) showed with their DLA sample that [α/Zn] is constantly solar in DLAs over a large span of metallicity ($-2.1 \leq$ [Zn/H] ≤ 0.3), suggesting that Zn behaves more like an α-element rather than belonging to the iron-peak. However for metallicities [Zn/H]≤ -2.0, it would

[3]Zn is somewhat rare, with a solar abundance of $(\mathrm{Zn/Fe})_\odot \sim -2.8$ (Asplund et al., 2009)

appear that a slight α-enhancement effect begins (see Section 3.1.4). With dSph losing their α-enhancement at lower metallicities than the Milky Way due to different star formation histories (Tolstoy et al., 2009), it may be the case that a similar effect is being seen in DLAs, although more metal-poor DLA observations are needed to conclude this effect. This is further discussed in Sections 3.1.3 and 3.1.4.

Despite the effects of dust depletion, the value of [Zn/Fe] at low metallicities ([Fe/H]≤ -1.3) appears to be consistent with measurements in the halo. As discussed above, supersolar [Zn/Fe] appears to be nucleosynthetic in origin at low metallicities, which could be the case for low metallicity DLAs as well. It is also interesting to note that dSph have consistently subsolar [Zn/Fe]. Both Shetrone et al. (2003) and Venn et al. (2012) attribute this to higher energy SNe II (or *hypernovae*) blowing all the Zn out of the potential wells of the dSph galaxies.

The increase in [Zn/Fe] with increasing metallicity in stars suggests that another tracer of the iron-peak elements is required in DLAs at [Fe/H]< -1.5, or abundance corrections may be necessary for either to iron (for dust depletion) or Zn (due to varying [Zn/Fe] in stars at low metallicities). As dust depletion affects all other iron-peak elements measured in DLAs (see Figure 4 in Savage & Sembach, 1996), and modelling dust depletion in DLAs is complicated and requires an individual understanding of the model parameters in each DLA (Vladilo, 2002a); it would be more reasonable to check what correction is necessary for the apparent increase in [Zn/Fe] with decreasing metallicity. To investigate the size of these corrections, two different models were used to determine the relation between [Zn/Fe] and [Fe/H] in stars. The fits were performed on the combination of the data from Gratton et al. (2003), Cayrel et al. (2004)[4], Nissen et al. (2007), and the Milky Way stars in the stellar sample. One model is a single best-fit line ([Zn/Fe]=m[Fe/H]+c); the other is a two-component fit, with the first component being a single line ([Zn/Fe]=m[Fe/H]+c), but remains at a constant value of [Zn/Fe] at [Fe/H]$\geq n$. This second model is motivated by the hypothesis that Zn is being primarily produced in SNe II, where it would trace a similar pattern to the α-elements with respect to iron. The two models were fitted using a least-squares analysis and are shown in Figure 3.9, with their best-fit parameters and corresponding residuals in Table 3.3. The data were first binned into equally-sized bins of metallicity before fitting to avoid any bias to the larger number of disk stars in comparison to the metal-poorer stars. The mean

[4]Both contain Zn abundances derived from Caffau et al. (2005) and Spite et al. (2011); respectively.

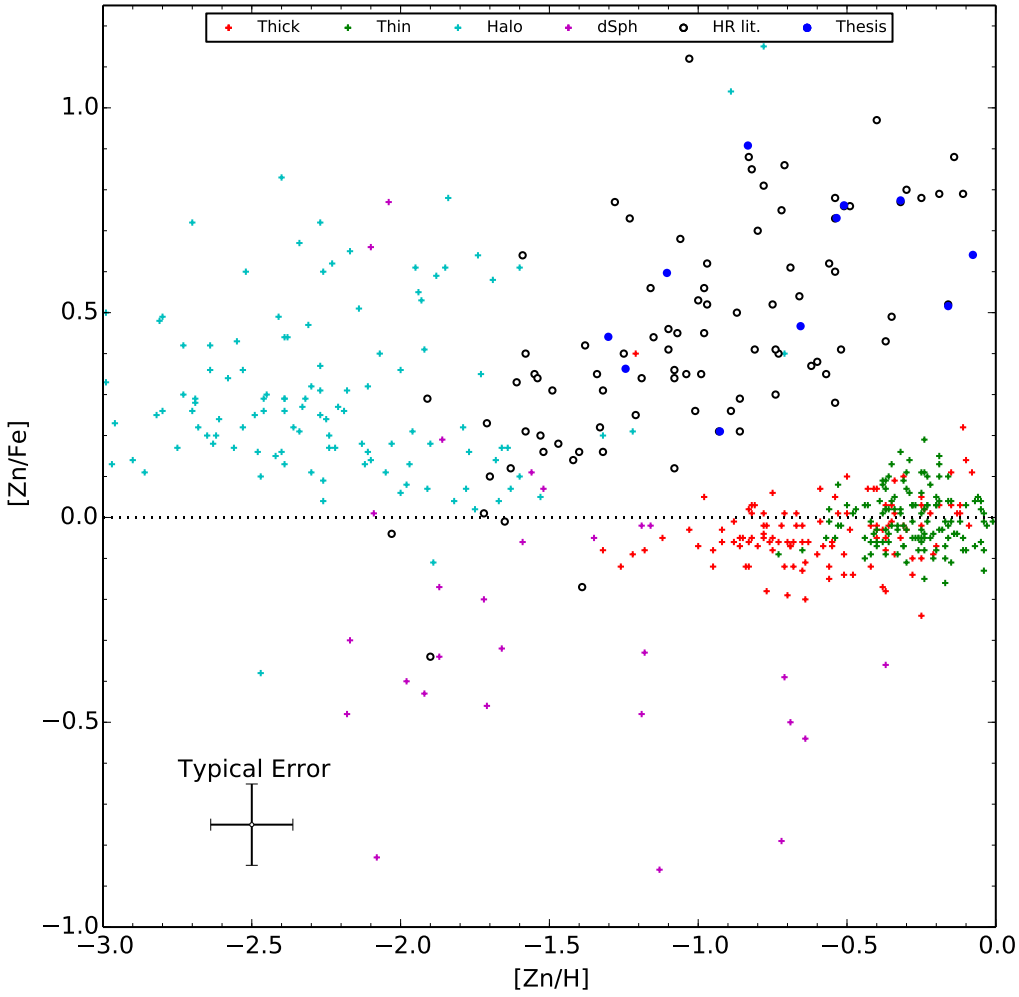

Figure 3.8 [Zn/Fe] as a function of [Zn/H] in the DLA samples (circles; HR literature sample in black, Thesis sample in blue) and stellar literature (crosses; red for the thick disk, green for thin disk, cyan for halo, and magenta for satellites). The typical errorbar in DLAs is shown, while the typical error in stellar data is reflected by the scatter. The increase in [Zn/Fe] towards lower metallicities in stars is attributed to a combination of non-LTE effects and nucleosynthetic origins in the first stars. The increase in [Zn/Fe] with increasing metallicity in DLAs is thought to be dust depletion, but could also be a result of a different nucleosynthetic origin of Zn.

Table 3.3 Model parameters of [Zn/Fe] vs. [Fe/H] relation in stars

Model	m	c	n	Residual
1-component	-0.123	-0.052	n/a	0.664
2-component	-0.146	-0.110	-0.612	0.526

[Zn/Fe] ratio of each bin was fitted using the inverse of the standard deviation as the weight for each point to account for the spread. Based on the residual, as well as the general distribution of points on either side of the two fits, the two-component model appears to be the better fit. However, as the DLA sample is generally more metal rich than [Fe/H]$= -2.0$ ([Zn/H]$= -1.9$ with the conversion), the correction is at most ~ 0.1 dex and is on the order of the typical errors in the stars. Therefore, although the correction is on the order of ~ 0.1 dex, this correction is not adopted in this thesis and it is assumed that Zn is still a good tracer of iron.

Overall, for metallicities of [Fe/H]$\gtrsim -2.0$, Zn appears to be a tracer of iron in stars to within 0.1 dex. The comparison of [Zn/Fe] in both DLA literature and Thesis samples to the stellar literature sample confirms that [Zn/Fe] in DLAs is primarily affected by dust depletion at high metallicities (Figure 3.8). However at [Zn/H]$\lesssim -1.5$, DLAs appear to agree with [Zn/Fe] in the halo stars when dust depletion is not believed to be dominant (despite the 0.1 dex correction that would apply from Zn and iron not tracing each other nucleosynthetically).

3.1.3 Sulphur

Sulphur (S) is primarily produced in the oxygen burning layer of massive stars. Silicon (the end product of oxygen burning) undergoes α-rich freezeout during Type II SNe, and produces S (Woosley & Weaver, 1995). The combination of SNe II yielding $\sim 10\times$ more S than SNe Ia while being $\sim 5\times$ more frequent, ensures that SNe II are the dominant source of S in the galaxy (Clayton, 2003). Figure 3.10 shows the predictions of S production in stars from the NuGrid simulations. It is clear that the largest contributors to the S abundances are from stellar nucleosynthesis in massive stars (small circles) and a little from explosive nucleosynthesis.

There are many lines available for observing S in stars, mostly using SI. However, many of these lines produce abundances that are inconsistent with each other (Caffau et al., 2005; Takeda et al., 2005). Caffau et al. (2005) were the first to review which lines are useful, and regard Mult. 1, 6, and 8 to be the most reliable.

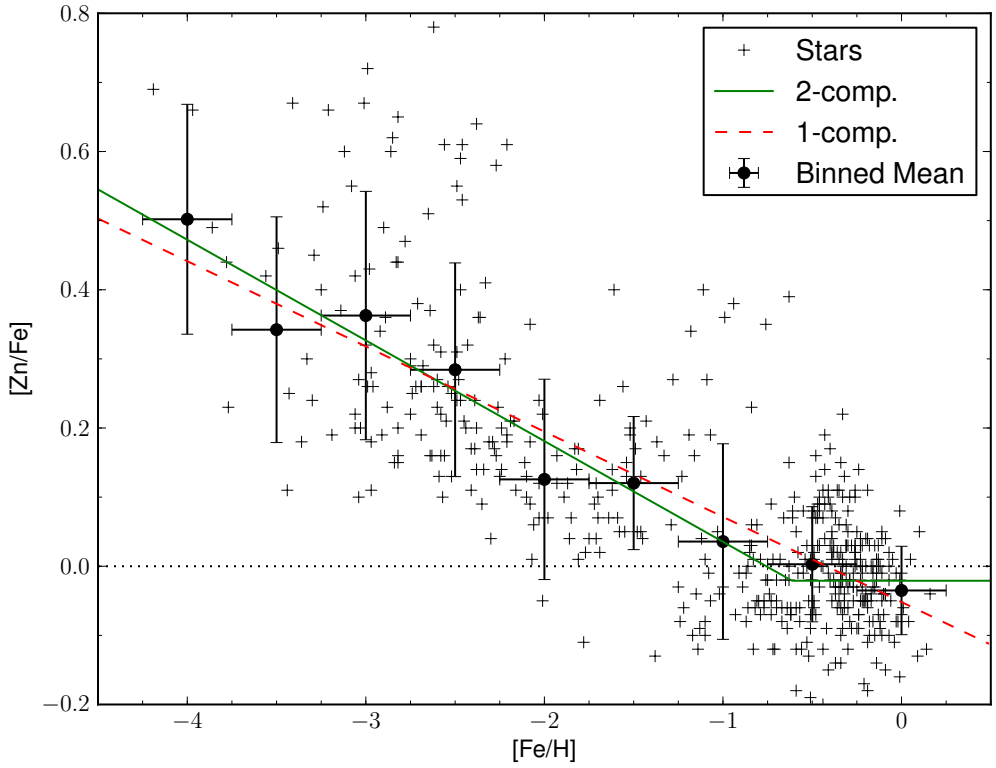

Figure 3.9 Fits of [Zn/Fe] as a function of [Fe/H] in stars. The stars (black crosses) are from Gratton et al. (2003), Cayrel et al. (2004), Nissen et al. (2007), and the stellar literature sample. The data was binned prior to fitting and is shown as the solid black circles, where the vertical error bars represent the standard deviation of the bin. The two-component fit (solid green line) is a slightly better fit than the single line (red-dashed line) based the comparison of the total residual.

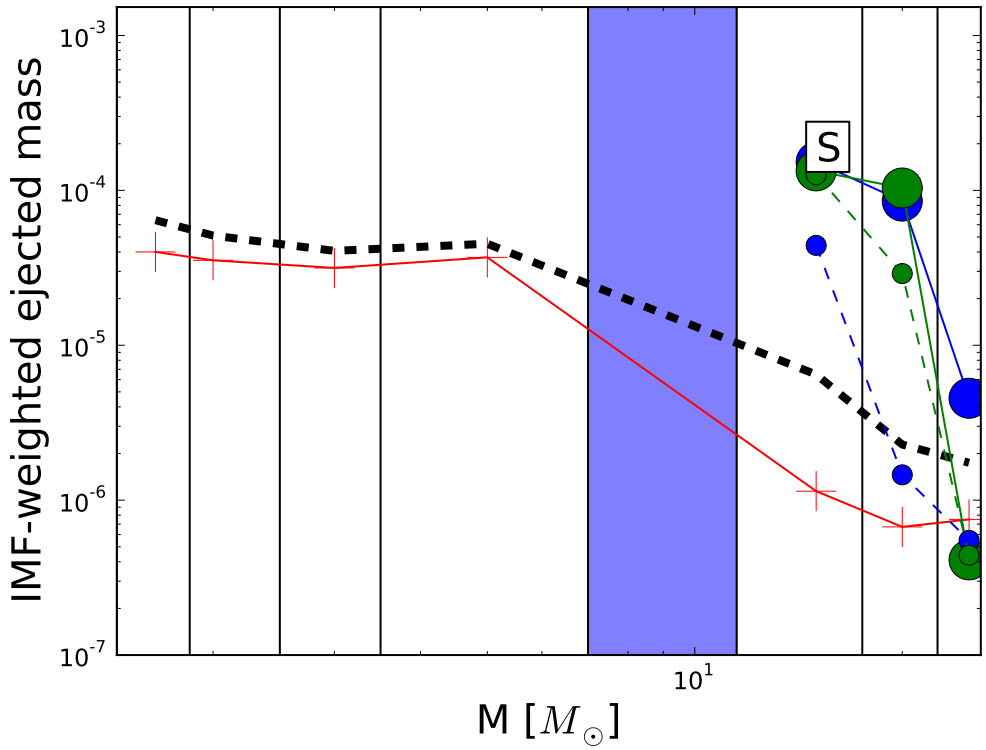

Figure 3.10 Expected S nucleosynthesis from the NuGrid simulations. The symbols are the same as Figure 3.1. S is produced both in stellar and explosive nucleosynthesis of massive stars.

Caffau et al. (2005) discuss that Mult. 1 lines (921.2863 nm, 921.2970 nm, 922.8903 nm, and 923.7538 nm), which are typically strong lines, are often blended or near other features. As the Mult. 1 lines are the strongest lines, they are often used for measuring S in metal-poor stars. Mult. 6 (869.3931 nm and 869.4626 nm) are about 10 times weaker than Mult 1., but are not near any other lines that can potentially blend. However, Caffau et al. (2005) mention that there are large discrepancies in the oscillator strengths adopted between studies for these lines, making comparisons difficult. The most reliable lines seem to be the Mult. 8 lines which are free from blending and have consistently measured oscillator strengths. As the lines originate from the same lower level as Mult. 6. their dependence on the effective temperature and surface gravity of the stars are the same, providing consistent abundances between multiplets. Although both Nissen et al. (2004) and Caffau et al. (2005) claim that non-LTE corrections are small and can be ignored, Takeda et al. (2005) suggests the opposite and that non-LTE should be included for Mult. 1 and 6 lines as abundances can be overestimated by up to 0.3 dex (by not including non-LTE corrections). The combination of selecting certain lines and the inclusion of non-LTE corrections has caused difficulty in comparing results between multiple studies of S in the literature.

With the large variety in determining consistent S abundances, it has made understanding the observed nucleosynthetic trends of S very difficult. The main question has been whether or not S behaves like oxygen (and other α-elements) at low metallicities (i.e. [S/Fe] and [S/Zn] $\sim +0.4$ dex plateau at low metallicities [Fe/H]≤ -1.0 dex.). The first studies completed by Francois (1987, 1988) suggest [S/Fe] in the halo are in agreement with other α-elements such as Mg and O. However, Israelian & Rebolo (2001) claim that no such plateau exists. Using a small sample of stars and a reanalysis of the Francois (1987) data, Israelian & Rebolo (2001) found that [S/Fe] increased with decreasing metallicity to about $\sim +0.7$ dex using the Mult. 6 lines. This decrease was also confirmed by Takada-Hidai et al. (2002) who did a similar analysis with 67 dwarf and giant stars. Subsequent studies (Nissen et al., 2004, 2007; Spite et al., 2011, using combinations of Mult. 1, 3 with non-LTE corrections, 6, and 8) did find the plateau at low metallicities. However, Caffau et al. (2005) showed that the large scatter can confirm both cases. Furthermore, there has been disagreement on the level of the plateau. Spite et al. (2011), Caffau et al. (2005) (for the stars that do plateau), and Nissen et al. (2004) agree that [S/Fe] should be at about +0.35 dex; whereas Israelian & Rebolo (2001) suggests that [S/Fe] continuously goes up to 0.7

Table 3.4 Common S II absorption lines in DLAs

λ (Å)	f
1250.584	5.43×10^{-3}
1253.811	1.09×10^{-2}
1259.519	1.66×10^{-2}

REFERENCE–Morton (2003)

dex.

In DLAs, S is one of the best α-elements to measure. With a low condensation temperature ($T_{\rm cond}$ = 648 K Savage & Sembach, 1996), S is likely not depleted into dust and provides accurate α-element measurements. However, only three lines are available to measure S (see Table 3.4). As the lines are near the Lyα transition, the absorption lines are often found in the Lyα forest, and require large column densities to be detected (see Section 2.1). As a result, there is a tendency for S to only be found in the higher column density DLAs.

Figure 3.11 shows how [S/Zn] ([S/Fe] in stars) varies with [Zn/H] ([Fe/H] in stars) in DLAs and stars. This plot clearly shows the difficulties in comparing S in stars and DLAs as there are relatively few S measurements in the large stellar datasets, especially in the halo, to show the expected [α/Fe] trend. Despite the lack of stellar data, it is apparent that DLAs seem to remain at nearly solar [S/Zn] on average, with a significant scatter ($\pm$0.25 dex) as seen in other studies (Centurión et al., 2000; Prochaska & Wolfe, 2002; Nissen et al., 2004). It is difficult to judge whether the low metallicity DLAs ([Zn/H]~ -1.5) are indeed following the few dSph measurements, or whether it is an effect of scatter. If the two [S/Zn]$\sim$ 0.5 dex DLAs are outliers, there would be no rise (similarly for the dSphs as well). To test whether this is the case, one would need to overcome the difficulty in measuring S in the metal-poor DLAs and check to see if this rise does indeed continue to [S/Zn]$\sim$ 0.5 dex, or use another iron-peak tracer at lower metallicities as Figure 3.9 suggests that [S/Zn] would underestimate [α/Fe] at low metallicities.

The flat evolution of [S/Zn] over the entire metallicity range of the HR literature and Thesis DLA samples suggests that DLAs have faster star formation histories relative to dSphs. However, the lack of sulphur measurements in the samples used at low metallicities ([Zn/H] or [Fe/H]< -1.5) in both stars and DLAs makes the interpretation of Figure 3.11 difficult to confirm whether the star formation history of DLAs and dSphs agree when using S as an α-element tracer. Further studies of S

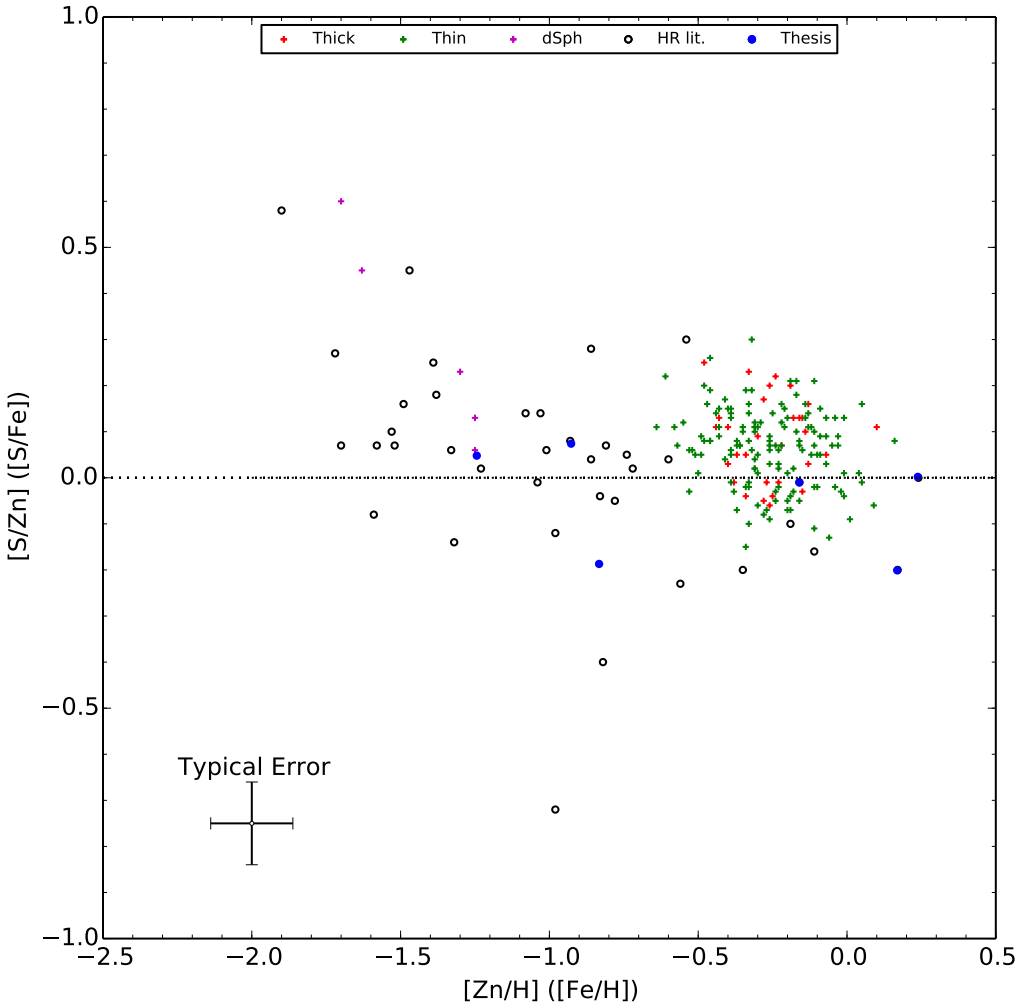

Figure 3.11 [S/Zn] vs. [Zn/H] in the HR literature and thesis DLA samples. [S/Fe] vs. [Fe/H] is shown for stars in order to avoid any dust depletion corrections. The symbols are the same as in Figure 3.8. DLAs seem to follow a near solar trend in [S/Zn] down towards lower metallicities whereas dSphs seem to rise to higher [S/Fe] at metallicities of [Fe/H]~ -1.5. The metallicity of the rise would suggest that DLAs may have even faster star formation histories compared to dSphs.

in low and high metallicities DLAs may provide more information on whether [S/Zn] could be solar for all DLAs.

3.1.4 Silicon

Silicon (Si) is an α-element formed during the oxygen burning phases in stars. It is created either from the combination of two oxygen nuclei, or helium and magnesium (Woosley & Weaver, 1995). Although both Type Ia and Type II SNe produce equal amounts of Si, SNe II are five times more frequent, thus dominating the production of Si (Clayton, 2003). Figure 3.12 summarizes the production of Si in stars in the NuGrid simulations. It is clear that the significant contributors of Si production are both nucleosynthesis in stars (small circles) and explosive nucleosynthesis during SNe II (large circles).

Si is typically measured by two lines in stars; the Si I 3905.5 Å and 4102.9 Å. Recently, Shi et al. (2012) has also used several IR lines to derive Si abundances in nearby stars. The trouble with measuring Si in stars is that neither of the Si I lines give systematically consistent results between studies (see Figure 3.13; Shi et al., 2009). Although the variety in stellar atmosphere codes and adopted parameters play a significant role in these discrepancies between studies (Zhang et al., 2011), part of the problem is potential blending from other features. The 3905 Å line is often severely blended with a CH line, while the 4102 Å line falls within the wings of the Hδ absorption feature (Cayrel et al., 2004). However for metal-poor stars, only the 3905 Å line is available for metallicities below [Fe/H]< -2.5. At these low metallicities, there is an enhancement in the carbon abundance (e.g. Akerman et al., 2004), greatly increasing the contribution of the CH line. In the past, LTE was generally assumed for the 3905 Å line. However, Preston et al. (2006) were the first to notice in their sample of red horizontal branch stars that [Si/Fe] decreased with increasing surface temperature and did not find significant CH blending. The non-LTE models from Shi et al. (2009) demonstrated that the decrease in [Si/Fe] was a result of not including non-LTE corrections in their own non-LTE models. Although non-LTE effects should be included, the work by Shi et al. (2012) demonstrated that the Si I IR lines can be used with LTE assumptions to determine Si abundances. As with other α-elements, Si shows a constant enhancement relative to iron ([Si/Fe]~ 0.4) at low metallicities, with a decrease towards solar values with increasing metallicity starting at [Fe/H]$= -1$ (e.g. García Pérez et al., 2013).

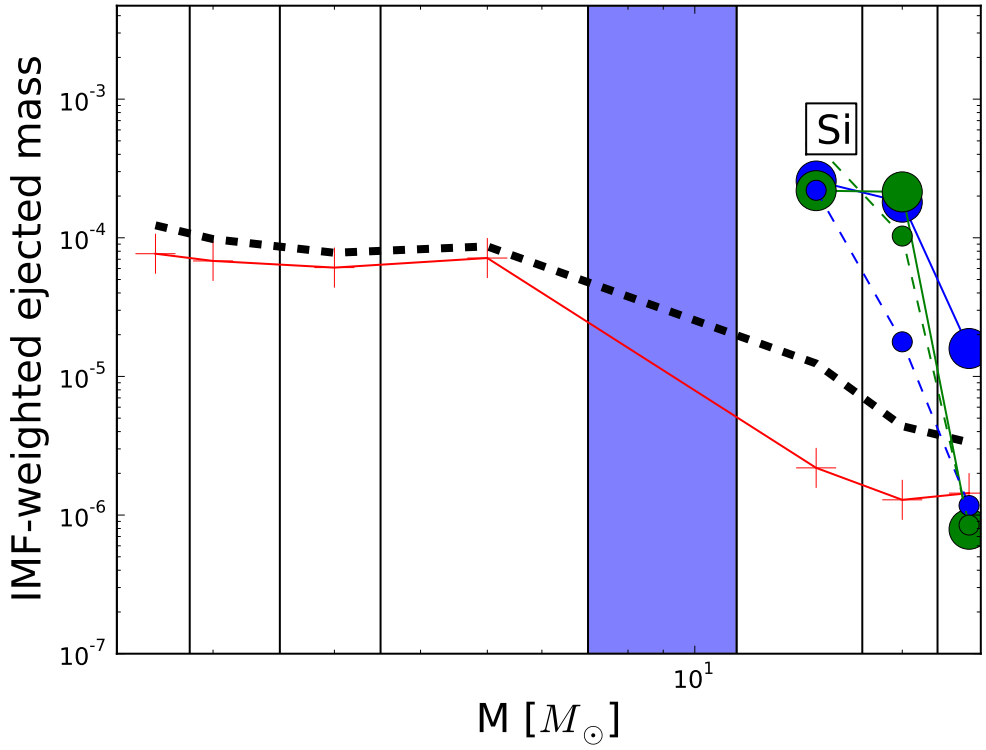

Figure 3.12 Salpeter plot for Si from the NuGrid simulations. The legend is the same as Figure 3.1. With both small and large circles significantly above the black dashed line suggest that massive stars produce Si during their evolution and their resulting supernovae.

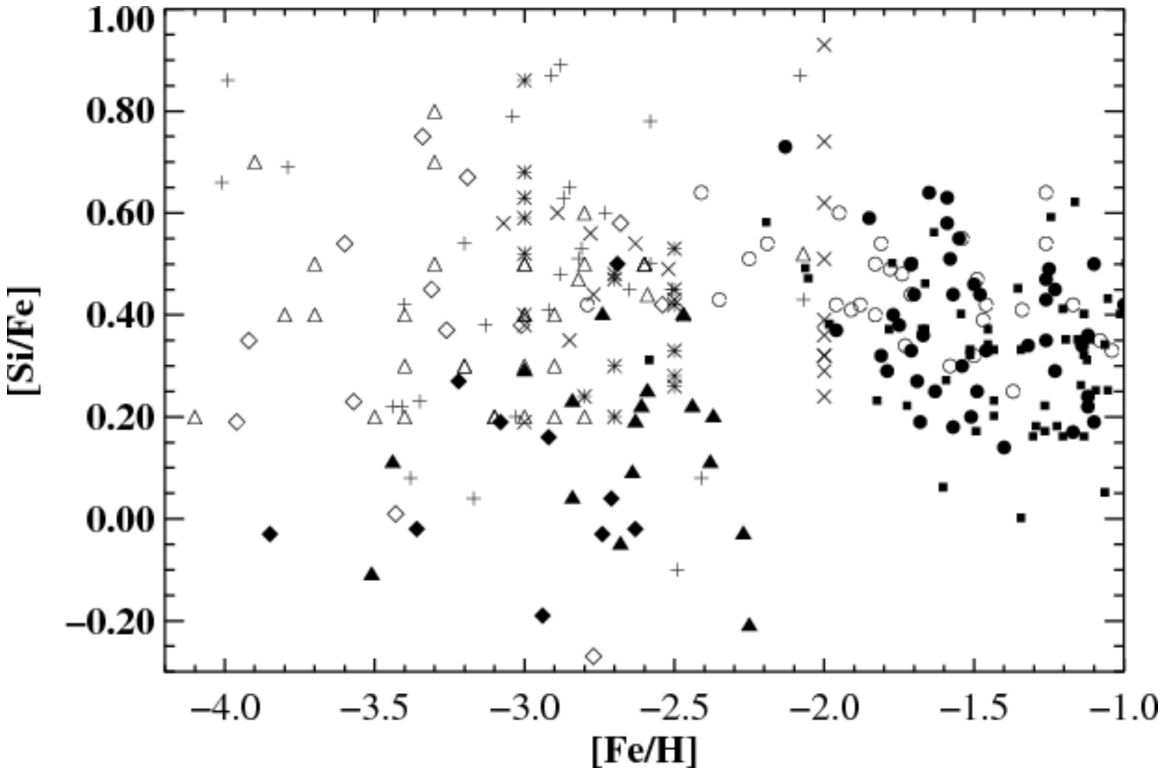

Figure 3.13 Figure 1 from Shi et al. (2009) showing the [Si/Fe] for metal-poor stars from various literature sources (each symbol representing a different study) using different lines and LTE assumptions. The large scatter demonstrates the variance resulting from using the various different models with Si.

Table 3.5 Si II lines observable in DLAs

λ (Å)	f
1260.4221	1.18×10^{0}
1304.3702	8.63×10^{-2}
1526.7066	1.33×10^{-1}
1808.0130	2.08×10^{-3}

REFERENCE–Morton (2003)

Si is generally the only α-element that is always observed in DLAs (Prochaska & Wolfe, 2002). With four absorption lines of varying oscillator strengths (see Table 3.5), there is often at least one line to provide a Si abundance reliably. The difficulty with Si is that it is somewhat depleted into dust ($T_{cond} = 1311$ K; Savage & Sembach, 1996). Comparing to sulphur abundances in DLAs, Vladilo et al. (2011) found an average Si depletion of 0.27 ± 0.16 dex. Despite its affinity to go into dust, Si is still used to study α-elements and understand the star formation history in DLAs (Prochaska & Wolfe, 2002).

To test the nature of Si depletion, Figure 3.14 shows the ratio of [Si/S] as a function of metallicity. Both Si and sulphur are formed during Si burning in stars, and thus [Si/S] should remain solar over all metallicities. In stars, [Si/S] appears to be slightly subsolar at [Si/S]~ -0.05, but is constant over the range of metallicities in the disk ($-0.7 \lesssim$[Fe/H]$\lesssim 0.2$). For DLAs, there is very little difference between sulphur and Si in Figure 3.14, although at low metallicities ([Fe/H]$\lesssim -1.0$) [Si/S] is solar or supersolar, whereas the more metal-rich DLAs show [Si/S]< -0.05 (i.e. less than the stars in the disk). The [Si/S] below the disk stars suggests that dust depletion of Si is important at [Zn/H]> -0.5, but could be interpreted as poor sampling of stars and DLAs at high metallicities with this dataset.

The [Si/Fe] as a function of metallicity has been used to study the contribution of SNe II and SNe Ia in DLAs. Much of the literature (Lu et al., 1996a; Prochaska & Wolfe, 1999; Pettini et al., 2000; Prochaska & Wolfe, 2002) have found enhancements in [Si/Fe] irrespective of the metallicity of the system, although the spread between studies appears large (0.2–0.6 dex). Although this enhancement agrees with what is expected in stars, dust depletion could explain this enhancement as iron has a higher affinity onto dust compared to Si. Therefore the question has been whether [Si/Fe] is actually enhanced in DLAs at low metallicities like stars.

Figure 3.15 shows [Si/Zn] as a function of metallicity in DLAs. For comparison,

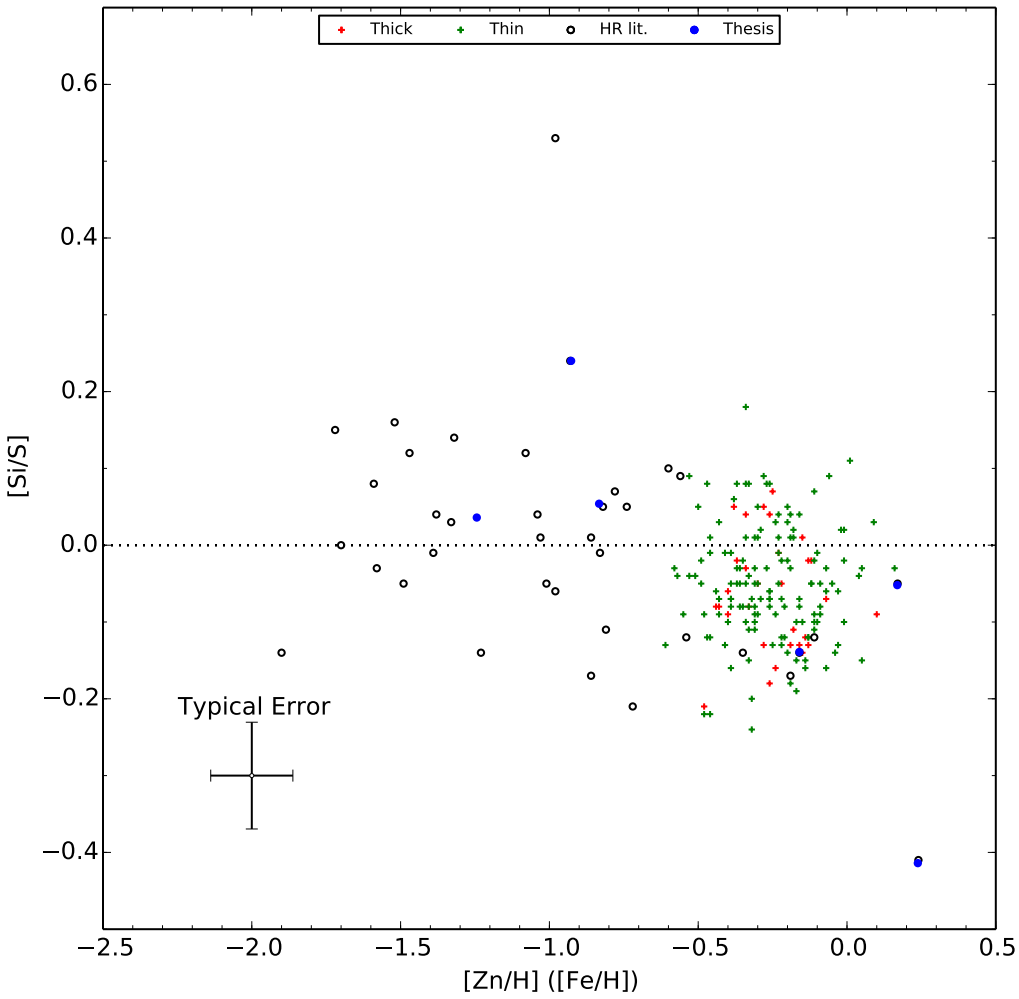

Figure 3.14 [Si/S] as a function of metallicity in DLAs ([Zn/H]) and stars ([Fe/H]). The symbols are the same as in Figure 3.8. [Si/S] in DLAs appears to decrease slightly with increasing metallicity, a likely sign that dust depletion is significant at higher metallicities.

[Si/Fe] is shown instead for stars as [Si/Zn] in DLAs was selected to only avoid the effects of dust depletion from iron. There appears to be a decrease in [Si/Zn] with increasing metallicity in DLAs. As shown in Figure 3.14, there is a slight depletion of Si with increasing metallicity as well; which must be inherent in Figure 3.15. However, the magnitude of dust depletion in Figure 3.14 cannot account for the entire decrease in [Si/Zn], therefore it is likely that part of the decrease in [Si/Zn] with increasing [Zn/H] may be due to the onset of SNe Ia in DLAs.

In summary, Si appears to be mildly depleted into dust as demonstrated by the slight decrease in [Si/S] with increasing metallicity (Figure 3.14). However, the scatter of [Si/S] in DLAs in Figure 3.14 is similar to the scatter in the stellar [Si/S] measurements, making it difficult to conclude the magnitude of the [Si/S] depletion. Combining the trends from Figures 3.14 and 3.15, part of the decrease in [Si/Zn] with increasing metallicity must be nucleosynthetic in origin. If DLAs were corrected to account for the slight enhancement of zinc relative to iron seen in stars (Figure 3.9), [Si/Zn] would further be enhanced in DLAs. Therefore it is likely that Si does show an α-enhancement that is nucleosynthetic in origin, contrary to the solar [S/Zn] values seen in DLAs (Figure 3.11). The discrepancy between in the [α/Fe] trends from Figures 3.11 and 3.15 may be a result of the large scatter in [Si/Zn] combined with the dust depletion of Si, but more measurements of sulphur and zinc in DLAs are needed to shed more light on this discrepancy and test whether there is any [α/Fe] enhancement in DLAs. Taking the [Si/Zn] trend with metallicity to be purely nucleosynthetic, DLAs appear to trace the satellite data suggesting a similar star formation history as the satellite galaxies.

3.1.5 Chromium

Chromium (Cr) is typically labelled as an iron-peak element that is primarily formed as an unstable iron isotope (such as ^{52}Fe) that decays into Cr. Although Cr is mainly produced by SNe Ia (e.g. Travaglio et al., 2004; Seitenzahl et al., 2013), Type II SNe also produce Cr (Pignatari et al., 2013). Figure 3.16 shows the results from the NuGrid simulations. Pignatari et al. (2013) suggest that Cr is only produced in explosive nucleosynthesis in massive stars (large circles). Overall, the total contributions of Cr from both SNe Ia and SNe II are in equal parts, although an individual SNe Ia contribute about five times as much as a single SNe II (Clayton, 2003), therefore SNe Ia dominate the production of Cr (e.g. Bergemann & Cescutti, 2010).

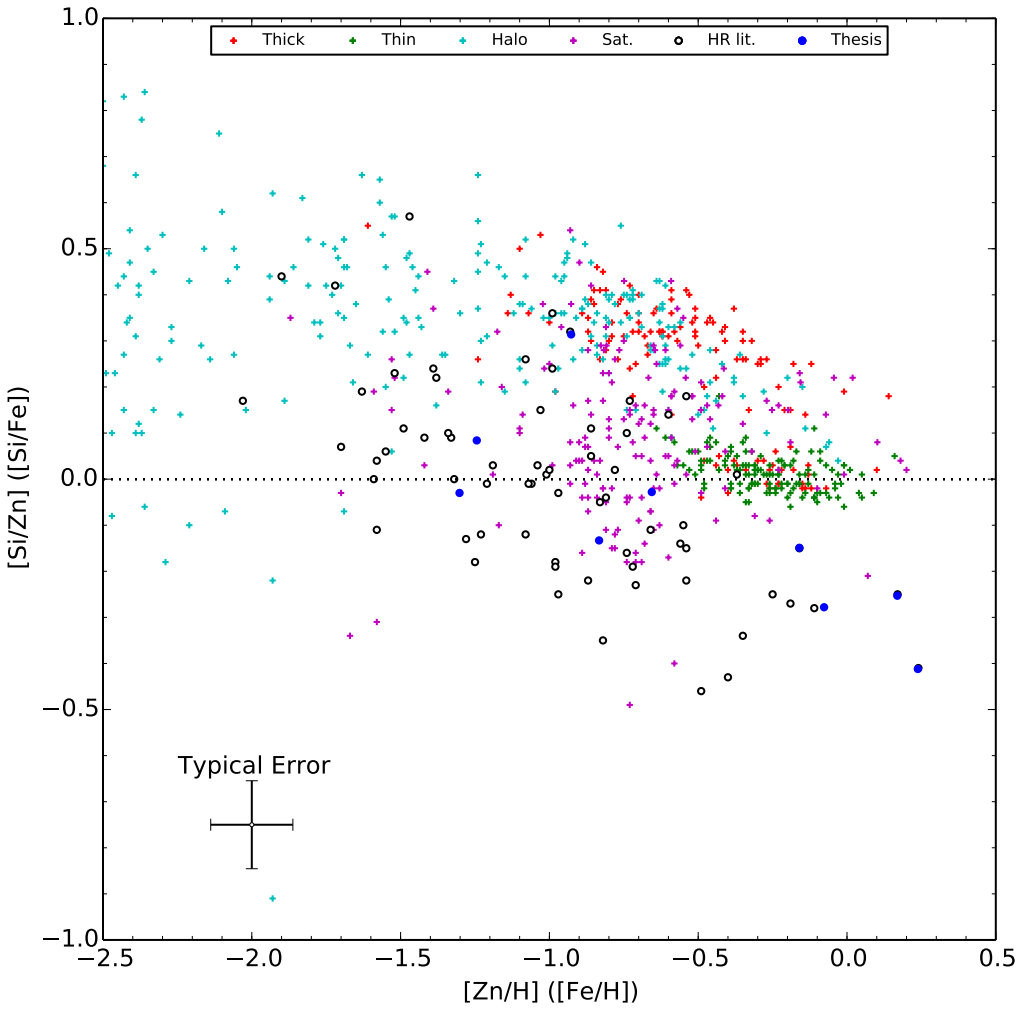

Figure 3.15 [Si/Zn] as a function of [Zn/H] in DLAs. [Si/Fe] vs. [Fe/H] is shown for stars. The symbols are the same as in Figure 3.8, although the magenta crosses include the LMC data and are not exclusive to dSphs. [Si/Zn] decreases with increasing metallicity, which could be a reflection of both dust depletion or the onset of SNe Ia in DLAs.

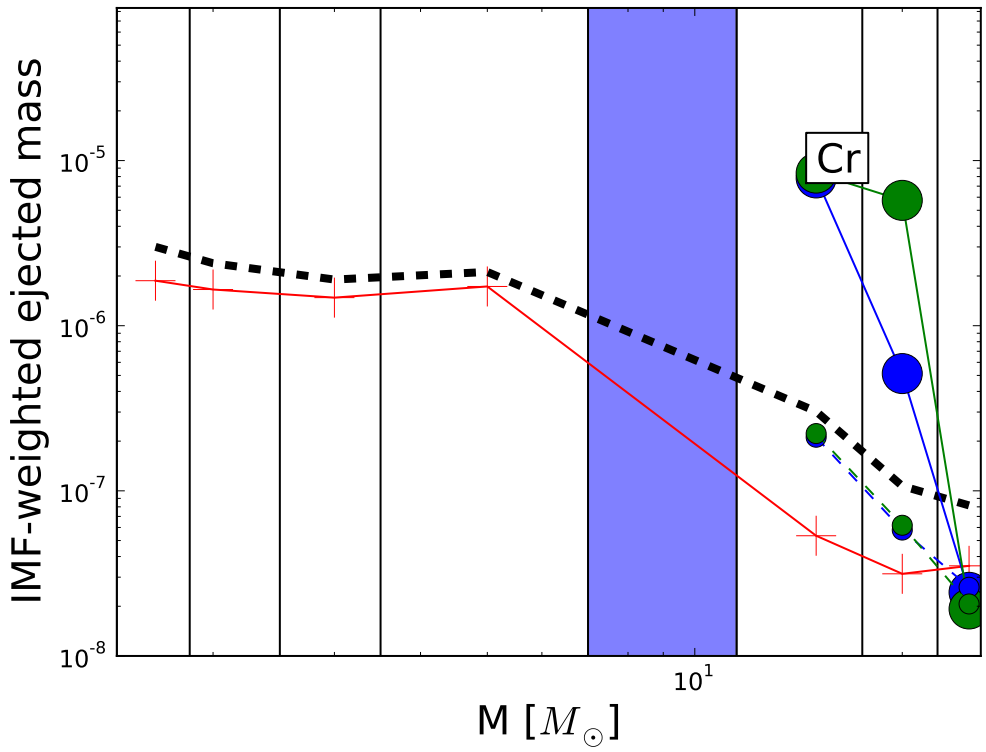

Figure 3.16 The Cr yields from the NuGrid simulations. The symbols are identical as in Figure 3.1. With the larger circles being the only points above the dashed line, it is clear that Cr is only produced in explosive nucleosynthesis.

Table 3.6 Cr II absorption lines commonly observed in DLAs

λ (Å)	f
2056.2539	1.03×10^{-1}
2062.234	7.59×10^{-2}
2066.161	5.12×10^{-2}

REFERENCE–Morton (2003)

For the most part, Cr is seen to trace iron in Galactic stars ([Cr/Fe]$\sim$ 0), with a very tight scatter over all metallicities ($-1.6 \lesssim$[Fe/H]$\lesssim 0.5$; e.g. Bensby et al., 2005; Nissen & Schuster, 2010). However, at low metallicities there appears to be a decrease in [Cr/Fe] with decreasing metallicity starting at [Fe/H]~ -2 (Cayrel et al., 2004; Lai et al., 2008; Bonifacio et al., 2009). Although this difference was thought to be nucleosynthetic in origin (Cayrel et al., 2004), both Preston et al. (2006) and Lai et al. (2008) found a trend in [Cr/Fe] with surface temperature, suggesting that non-LTE effects may be contributing to the low [Cr/Fe] abundances. The first (and only) non-LTE model for Cr comes from Bergemann & Cescutti (2010), where they found that the non-LTE effects from their model did account for the $\sim$ 0.35 dex discrepancy in [Cr/Fe] from solar value. Even at solar metallicities, a small ($\sim$ 0.1 dex) correction is often still required on Cr abundances.

Measuring Cr in DLAs relies on three lines (Table 3.6), although the CrII 2062 line is usually blended with ZnII 2062 and is not as reliable as the other lines (although the CrII 2062 and ZnII 2062 lines can typically be resolved using R$>$ 5000 observations). The difficulty with measuring Cr in DLAs, however, results from dust depletion. With its high condensation temperature of $T_{\rm cond} = 1277$ K (Savage & Sembach, 1996), Cr is heavily depleted onto dust. As a result, studies of Cr in DLAs have focussed on using Cr as an indicator of dust depletion.

The early work by Meyer & Roth (1990); Meyer & York (1992) and Pettini et al. (1990, 1994) used [Cr/Zn] to determine the amount of dust depletion in DLAs. Under the assumptions that (*i*) zinc is a non-refractory element, (*ii*) Cr and zinc have the same nucleosynthetic origin, and (*iii*) the solar (Cr/Zn) ratio is identical to (Cr/Zn) in all ISM gas clouds; an underabundance of the [Cr/Zn] ratio along a DLA sightline would be indicative of dust depletion of Cr. All the literature on the [Cr/Zn] ratio in DLAs (Meyer & Roth, 1990; Pettini et al., 1994; Kulkarni et al., 2005; Akerman et al., 2005) shows this [Cr/Zn] underabundance with DLAs, and an evolution of the underabundance with metallicity (i.e. [Zn/H]). Pettini et al. (1994) and Akerman

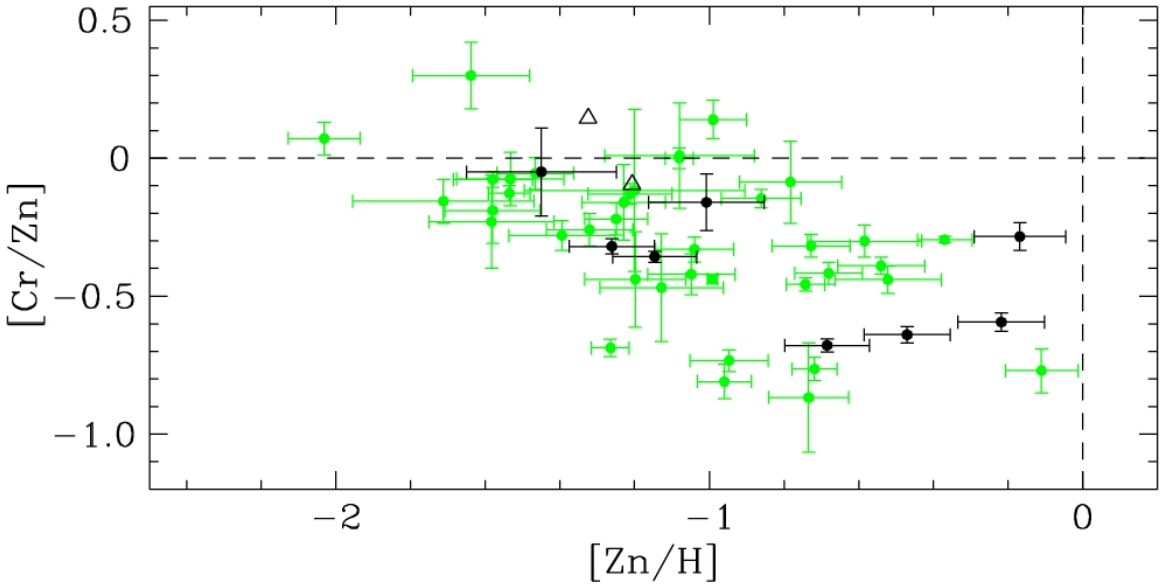

Figure 3.17 Figure 5 from Akerman et al. (2005). Using a combination of their DLA sample (black points) with a literature compilation (green points) from Kulkarni et al. (2005), they find a decrease in [Cr/Zn] as a function of metallicity. This has been suggested by many to be from the metallicity dependence of dust depletion; where higher metallicity systems have higher dust contents.

et al. (2005) have suggested that the metallicity dependence of the underabundance of [Cr/Zn] results from the variation in the amount of dust depletion with metallicity; where the depletion effect is strong at higher metallicities (see Figure 3.17).

Figure 3.18 shows [Cr/Zn] as a function of metallicity in DLAs (both the Thesis and the HR literature samples) and stars (stellar literature sample). The deviation from solar [Cr/Zn] at low metallicities in halo stars results from assuming LTE, and is not nucleosynthetic in origin. However, the origin of subsolar [Cr/Fe] stars in the Fornax dSph (at [Cr/Fe]~ -0.3 at [Fe/H]~ -0.7) is uncertain. Letarte et al. (2010) suggested that this disagreement is nucleosynthetic in origin resulting from metallicity dependent SNe Ia yields. If the yields were metallicity dependent, the observed [Cr/Fe] in Fornax is not consistent with all the other satellite galaxy stars that follow the Galactic trend. The discrepancy between Fornax and other dSphs suggests that a combination of different CrI lines and the use of oscillator strengths tweaked by Letarte et al. (2010) may account for this discrepancy. Therefore it is not clear whether the subsolar [Cr/Fe] in Fornax is indeed nucleosynthetic or not. As in Figure 3.17, the DLAs in Figure 3.18 show a metallicity dependent [Cr/Zn], which

could be either a signal of dust depletion dominating the higher metallicity systems or that the change in [Cr/Zn] is nucleosynthetic in origin.

With respect to iron, Lu et al. (1996a); Prochaska & Wolfe (1999, 2002) consistently found a slightly super-solar value of [Cr/Fe] in all DLAs. Prochaska & Wolfe (2002) suggest that this slight enhancement results from dust depletion as [Cr/Fe] is also slightly enhanced in the local ISM and no enhancement is seen in stars. Both Prochaska & Wolfe (1999, 2002) also suggest a slight metallicity dependence in [Cr/Fe], where at low metallicities, [Cr/Fe] is even more enhanced. This is contrary to Dessauges-Zavadsky et al. (2006), who suggested that all DLAs exhibit little scatter in [Cr/Fe] and [Si/S] with metallicity, therefore the dust content of DLAs is very uniform. Indeed, both [Cr/Fe] and [Si/S] are both nearly solar in all DLAs with little scatter (Figures 3.19 and 3.14; respectively), but do deviate slightly with increasing metallicities in the directions of dust depletion (i.e. [Cr/Fe] increases and [Si/S] decreases) suggesting that there is a metallicity dependence of dust depletion.

Prochaska & Wolfe (2002) tested whether the observed [Cr/Fe] enhancement could be nucleosynthetic by plotting [Cr/Fe] vs. [Zn/Cr]; expecting a positive correlation if dust depletion was the dominant factor and [Cr/Fe]= 0 in all systems. As shown in Figure 3.20, the results suggested that the observed decrease in [Cr/Fe] with increasing [Zn/Cr] must be nucleosynthetic in nature, and is most likely related to independent production of Cr relative to iron and zinc.

To investigate whether Cr, zinc, and iron have different nucleosynthetic origins, Figure 3.21 shows the [Cr/Fe] vs. [Zn/Cr] relation for the Thesis DLA, HR literature DLA, and stellar literature samples. The stellar data from the disk stars show a clear anti-correlation (Pearson r-coefficient of $r = -0.57$; i.e. quite significant). However, the halo stars that continue the anti-correlation (from the disk stars) to higher [Zn/Cr] are those that are affected by non-LTE effects (see Figure 3.18). In addition to the fact that zinc and iron trace each other at solar values in the disk stars (Figure 3.8), Figure 3.21 suggests that Cr in the disk stars are affected by non-LTE corrections. If one were to include the non-LTE corrections for the metal-poor halo star (+0.35 dex) and the solar metallicity disk stars (+0.1 dex) from Bergemann & Cescutti (2010), all the stellar data would shift to the upper left, forming a large scatter of points about the solar value. This clearly indicates that there is no apparent nucleosynthetic difference in Cr, zinc, and iron in stars.

What is interesting in Figure 3.21 is how similar the DLAs appear to follow the expected scatter of stars (when non-LTE corrections are included) around solar metal-

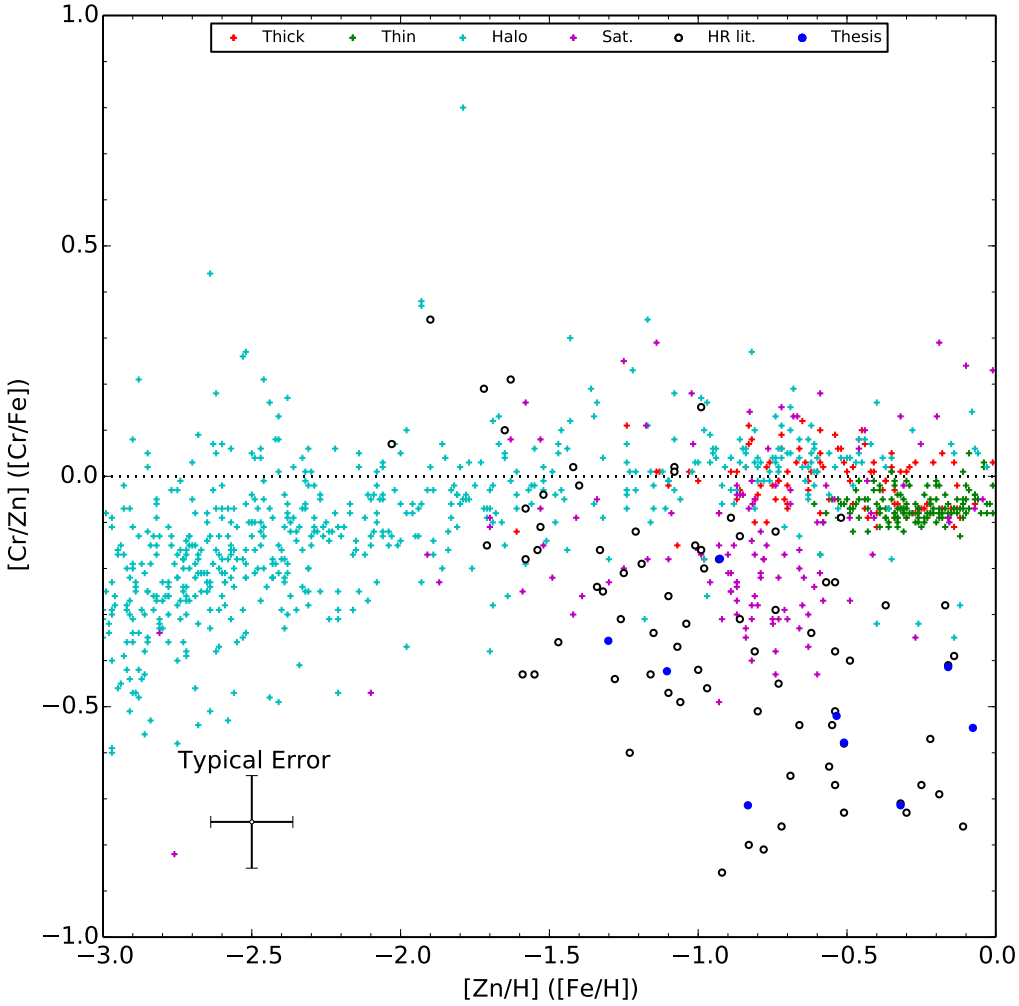

Figure 3.18 [Cr/Zn] as a function of metallicity ([Zn/H] in DLAs; [Fe/H] in stars). The symbols are the same as Figure 3.15. Similar to Figure 3.17, there is a decrease in [Cr/Zn] with metallicity in DLAs suggesting that dust depletion is metallicity dependent.

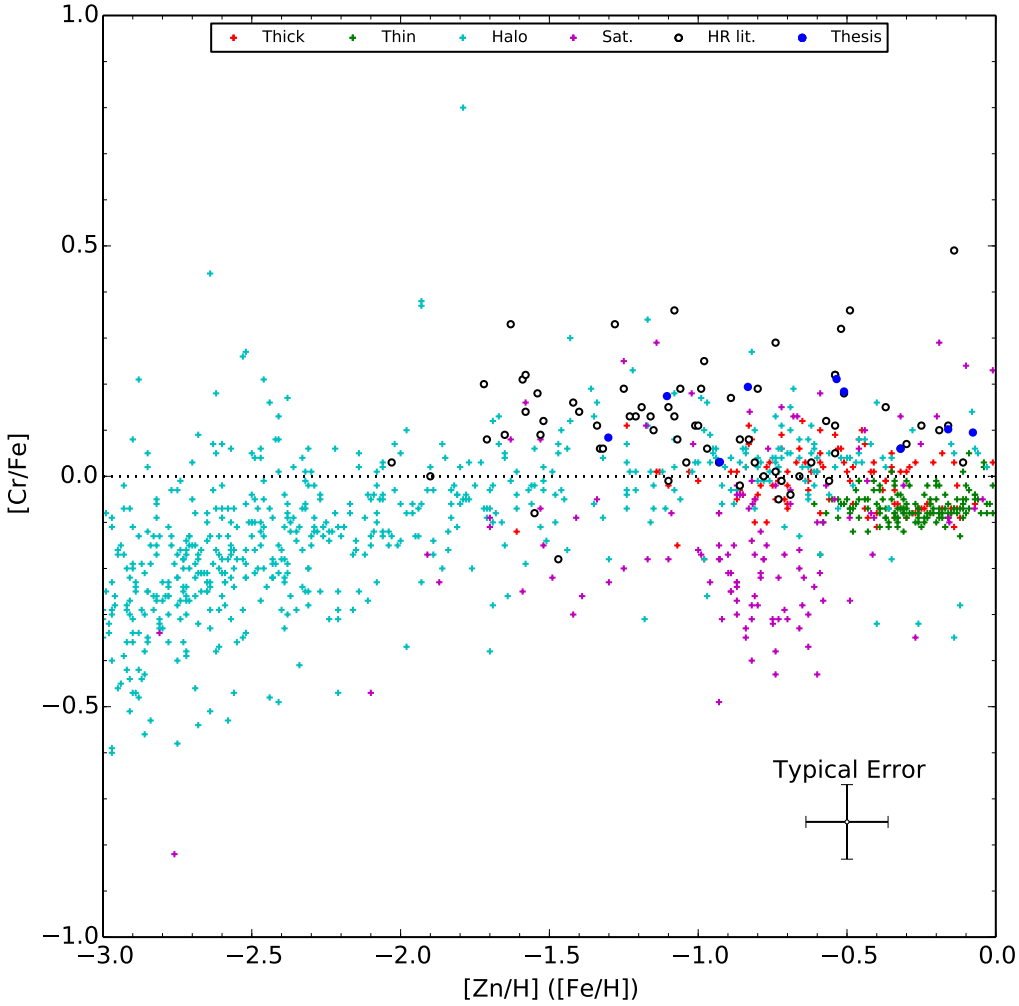

Figure 3.19 [Cr/Fe] as a function of metallicity ([Zn/H] in DLAs; [Fe/H] in stars). The symbols are the same as Figure 3.15. Although the scatter is very tight and [Cr/Fe]$\sim$ 0, there is a slight increase in [Cr/Fe] with increasing metallicity; a trend expected if dust depletion is metallicity dependent.

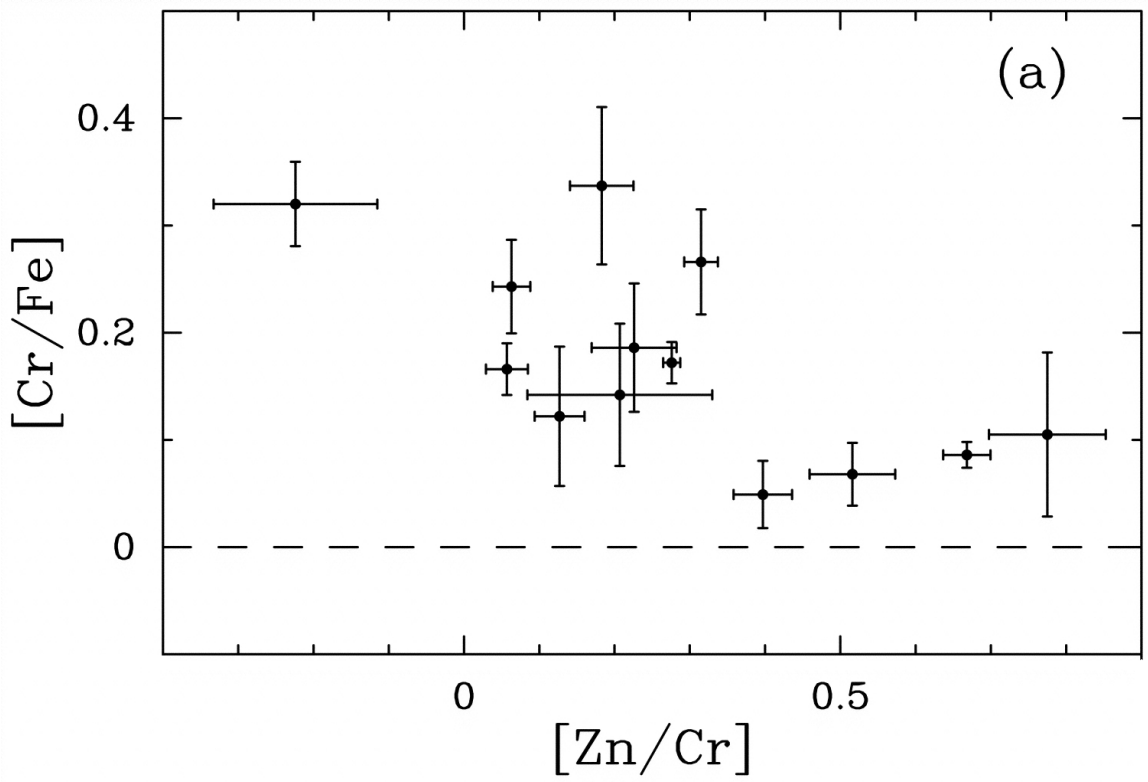

Figure 3.20 Figure 15 from Prochaska & Wolfe (2002) showing the relation between [Cr/Fe] and [Zn/Cr]. If zinc, Cr, and iron all have a similar nucleosynthetic origin, one would expect the trend to be correlated as both [Cr/Fe] and [Zn/Cr] should become more enhanced as dust depletion increases. Prochaska & Wolfe (2002) argue based on the anti-correlation that there must be some differences in the nucleosynthetic origins of the three elements.

licities, just slightly offset to the right. This offset to the right is likely due to dust depletion. However, the Pearson r-coefficient ($r = -0.29$) suggests that any anti-correlation is moderately weak. If an anti-correlation was present, it would be likely that [Cr/Fe] would drop below -0.1 dex at high [Zn/Cr] in DLAs. With the large scatter of data added to Figure 3.20, it is impossible to determine whether the plot of [Cr/Fe]-[Zn/Cr] can provide any information about the nucleosynthesis of zinc, Cr, and iron as claimed by Prochaska & Wolfe (2002), but it is likely that no nucleosynthetic trends are present.

In summary, measuring Cr in DLAs is a good indicator of dust depletion. Other than non-LTE effects dominating at [Fe/H]$\lesssim -1.5$ in halo stars (and potentially even the disk stars), Cr appears to trace iron in stars. Therefore, the deviations from solar

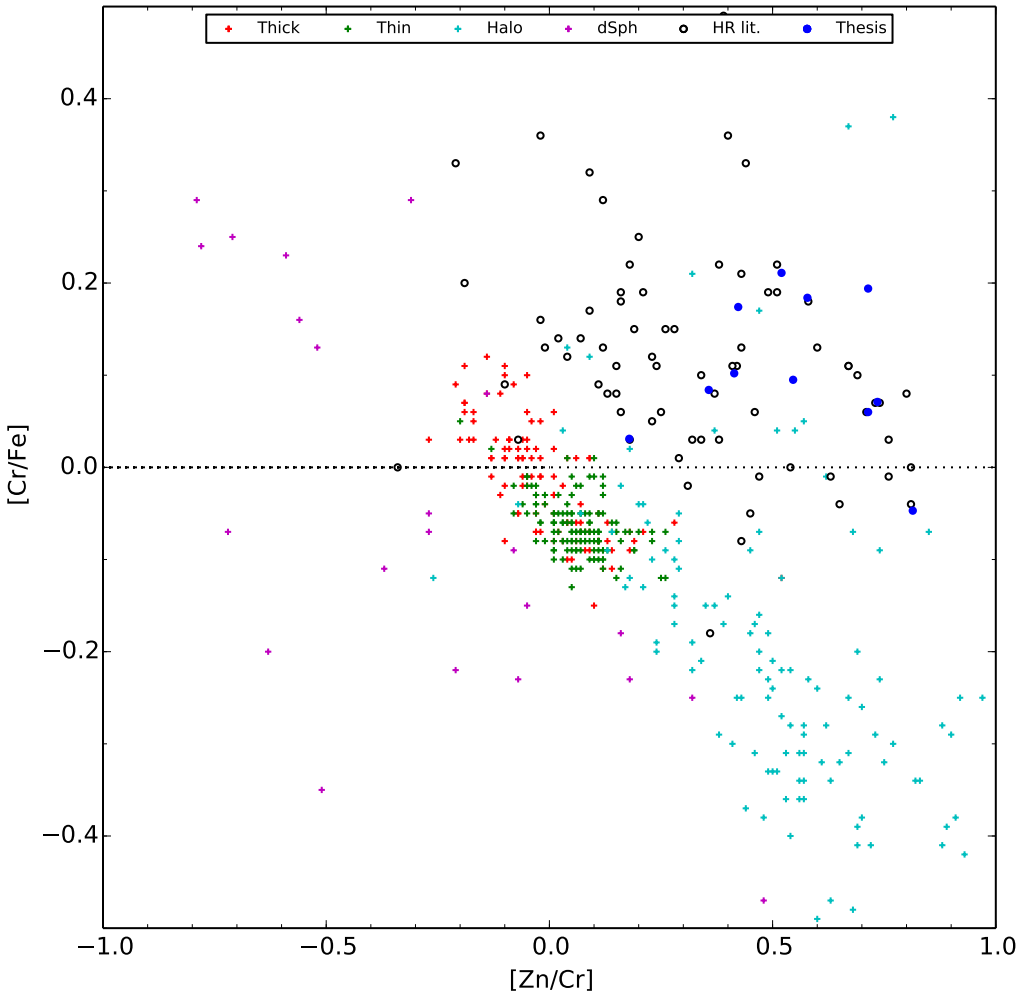

Figure 3.21 [Cr/Fe] as a function of [Zn/Cr] for the Thesis, HR literature, and stellar samples. As in Figure 3.20, an observed anti-correlation is believed to suggest that zinc, Cr, and iron do not have a similar nucleosynthetic origin. If non-LTE corrections (from Bergemann & Cescutti, 2010) are included for Cr abundances in the halo and disk stars, all the data would scatter about the solar values, suggesting no anti-correlation. This is the same pattern seen in the DLAs, however, the DLAs are naturally shifted to the right as [Zn/Cr] is overestimated due to dust depletion. Therefore no anti-correlation is seen in the either the DLAs nor stars.

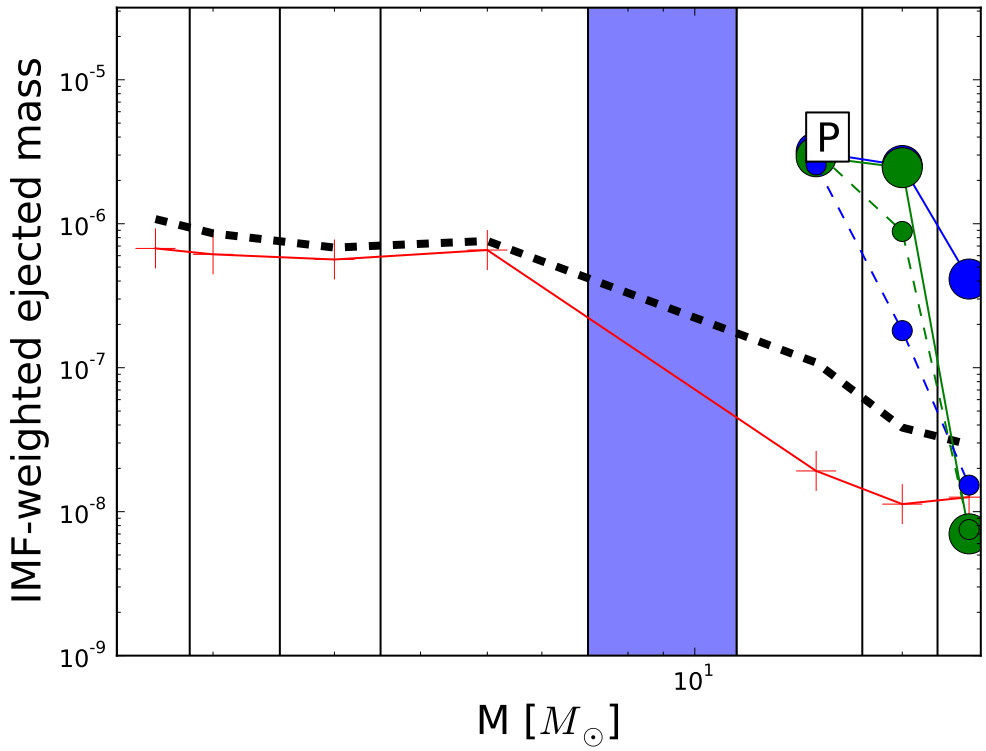

Figure 3.22 Salpeter diagram of P. It appears that only massive stars contribute to the production of P, being both expelled and slightly produced during the explosion.

[Cr/Fe] and [Cr/Zn] seen in DLAs is likely a result of dust depletion. Even with the addition of data to Figure 3.20 , Figure 3.21 indicates that dust depletion is the main reason the DLA points are offset from the stellar data, and there is likely no major nucleosynthetic reason for this pattern.

3.1.6 Phosphorus

Phosphorous (P) is an odd-Z light element that is primarily believed to be formed by neutron capture on silicon in the carbon-neon burning shell of massive stars (Woosley & Weaver, 1995). It is estimated that 95% of P is believed to come from SNe II (Clayton, 2003). Figure 3.22 shows the production of P from NuGrid simulations. The major production of P in massive stars appears to be both in nuclear burning and explosive nucleosynthesis.

Although P is one of the most abundant light elements in the sun, it is one of the least studied elements in stars. This is primarily due to cool stars (F,G,K) only having a single PI line accessible in the infrared. With the recent development of new IR spectrographs such as CRIRES on the VLT, obtaining high resolution spectra for detailed chemical abundances is only a new thing. The first (and so far only) comprehensive study of P in cool stars to date is by Caffau et al. (2011), who determined P abundances in the same sample of stars from Caffau et al. (2005, for which they derived sulphur abundances) using LTE ATLAS12 models. Since P has not been extensively studied, it is unknown whether P suffers from any non-LTE effects during abundance determinations in stars. Table 3.7 contains the abundances used in Caffau et al. (2011). In summary, Caffau et al. (2011) found that both [P/Fe] and [P/S] are effectively constant over the metallicity range of their sample ($-3 \leq$ [Fe/H] ≤ -1). Since metallicity traces the neutron excess (as the available nuclei can provide the neutron excess increases) a flat [P/Fe] with increasing metallicity would imply that P is independent of the excess neutron density. The flat [P/S] ratio implies that S and P are produced in the same amounts at all metallicities. This study was followed up by a comparison to various chemical evolution models to attempt to constrain the P yields. Cescutti et al. (2012) used various models under the constraints of the data from Caffau et al. (2011) and found that to reproduce the [P/Fe] ratios observed, they required metallicity dependent yields of P (a factor of 3 larger than Woosley & Weaver, 1995) and the inclusion of hypernovae yields.

In DLAs, there are four observable lines of P II (963, 1152, 1301, and 1532 Å; see Table 3.8). Although they have the largest oscillator strengths, the PII 963 and PII 1152 lines typically lie in the Lyα forest, making them difficult to observe, whereas the two redder lines are the weakest of the P lines. No in-depth studies have been done on P in DLAs, although it has been detected previously in 13 DLAs (Outram et al., 1999; Molaro et al., 2001; Prochaska et al., 2001a; Dessauges-Zavadsky et al., 2004, 2006; Battisti et al., 2012; Kulkarni et al., 2012). The extent of the discussion has been about the depletion of P, where both Molaro et al. (2001) and Kulkarni et al. (2012) claim that P is mildly depleted due to the low density, neutral clouds in DLAs. As P has a similar condensation temperature to silicon ($T_{cond} = 1151$ K), the depletion corrections should be relatively small (e.g. Figure 3.14). However, Prochaska & Wolfe (2002) note that P, along with manganese, could be used to constrain Population III yields as an observed underabundance of odd-Z element (relative to their even-Z counterparts; e.g. [P/Si] or [P/S]) would suggest a lack of free neutrons (which scales

Table 3.7 Stellar P abundances

Star	[P/H]	[S/H]	[Fe/H]
HD1461	0.14 ± 0.01	-0.05	0.19
HD13555	-0.28 ± 0.03	-0.25	-0.27
HD25704	-0.55 ± 0.05	-0.71	-0.91
HD33256	-0.20 ± 0.04	-0.30	-0.37
HD69897	-0.17 ± 0.06	-0.34	-0.50
HD74156	0.05 ± 0.04	-0.13	0.16
HD75289	0.16 ± 0.01	-0.03	0.28
HD84117	0.09 ± 0.07	-0.10	-0.03
HD91324	-0.30 ± 0.02	-0.49	-0.60
HD94388	0.03 ± 0.07	0.12	0.07
HD120136	0.26 ± 0.08	0.05	0.23
HD139211	0.03 ± 0.05	-0.16	-0.26
HD207129	-0.09 ± 0.02	-0.05	0.00
HD207978	-0.47 ± 0.05	-0.53	-0.63
HD209458	0.00 ± 0.03	-0.20	0.02
HD213240	0.15 ± 0.01	-0.10	0.17
HD215648	-0.19 ± 0.02	-0.19	-0.24
HD216385	-0.18 ± 0.02	-0.18	-0.27
HD216435	0.26 ± 0.02	0.10	0.24
HD222368	-0.03 ± 0.02	-0.07	-0.13

Reference–Caffau et al. (2011)

Table 3.8 PII absorption line wavelengths and oscillator strengths observed in DLAs

λ (Å)	f
963.801	1.46
1152.818	0.245
1301.874	1.27×10^{-2}
1532.533	3.03×10^{-3}

REFERENCE–Morton (2003)

with metallicity).

As well as the 13 detections (and 7 limits) of phosphorus in DLAs in the literature, an additional 7 detections have been added from the Thesis sample. Figure 3.23 shows the absorption profiles of P in the Thesis DLAs. 8 upper limits are also derived for those with clean spectra at the locations of the lines. Table 3.9 summarizes the column densities derived for the Thesis DLAs, and the previous observations in the literature DLAs. The sulphur and zinc columns are included for reference, despite being already presented in Table 2.5.

Figure 3.24 shows how [P/Zn] (left panels) and [P/S] (right panels) vary as a function of [Zn/H] and [S/H] in DLAs (respectively). The top panels of Figure 3.24 only include detections whereas the bottom panels include the limits in addition to the detections. Note that zinc is used in DLAs to avoid the dust depletion problems of iron; however iron is used for the stellar points. Starting with the [P/Zn] (left) panels, the stellar points seem indicate a flat or potentially downward evolution of [P/Fe] as a function of metallicity as identified by Caffau et al. (2011). Caffau et al. (2011) interpret the flat ratio to imply that P nucleosynthesis is independent of the excess neutron density. With the addition of DLAs, there still seems to be a lack of evolution with metallicity. The literature DLAs appear to have slightly lower [P/Zn], which may indicate a metallicity dependence but is likely due to zinc no longer tracing iron at [Zn/H]~ -2 (Figure 3.9), which can maintain a constant value of [P/Zn].

The right panels of Figure 3.24 describe the relative ratio of P to silicon over varying amounts of sulphur. Silicon is used instead of sulphur (i.e. [P/Si] rather than [P/S]) in DLAs in attempt to account for dust depletion, as both silicon and P have similar condensation temperatures and [S/Si]~ 0 in DLAs (Figure 3.14). The stellar data clearly indicates that [P/S] is flat, implying P and sulphur form in equal amounts at metallicities ($-1 \lesssim$[Fe/H]$\lesssim 0$). However, understanding the trend in the DLAs is trickier. Solely looking at the detections-only panel (top right), it would appear that

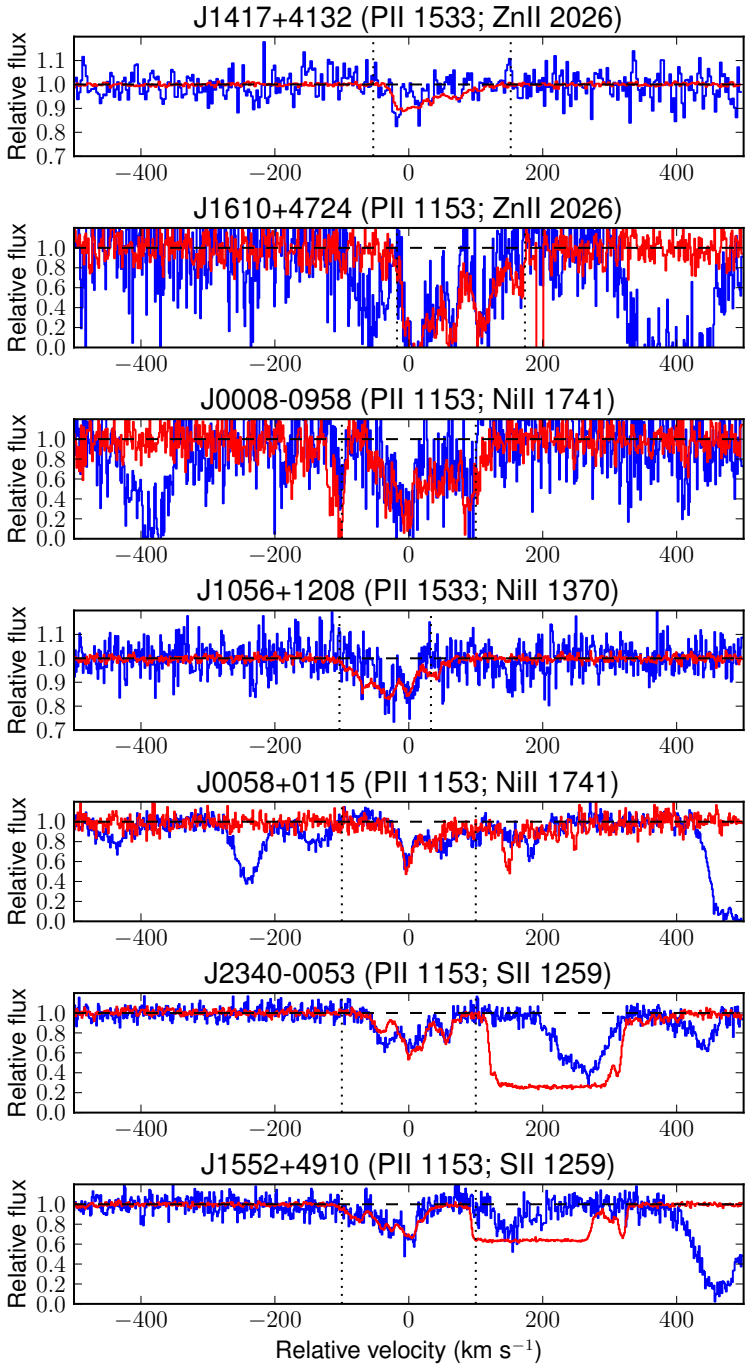

Figure 3.23 The absorption profiles of P (blue) in the DLAs which have detections. The red lines show a scaled-down version of another unblended, prominent absorption line in the DLA to demonstrate the expected shape of the P detection. The P and scaled down lines used in each panel are shown beside the DLA sightline.

Table 3.9 P abundances

QSO	logN(HI)	logN(PII)	logN(SII)	logN(SiII)	logN(ZnII)
Thesis Sample					
J0008-0958	20.85 ± 0.15	14.22 ± 0.06	15.83 ± 0.02	16.05 ± 0.01	13.32 ± 0.01
J0058+0115	21.10 ± 0.15	13.79 ± 0.01	15.41 ± 0.01	< 15.54	. . .
Q0201+36	21.00 ± 0.15	. . .	. . .	15.54 ± 0.01	. . .
Q0458-02	21.65 ± 0.09	. . .	. . .	> 15.89	13.18 ± 0.02
FJ0812+3208	21.35 ± 0.15	. . .	15.48 ± 0.02	15.89 ± 0.01	13.15 ± 0.02
J0927+1543	21.45 ± 0.15	. . .	< 15.86	15.98 ± 0.01	13.72 ± 0.03
J0927+5823	21.05 ± 0.15	. . .	15.79 ± 0.14	15.74 ± 0.01	13.27 ± 0.01
J1010+0003	. . .	< 15.00	. . .	15.87 ± 0.08	13.02 ± 0.02
J1013+5615	21.45 ± 0.15	. . .	. . .	16.14 ± 0.01	. . .
J1049-0110	20.35 ± 0.15	< 14.56	15.47 ± 0.01	15.78 ± 0.01	13.15 ± 0.02
J1056+1208	21.45 ± 0.15	14.93 ± 0.03	> 15.66	> 16.34	13.76 ± 0.01
J1155+0530	20.85 ± 0.15	. . .	15.35 ± 0.00	15.95 ± 0.02	. . .
J1159+0112	21.80 ± 0.10	< 14.46	> 15.16	15.98 ± 0.01	13.13 ± 0.01
J1200+4015	21.45 ± 0.25	. . .	15.37 ± 0.01	. . .	. . .
J1249-0233	21.45 ± 0.25	. . .	15.50 ± 0.02	. . .	< 13.11
J1310+5424	21.45 ± 0.15	< 14.83	> 15.97	> 16.22	13.57 ± 0.01
J1313+1441	. . .	< 14.55	15.71 ± 0.01	. . .	13.22 ± 0.01
J1417+4132	21.45 ± 0.25	14.73 ± 0.05	. . .	> 16.28	13.54 ± 0.01
J1524+1030	. . .	< 14.46	> 15.53	> 16.00	> 13.32
J1552+4910	. . .	13.63 ± 0.02	15.34 ± 0.00	15.98 ± 0.01	12.96 ± 0.02
J1555+4800	21.10 ± 0.10	. . .	> 15.88	> 16.52	< 13.93
J1604+3951	21.05 ± 0.15	. . .	15.70 ± 0.04	16.10 ± 0.01	13.14 ± 0.02
J1610+4724	21.00 ± 0.15	14.22 ± 0.15	> 16.01	16.16 ± 0.01	13.55 ± 0.01
Q1755+578	21.40 ± 0.15	< 14.55	> 15.97	> 16.42	< 13.82
J2100-0641	21.05 ± 0.15	< 14.15	15.64 ± 0.00	15.89 ± 0.00	< 13.20
J2222-0945	21.45 ± 0.15	. . .	15.33 ± 0.02	15.56 ± 0.12	. . .
Q2230+02	21.45 ± 0.15	. . .	. . .	15.68 ± 0.01	12.82 ± 0.03
J2241+1225	21.80 ± 0.10	. . .	14.94 ± 0.04	. . .	. . .
J2340-0053	20.35 ± 0.15	13.65 ± 0.01	14.95 ± 0.00	15.23 ± 0.01	. . .
Q2342+34	21.10 ± 0.10	. . .	15.16 ± 0.01	15.62 ± 0.02	. . .
DLA Literature					
Q0000−2620[a]	21.41 ± 0.08	12.63 ± 0.09	14.7 ± 0.09	15.06 ± 0.02	12.01 ± 0.09
J1009+0713[b]	20.68 ± 0.1	< 13.80	15.25 ± 0.12	> 15.00	. . .
Q1135−0010[c]	22.05 ± 0.1	14.58 ± 0.21	-99 ± -99	16.49 ± 0.003	13.62 ± 0.03
J1616+4154[b]	20.60 ± 0.2	13.46 ± 0.1	15.37 ± 0.11	> 15.08	. . .
J1619+3342[b]	20.55 ± 0.1	13.16 ± 0.19	15.08 ± 0.09	> 13.93	. . .
GB1759+7539[d]	20.76 ± 0.01	13.18 ± 0.07	15.21 ± 0.01	$15.52 \pm 0.02^{\star}$	$> 11.65^{\star}$
Q0100+13[e]	21.37 ± 0.08	13.05 ± 0.08	15.09 ± 0.06	12.47 ± 0.01	> 14.72
Q1331+17[e]	21.14 ± 0.08	13.25 ± 0.10	15.08 ± 0.11	12.54 ± 0.02	15.30 ± 0.01
Q2231−00[e]	20.53 ± 0.08	< 13.51	15.10 ± 0.15	12.30 ± 0.05	15.29 ± 0.04
Q0450−13[f]	20.53 ± 0.08	12.76 ± 0.06	14.18 ± 0.02	< 11.60	$14.68 \pm 0.02^{\star}$
Q0841+129[f]	20.99 ± 0.08	12.82 ± 0.06	14.69 ± 0.04	12.10 ± 0.02	15.21 ± 0.03
Q0841+129[f]	20.78 ± 0.08	12.56 ± 0.07	14.48 ± 0.09	11.69 ± 0.10	14.99 ± 0.02
Q1157+014[f]	21.60 ± 0.10	13.86 ± 0.05	$> 15.16^{\star}$	12.99 ± 0.03	15.97 ± 0.01
Q1210+17[f]	20.63 ± 0.08	< 13.95	14.96 ± 0.01	12.40 ± 0.03	15.33 ± 0.02
Q2230+02[f]	20.83 ± 0.05	13.69 ± 0.04	15.29 ± 0.03	12.72 ± 0.03	15.70 ± 0.01
Q0336−01[g]	21.20 ± 0.10	13.13 ± 0.08	14.99 ± 0.01	. . .	> 15.14
HS0741+4741[g]	20.48 ± 0.10	< 12.08	14.00 ± 0.02	. . .	14.35 ± 0.01
Q1223+17[g]	21.50 ± 0.10	< 13.88	$15.14 \pm 0.03^{\star}$	12.55 ± 0.03	15.47 ± 0.01
Q1759+75[g]	20.80 ± 0.10	> 13.05	15.24 ± 0.01	> 11.65	$15.54 \pm 0.08^{\star}$
Q2344+12[g]	20.36 ± 0.10	< 12.74	< 14.20	. . .	14.18 ± 0.01

References

[a] Molaro et al. (2001)
[b] Battisti et al. (2012)
[c] Kulkarni et al. (2012)
[d] Outram et al. (1999)
[e] Dessauges-Zavadsky et al. (2004)
[f] Dessauges-Zavadsky et al. (2006)
[g] Prochaska et al. (2001a)
* Taken from HR literature sample.

DLAs show an evolution of [P/Si] with increasing metallicity. However, the inclusion of the limits suggest that most DLAs lie within $-0.5 \lesssim$[P/Si]$\lesssim 0.5$. In fact, the point with a lower limit in sulphur ([S/H]> -0.2) but detection of [P/Si]~ 0.2 suggests that [P/Si] is much more constant with increasing metallicity than the upper panel suggests.

At face value, Figure 3.24 suggests that P yields in DLAs are metallicity independent (as shown by a flat [P/Zn]) and does not strongly suggest that there is a clear odd-even effect in DLAs (flat or slightly increasing [P/Si] with increasing metallicity). Both of these points indicate that (*i*) P does not have a metallicity dependent yield, and may not trace the odd-even effect, or (*ii*) DLAs have already undergone multiple generations of star formation at all metallicities and have washed out the odd-even effect. To test which of these possibilities are true, more observations of P (particularly at [S/H]≥ -0.5) will constrain whether [P/Si] does show signs of an odd-even effect in DLAs.

3.1.7 Manganese

Manganese (Mn) is an iron-peak element formed from explosive silicon burning as ^{55}Co, which decays into ^{55}Mn. It is produced both in Type Ia and Type II SNe, but it is unclear whether either source of Mn has metallicity dependent yields (Woosley & Weaver, 1995). Figure 3.25 demonstrates from NuGrid simulations that Mn is primarily produced in SNe II explosive burning, similar to chromium. The metallicity dependence seen by Woosley & Weaver (1995) is likely a result of the odd-even effect (i.e. increased number of metals results in an increase in the number of neutrons that can form ^{55}Co).

The trouble with observing Mn (or any odd-Z element) in stars is that hyperfine splitting corrections must be included (e.g. Prochaska & McWilliam, 2000; North et al., 2012). Feltzing et al. (2007) checked for deviations in LTE effects by looking for trends of the difference in abundance between two Mn lines with T_{Eff}, log$g$, or [Fe/H]. If non-LTE effects are present, a trend would appear with any of the atmospheric parameters. For the MnI lines at λ 539.4 nm, 549.2 nm, 601.3 nm, and 601.6 nm; no trends in the atmospheric parameters were apparent suggesting no non-LTE corrections are necessary. North et al. (2012) did an extensive comparison of many of the optical Mn lines, deriving [Mn/Fe] for the four Mn I lines. North et al. (2012) found a disagreement between [Mn/Fe] derived with Mn I 5432 Å compared to

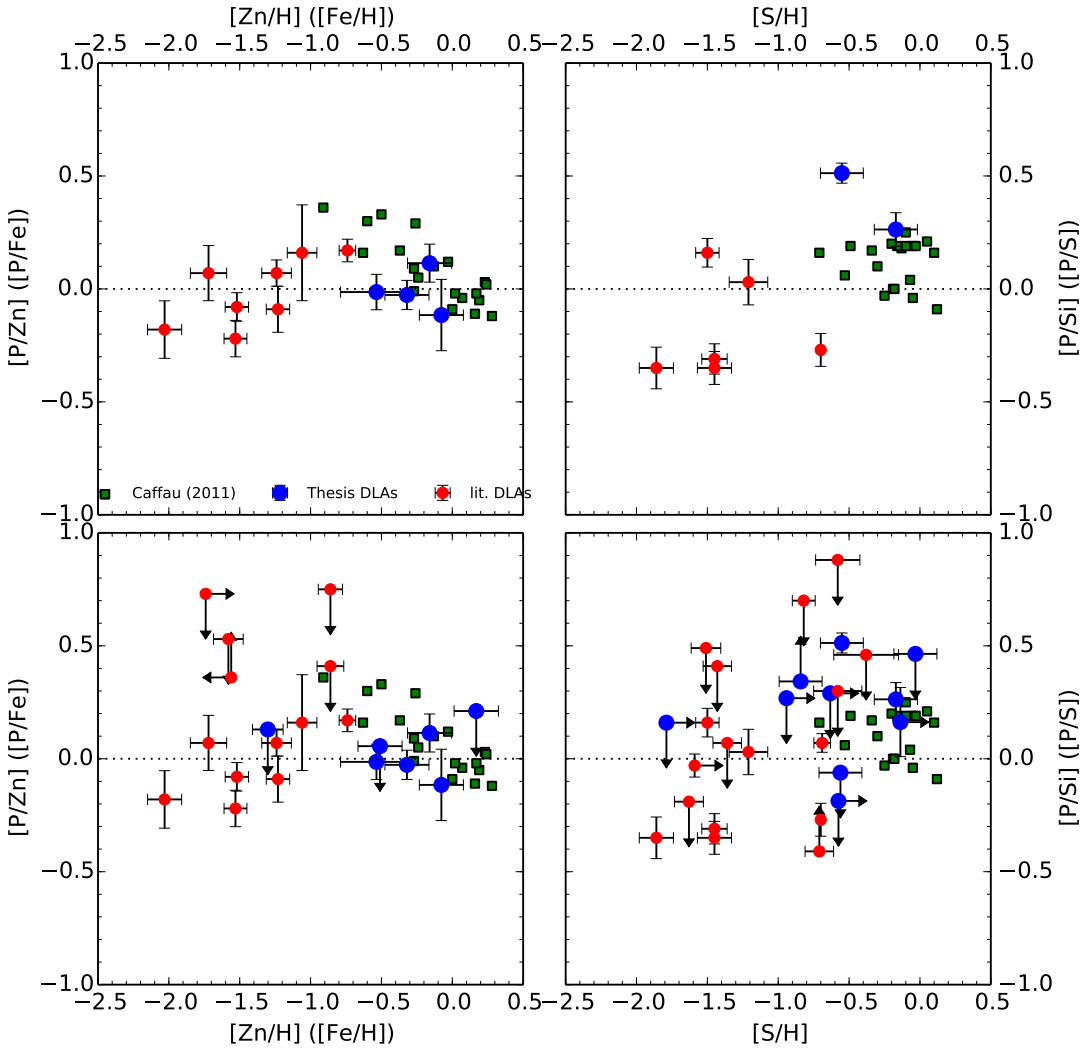

Figure 3.24 The nucleosynthetic trends of P. The upper panels only contain detections of P whereas the lower panels include upper limits as well. *Left Panels*: [P/Zn] as a function of metallicity ([Zn/H]). For the stellar data, zinc is replaced by iron (e.g. [P/Fe] instead of [P/Zn]) as iron is the typical metallicity tracer in stars, whereas zinc is used to avoid dust depletion in DLAs. It seems that, although the stellar data has a gradual decrease to solar [P/Fe] values with increasing metallicity, DLAs have nearly constant [P/Fe]. *Right Panels*: [P/Si] as a function of [S/H]. The stellar data shows [P/S] vs. [S/H]. DLAs seem to hint at a slight odd-even effect, but is unclear at high metallicities if the two Thesis Sample points in the upper right panel are anomalous as most of the upper limits suggest [P/Si] is likely solar.

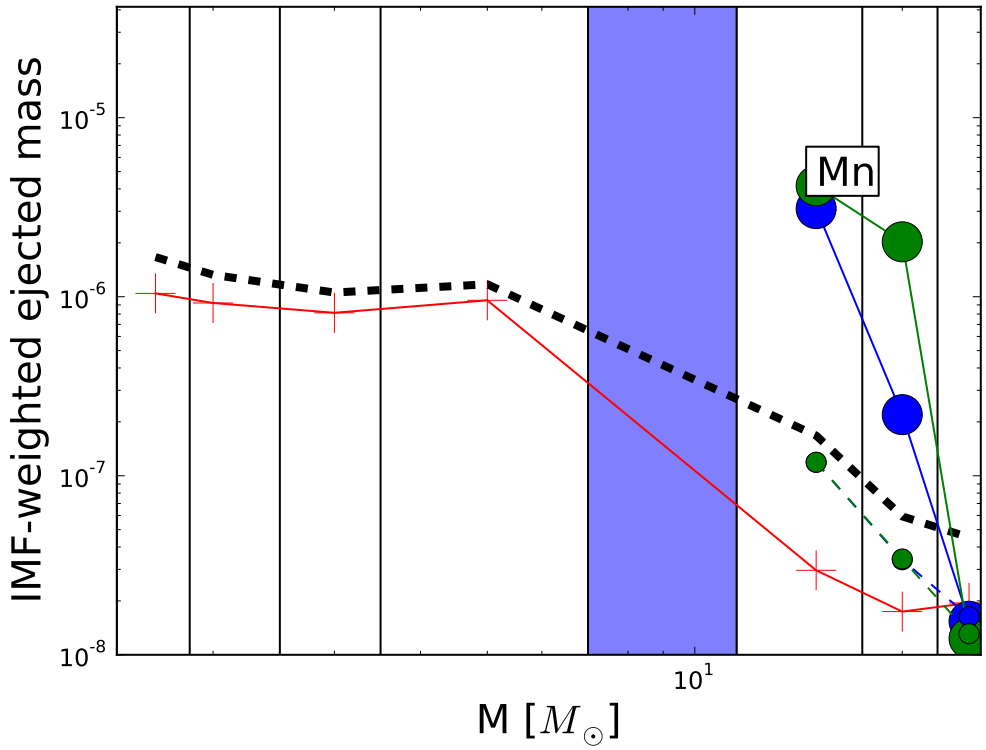

Figure 3.25 The NuGrid simulations of Mn production, following the same notation in Figure 3.1. With respect to the expected IMF mass of Mn (black dashed line); explosive nucleosynthesis (large circles) of massive stars produce the most Mn out of all sources.

the other three lines of their study (λ 5407Å, 5420Å, and 5516Å) for [Fe/H]> -1.0. Therefore, North et al. (2012) deemed the Mn I 5432 line unreliable for deriving Mn abundances.

To test whether Mn yields do have a metallicity dependence, there have been several observational studies to constrain the nucleosynthesis of Mn. One of the largest studies started with Nissen et al. (2000), where they observed 119 stars in the thin and thick disk, as well as the halo of the Milky Way. They found a steady increase in the [Mn/Fe] ratio with metallicity, supporting a metallicity dependence of Mn. However, they noticed that below a metallicity of [Fe/H]< -0.7 dex, the slope was much steeper than at higher metallicities. They claimed that the discontinuity mirrors the same discontinuity seen in [α/Fe], suggesting that Type II SNe contribute to Mn production in the lower metallicity components of the Milky Way (i.e. the halo and thick disk). This is contrary to what is argued by Prochaska & McWilliam (2000), where they reanalysed the Nissen et al. (2000) abundances by including more accurate hyperfine splitting corrections. Prochaska & McWilliam (2000) found a shallower slope, which they claim to be consistent with metallicity independent yields. Although the trend observed by Nissen et al. (2000) could be due to selection effects (as thick disk stars were only chosen to have a metallicity less than [Fe/H]< -0.7; thin disk stars with [Fe/H]~ -0.7 dex), work by Feltzing et al. (2007) confirms the observed change in slope trend by using a kinematically selected sample of stars. Feltzing et al. (2007) went one step further by comparing [Mn/O] as it evolves with [O/H], and found that [Mn/O] is a constant for [O/H]≤ -0.5, suggesting that Mn and O are produced in balanced amounts by Type II supernovae. For [O/H]≥ -0.5 dex, there is a steady increase in Mn with [O/H]. Feltzing et al. (2007) claim that because Type Ia SNe do not contribute until [O/H]=0 that the rise in [Mn/O] must be a result of metallicity dependent yields from SNe II. In dSphs, the sample provided by North et al. (2012) shows a clear overlap with the thick disk and halo stars in the [Mn/Fe] vs. [Fe/H] plot. After including models of various star formation histories and predicted nucleosynthetic yields of Mn, North et al. (2012) were only able to reproduce the observed amounts of [Mn/Fe] in dSphs if metallicity dependent yields were adopted.

To measure Mn in DLAs, there are five different absorption lines, all with very similar oscillator strengths, that can be used (see Table 3.10). The difficulty with Mn is that it has a relatively high condensation temperature (T_{cond} = 1190 K), making it prone to dust depletion. The main studies of Mn in DLAs have been completed

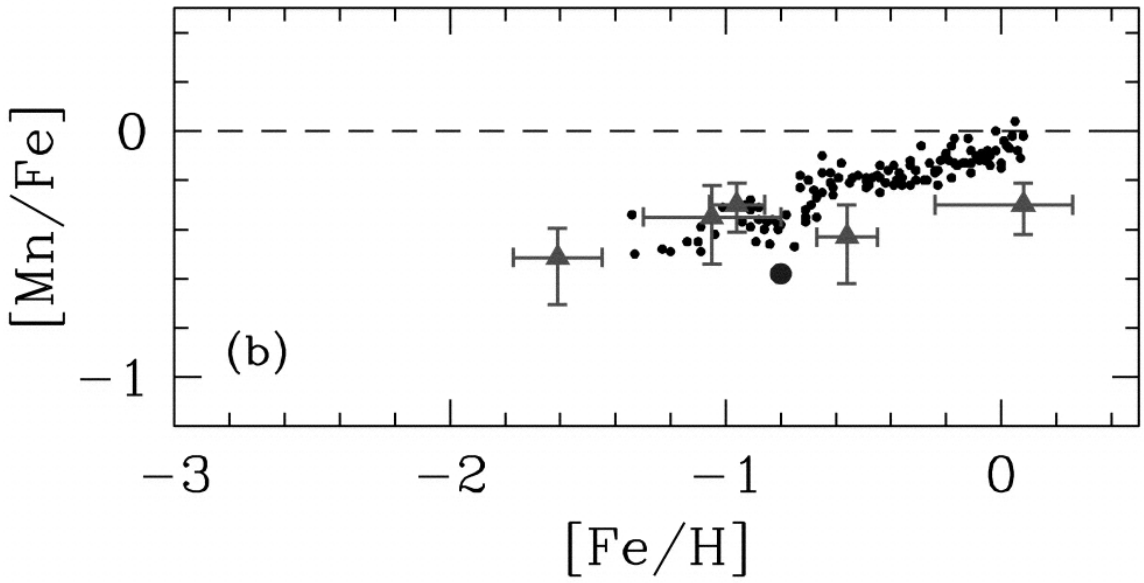

Figure 3.26 The evolution of [Mn/Fe] in DLAs and stars from Pettini et al. (2000). The triangles represent the DLAs with low dust content, whereas the circles represent the Mn abundances from Nissen et al. (2000). For the DLAs, Zn is used as a proxy for Fe. The DLAs appear to have a constant [Mn/Fe] with increasing metallicity as opposed to what is seen in the stars.

by Pettini et al. (2000) and Ledoux et al. (2002a). The work by Pettini et al. (2000) shows that [Mn/Fe] is constant with metallicity (or at least a much flatter evolution than in stars) for the range of metallicity between $-3 \leq$[Fe/H]≤ 0 (see Figure 3.26). However, the Pettini et al. (2000) study is based solely on a small sample of five DLAs that show minor dust depletion in sightlines. With such a small sample, it is difficult to conclude whether all DLAs demonstrate a metallicity-independent yield, despite the caution of avoiding strong effects of dust depletion. The constant [Mn/Fe] with increasing metallicity in DLAs is somewhat at odds with the sample presented by Ledoux et al. (2002a), which shows an increase in [Mn/Fe] as a function of [Zn/H] (Figure 3.27) with a similar slope as the data from stars (e.g. North et al., 2012). Although Ledoux et al. (2002a) were attempting to model dust depletion for Mn, they speculate that the only way to model the depletion correctly would be to include the metallicity dependence of [Mn/Fe].

Figure 3.28 shows the evolution of Mn in the Thesis and HR literature DLAs, and Milky Way samples. [Zn/H] is only adopted as the metallicity indicator in DLAs to avoid dust effects, whereas [Fe/H] is used for the stellar data. As Mn is easily depleted

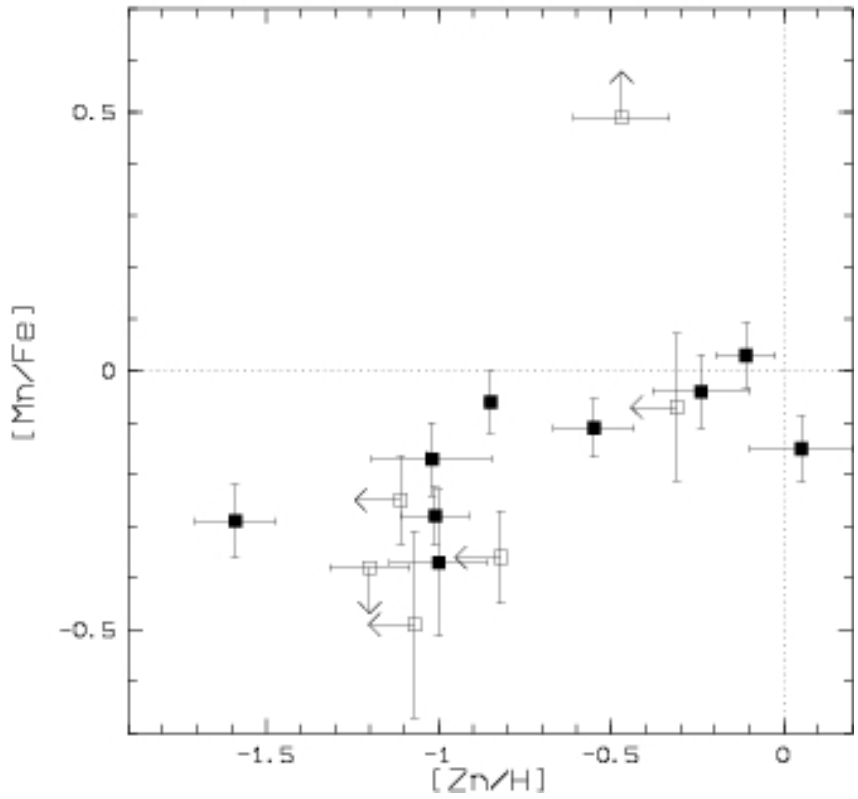

Figure 3.27 The evolution of [Mn/Fe] in DLAs with metallicity ([Zn/H]), taken from Figure 4 in Ledoux et al. (2002a). The increase in [Mn/Fe] with increasing metallicity is contrary to the constant [Mn/Fe] seen by Pettini et al. (2000) in Figure 3.26.

Table 3.10 Mn II lines commonly observed in DLAs

λ (Å)	f
1197.184	2.17×10^{-1}
1199.391	1.69×10^{-1}
2576.877	3.61×10^{-1}
2594.499	2.80×10^{-1}
2606.462	1.98×10^{-1}

Reference–Morton (2003)

into dust, an attempt was made to account for the dust depletion by comparing the Mn abundance to an iron peak element with a similar dust depletion. The use of an iron peak element with a similar dust depletion would effectively remove the relative depletion between the two elements. However, only iron, chromium, and zinc are commonly measured iron-peak elements in DLAs. With zinc being considered undepleted, and iron and chromium being nearly twice as depleted as Mn (based on Figure 3.4; Savage & Sembach, 1996), an average between [Mn/Fe] and [Mn/Zn] should provide a more accurate representation of of the Mn to iron-peak element ratio than either [Mn/Zn] or [Mn/Fe]. To illustrate this, Figure 3.28 shows [Mn/Fe] (upper panel), [Mn/Zn] (lower panel), and the average between the two (i.e. [2Mn/Fe+Zn]/2; middle panel) for the DLAs. It is clear that the middle panels seems to imply a constant value of Mn (relative to the iron-peak elements) as a function of metallicity. This constant value of [Mn/Fe-peak] agrees with the results from Pettini et al. (2000), suggesting that the overall Mn yield in DLAs is metallicity independent, but is within the scatter of the dSph and halo points.

With respect to the α-elements, Figure 3.29 shows the [Mn/Si] ratio for DLAs as a function of [S/H]. Silicon is used in place of sulphur as it is mildly depleted in DLAs like Mn (as both have a similar condensation temperature), therefore the relative ratio of [Mn/Si] should not be greatly influenced by the affects of dust depletion. For stars, magnesium is chosen as the α-element as it is the most commonly measured α-element in the stellar data that traces silicon (Spite et al., 2011). However, caution should be taken with magnesium because it is formed in hydrostatic burning in massive stars, and not during the explosion of Type II SNe (Pignatari et al., 2013); therefore it may not be a typical α-element for tracing SNe II. The constant [Mn/Si] ratio in the DLAs seems to imply that the metallicity-dependent yields of SNe II have not yet kicked in, and that the largest source of Mn appears to be from massive stars. However, the DLA abundances are within the scatter of the stars, so it is unclear whether or not there is evolution in [Mn/Si] in DLAs.

The trends of [Mn/Fe-peak] and [Mn/Si] have shown very little evidence for metallicity dependent yields of Mn expected if DLAs have an inherent odd-even effect ([Mn/Fe-peak]; Figure 3.28) or if SNe II is a significant contributor to Mn at low metallicities ([Mn/Si]; Figure 3.29). However, the scatter of the DLAs is consistent with the stellar literature sample (that supports metallicity dependent yields of Mn). Further observations of Mn in DLAs are needed at solar metallicities in order to determine if Mn always has an inherent metallicity-dependent yield.

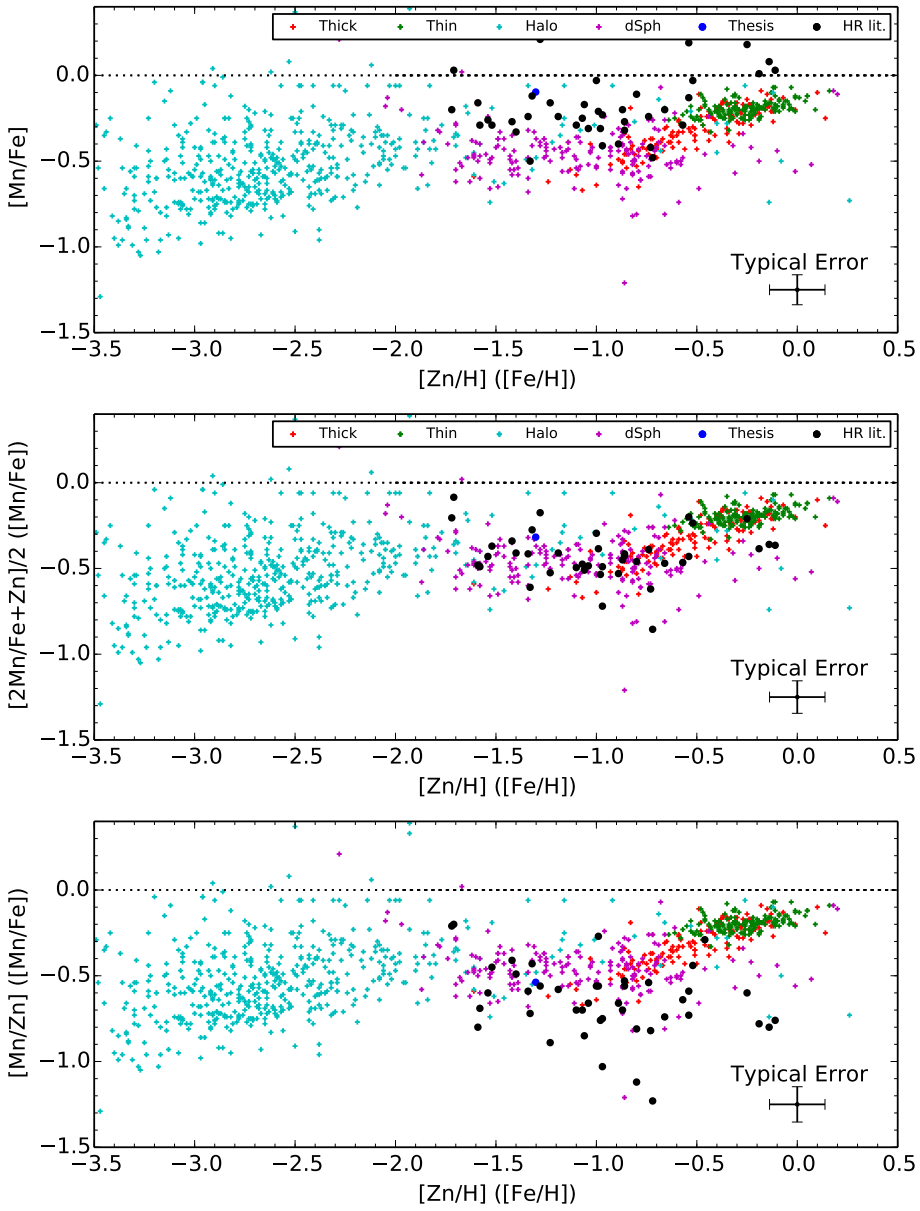

Figure 3.28 Mn abundances relative to the Fe-peak elements. To account for dust depletion in metallicity, Zn is used in place of Fe for DLAs. [Mn/Fe] (top panel), [Mn/Zn] (bottom panel) show the upper and lower limits (respectively) of the Mn to Fe-peak ratio to account for dust in the HR literature (black) and thesis (blue) sample. The middle panel DLA points represent the best estimate of the relative ratios to include dust depletion effects (i.e. the midpoint of [Mn/Fe] and [Mn/Zn]; [2Mn/Fe+Zn]/2). Relative to the stellar data, it is apparent that there seems to be no metallicity dependence of Mn yields in DLAs.

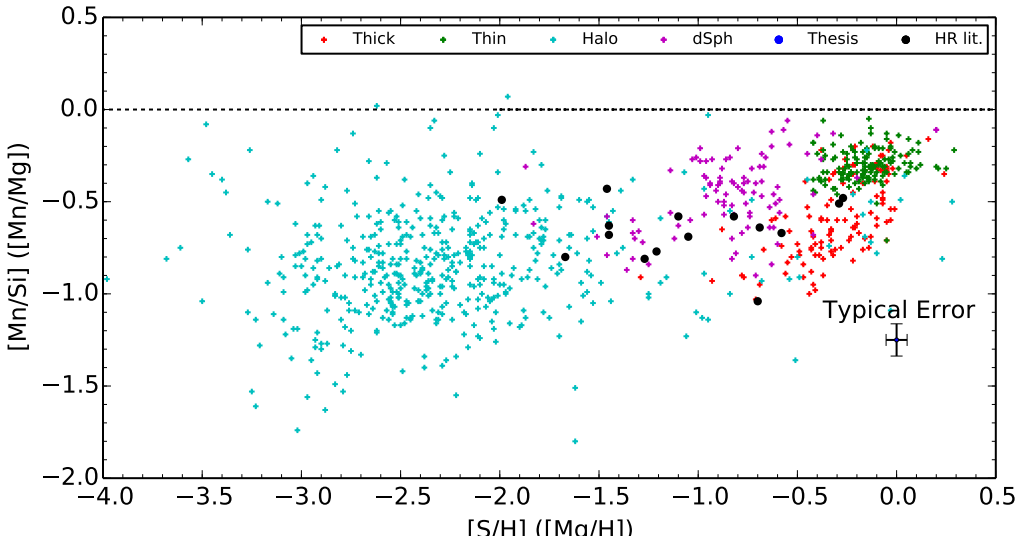

Figure 3.29 [Mn/α] as a function of [α/H] for both the DLA and stellar data. [Mn/Si] is used for the DLA samples as both silicon and Mn have similar condensation temperatures (therefore similar depletion patterns), while [S/H] is required on the x-axis to circumvent dust depletion. Magnesium is used as the α-element in stars. It is clear that constant [Mn/Si] in DLAs suggest there are no metallicity-dependent yields; contrary to what is seen in stars.

3.2 Summary of Comparison

The comparison of DLA metal yields with stars in Sections 3.1.2–3.1.7 demonstrate that DLAs are unique populations compared to many of the Milky Way subcomponents. This is the first detailed comparison of abundances from DLAs and stars in over a decade (Lu et al., 1996a; Pettini et al., 1997, 1999; Prochaska & Wolfe, 2002). In addition, it is also the first study to include a careful analysis of the stellar abundances (i.e. discuss the effects of non-LTE and hyperfine structure corrections on the stellar data) to further refine the understanding of DLA abundances in the context of the stellar data. To summarise the contributions of this work, Table 3.11 provides a brief summary of the Chapter, including condensation temperatures to judge whether the element is depleted, and what corrections are necessary for accurate stellar abundance measurements.

In general, the α-elements (Si and S) do not show any significant evolution with metallicity (independent of dust depletion), as seen in both the Milky Way and dSphs. It is possible that DLAs have undergone rapid evolution (i.e. SNe Ia contribution at earlier metallicities relative to the Milky Way), and start to show an enhancement in [α/Fe] at even lower metallicities than dwarfs. However, the combination of using Zn as an iron-peak indicator at low metallicities, and dust depletion at high metallicities (at least for [Si/Zn]) makes it difficult to determine whether the intrinsic [α/Fe] in DLAs is indeed solar. The comparison of the iron peak elements ([Fe/Zn], [Cr/Zn], and [Cr/Fe]) demonstrate that dust depletion is significant at high metallicities in DLAs (in particular for the Thesis Sample DLAs), as all of these ratios are nearly solar over all metallicities in stars. As opposed to the Milky Way data, both P and Mn show no evolution with metallicity in DLAs (which may be the case for Mn in dSphs as well), suggesting that any odd-even effects are not apparent in DLAs and there are no metallicity-dependent yields. Overall, the constant [α/Fe], [P/Si], and [Mn/Zn] in DLAs supports the idea that DLAs have undergone multiple generations of star formation to pollute the ISM with sufficient metals.

Although the addition of the DLAs from the Thesis Sample has not furthered the understanding of most elements (apart from phosphorous), the metallicity range of the Thesis Sample (and other metal-rich systems within the HR Literature sample) has facilitated the comparison of the nucleosynthetic trends of the elements in higher metallicity Galactic stars (in particular disk stars). In addition, the Thesis DLA sample has provided the opportunity to measure phosphorous abundances. Simi-

lar to other weak (or moderately weak) lines, having a sample of DLAs with large metal column densities provides the opportunity to detect and study such rarely seen elements in the DLA literature.

Table 3.11 Summary of the nucleosynthetic origin of the elements

Element	$\log(\frac{X}{H})^1_\odot$	T^2_{cond} (K)	Type	Dominant formation site	Stellar corrections?	Stellar trend with increasing [Fe/H]	DLA trend with increasing [Zn/H]
Silicon	-4.49 ± 0.01	1311	α	SNe II	non-LTE (optical)	[Si/Fe]–[α/Fe][7]	[Si/Zn]–Flat/$\downarrow$
Phosphorous	-6.57 ± 0.04	1151	odd-Z	n-capture[3] (Si)	Unknown	[P/Fe]–$\downarrow$; [P/S]–Flat	[P/Zn]–Flat; [P/Si]–Flat/$\uparrow$
Sulphur	-4.85 ± 0.02	648	α	SNe II, α[4]	non-LTE (Mult. 1, 6)	[S/Fe]–Flat?	[S/Zn]–Flat
Chromium	-6.36 ± 0.01	1277	Fe-peak	SNe Ia	non-LTE	[Cr/Fe]–Flat	[Cr/Zn]–$\downarrow$; [Cr/Fe]–Flat
Manganese	-6.52 ± 0.01	1190	odd-Z	Exp. Si[5]	HFS[6]	[Mn/Fe]–$\uparrow$	[Mn/Zn]–Flat
Iron	-4.55 ± 0.01	1336	Fe-peak	SNe Ia	non-LTE (Fe I)	. . .	. . .
Zinc	-7.37 ± 0.04	660	Fe-peak	Exp. Si	non-LTE	[Zn/Fe]–$\downarrow$/Flat	[Zn/Fe]–$\uparrow$

[1]Reference – Asplund et al. (2009)
[2]Reference – Savage & Sembach (1996)
[3]Neutron capture.
[4]α-rich freeze-out.
[5]Explosive burning.
[6]Hyperfine structure.
[7]Follows [α/Fe] trend as in Figure 1.7.

Chapter 4

Detection Of Rare Elements In Metal Enhanced DLAs: A Case Study Of Boron

As an example of the type of analysis one can perform on rare elements in metal enhanced DLAs, this chapter looks at the element boron. Boron is a relatively rare element and has fairly weak absorption lines. DLAs with large columns of metals are more likely to contain larger columns of rarer elements (like boron) and provide detections, despite the weak oscillator strengths of these rare elements. Therefore, the Thesis sample provides an opportunity to search systematically for boron in the high redshift universe and constrain its nucleosynthetic origin. The work in this chapter has been published in Berg et al. (2013).

4.1 The Origin Of Boron

Although most elements are primarily formed through stellar or Big Bang nucleosynthesis, beryllium (Be) and boron (B) are notable exceptions. Reeves et al. (1970) first described Be and B formation through the spallation of galactic cosmic rays (GCRs) with CNO nuclei. The original picture of Be and B production from spallation involved interstellar protons and α-particles that are accelerated by supernovae and which subsequently collide with interstellar CNO. The production of B and Be through this *forward* mechanism (also known as *direct* spallation; top panel of Figure 4.1) depends on both the rate of GCR production (i.e. supernova rate) and the

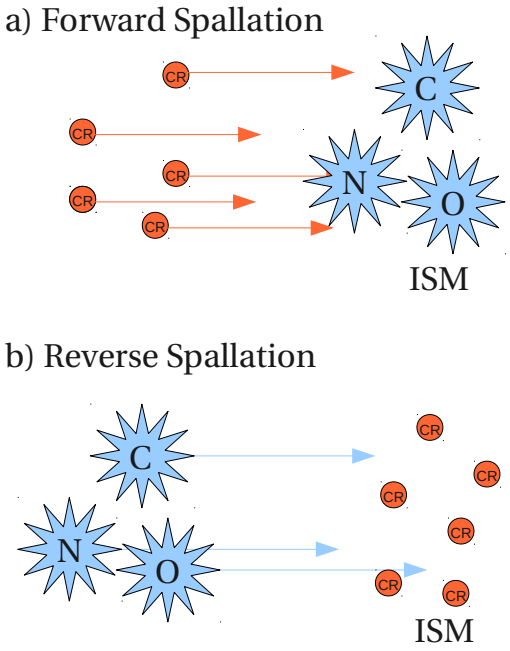

Figure 4.1 Top panel: Forward spallation result from accelerated protons and helium nuclei (CR; orange circles) colliding with ambient CNO (blue stars) in the ISM. Bottom panel: Accelerated CNO smashing into ambient protons and helium nuclei is reverse spallation.

metallicity of the interstellar medium (ISM). Forward spallation is therefore considered to be a *secondary* process with a predicted dependence of Be and B $\propto$[CNO]^2 (i.e. $m = 2$ where m is the slope of the logarithmic dependence between Be and B with CNO).

However, the simple model of forward spallation is in conflict with the metallicity-independent production of the light elements which is observed in halo stars (e.g. Duncan et al., 1992; Boesgaard et al., 1999a). Models of B and Be production have therefore tried to identify *primary* mechanisms (Be, B $\propto$[CNO], $m = 1$) such as the ν-process in stars (Woosley et al., 1990), or spallation in which the GCRs always have the same CNO content (Duncan et al., 1992). The latter class of processes is referred to as *reverse* spallation and generally entails the acceleration of CNO nuclei which then collide with ambient protons or α-particles (bottom panel of Figure 4.1). Various mechanisms have been suggested to accomplish reverse spallation, including

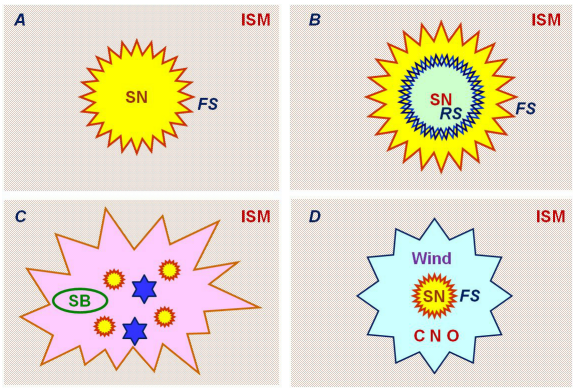

Figure 4.2 The four different scenarios of cosmic ray spallation (Figure 3 from Prantzos, 2012). Top left: Supernovae ejecta (yellow) hitting the ISM induces forward spallation (FS; red). Top right: Forward spallation occurs with supernovae ejecta hitting the ISM. Material that falls back from the supernova (green) undergoes reverse spallation (RS; blue). Bottom left: Superbubble material (rich in metals) is accelerated by both stellar winds and supernovae ejecta and spalls ISM material. Bottom right: Stellar CNO-rich winds from massive, rotating stars is spalled by the supernova.

supernovae accelerating either 1) their own ejecta, 2) locally enriched superbubble material or 3) wind-enriched material around massive rotating stars; see Figure 4.2 (taken from Prantzos, 2012) for a schematic. In reality, there may be multiple processes that contribute to Be and B production, where an intuitive combination may be one where reverse spallation (with interstellar protons and α-particles as the targets) dominates in a metal-poor ISM. As the ISM enriches and more CNO targets accumulate, forward spallation can become more effective. Quantifying the relative contributions of different processes requires detailed chemical modeling which can simultaneously account for the observed abundances of B, Be, and Li (which can also be produced through spallation), as well as isotopic ratios (Fields et al., 2000; Prantzos, 2012).

4.1.1 Stellar Observations of Boron

Although Galactic beryllium abundances have been studied fairly extensively (e.g. Boesgaard et al., 1999a; Smiljanic et al., 2009; Rich & Boesgaard, 2009; Boesgaard et al., 2011), observational studies of boron are quite limited. The strongest boron transitions required for determining stellar abundances are situated in the ultra-violet

(UV) and have very weak oscillator strengths. Furthermore, boron astration due to rotational mixing in stars also impacts measurements (Venn et al., 2002; Mendel et al., 2006). The depletion of boron by rotational mixing would imitate a greater dependence on the oxygen abundance and therefore m would increase. Fortunately, the effects of rotational mixing on boron can be avoided by judicious sample selection. For example, F and G type stars suffer much less from rotational mixing than B stars due to their cooler convection zones and slower rotation rates.

In addition to the observational challenge of measuring boron, a further complication for the interpretation of boron (and Be) abundances is the comparison with the oxygen abundance (e.g., Fields et al., 2000). Despite its high cosmic abundance and variety of spectral features available for measurement, determining accurate O/H abundances has been a subject of much controversy (e.g., Boesgaard et al., 1999b; Israelian et al., 2001). In brief, there are four different features that are commonly used for determining oxygen abundances (the [OI] $\lambda\lambda$6300, 6363 Å forbidden lines, near infra-red (IR) OH vibration-rotation $\lambda\lambda$1.6, 3.4 μm lines, the UV OH λ 3100-3200Å lines, and the OI triplet at λ 7771-7775 Å) yet they result in internally inconsistent abundances. Specifically, the UV OH lines tend to find a rising [O/Fe] at low [Fe/H], in contrast with an [O/Fe] plateau from [OI] measurements (e.g. Kraft et al., 1992; Carretta et al., 2000). Possible reasons for these discrepancies include non-LTE effects and varying sensitivity to the adopted stellar parameters, which may be particularly detrimental to oxygen abundances obtained from the UV OH and O I lines. For this reason, some studies have supported the use of the [OI] lines (Fulbright & Kraft, 1999; Nissen et al., 2002) which produces the [O/Fe] plateau at low metallicities. Indeed, an [O/Fe] plateau is supported by other α-elements such as sulphur (Nissen et al., 2007) whose abundance relative to iron also flattens at low metallicities.

Nonetheless, it is clear that the uncertainty in oxygen abundances complicates both the direct comparisons of Be and B with O, but also hinders observational studies that rely on converting Fe to O via calibrated relative abundances. For example, the boron study of Smith et al. (2001) attempted to derive oxygen abundances in halo stars from Fe measurements taken from Duncan et al. (1997) and Garcia Lopez et al. (1998). To convert from Fe to O, three different models were applied to describe [O/Fe] as a function of [Fe/H], representing the uncertainty in the conversion. Depending on the choice of conversion, they determined a dependence of B on O that ranged from purely primary (m=0.92, 1.05), to a mix of primary and secondary processes (m =1.44) (see bottom panel of Figure 4.3). An accurate interpretation

of Be and B production mechanisms clearly requires a reliable oxygen (or proxy of oxygen) abundance.

Despite these challenges, observations of Be and B in stars have been used to infer that their production is a combination of both primary and secondary processes. Smith et al. (2001) determined oxygen abundances from the weak [O I] lines for 13 F and G field stars for which Cunha et al. (2000) derived the boron abundances. The best-fit slope of the B–O relation was found to be $m = 1.39$, suggesting a combination of primary and secondary processes (Figure 4.3). This agrees with an analysis of beryllium done by Rich & Boesgaard (2009), who observed 24 stars and compared the best-fit double power model ([O/H]> -1.8 and [O/H]< -1.4; $m = 1.59$, 0.74 respectively) and a single line best fit ($m = 1.21$) of their Be-O relation. They found that there appeared to be a two-component trend with a break point at [O/H]~ -1.6 ([Fe/H]~ -2.2), indicating a transition from primary to secondary processes (see Figure 4.4).

4.1.2 Interstellar Observations of Boron

Interstellar boron can also contribute to the understanding of the origin of boron, although relatively few observational studies exist. The first observation of interstellar boron was made by Meneguzzi & York (1980) using the Copernicus satellite. However, it was the launch of the Hubble Space Telescope (HST) that allowed real progress in this area with observations made first with the Goddard High Resolution Spectrograph (GHRS) (Federman et al., 1993; Jura et al., 1996), and later with the Space Telescope Imaging Spectrograph (STIS) (Howk et al., 2000). Importantly, Howk et al. (2000) found that boron can be significantly depleted on to dust in the ISM, leading to potential under-estimates of its actual abundance. They found that boron is more easily depleted in the cold diffuse ISM, and demonstrated an anti-correlation of the boron abundance with hydrogen gas density. The most recent measurements of interstellar boron have been made by Ritchey et al. (2011) who added a further 56 Galactic sight-lines observed with STIS. Based on their sight-lines through warm, low density gas (assumed to be relatively undepleted) Ritchey et al. (2011) determine an ISM abundance of $\log(\mathrm{B/H}) = 9.62 \pm 0.11$, agreeing with the results from undepleted B-type stars (Venn et al., 2002) and previous ISM studies (Howk et al., 2000, see Figure 4.5).

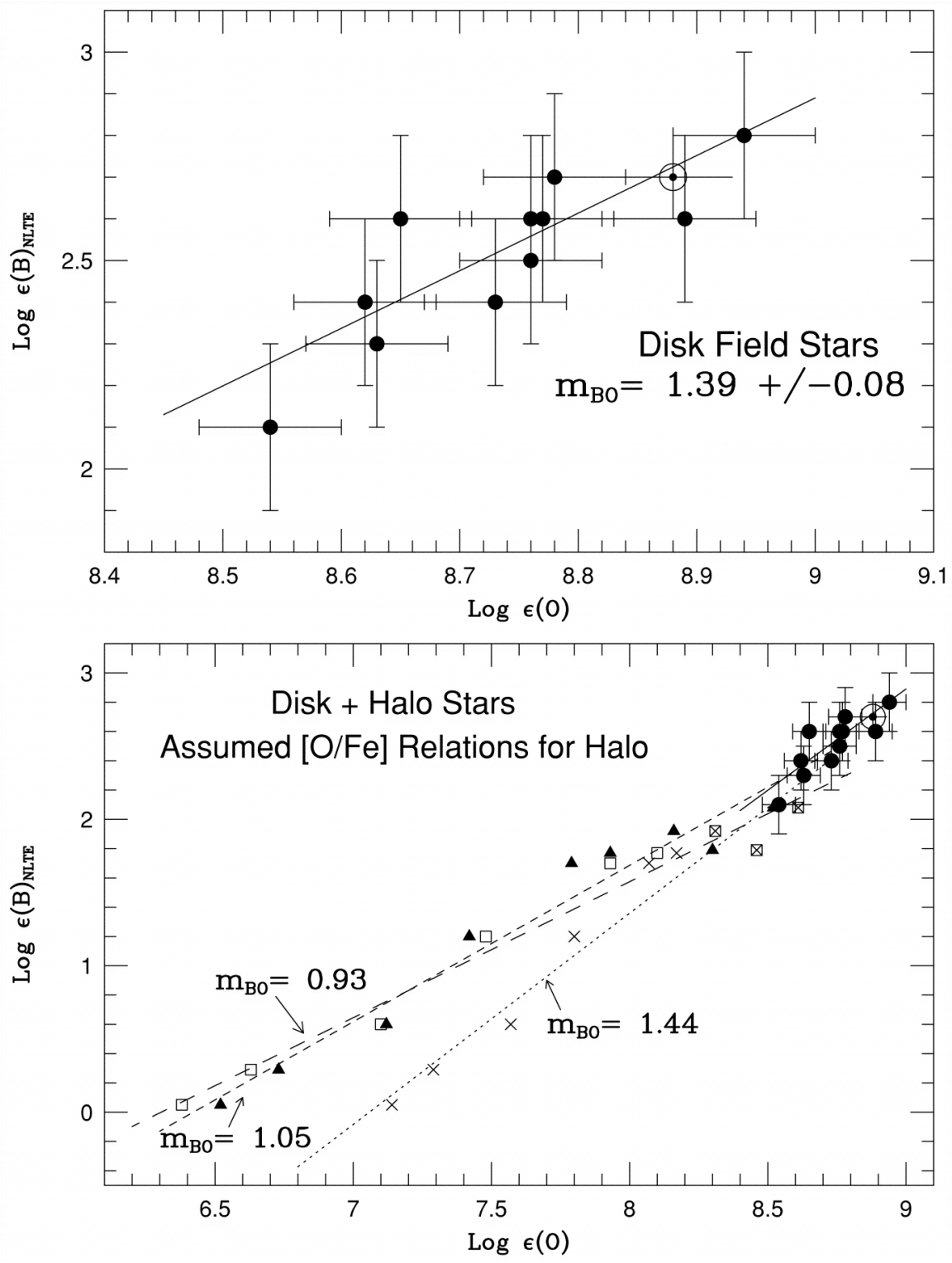

Figure 4.3 Observed boron-oxygen relation from Smith et al. (2001) (Figure 3). The top panel only looks at the 13 disk stars. Their linear fit provides a slope of $m = 1.39 \pm 0.08$; which indicates a combination of both primary and secondary processes. The bottom panel shows the boron-oxygen relation in halo stars using three different [O/Fe] ratio conversions. The uncertainty of oxygen abundances in halo stars demonstrates that boron can either be completely primary or contain a mix of primary and secondary.

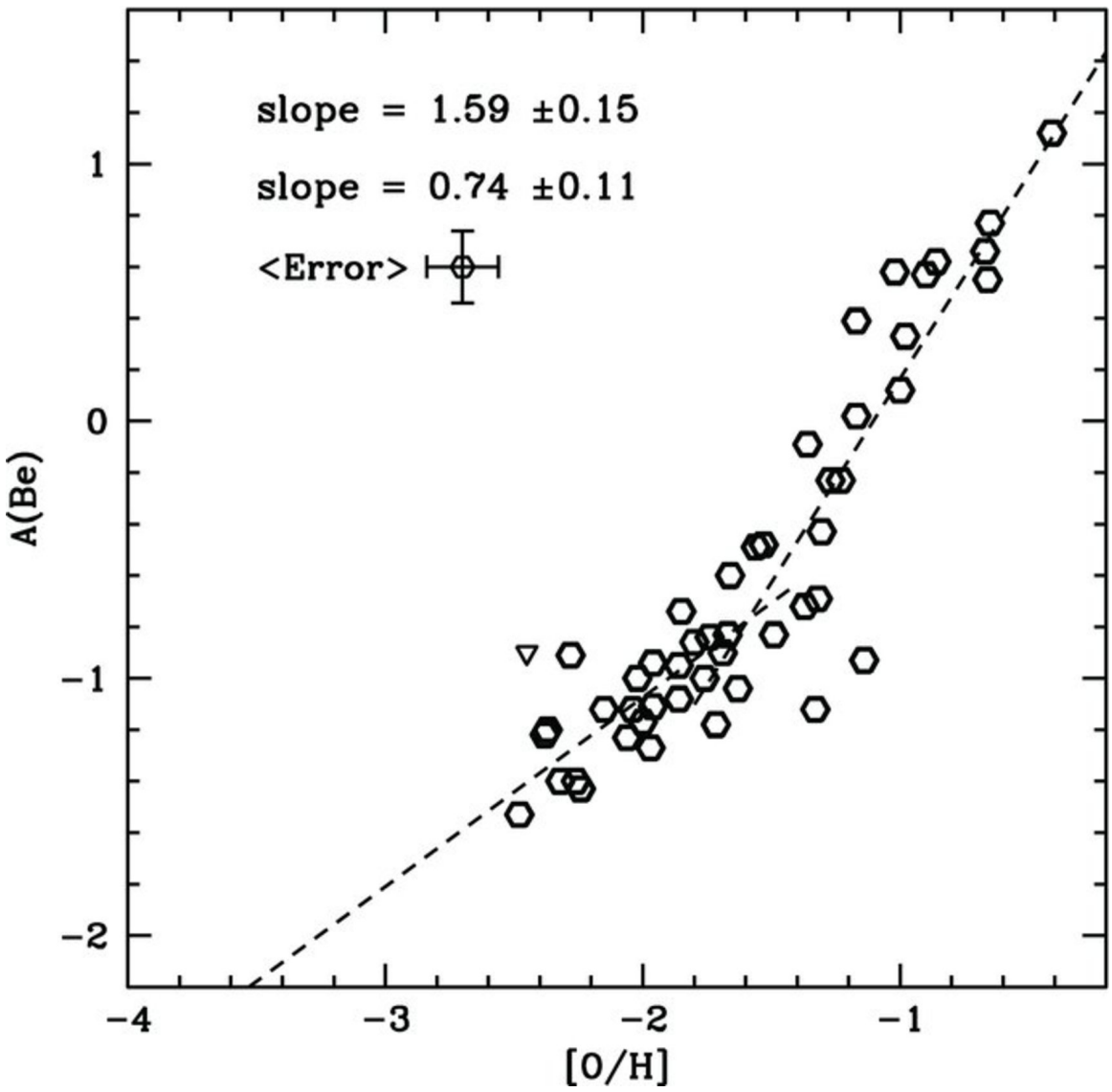

Figure 4.4 The beryllium-oxygen relation in halo stars from Rich & Boesgaard (2009) (Figure 8). The distinct break at [O/H]~ -2 suggests that the most metal-poor environments produce primary beryllium (and boron), whereas higher metallicities produce a combination of both primary and secondary beryllium (and boron).

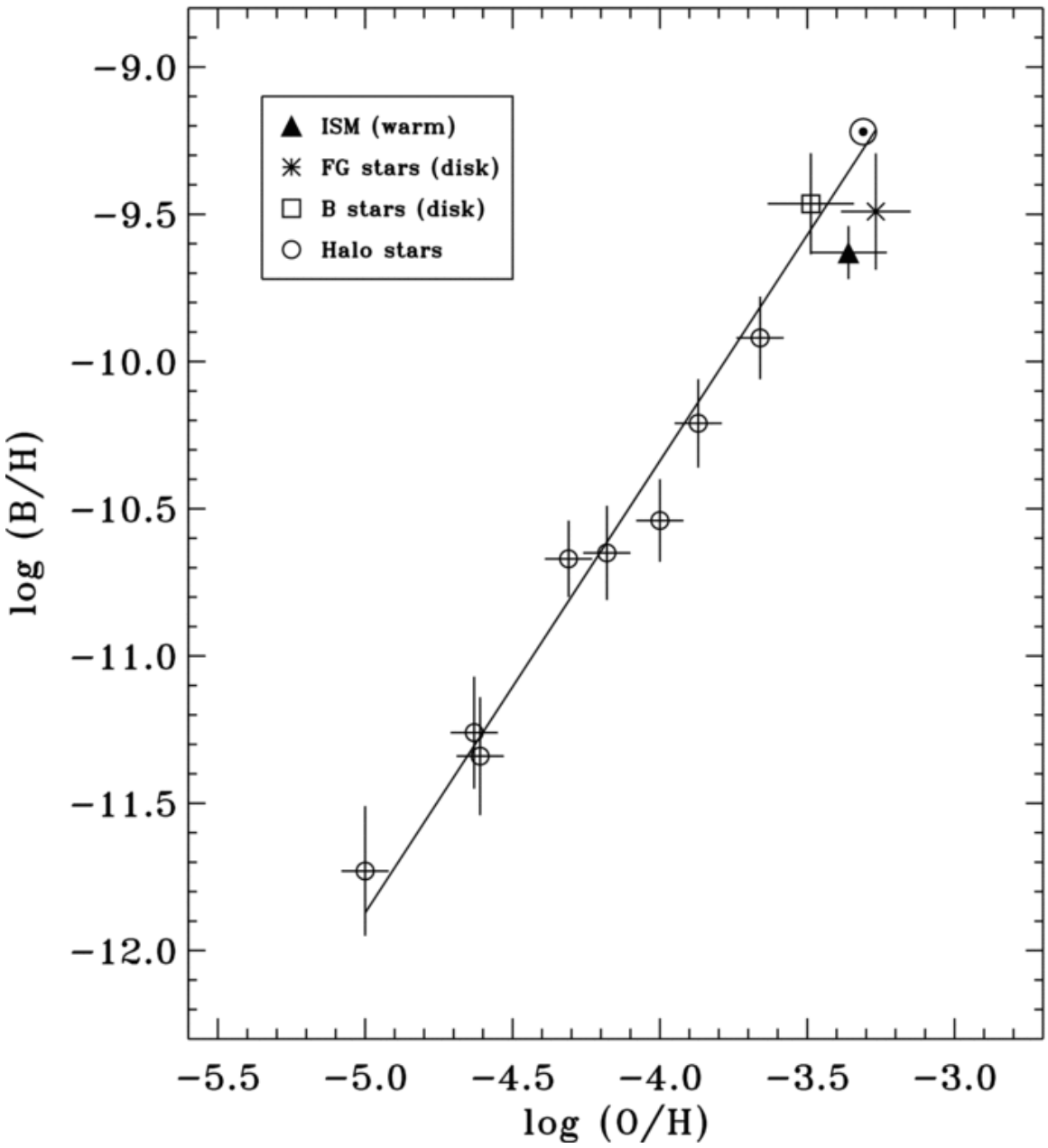

Figure 4.5 Figure 18 from Ritchey et al. (2011) shows the boron-oxygen relation; combining the stellar observations from Smith et al. (2001) (star; averaged), Venn et al. (2002) (square; averaged), and Tan et al. (2010) (circles). The solid triangle represents the average of the ISM sight-lines identified to be free of dust depletion. Overall, there is a single best-fit line with slope of $m = 1.5 \pm 0.1$ over all metallicities.

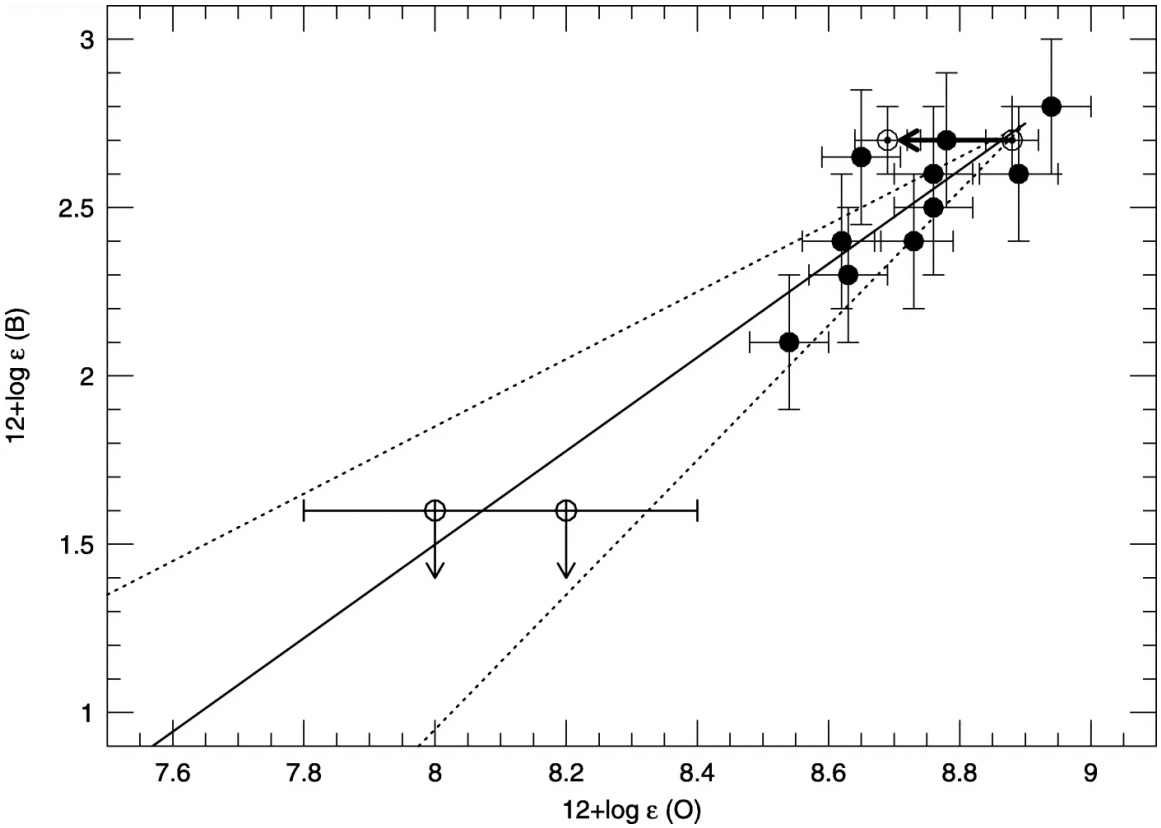

Figure 4.6 The two boron upper limits in the SMC inferred from Brooks et al. (2002) (Figure 6) with respect to the data from Smith et al. (2001). Although they are only upper limits, the observations suggest that boron is produced by secondary processes in the SMC.

4.1.3 Extragalactic Observations of Boron

Beyond the stellar and interstellar measurements in the Milky Way, there has been only one extra-Galactic study of boron. Brooks et al. (2002) observed two B-type stars in the Small Magellanic Cloud (SMC) in an attempt to compare boron production relative to the Milky Way. The two boron upper limits presented by Brooks et al. (2002) lie below the expectation for primary boron production, but are consistent with a secondary production mechanism (Figure 4.6). However, Brooks et al. (2002) acknowledge that their measurements do not account for depletion of boron due to rotational mixing, hence they suggest that their limits do not necessarily rule out primary production.

The interpretation of boron abundances in other galaxies depends on both the cosmic ray flux (CRF) and the abundance of spallation targets. The SMC has an

oxygen abundance around one quarter of that in the solar neighbourhood (Korn et al., 2000; Salmon et al., 2012), and 15% of its current CRF (based on Fermi/Large Area Telescope (LAT) gamma ray observations of the SMC, see Abdo et al., 2010; Sreekumar et al., 1993). Brooks et al. (2002) point out that the lower oxygen abundance and CRF in the SMC might be expected to have a compound effect that leads to a production of boron that is $\sim$1/20 lower than the solar neighbourhood for secondary boron production, but also discuss the effect of higher past star formation rates and CRF confinement times. The discussion in Brooks et al. (2002) reveals that high boron abundances that exceed the primary dependence (i.e. [B/H] > [O/H]) can indicate high CRFs, which in turn may be related to high rates of star formation. The study of boron in other galaxies therefore provides a novel approach to constraining their star formation histories.

To study boron in other galaxies, and in particular, to push to higher redshifts, DLAs offer a plausible prospect. Studies of DLAs allow us to track the chemical evolution over redshifts of 0 to 5 (Rafelski et al., 2012), as well as constrain the origin of individual elements (e.g. Cooke et al., 2011b; Ellison et al., 2001b; Prochaska & Wolfe, 2002; Pettini et al., 1997). Conveniently for the present study, their cosmological distances provide the advantage of observing the redshifted B II λ1362 line in the optical, avoiding the use of space-based telescopes which currently limits Galactic boron observations. Due to the weakness of the B II λ1362 line (the only line available for observations in DLAs), the most promising first targets for boron observations in DLAs will be absorbers with relatively strong metal lines (i.e. MSDLAs). Large metal column densities can be due to either an average metallicity in a high N(HI) absorber, or (as is found to be mostly the case) an inherently high metallicity (Kaplan et al., 2010). The possibility of boron detection in MSDLAs has been demonstrated by a tentative detection in the proto-typical MSDLA FJ0812+3208 (z_{abs}=2.626, log N(HI)=21.35) by Prochaska et al. (2003d). They compared the abundance pattern of boron and other elements and concluded that their detection of a solar B/O ratio was indicative of primary production of boron.

This case study presents the first systematic search for boron in DLAs. The Thesis Sample defined in Section 2.3 presents a list of promising targets for boron detection based on either the strength of their metal lines, or overall metallicity. A further novelty of this study is that, for the first time in a boron study, sulphur is adopted as a proxy for oxygen to circumvent the problem with absolute oxygen abundances described above. The substitution of sulphur for oxygen has been frequently used in

DLAs, both for consistency in comparisons with Galactic stellar data (Nissen et al., 2004, 2007) and because the oscillator strengths of the OI transitions often preclude an oxygen abundance determination (Pettini et al., 2002). Although both are α-elements, it should be emphasized they do not have the same nucleosynthetic origin. Oxygen is primarily a product of helium and neon burning in massive stars, whereas sulphur is produced in oxygen burning and α-rich freezeout of core collapse supernovae (Woosley & Weaver, 1995). The substitution of sulphur for oxygen is explicitly tested. High resolution echelle spectra have been obtained for each of the 30 Thesis Sample DLAs and measurements (or limits) made for the abundances of oxygen, boron and sulphur. The sample includes additional data for FJ0812+3208, increasing the spectral signal-to-noise ratio (S/N) and permitting a re-analysis of this system.

4.2 Observations

To summarize the quality of the Thesis Sample for observing boron, Table 4.1 lists the QSOs that have been observed, exposure time, and the S/N (per pixel) near to the BII λ 1362 Å line. The systems without an N(HI) measurement are still included in our sample, since a measurement of the B/S or B/O can still help us to constrain production mechanisms. As discussed in Section 2.3, the Thesis Sample spans a wide range in N(HI) and specifically targets the metal-rich end of the DLA literature sample. Figures 2.9 and 2.10 show that higher metal contents are probed in the Thesis Sample, along with a range of hydrogen column densities.

Table 4.1 Target list

Quasar	Exposure Time (s)	S/N^a_{1362} (pixel^{-1})
J0008−0958	15029	11
J0058+0115	14400	23
Q0201+36	13000	. . .
Q0458−02	11500	4
FJ0812+3208	56000	45
J0927+1543	12800	4
J0927+5823	21600	14
J1010+0003	7200	1
J1013+5615	3600	5
J1049−0110	4800	13
J1056+1208	21300	18
J1155+0530	7200	10
J1159+0112	9000	22
J1200+4015	10800	13
J1249−0233	7300	10
J1310+5424	10800	11
J1313+1441	10200	9
J1417+4132	25800	30
J1524+1030	9000	6
J1552+4910	9000	20
J1555+4800	21600	6
J1604+3951	10300	15
J1610+4724	10800	8
Q1755+578	19000	11
J2100−0641	20000	28
J2222−0945	10800	16
Q2230+02	8100	7
J2241+1225	7200	6
J2340−0053	18600	23
Q2342+34	5400	11

[a] The S/N is quoted near the observed position of the BII λ1362 line.

Table 4.2 Boron, oxygen, and sulphur column densities and abundances

QSO	$z_{\rm em}$	$z_{\rm abs}$	logN(HI)	logN(BII)	logN(SII)	logN(OI)	[B/H]	[S/H]	[O/H]
J0008−0958	1.95	1.76753	20.85 ± 0.15 (1)	< 12.07	15.83 ± 0.02	< 18.03	< 0.43	-0.17 ± 0.15	< 0.49
J0058+0115	2.49	2.00953	21.10 ± 0.15 (1)	11.95 ± 0.04	15.41 ± 0.01	. . .	0.06 ± 0.16	-0.84 ± 0.15	. . .
Q0201+36	2.49	2.46280	20.38 ± 0.15 (2)	. . .	. . .	. . .	. . .	. . .	. . .
Q0458−02	2.29	2.03950	21.65 ± 0.09 (3)	< 12.53	. . .	< 18.452	< 0.09	. . .	< 0.18
FJ0812+3208	2.71	2.62593	21.35 ± 0.15 (4)	11.43 ± 0.08	15.48 ± 0.02	< 17.69	-0.71 ± 0.17	-1.02 ± 0.15	< -0.35
J0927+1543	1.80	1.73113	. . .	< 12.96	< 15.86	< 18.97	. . .	. . .	
J0927+5823	1.91	1.63515	20.40 ± 0.25 (2)	. . .	15.79 ± 0.14	< 18.33	. . .	0.24 ± 0.28	< 1.24
J1010+0003	1.40	1.26514	. . .	. . .	. . .	. . .	. . .	. . .	
J1013+5615	3.61	2.28400	. . .	. . .	. . .	. . .	. . .	. . .	
J1049−0110	2.12	1.65760	20.35 ± 0.15 (1)	. . .	15.47 ± 0.01	< 18.11	. . .	-0.03 ± 0.15	< 1.07
J1056+1208	1.92	1.60954	21.45 ± 0.15 (2)	< 12.21	> 15.66	< 18.20	< -0.03	> -0.94	< 0.06
J1155+0530	3.48	3.32607	21.05 ± 0.10 (4)	< 12.02	15.35 ± 0.003	< 17.66	< 0.18	-0.85 ± 0.10	< -0.08
J1159+0112	2.00	1.94375	21.80 ± 0.10 (5)	< 12.04	> 15.16	. . .	< -0.55	> -1.79	. . .
J1200+4015	3.36	3.22000	20.65 ± 0.15 (4)	< 11.82	15.37 ± 0.01	< 17.79	< 0.38	-0.43 ± 0.15	< 0.45
J1249−0233	2.12	1.78085	21.45 ± 0.15 (6)	< 12.34	15.50 ± 0.02	< 18.23	< 0.10	-1.10 ± 0.16	< 0.09
J1310+5424	1.93	1.80070	21.45 ± 0.15 (2)	< 12.39	> 15.96	< 18.39	< 0.15	> -0.64	< 0.25
J1313+1441	1.88	1.79480	. . .	< 12.21	15.71 ± 0.01	< 18.19	. . .	. . .	
J1417+4132	2.02	1.95090	21.45 ± 0.25 (6)	< 12.02	> 15.8	17.98 ± 0.07	< -0.22	> -0.80	-0.16 ± 0.26
J1524+1030	2.06	1.94094	. . .	< 12.13	> 15.53	< 18.05	. . .	. . .	. . .
J1552+4910	2.04	1.95987	. . .	< 11.95	15.34 ± 0.004	< 17.96	. . .	. . .	. . .
J1555+4800	3.30	2.39089	21.50 ± 0.15 (4)	. . .	> 15.88	. . .	. . .	> -0.77	. . .
J1604+3951	3.13	3.16400	21.75 ± 0.20 (4)	< 11.71	15.70 ± 0.04	< 17.69	< -0.83	-1.20 ± 0.20	< -0.75
J1610+4724	3.22	2.50661	21.00 ± 0.15 (4)	< 12.38	> 16.01	< 18.35	< 0.59	> -0.14	< 0.66
Q1755+578	2.11	1.97110	21.40 ± 0.15 (7)	< 11.91	> 15.97	< 17.88	< -0.28	> -0.57	< -0.21
J2100−0641	3.14	3.09130	21.05 ± 0.15 (4)	< 11.78	15.64 ± 0.002	< 17.71	< -0.06	-0.56 ± 0.15	< -0.03
J2222−0945	2.93	2.35430	20.55 ± 0.15 (4)	< 12.05	15.33 ± 0.02	. . .	< 0.71	-0.37 ± 0.15	. . .
Q2230+02	2.15	1.86440	20.85 ± 0.08 (3)	< 12.56	. . .	< 18.55	< 0.92	. . .	< 1.01
J2241+1225	2.63	2.41800	21.15 ± 0.15 (4)	< 12.01	14.94 ± 0.04	< 17.98	< 0.07	-1.36 ± 0.16	< 0.14
J2340−0053	2.09	2.05452	20.35 ± 0.15 (4)	< 11.60	14.95 ± 0.004	< 17.56	< 0.46	-0.55 ± 0.15	< 0.52
Q2342+34	2.92	2.90899	21.10 ± 0.10 (8)	< 11.96	15.17 ± 0.01	< 17.96	< 0.07	-1.08 ± 0.10	< 0.17

HI References – (1) Herbert-Fort et al. (2006); (2) Kaplan et al. (2010); (3) Pettini et al. (1994); (4) Prochaska & Wolfe (2009); (5) Kanekar et al. (2009); (6) This paper; (7) Jorgenson et al. (2006); (8) Prochaska et al. (2003c);

Table 4.3 Wavelengths and oscillator strengths of transitions

Element	Wavelength (Å)	f
SII	1250.584	$5.453 \cdot 10^{-3}$
SII	1253.811	$1.088 \cdot 10^{-2}$
SII	1259.519	$1.624 \cdot 10^{-2}$
OI	1355.598	$1.248 \cdot 10^{-6}$
BII	1362.461	$9.870 \cdot 10^{-1}$

Reference – Morton (2003)

4.3 Abundance Determination

All metal column densities (Table 4.2) were obtained using the AODM (see Section 2.3 for more details). The limits for the optical depth integrations for the boron and oxygen absorption lines are shown by the vertical dotted lines in Figures 4.8, 4.10, and 4.12 (although these have been adjusted from their fiducial values in cases of suspected contamination and are discussed on a case by case basis below). The errors quoted in Table 4.2 were determined from the photon noise. As discussed in Section 2.3 continuum errors start to become the main source of error for weak detections like boron and oxygen. Therefore for the weak detections presented in Section 4.3.1, continuum fitting is further discussed on a case by case basis in Section 4.3.2.

To estimate 3σ upper limits in the case of non-detections, the value of the full width at half maximum (FWHM) of the most prominent feature is measured in the absorption profile of a strong transition. This feature should correspond to the most easily detected absorption of any element in the DLA. From the S/N of the spectrum at the location of the absorption line (see Table 4.1[1], the rest frame equivalent width (W; at $n\sigma$ significance) of a line at redshift z is calculated from

$$W = \frac{n \cdot FWHM}{S/N \cdot (1+z)}. \tag{4.1}$$

From equation 4.1, the column density of a species with rest wavelength λ_0 and oscillator strength f is calculated from

$$N = \frac{\pi e^2}{m_e c^2} \frac{W}{f \lambda_0^2}. \tag{4.2}$$

All wavelengths, oscillator strengths (Morton, 2003), and solar values (Asplund

[1]The blank S/N entry represents no coverage in the spectrum and is included for completeness.

Table 4.4 Solar abundances

Element	$\log N(X/H)_{\odot}+12$	Source
B	2.79 ± 0.04^{a}	Meteoritic
C	8.43 ± 0.05	Photospheric
N	7.83 ± 0.05	Photospheric
O	8.69 ± 0.05	Photospheric
S	7.15 ± 0.02	Meteoritic

Reference – Asplund et al. (2009)
[a] The measured solar abundance of boron by Asplund et al. (2009) is higher by ~ 0.3 dex relative to the local ISM and B-type stars that have been used in previous works such as Venn et al. (2002), see also the discussion in Cunha et al. (1997). The impact of the uncertainty in the solar boron abundance is discussed in Section 4.4.

et al., 2009) adopted are listed in Tables 4.3 and 4.4, respectively. The measured column densities and derived upper limits are presented in Table 4.2, along with the quasar emission redshift ($z_{\rm em}$), DLA absorption redshift ($z_{\rm abs}$), and HI column densities of the DLAs. All 3σ upper limits presented are only obtained for the spectra where little or no contamination is present using the S/N near the absorption. Otherwise, no upper limit was obtained despite S/N being reported for all DLAs near the line in Table 4.1.

This analysis is solely focussed on the abundances of B, O, and S. It is assumed that the gas phase abundances that have been measured are representative of the total elemental abundance in the DLA. Oxygen and sulphur are indeed non-refractory and little depleted on to dust grains (Savage & Sembach, 1996). Although boron is depleted in dense Galactic disk clouds (Howk et al., 2000), sight-lines through low density gas should yield a robust estimate of the boron abundance (Ritchey et al., 2011). The abundance pattern of DLAs (Pettini et al., 2000), typically low molecular content (Ledoux et al., 2003) and high spin temperature (Ellison et al., 2012) indicate that most DLA sight-lines do not intersect cold, high density clouds. Hence the boron abundances measured in these systems should not be greatly affected by depletion. However, due to the generally higher metallicities of the Thesis Sample, higher density sight-lines may have been probed and may have enhanced dust depletion. It is also assumed that the measured ionization state for each element is the dominant one and that no ionization corrections are necessary. The effect of possible depletion and ionization effects are explicitly discussed in Section 4.4.

4.3.1 Possible Detections

Three of the DLAs in our sample have visibly significant absorption features at the expected wavelength of BII λ 1362. The profiles from each are discussed below, including possible sources of blending and contamination. Figures 4.7, 4.9, and 4.11 show the absorption profiles for several different species; whereas Figures 4.8, 4.10, and 4.12 zoom in and show the profiles for both boron and oxygen. For comparison the scaled profiles of moderately strong lines are shown for visual guidance of the general shape of absorption profiles for these DLAs[2].

J0058+0115

Figure 4.7 displays the absorption features for various transition lines in J0058+0115, whereas Figure 4.8 shows an absorption feature at the expected wavelength of BII λ 1362 and OI λ 1355. The scaled nickel line is overplotted in Figure 4.8 for comparison. The shape of the boron absorption is in very good agreement with that of the Ni II λ 1741 line, hence a possible detection of boron for the first time in this DLA is reported, where the measured equivalent width is 3.55σ significant[3]. However, it is not feasible to rule out the possibility that this feature is actually a weak Lyα line. The OI λ 1355 line is completely blended with the Lyα forest, therefore no reliable limit was determined.

FJ0812+3208

Boron was detected in the FJ0812+3208 sight-line at a redshift of $z = 2.626$ by Prochaska et al. (2003d) with a column density logN(B)= 11.43. The data presented here for this sight-line have been improved from that presented in Prochaska et al. (2003d) by the addition of ~ 10 hours of HIRES data (Jorgenson et al., 2009). Both the BII λ 1362 and OI λ 1355 lines are shown in Figure 4.10, with scaled CrII λ 2066 shown for comparison. It can be seen that the CrII line has two components: the stronger one centred at $v \sim 0$ km s^{-1} and a weaker component at ~ -40 km s^{-1}. The CrII profile is used to define the velocity range over which the optical depth

[2]The scaling is done by matching the area integrated within the AODM bounds for the reference metal line profile to the area determined for boron or oxygen.

[3]The significance is calculated by combining Equations 4.1 and 4.2, then solving for the number of sigma (n) needed to obtain the derived AODM abundance. The FHWM was measured from a prominent absorption component of a strong metal line in the spectrum, and is equivalent to the value used in the calculation for the upper limits.

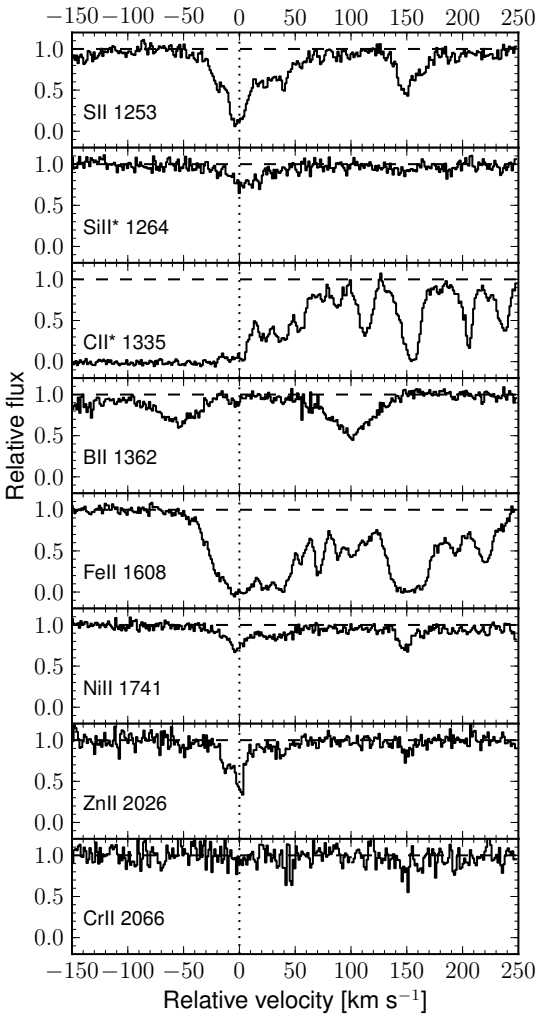

Figure 4.7 Absorption profiles for various singly ionized species in J0058+0115. From panel to panel, it is apparent that the absorption profiles for all the species (other than CII*) traces out an identical shape for various absorption strengths. It is important to note that there appears to be a detection of Si II* $\lambda\lambda$ 1264 in this sight-line.

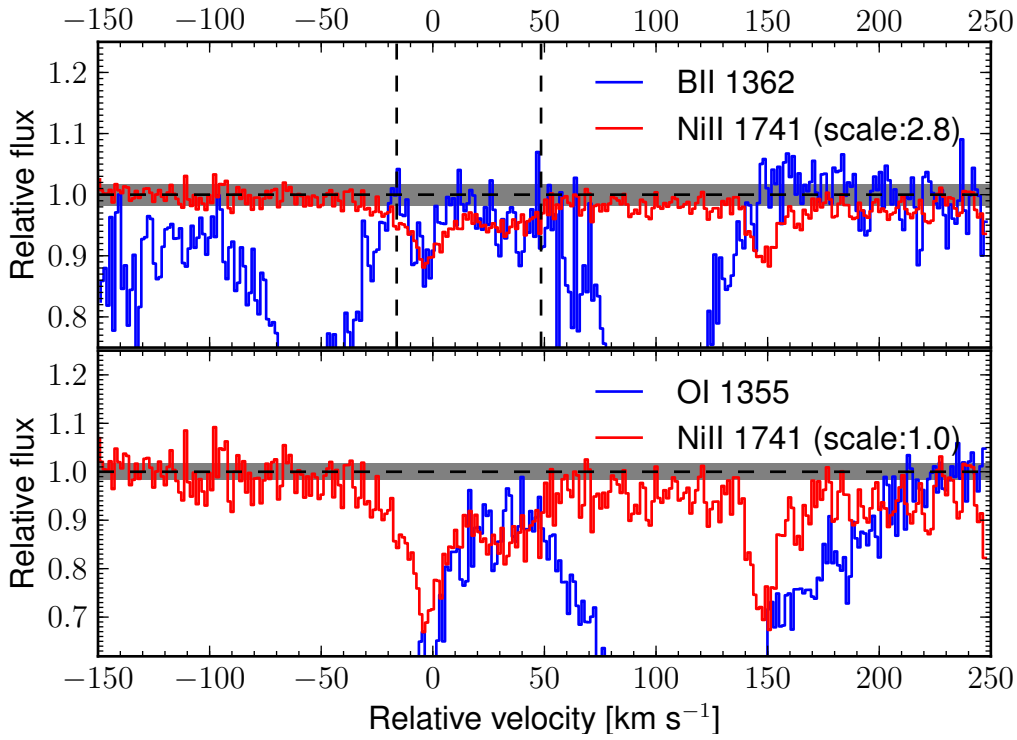

Figure 4.8 The absorption profile of BII λ1362 (top, blue), OI λ1355 (bottom, blue) and NiII λ1741 (red) for J0058+0115. The black horizontal dashed line indicates the continuum, and the black vertical dotted lines are the bounds for the apparent optical depth integration for the species in blue. The nickel profile is scaled down to match the intensity of the boron and oxygen lines by matching the areas within the AODM bounds of the absorption. Oxygen is not detected in this DLA as it is blended within the Lyα forest. Overall, the scaled profile matches that of boron absorption. The grey regions mark where the continuum has been over and underestimated for determining errors in the continuum (see Section 4.3.2).

is integrated in both OI and BII (vertical dotted lines). The BII λ1362 line is well aligned with CrII λ 2066. The determined column density is log(B/H)=11.43 $\pm$ 0.08 (measured at 3.84σ significance) which is in agreement with the result of Prochaska et al. (2003d). Figure 4.10 shows that there is an additional BII λ1362 component at $v \sim -20$ km s^{-1} (bounded by the solid vertical green lines) that is not seen in CrII; and has been excluded in the abundance determination. The additional absorption at $v \sim +40$ km s^{-1} is unrelated absorption and has been excluded from the analysis. The oxygen profile is detected only in the strongest component at $v \sim 0$ km s^{-1}, but not the weaker component seen in other lines at $v \sim -40$ km s^{-1} (see Figure 4.7). Given the S/N, one might have expected a detection (albeit weak) in the $v \sim -40$ km s^{-1} component, if the column densities of the two components have the same relative ratio in oxygen as sulphur. Therefore the possibility that the oxygen detection may be contaminated by a different species must be considered. Indeed, if the absorption was entirely due to OI, it would yield a [S/O] = -0.67, which is a surprising discrepancy from the solar value. However, Prochaska et al. (2003d) determines [S/O] = -0.33 which is closer to the relative abundance in nearby disk stars (e.g. Reddy et al., 2003, see Section 4.4.1). This discrepancy with Prochaska et al. (2003d) is due to both a lower N(SII) and a higher N(OI) in this study. To be conservative and because there is a robust detection of sulphur for the analysis; the oxygen abundance is reported as an upper limit from the equivalent width of the detected absorption feature in recognition of possible contamination.

J1417+4132

J1417+4132 contains a possible detection of boron (see Figure 4.12) that is reported here for the first time. The scaled ZnII λ2026 line is shown for comparison. The detection is challenging in this case because of the broad, shallow nature of the profile; but there is a clear drop below the continuum over the same velocity range where the boron profile would lie for both OI and BII. However, the feature is broad and shallow, with a total equivalent width significant to 2.97σ, making it a very tentative detection. Despite being nearly 3σ, the column density is adopted as an upper limit due to the challenging nature of the detection. However, a discussion on how the continuum errors may affect the yields of both boron and oxygen is furthered in Section 4.3.2 for completeness. Unfortunately, all of the SII lines are saturated or severely blended, so only a lower limit for N(SII) can be determined.

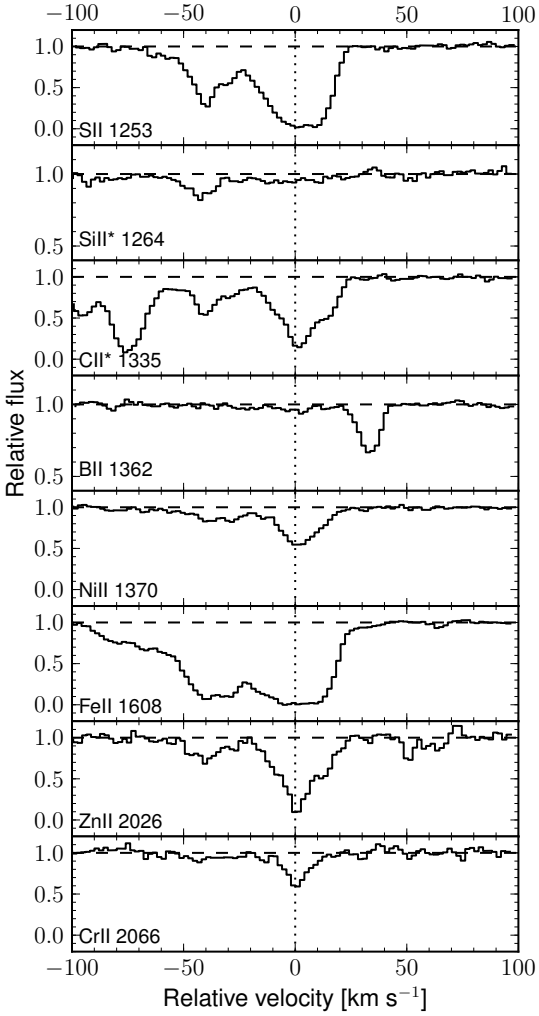

Figure 4.9 Similar to Figure 4.7, the same absorption profile is seen for all singly ionized species detected in FJ0812+3208.

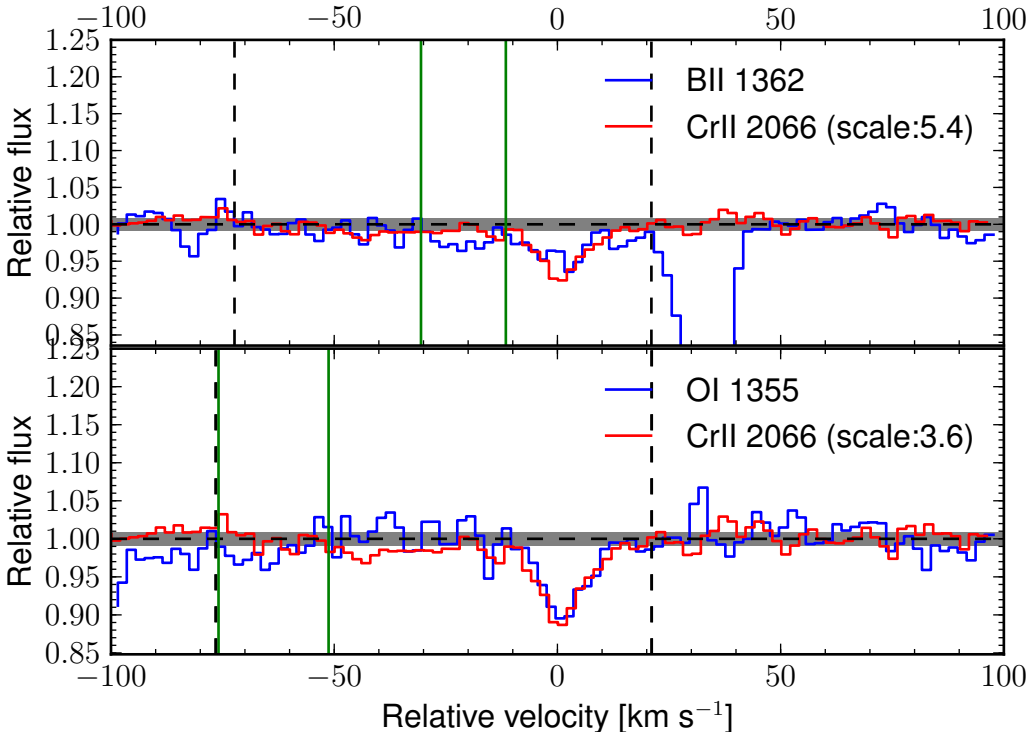

Figure 4.10 The absorption profile of boron and oxygen for FJ0812+32 following the notation in Figure 4.8. Extra components that are not present in the chromium profile are bounded by the solid green vertical lines and are not included in the abundance determination. Boron appears to be blended by a feature at $v \sim -20$ km s^{-1}, which has been removed from the abundance determination. The oxygen absorption at ~ -40 km s^{-1} does not appear, despite the strength of the component at ~ 0 km s^{-1} and high S/N. See Section 4.3.1 for a discussion of possible contamination of the oxygen line. The grey regions mark where the continuum has been over and underestimated for determining errors in the continuum (see Section 4.3.2).

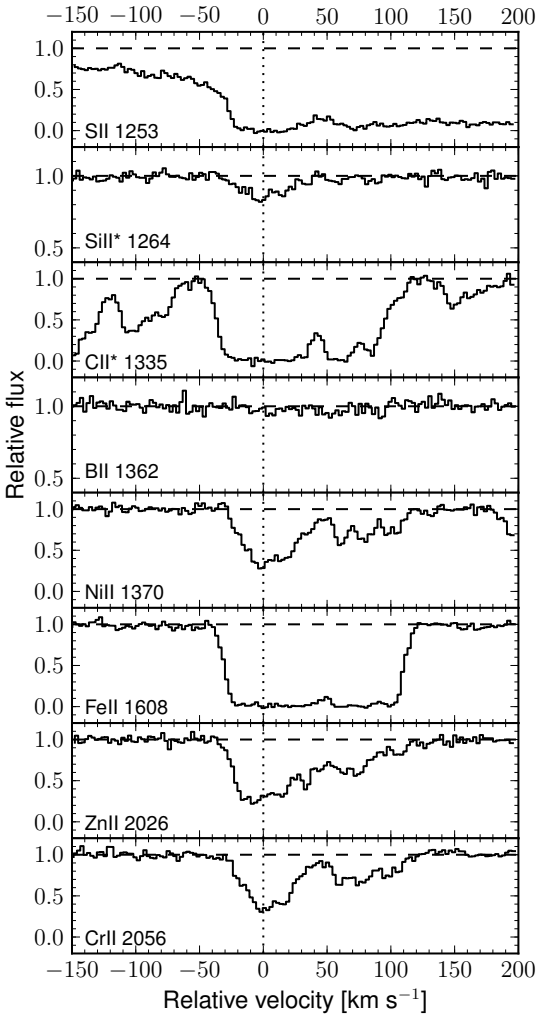

Figure 4.11 Absorption profiles for various species in J1417+4132. Identical absorption profiles are seen for all singly ionized species (other than SII; which is lost by broad absorption). Again, there seems to be absorption at the Si II* λ 1264.

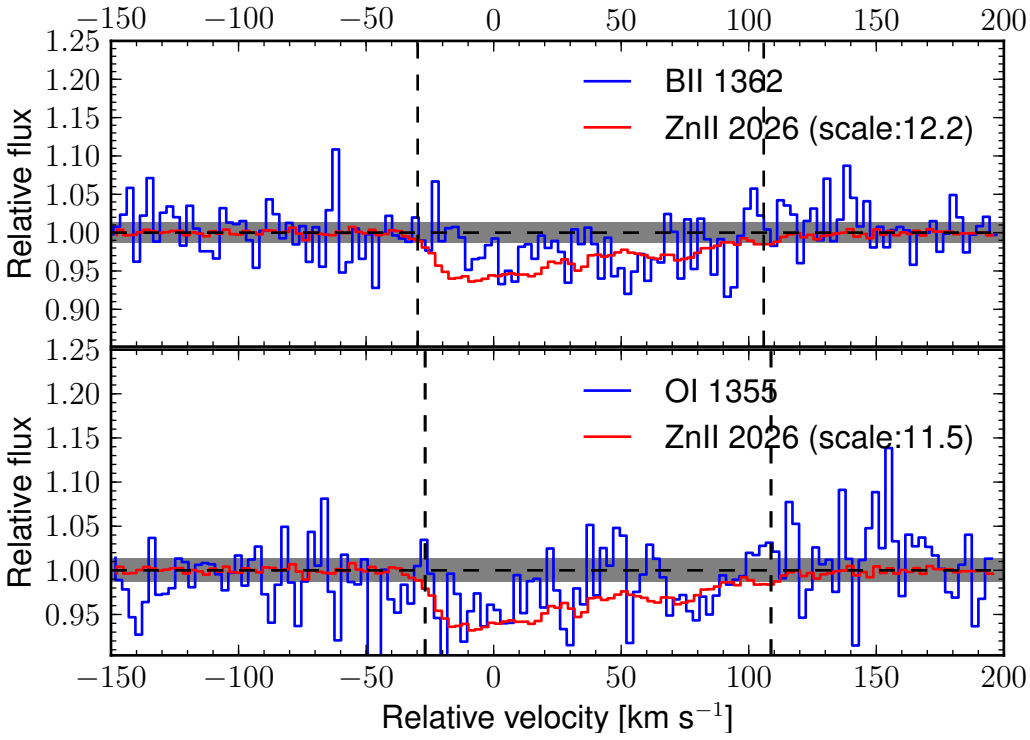

Figure 4.12 The absorption profiles of boron, oxygen and zinc for J1417+4132 following the same notation as in Figure 4.10. The grey regions mark where the continuum has been over and underestimated for determining errors in the continuum (see Section 4.3.2). The absorption is only significant to 2.97σ, so it is treated as an upper limit.

Table 4.5 Continuum errors

QSO	Continuum Offset	ΔlogN(B)[a]	ΔlogN(O)[a]	$\sigma_{B_{orig}}$ [b]	$\sigma_{O_{orig}}$ [b]	$\sigma_{B_{new}}$ [c]	$\sigma_{O_{new}}$ [c]
J0058+0115	±0.013	±0.14	. . .	±0.16	. . .	±0.21	. . .
FJ0812+3208	±0.007	±0.18	. . .	±0.17	. . .	±0.24	. . .
J1417+4132	±0.014	(±0.17)[d]	±0.15	(±0.26)	±0.26	(±0.31)	±0.30

[a] The error in the column density resulting from offsetting the continuum.
[b] The error budget in the abundance [X/H] from the AODM calculation (Table 4.2).
[c] The total error budget in the abundance [X/H] including the error from continuum placement.
[d] The errors in parentheses represent the derived AODM errors from assuming the detection is real.

4.3.2 Continuum Errors

Due to the weakness of the putative boron features, continuum errors may play a role for the three DLAs discussed above. To check how much the continuum placement may affect our results, the continuum was artificially placed at higher and lower values to estimate the difference in column density resulting from bad continuum fitting. This is represented by the top and bottom edges of the grayed regions in Figures 4.8, 4.10, and 4.12. These offsets correspond to 40% of the inverse of the S/N of the spectrum near the absorption. The resulting differences in the column densities (ΔlogN) for the associated continuum offsets are shown in Table 4.5 for both boron and oxygen. In general, the change in column density for both oxygen and boron (< 0.18 dex) is about the same magnitude or smaller than the typical error in the hydrogen column density (0.15–0.25 dex; see Table 4.2). Specifically, for J1417+4132 (where ΔlogN(B) is ~ 0.17 dex) the difference is small relative to the overall error budget in [B/H] (0.26 dex) which is primarily dominated by the uncertainty in the hydrogen column (0.25 dex). However the change in column density for boron in both J0058+0115 and FJ0812+3208 is of the same order as the hydrogen column error. The uncertainty in the total error budgets in [O/H] and [B/H] (σ_O and σ_B; respectively) have been recalculated from Table 4.2 to include this continuum error and are shown in Table 4.5. Including the continuum fitting error in the total error budget results in at most a 0.07 dex change, which is relatively small. Based on these results, continuum errors do not have a significant contribution in any of these three DLAs.

4.4 Discussion

4.4.1 Sulphur-Oxygen Relation

In order to overcome the difficulties of determining oxygen abundances in stars[4] and DLAs, the possibility of using sulphur as an alternative α-capture reference element is investigated. The comparison of boron with sulphur in the DLAs and stellar data therefore hinges on whether the sulphur abundance intrinsically tracks oxygen in stars. Other than stars containing boron, the stellar literature sources were selected on the basis of what lines and corrections were used in attempts to homogenize the sample and remove systematic errors (see Table A.2[5]). For oxygen, only literature samples that used [O I], UV OH lines with proper continuum placement, or the OI triplet with non-LTE corrections were selected. Following the analysis done by Caffau et al. (2005), sulphur studies that used the S I multiplet 1 (with non-LTE corrections), 6, and 8 for abundance determinations were selected. DLAs from Table A.1 not present in the sample which contained both oxygen and sulphur abundances are included as well solely for comparison.

Figure 4.13 shows the relation between [S/O] and [O/H] for the literature sample used. DLAs are not included in determining the mean offset as they are only shown for interest. Although the scatter about the mean appears substantial, most of the stellar data are consistent within 1.5σ of the mean. Having a constant offset in stars suggests that the interchange of oxygen and sulphur is valid, and should not change the slope of the best fit line between B/O and B/S. Due to the variety in non-LTE corrections, model atmospheres, and choice of lines; a more homogeneous data set of oxygen and sulphur in stars should tighten the relation.

4.4.2 Boron-Oxygen Relation

Figure 4.14 presents the main scientific results, the comparison of DLA and Galactic boron abundances plotted as a function of oxygen (left) and sulphur (right). Both panels contain the primary and secondary lines (of slopes $m = 1$ and $m = 2$, respectively) and the best fit lines derived from a linear least squares fit:

[4]Although the comparison with the ISM is more realistic; stars are included as well since we are motivated by determining the nucleosynthetic origin of boron. Previous studies of stars and the ISM provide this information, hence both are included.

[5]Abundances have been converted to the Asplund et al. (2009) scale.

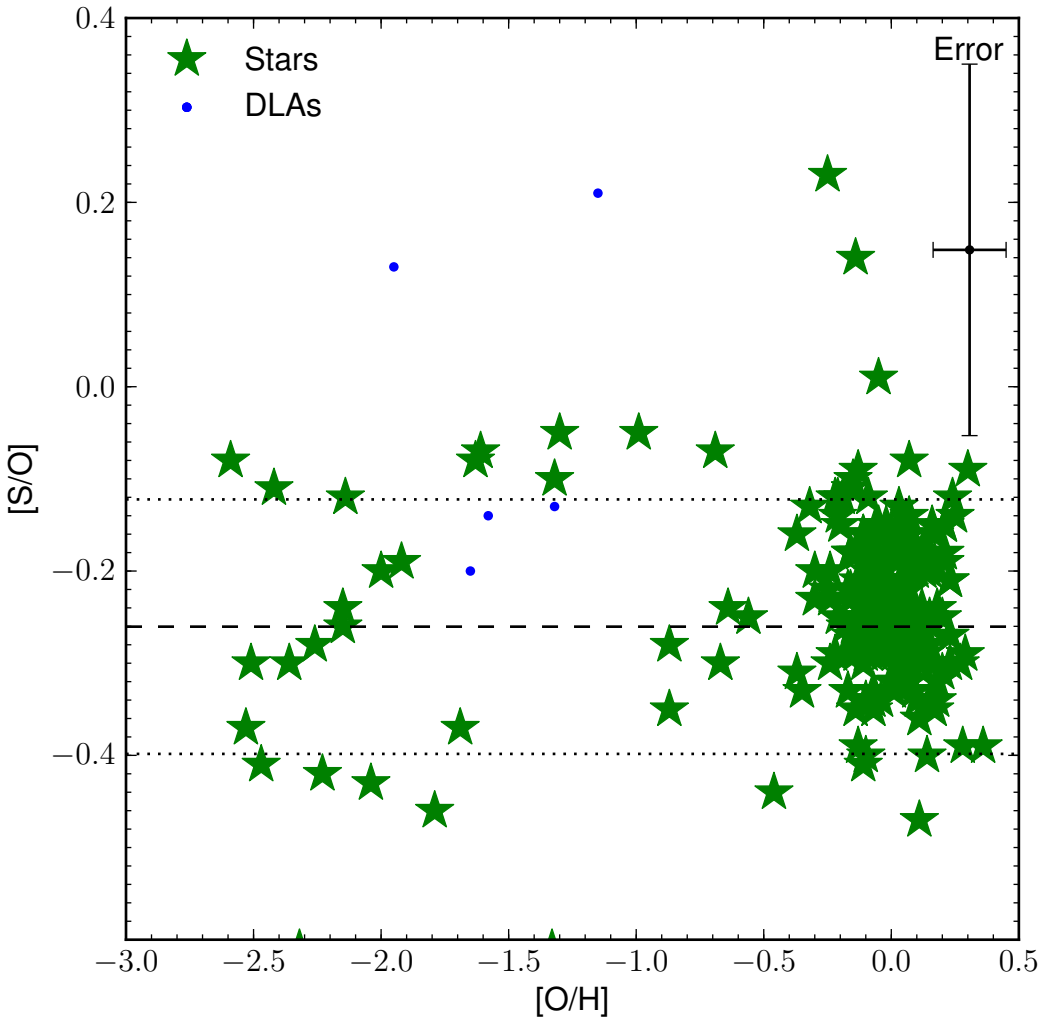

Figure 4.13 [S/O] is plotted as a function of [O/H] for stellar data to determine whether these two element track each other in stars. The data plotted include the entire literature compilation presented in Table A.2, including both stars and DLAs. The dashed line is the mean value of [S/O]= -0.27 ± 0.15 (with dotted lines as 1σ errors) of the plotted data. The error bar in the top right shows the typical uncertainty in the stellar abundances.

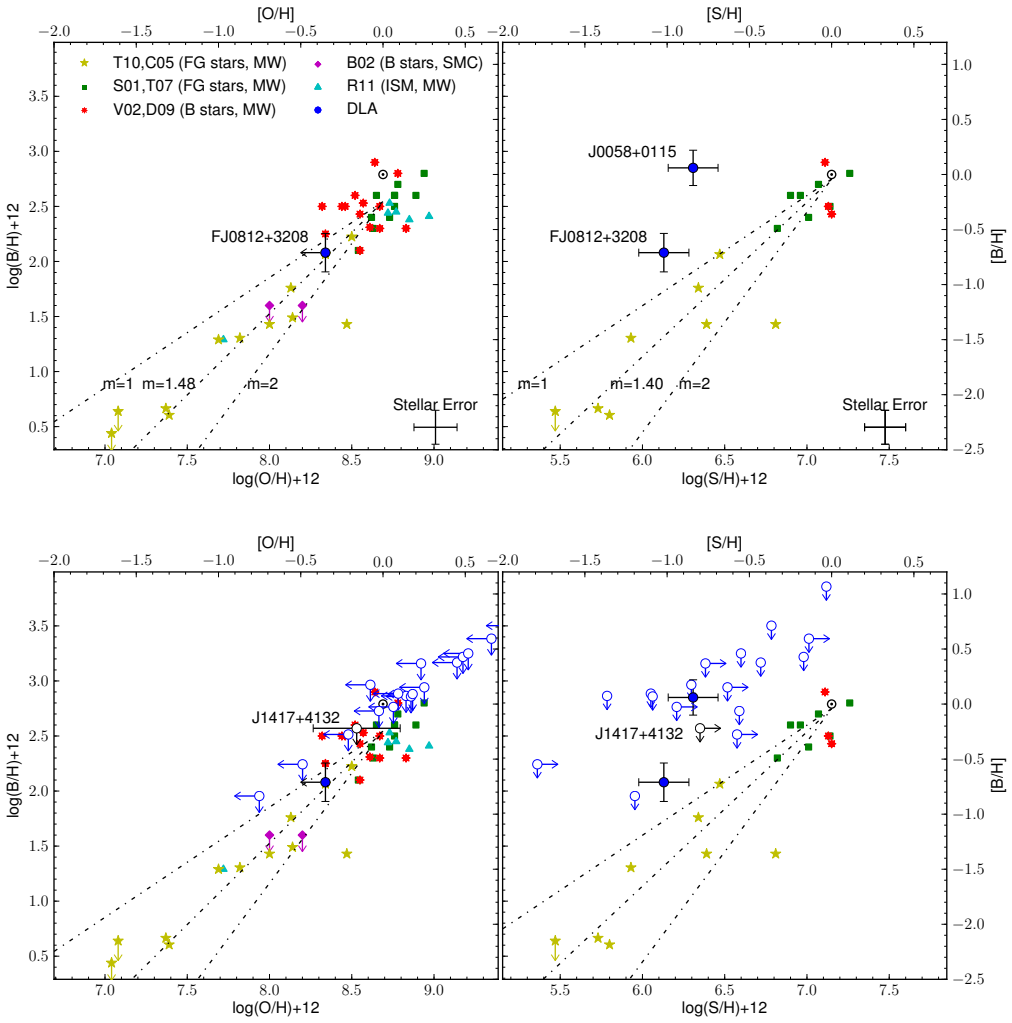

Figure 4.14 B/H is plotted as a function of O/H (left panels) and S/H (right panels). The stellar boron data are from Smith et al. (2001) (S01), Tan et al. (2010) (T10), Venn et al. (2002) (V02), Brooks et al. (2002) (B02). The sulphur abundances for the Galactic data were adopted from Caffau et al. (2005) (C05), Takeda (2007) (T07), and Daflon et al. (2009) (D09). Open circles are used for any boron upper limits in DLAs, whereas the filled circles represent possible detections. The top set of panels only show the data of the two identified DLAs (J0058+0112 and FJ0812+3208), whereas the bottom panels include all upper limits as well. Typical errors in the stellar data are shown in the bottom right of the top panels. The solar (Asplund et al., 2009) scale is included along the top and right axes in both panels. The best fit equations are: $[B/H] = (1.48 \pm 0.059)[O/H] - (0.26 \pm 0.110)$ (left); $[B/H] = (1.40 \pm 0.117)[S/H] - (0.04 \pm 0.121)$ (right). As the Asplund et al. (2009) values are included in the fit, the lines are not forced to pass through the origin.

$$[B/H] = (1.48 \pm 0.059)[O/H] - (0.26 \pm 0.110) \tag{4.3}$$

and

$$[B/H] = (1.40 \pm 0.117)[S/H] - (0.04 \pm 0.121). \tag{4.4}$$

These best fit lines only include all detections in the Milky Way from Smith et al. (2001) and Tan et al. (2010), as well as the solar value (Asplund et al., 2009)[6]. Included in the fit are B stars that appeared not to be affected by rotational mixing[7] and ISM sight-lines that contained warm gas (Ritchey et al., 2011)[8]. Both primary and secondary lines are forced to go through the origin of the best fit. The B-O relation agrees with the best fit equations presented in Smith et al. (2001) and Ritchey et al. (2011) (which have $m = 1.39 \pm 0.08$, 1.5 ± 0.1; respectively).

For the first time, high redshift data points are placed on the boron abundance plot. The traditional presentation of oxygen and boron abundances is shown in the left panels of Figure 4.14. Note that, for convenience, axes are labeled for both B/H and [B/H] (similarly for oxygen). Only the potential detections are plotted in the top panels of Figure 4.14, whereas all data (including the limits) are shown in the bottom panels. The DLA boron upper limits are above the primary ($m = 1$) line and therefore do not provide useful constraints on boron production in the DLAs. Moreover, there are no further measurements of O/H, so the DLA points are limits in both quantities. Note that these limits cluster parallel to the $m = 1$ line because the BII λ 1362 and OI λ1355 lines are so close in wavelength that their S/N are essentially identical. In combination with the same assumed FWHM of the strongest feature (see Section 4.3) and similar $f \cdot (\frac{X}{H})_\odot$, Equation 4.2 implies nearly equal abundance limits of boron and oxygen for each system.

Relative to oxygen, FJ0812+3208 is still consistent with the primary line. However, the oxygen abundance in FJ0812+3208 is conservatively reported as an upper limit.

[6]As the solar point is included, the primary, secondary, and best-fit lines are not forced through the solar value.

[7]Based on stars with log(N/H)< -4.2; log(B/H)> -10.0 from (Venn et al., 2002). Note that there still may be boron depletion (Mendel et al., 2006) as boron depletion occurs before nitrogen enrichment.

[8]The Ritchey et al. (2011) sample contains a compilation of 56 sight-lines. Only the 6 lowest density sight-lines from the sample were chosen for the literature dataset as they are relatively unaffected by dust depletion.

Turning now to the B-S abundances which are shown in the right panels of Figure 4.14. In addition to circumventing the problem of uncertain stellar O/H abundances, it can be seen that sulphur has the added advantage of being measurable in many of the DLAs. Nonetheless, the boron non-detections all lie above the primary line, so the production of boron is *not constrained*. However, both J0058+0115 and FJ0812+3208, which have robust detections in both B and S are above the primary line, with the inclusion of the continuum errors mentioned in Section 4.3.2.

The data presented here reveal the *possibility* of super-primary boron abundances in two DLAs (indeed, the only two where boron is tentatively detected) at high z. Although these two DLAs are unlikely to be representative of the DLA population, their high N(HI) and relatively high metallicities are unusual but make them ideal for a conceptual study of boron. The following points discuss the possible corrections that are required to the determined abundances, and the impact on the interpretation of the data.

- *Dust depletion.* Sulphur and oxygen are not expected to have appreciable depletion on to dust, but boron is mildly refractory (Howk et al., 2000). Dust depletion would raise the boron abundance above the gas phase value measured, pushing the DLA data points upwards, and hence even further above the primary line. Hence, dust can not explain the possible super-primary boron abundances in the two DLAs.

- *Ionization effects.* Ionization has little effect on the oxygen and sulphur abundances. Corrections for ionization have been modeled extensively for DLAs in both hard and soft ionizing radiation fields (e.g. Vladilo et al., 2001; Rix et al., 2007). Due to charge exchange reactions, the ionization correction for oxygen is negligible. Although photoionization by a stellar radiation field could lead to an under-estimate of the [S/H] from SII, and push the DLA data points closer to the $m = 1$ line, at the hydrogen column density of FJ0812+3208 the correction is less than 0.05 dex (Vladilo et al., 2001). Although boron has not been included in previous ionization models, the high N(HI) in FJ0812+3208 (logN(HI)=21.35) means that it is unlikely that a ~ 0.5 dex correction is required, ruling out ionization effects as the reason for high boron abundances in these two DLAs.

- *Blending/contamination.* It cannot be ruled out that the main features identified as boron absorption are in fact due to contaminating Lyα forest (or other

species) lines (e.g. J0058+0115). The presence of other weak features within the velocity window over which the integrated optical depth has been calculated are also considered. For example, the absorption profiles for FJ0812+3208 in Figure 4.10 do show signs of other absorption features within the velocity window for both oxygen and boron.

- *Misplaced continuum.* For very weak lines, the continuum placement can be critical. Each spectrum has been visually inspected to see if the continuum fit seems reasonable and manual adjustments made if necessary. Overall, the continuum appears to be well-defined. Section 4.3.2 demonstrates that continuum placements can account for a difference in the boron column density by as much as ~ 0.18 dex in the most extreme case (FJ0812+3208). These continuum offsets can add up to 0.07 dex to the total error budget, thus having a minimal effect to the overall observations.

After excluding corrections due to dust, ionization, continuum errors and additional components as possible causes for potential super-primary boron abundances, the possible physical mechanisms for high boron abundances are now considered. One intriguing possibility is an enhanced CRF that would result in a higher spallation rate of CNO targets to produce the excess boron. Assuming that the CRF scales linearly with the boron abundance; J0058+0115 and FJ0812+3208 would have a CRF of $\sim 8\times$ and $\sim 2\times$ (respectively) the expected flux for primary production of boron in the Milky Way. A high CRF could be associated with a line of sight that intersects gas near a supernova remnant, star forming region, or young cluster (for a list of observed sight-lines see Ritchey et al., 2011). Such sight-lines through enhanced star forming environments might explain the high N(HI) and high metallicity of the two DLAs with boron detections in the sample. Prochaska et al. (2003d) also note the rare detection of the excited SiII* in FJ0812+3208 (see Figure 4.9), a species that can be used in conjunction with CII* to constrain the gas temperature (Howk et al., 2005)[9]. Remarkably, J1417+4132 also has a detection of SiII*. To date, SiII* has only been seen in one other DLA (Kulkarni et al., 2012).

As discussed in Section 4.1, carbon is also a potential spallation target. Typically it is disregarded during cosmic ray spallation as it is less abundant than oxygen. For example, in the Milky Way, there are typically 6 oxygen nuclei for every carbon, logN(C)/N(O)~ -0.8 (Akerman et al., 2004; Fabbian et al., 2009), for $-2.5 \leq$[O/H]$\leq$

[9]This calculation is beyond the scope of this thesis. Interested readers can see Wolfe et al. (2003).

-0.5. This is not true at [O/H]~ -3 and [O/H]~ 0, where [C/O] becomes solar (logN(C)/N(O)~ -0.3; 2 oxygen nuclei for every carbon). For the detections in Figure 4.14, carbon spallation is expected to contribute to boron production slightly. Assuming that there is one carbon atom for every two oxygen as an upper limit, a shift of ~ 0.18 dex to the right is expected in Figure 4.14 to account for the extra spallation target (as there are $1.5\times$ as many targets). However, this is an overestimate as there are probably more than two oxygen per carbon atom (as [O/H]< 0) so both detected points would still lie above the primary line. If a galaxy were enriched in carbon relative to oxygen, it is plausible that the boron production could exceed that expected from primary oxygen-only spallation. Due to the difficulty of measuring carbon in DLAs (C II λ1334 is generally saturated whereas C II λ2325 is too weak to be detected), it is difficult to test whether the DLAs are indeed carbon rich. However studies of carbon in DLAs (Pettini et al., 2008; Penprase et al., 2010; Cooke et al., 2011b) follow a similar pattern in the [C/O] to the Milky Way at low metallicities.

The results presented in this study demonstrate the possibility of boron detection in DLAs, but also clearly illustrate its challenges. In most of the sight-lines of this study, despite the selection of DLAs with strong metal lines, the upper limits are not deep enough to constrain boron production. In order to assess future prospects for more boron detections, Figure 4.15 shows the required S/N per pixel at the BII λ1362 line as a function of the sulphur abundance based on Equations 4.1 and 4.2 for three different hydrogen column densities, assuming the corresponding FHWM for a b-value[10] of 10 km s^{-1}. Figure 4.15 suggests that for a DLA with a reasonably high log N(HI)=21 and high metallicity ([S/H]> -0.6), boron that has been synthesized via a primary process could be detected in a spectrum with S/N~ 50, which remains moderately demanding on current 8–10 metre class telescopes. Assuming that the exposure time varies as the square of the S/N, the sample of DLAs with upper limits of boron would need exposure times of at least an order of magnitude greater than those listed in Table 4.1. The detection of high redshift boron would be a excellent science case for the next generation of large optical telescopes with blue optimized echelle spectrographs, such as the High-Resolution Optical Spectrometer for the Thirty Meter Telescope.

[10]The b-value is related to the FWHM by $FWHM = 2\sqrt{ln2}b$

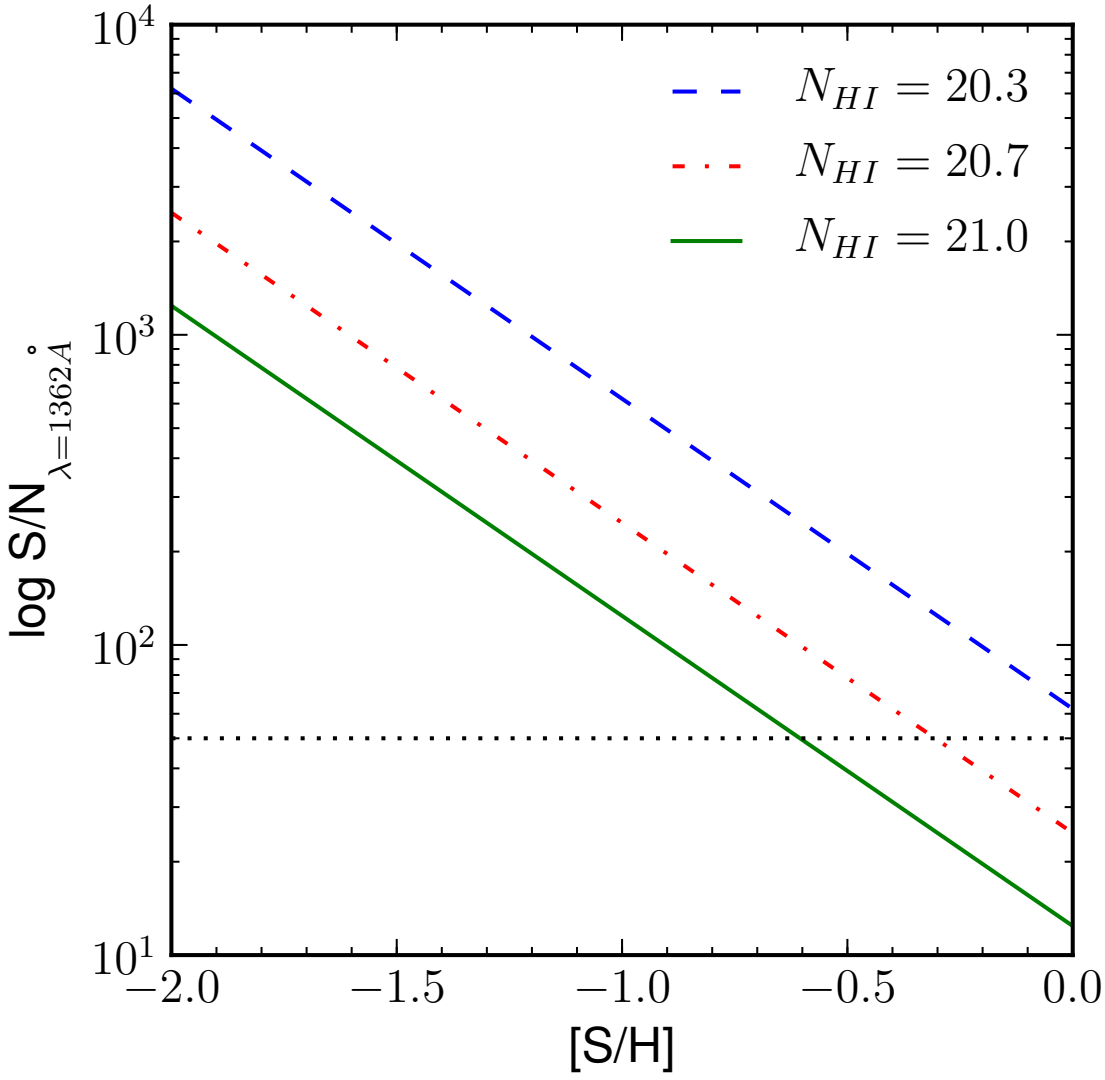

Figure 4.15 The S/N (per pixel) required to observe primary boron is plotted from Equations 4.2 and 4.1 for the range in sulphur values for a fixed redshift of $z_{abs} = 2$. A FWHM corresponding to a $b = 10$ km s^{-1} is assumed as it represents the minimum detectable line width by HIRES. The black dotted line at S/N of 50 is drawn to represent an achievable S/N.

4.5 Conclusion

This case study presented 2 detections of boron at $> 3\sigma$, 21 upper limits, and one further DLA in which the absorption is suggestive of a boron detection, but formally only significant at 2.97 sigma. The results hint at an excess of boron relative to predictions from primary production in the two cases where there are positive detections; albeit they are still consistent with the primary production mechanism. Although they are presented, it is unclear whether detections are truly real. Potential super-primary boron abundances due to dust or ionization effects are ruled out, and the possible physical reasons for the overabundance were discussed. Higher boron abundances might be due to higher CRFs in these two DLAs, relative to the Galactic value. This study also has shown that sulphur can be used in place of oxygen for studies of boron. This is useful as oxygen abundances are often unreliable and difficult to obtain in Milky Way stars, the ISM, and DLAs. Figure 4.15 demonstrates that for high S/N of ~ 50, DLAs with high metallicites ([S/H]> -0.6 dex) and high HI columns (logN(HI)~ 21) are needed to test whether DLAs do in fact exhibit higher boron abundances relative to primary production.

Chapter 5

Conclusions

5.1 Conclusions

DLAs have proven to be useful tools for studying the chemical evolution of galaxies, as compared to the chemistry of the Milky Way. Chapter 2 has demonstrated that DLAs in general are metal-poor, probing metallicities sampled by the 'metal-poor' dSphs and the halo stars. However, using the Thesis Sample of metal-rich absorbers has demonstrated that comparisons can be made to the 'metal-rich' components of the Milky Way (i.e. the thin and thick disk). Therefore, most metallicity regimes of the Milky Way are now be probed by DLAs.

The elemental abundance comparison completed in Chapter 3 has been the first comparison to Galactic populations since the late 1990s and early 2000s (Lu et al., 1996a; Pettini et al., 1997, 1999; Prochaska & Wolfe, 2002). With the increase in the number of observations in both stars and DLAs, it has been demonstrated that such comparisons can provide significant constraints on chemical evolution. Although the addition of the DLA abundances of some elements (e.g. silicon and sulphur) has not impacted the current understanding of the nucleosynthetic patterns seen in DLAs (and stars), there has been some significant advances for understanding other elements. These include:

- *Phosphorous and Manganese* – The Thesis Sample has added another 7 detections of phosphorous in DLAs to the existing 13 detections throughout the DLA literature. As Section 3.1.6 presents the first systematic study of phosphorous in DLAs, the constant value of [P/Zn] with increasing metallicity suggests that phosphorous has no metallicity-dependent yields. However, whether there is

an odd-even effect present in DLAs is unclear, as there appears to be a slight increase in [P/Si] with increasing metallicity. With the additional constraint of a constant [Mn/Fe-peak] with increasing metallicity, it would suggest that no clear odd-even effect is seen in DLAs. The lack of an odd-even effect suggests that there has been a high density of metals to provide neutrons to form the odd-Z elements in all DLAs, therefore most DLAs have undergone multiple generations of star formation.

- *Chromium and Zinc* – Although the effects of dust depletion of chromium was previously studied (e.g. Pettini et al., 1994; Akerman et al., 2005), it was left unclear from Prochaska & Wolfe (2002) whether chromium, zinc, and iron have a similar nucleosynthetic origin. With the addition of data to the HR literature sample, the plot of [Cr/Fe] vs. [Zn/Cr] shows no anti-correlation that is expected from a nucleosynthetic difference between the three elements (Figure 3.21). However, at low metallicities in DLAs ([Zn/H]$\lesssim -2$), [Zn/Fe] begins to significantly deviate from the solar value, suggesting such a nucleosynthetic difference of zinc and iron. However, as DLAs are generally much more metal rich than [Zn/H]~ -2, zinc can be used as a tracer for the iron-peak elements in DLAs.

Lastly, the Thesis Sample of DLAs has proven to be an effective means of measuring rarely detected elements such as boron (Chapter 4) and phosphorus (Section 3.1.6). With their large column densities of metals, two (or three) DLAs have shown to have significant boron absorption present in the spectra. The detection of boron in these DLAs (and all the upper limits provided by non-detections) support the idea that DLAs may have higher cosmic ray fluxes relative to the Milky Way. Furthermore, this work has demonstrated that sulphur can be used in place of oxygen in studies of boron, avoiding any difficulties that arise from using oxygen abundances in stars.

5.2 Future Work

Chapter 3 has demonstrated that there are still difficulties in comparing the nucleosynthetic trends in DLAs with stars. The large scatter in [α/Fe] in low metallicity DLAs (e.g. Figures 3.15 and 3.11) has effectively shown that it is unclear if there are

any [α/Fe] enhancements resulting from only SNe II contributions. The paucity of sulphur abundances in both stars (halo and dSphs) and low metallicity ([Zn/H]$\lesssim -1.25$) DLAs obscures whether any [α/Fe] enhancement exists in DLAs. By obtaining more sulphur abundances for dSph stars and metal-poor DLAs, the [α/Fe] enhancement can be probed. Furthermore, if more oxygen abundances could be obtained in DLAs at low metallicities (as the OI 1302Å line is likely not saturated), [α/Fe] could also be probed using undepleted oxygen.

Observing more MSDLAs and high metallicity systems will provide a wealth of data for understanding the nucleosynthesis of many elements. The addition of high metallicity observations of phosphorous and manganese can further test whether DLAs do not show an odd-even effect; and sulphur and silicon to understand how depleted silicon is at high metallicities and understand how much the subsolar [Si/Zn] seen in Figure 3.15 can be accounted for by dust.

Furthermore, other rarely detected (or never detected) elements can be studied with observations of MSDLAs. As highlighted in Chapter 4, more observations are required to check that boron is enhanced in all DLAs. Summarizing the end of Section 4.4, the best opportunities for measuring boron in DLAs with modest signal-noise spectra would be in DLAs with [S/H]> -0.5. With the additional HIRES data obtained of the Herbert-Fort et al. (2006) candidate MSDLAs, a larger search for boron can be completed.

Although not presented in this Thesis, other rare elements have been observed in the Thesis DLA sample. Some work has been done on copper, where some copper has been detected in the Thesis Sample. As another odd-Z element, it will be interesting to see if it shows metallicity dependent yields in DLAs, or whether it follows a similar trend to [P/Si] and [Mn/Fe] which suggest no odd-even effects in DLAs. Other rarely detected elements like cobalt (to understand the origin of cobalt; e.g. Ellison et al., 2001b), argon (to study ionization sources within and nearby DLAs; e.g. Vladilo et al., 2003), or fluorine (to test the contribution of the ν-process in boron production; e.g. Renda et al., 2004, in stars) may also be detected in the Thesis Sample or other MSDLA candidates.

Lastly, it would be interesting to find a tracer for the heavy, neutron-capture elements (e.g. barium, lead) associated with the *s-process* in asymptotic giant branch (AGB) stars. By having such a tracer of AGB stars, the contributions of the different masses of stars could be better understood within any DLA. In addition, the inclusion of non-LTE effects within the abundances of the entire stellar literature sample would

make the comparison between stellar and DLA yields easier (especially for chromium).

Bibliography

Abdo, A. A. et al. 2010, Astronomy and Astrophysics, 523, A46

Adelman-McCarthy, J. K. et al. 2008, Astrophysical Journal, Supplement Series, 175, 297

Akerman, C. J., Carigi, L., Nissen, P. E., Pettini, M., & Asplund, M. 2004, Astronomy and Astrophysics, 414, 931

Akerman, C. J., Ellison, S. L., Pettini, M., & Steidel, C. C. 2005, Astronomy and Astrophysics, 440, 499

Arnett, W. D. 1971, Astrophysical Journal, 166, 153

Asplund, M., Grevesse, N., Sauval, A. J., & Scott, P. 2009, Annual Review of Astronomy and Astrophysics, 47, 481

Battisti, A. J. et al. 2012, Astrophysical Journal, 744, 93

Bensby, T., Feltzing, S., Lundström, I., & Ilyin, I. 2005, Astronomy and Astrophysics, 433, 185

Berg, T. A. M., Ellison, S. L., Venn, K. A., & Prochaska, J. X. 2013, Monthly Notices of the RAS, 434, 2892

Bergemann, M. & Cescutti, G. 2010, Astronomy and Astrophysics, 522, A9

Bergeron, J. & Boissé, P. 1991, Astronomy and Astrophysics, 243, 344

Boesgaard, A. M., Deliyannis, C. P., King, J. R., Ryan, S. G., Vogt, S. S., & Beers, T. C. 1999a, Astronomical Journal, 117, 1549

Boesgaard, A. M., King, J. R., Deliyannis, C. P., & Vogt, S. S. 1999b, Astronomical Journal, 117, 492

Boesgaard, A. M., Rich, J. A., Levesque, E. M., & Bowler, B. P. 2011, Astrophysical Journal, 743, 140

Boisse, P., Le Brun, V., Bergeron, J., & Deharveng, J.-M. 1998, Astronomy and Astrophysics, 333, 841

Bonifacio, P. et al. 2009, Astronomy and Astrophysics, 501, 519

Bowen, D. V., Jenkins, E. B., Pettini, M., & Tripp, T. M. 2005, Astrophysical Journal, 635, 880

Brooks, A. M., Venn, K. A., Lambert, D. L., Lemke, M., Cunha, K., & Smith, V. V. 2002, Astrophysical Journal, 573, 584

Burbidge, E. M., Burbidge, G. R., Fowler, W. A., & Hoyle, F. 1957, Reviews of Modern Physics, 29, 547

Caffau, E., Bonifacio, P., Faraggiana, R., François, P., Gratton, R. G., & Barbieri, M. 2005, Astronomy and Astrophysics, 441, 533

Caffau, E., Bonifacio, P., Faraggiana, R., & Steffen, M. 2011, Astronomy and Astrophysics, 532, A98

Carretta, E. et al. 2010, Astronomy and Astrophysics, 520, A95

Carretta, E., Gratton, R. G., & Sneden, C. 2000, Astronomy and Astrophysics, 356, 238

Carroll, B. W. & Ostlie, D. A. 2006, An introduction to modern astrophysics and cosmology

Carswell, R. F., Becker, G. D., Jorgenson, R. A., Murphy, M. T., & Wolfe, A. M. 2012, Monthly Notices of the RAS, 422, 1700

Carswell, R. F., Webb, J. K., Baldwin, J. A., & Atwood, B. 1987, Astrophysical Journal, 319, 709

Cayrel, R. et al. 2004, Astronomy and Astrophysics, 416, 1117

Centurión, M., Bonifacio, P., Molaro, P., & Vladilo, G. 2000, Astrophysical Journal, 536, 540

Centurión, M., Molaro, P., Vladilo, G., Péroux, C., Levshakov, S. A., & D'Odorico, V. 2003, Astronomy and Astrophysics, 403, 55

Cescutti, G., Matteucci, F., Caffau, E., & François, P. 2012, Astronomy and Astrophysics, 540, A33

Chen, H.-W., Kennicutt, Jr., R. C., & Rauch, M. 2005, Astrophysical Journal, 620, 703

Chen, H.-W. & Lanzetta, K. M. 2003, Astrophysical Journal, 597, 706

Chen, Y. Q., Nissen, P. E., & Zhao, G. 2004, Astronomy and Astrophysics, 425, 697

Churchill, C. W., Mellon, R. R., Charlton, J. C., Jannuzi, B. T., Kirhakos, S., Steidel, C. C., & Schneider, D. P. 2000, Astrophysical Journal, 543, 577

Clayton, D. 2003, Handbook of Isotopes in the Cosmos, ed. Clayton, D.

Condon, E. U. & Shortley, G. H. 1935, The Theory of Atomic Spectra

Cooke, R., Pettini, M., & Murphy, M. T. 2012, Monthly Notices of the RAS, 425, 347

Cooke, R., Pettini, M., Steidel, C. C., King, L. J., Rudie, G. C., & Rakic, O. 2010, Monthly Notices of the RAS, 409, 679

Cooke, R., Pettini, M., Steidel, C. C., Rudie, G. C., & Jorgenson, R. A. 2011a, Monthly Notices of the RAS, 412, 1047

Cooke, R., Pettini, M., Steidel, C. C., Rudie, G. C., & Nissen, P. E. 2011b, Monthly Notices of the RAS, 417, 1534

Cunha, K., Lambert, D. L., Lemke, M., Gies, D. R., & Roberts, L. C. 1997, Astrophysical Journal, 478, 211

Cunha, K., Smith, V. V., Boesgaard, A. M., & Lambert, D. L. 2000, Astrophysical Journal, 530, 939

Daflon, S., Cunha, K., de la Reza, R., Holtzman, J., & Chiappini, C. 2009, Astronomical Journal, 138, 1577

de la Varga, A., Reimers, D., Tytler, D., Barlow, T., & Burles, S. 2000, Astronomy and Astrophysics, 363, 69

Dekker, H., D'Odorico, S., Kaufer, A., Delabre, B., & Kotzlowski, H. 2000, in Society of Photo-Optical Instrumentation Engineers (SPIE) Conference Series, Vol. 4008, Optical and IR Telescope Instrumentation and Detectors, ed. M. Iye & A. F. Moorwood, 534–545

Dessauges-Zavadsky, M., Calura, F., Prochaska, J. X., D'Odorico, S., & Matteucci, F. 2004, Astronomy and Astrophysics, 416, 79

— 2007, Astronomy and Astrophysics, 470, 431

Dessauges-Zavadsky, M., D'Odorico, S., McMahon, R. G., Molaro, P., Ledoux, C., Péroux, C., & Storrie-Lombardi, L. J. 2001, Astronomy and Astrophysics, 370, 426

Dessauges-Zavadsky, M., Ellison, S. L., & Murphy, M. T. 2009, Monthly Notices of the RAS, 396, L61

Dessauges-Zavadsky, M., Péroux, C., Kim, T.-S., D'Odorico, S., & McMahon, R. G. 2003, Monthly Notices of the RAS, 345, 447

Dessauges-Zavadsky, M., Prochaska, J. X., & D'Odorico, S. 2002, Astronomy and Astrophysics, 391, 801

Dessauges-Zavadsky, M., Prochaska, J. X., D'Odorico, S., Calura, F., & Matteucci, F. 2006, Astronomy and Astrophysics, 445, 93

D'Odorico, V. 2007, Astronomy and Astrophysics, 470, 523

D'Odorico, V. & Molaro, P. 2004, Astronomy and Astrophysics, 415, 879

Duncan, D. K., Lambert, D. L., & Lemke, M. 1992, Astrophysical Journal, 401, 584

Duncan, D. K., Primas, F., Rebull, L. M., Boesgaard, A. M., Deliyannis, C. P., Hobbs, L. M., King, J. R., & Ryan, S. G. 1997, Astrophysical Journal, 488, 338

Edvardsson, B., Andersen, J., Gustafsson, B., Lambert, D. L., Nissen, P. E., & Tomkin, J. 1993, Astronomy and Astrophysics, Supplement Series, 102, 603

Eggen, O. J., Lynden-Bell, D., & Sandage, A. R. 1962, Astrophysical Journal, 136, 748

Ellison, S. L., Hennawi, J. F., Martin, C. L., & Sommer-Larsen, J. 2007, Monthly Notices of the RAS, 378, 801

Ellison, S. L., Kanekar, N., Prochaska, J. X., Momjian, E., & Worseck, G. 2012, Monthly Notices of the RAS, 424, 293

Ellison, S. L. & Lopez, S. 2001, Astronomy and Astrophysics, 380, 117

Ellison, S. L., Pettini, M., Steidel, C. C., & Shapley, A. E. 2001a, Astrophysical Journal, 549, 770

Ellison, S. L., Prochaska, J. X., Hennawi, J., Lopez, S., Usher, C., Wolfe, A. M., Russell, D. M., & Benn, C. R. 2010, Monthly Notices of the RAS, 406, 1435

Ellison, S. L., Ryan, S. G., & Prochaska, J. X. 2001b, Monthly Notices of the RAS, 326, 628

Ellison, S. L., Yan, L., Hook, I. M., Pettini, M., Wall, J. V., & Shaver, P. 2001c, Astronomy and Astrophysics, 379, 393

Ellison, S. L., York, B. A., Pettini, M., & Kanekar, N. 2008, Monthly Notices of the RAS, 388, 1349

Erni, P., Richter, P., Ledoux, C., & Petitjean, P. 2006, Astronomy and Astrophysics, 451, 19

Fabbian, D., Nissen, P. E., Asplund, M., Pettini, M., & Akerman, C. 2009, Astronomy and Astrophysics, 500, 1143

Federman, S. R., Sheffer, Y., Lambert, D. L., & Gilliland, R. L. 1993, Astrophysical Journal, Letters to the Editor, 413, L51

Feltzing, S., Fohlman, M., & Bensby, T. 2007, Astronomy and Astrophysics, 467, 665

Fields, B. D., Olive, K. A., Vangioni-Flam, E., & Cassé, M. 2000, Astrophysical Journal, 540, 930

Francois, P. 1987, Astronomy and Astrophysics, 176, 294

— 1988, Astronomy and Astrophysics, 195, 226

Frebel, A. 2010, Astronomische Nachrichten, 331, 474

Freeman, K. & Bland-Hawthorn, J. 2002, Annual Review of Astronomy and Astrophysics, 40, 487

Fulbright, J. P. & Kraft, R. P. 1999, Astronomical Journal, 118, 527

Fulbright, J. P., McWilliam, A., & Rich, R. M. 2006, Astrophysical Journal, 636, 821

Fynbo, J. P. U. et al. 2013, Monthly Notices of the RAS, 436, 361

— 2011, Monthly Notices of the RAS, 413, 2481

Garcia Lopez, R. J., Lambert, D. L., Edvardsson, B., Gustafsson, B., Kiselman, D., & Rebolo, R. 1998, Astrophysical Journal, 500, 241

García Pérez, A. E. et al. 2013, Astrophysical Journal, Letters to the Editor, 767, L9

Ge, J., Bechtold, J., & Kulkarni, V. P. 2001, Astrophysical Journal, Letters to the Editor, 547, L1

Geisler, D., Smith, V. V., Wallerstein, G., Gonzalez, G., & Charbonnel, C. 2005, Astronomical Journal, 129, 1428

Gilmore, G. & Reid, N. 1983, Monthly Notices of the RAS, 202, 1025

Gratton, R. G., Carretta, E., Claudi, R., Lucatello, S., & Barbieri, M. 2003, Astronomy and Astrophysics, 404, 187

Guimarães, R., Noterdaeme, P., Petitjean, P., Ledoux, C., Srianand, R., López, S., & Rahmani, H. 2012, Astronomical Journal, 143, 147

Gustafsson, B., Bell, R. A., Eriksson, K., & Nordlund, A. 1975, Astronomy and Astrophysics, 42, 407

Gustafsson, B., Edvardsson, B., Eriksson, K., Jørgensen, U. G., Nordlund, Å., & Plez, B. 2008, Astronomy and Astrophysics, 486, 951

Gustafsson, B., Edvardsson, B., Eriksson, K., Mizuno-Wiedner, M., Jørgensen, U. G., & Plez, B. 2003, in Astronomical Society of the Pacific Conference Series, Vol. 288, Stellar Atmosphere Modeling, ed. I. Hubeny, D. Mihalas, & K. Werner, 331

Haehnelt, M. G., Steinmetz, M., & Rauch, M. 1998, Astrophysical Journal, 495, 647

Handrich, E., Steudel, A., & Walther, H. 1969, Physics Letters A, 29, 486

Hartwick, F. D. A. 1976, Astrophysical Journal, 209, 418

Hayashi, C. 1950, Progress of Theoretical Physics, 5, 224

Heger, A. & Woosley, S. E. 2002, Astrophysical Journal, 567, 532

— 2010, Astrophysical Journal, 724, 341

Heiter, U. & Eriksson, K. 2006, Astronomy and Astrophysics, 452, 1039

Henry, R. B. C. & Prochaska, J. X. 2007, Publications of the ASP, 119, 962

Herbert-Fort, S., Prochaska, J. X., Dessauges-Zavadsky, M., Ellison, S. L., Howk, J. C., Wolfe, A. M., & Prochter, G. E. 2006, Publications of the ASP, 118, 1077

Howk, J. C., Sembach, K. R., & Savage, B. D. 2000, Astrophysical Journal, 543, 278

Howk, J. C., Wolfe, A. M., & Prochaska, J. X. 2005, Astrophysical Journal, Letters to the Editor, 622, L81

Israelian, G. & Rebolo, R. 2001, Astrophysical Journal, Letters to the Editor, 557, L43

Israelian, G., Rebolo, R., García López, R. J., Bonifacio, P., Molaro, P., Basri, G., & Shchukina, N. 2001, Astrophysical Journal, 551, 833

Jorgenson, R. A., Wolfe, A. M., Prochaska, J. X., & Carswell, R. F. 2009, Astrophysical Journal, 704, 247

Jorgenson, R. A., Wolfe, A. M., Prochaska, J. X., Lu, L., Howk, J. C., Cooke, J., Gawiser, E., & Gelino, D. M. 2006, Astrophysical Journal, 646, 730

Jura, M., Meyer, D. M., Hawkins, I., & Cardelli, J. A. 1996, Astrophysical Journal, 456, 598

Kanekar, N. et al. 2014, Monthly Notices of the RAS

Kanekar, N., Smette, A., Briggs, F. H., & Chengalur, J. N. 2009, Astrophysical Journal, Letters to the Editor, 705, L40

Kaplan, K. F., Prochaska, J. X., Herbert-Fort, S., Ellison, S. L., & Dessauges-Zavadsky, M. 2010, Publications of the ASP, 122, 619

Kashikawa, N., Misawa, T., Minowa, Y., Okoshi, K., Hattori, T., Toshikawa, J., Ishikawa, S., & Onoue, M. 2014, Astrophysical Journal, 780, 116

Kippenhahn, R. & Weigert, A. 1994, Stellar Structure and Evolution

Korn, A. J., Becker, S. R., Gummersbach, C. A., & Wolf, B. 2000, Astronomy and Astrophysics, 353, 655

Kraft, R. P., Sneden, C., Langer, G. E., & Prosser, C. F. 1992, Astronomical Journal, 104, 645

Krogager, J.-K. et al. 2013, Monthly Notices of the RAS

Kulkarni, V. P., Fall, S. M., Lauroesch, J. T., York, D. G., Welty, D. E., Khare, P., & Truran, J. W. 2005, Astrophysical Journal, 618, 68

Kulkarni, V. P., Meiring, J., Som, D., Péroux, C., York, D. G., Khare, P., & Lauroesch, J. T. 2012, Astrophysical Journal, 749, 176

Kurucz, R. L. 1993, CD-ROM 13, Smithsonian Astrophysical

— 1998, `http://kurucz.harvard.edu/`

Lai, D. K., Bolte, M., Johnson, J. A., Lucatello, S., Heger, A., & Woosley, S. E. 2008, Astrophysical Journal, 681, 1524

Lanzetta, K. M. & Bowen, D. 1990, Astrophysical Journal, 357, 321

Lanzetta, K. M., Wolfe, A. M., & Turnshek, D. A. 1995, Astrophysical Journal, 440, 435

Lanzetta, K. M., Wolfe, A. M., Turnshek, D. A., Lu, L., McMahon, R. G., & Hazard, C. 1991, Astrophysical Journal, Supplement Series, 77, 1

Larson, R. B. 1972, Nature Physical Science, 236, 7

Ledoux, C., Bergeron, J., & Petitjean, P. 2002a, Astronomy and Astrophysics, 385, 802

Ledoux, C., Petitjean, P., Bergeron, J., Wampler, E. J., & Srianand, R. 1998, Astronomy and Astrophysics, 337, 51

Ledoux, C., Petitjean, P., Fynbo, J. P. U., Møller, P., & Srianand, R. 2006a, Astronomy and Astrophysics, 457, 71

Ledoux, C., Petitjean, P., & Srianand, R. 2003, Monthly Notices of the RAS, 346, 209

— 2006b, Astrophysical Journal, Letters to the Editor, 640, L25

Ledoux, C., Srianand, R., & Petitjean, P. 2002b, Astronomy and Astrophysics, 392, 781

Letarte, B. et al. 2010, Astronomy and Astrophysics, 523, A17

Levshakov, S. A., Dessauges-Zavadsky, M., D'Odorico, S., & Molaro, P. 2002, Astrophysical Journal, 565, 696

Lopez, S. & Ellison, S. L. 2003, Astronomy and Astrophysics, 403, 573

Lopez, S., Reimers, D., D'Odorico, S., & Prochaska, J. X. 2002, Astronomy and Astrophysics, 385, 778

Lopez, S., Reimers, D., Gregg, M. D., Wisotzki, L., Wucknitz, O., & Guzman, A. 2005a, Astrophysical Journal, 626, 767

— 2005b, Astrophysical Journal, 626, 767

Lopez, S., Reimers, D., Rauch, M., Sargent, W. L. W., & Smette, A. 1999, Astrophysical Journal, 513, 598

Lu, L., Sargent, W. L. W., Barlow, T. A., Churchill, C. W., & Vogt, S. S. 1996a, Astrophysical Journal, Supplement Series, 107, 475

Lu, L., Sargent, W. L. W., Womble, D. S., & Barlow, T. A. 1996b, Astrophysical Journal, Letters to the Editor, 457, L1

Mashonkina, L. 2013, ArXiv e-prints

Mashonkina, L., Gehren, T., Shi, J.-R., Korn, A. J., & Grupp, F. 2011, Astronomy and Astrophysics, 528, A87

McConnachie, A. W. 2012, Astronomical Journal, 144, 4

McWilliam, A. 1997, Annual Review of Astronomy and Astrophysics, 35, 503

McWilliam, A. & Rich, R. M. 1994, Astrophysical Journal, Supplement Series, 91, 749

Meiring, J. D. et al. 2006, Monthly Notices of the RAS, 370, 43

Meiring, J. D., Kulkarni, V. P., Lauroesch, J. T., Péroux, C., Khare, P., & York, D. G. 2009, Monthly Notices of the RAS, 393, 1513

Meiring, J. D., Lauroesch, J. T., Kulkarni, V. P., Péroux, C., Khare, P., York, D. G., & Crotts, A. P. S. 2007, Monthly Notices of the RAS, 376, 557

Meiring, J. D. et al. 2011, Astrophysical Journal, 732, 35

Mendel, J. T., Venn, K. A., Proffitt, C. R., Brooks, A. M., & Lambert, D. L. 2006, Astrophysical Journal, 640, 1039

Meneguzzi, M. & York, D. G. 1980, Astrophysical Journal, Letters to the Editor, 235, L111

Meyer, D. M., Lanzetta, K. M., & Wolfe, A. M. 1995, Astrophysical Journal, Letters to the Editor, 451, L13

Meyer, D. M. & Roth, K. C. 1990, Astrophysical Journal, 363, 57

Meyer, D. M., Welty, D. E., & York, D. G. 1989, Astrophysical Journal, Letters to the Editor, 343, L37

Meyer, D. M. & York, D. G. 1987, Astrophysical Journal, Letters to the Editor, 319, L45

— 1992, Astrophysical Journal, Letters to the Editor, 399, L121

Mo, H., van den Bosch, F. C., & White, S. 2010, Galaxy Formation and Evolution

Molaro, P., Bonifacio, P., Centurión, M., D'Odorico, S., Vladilo, G., Santin, P., & Di Marcantonio, P. 2000, Astrophysical Journal, 541, 54

Molaro, P., Levshakov, S. A., D'Odorico, S., Bonifacio, P., & Centurión, M. 2001, Astrophysical Journal, 549, 90

Morton, D. C. 2003, Astrophysical Journal, Supplement Series, 149, 205

Morton, D. C., Wright, A. E., Peterson, B. A., Jauncey, D. L., & Chen, J. 1980, Monthly Notices of the RAS, 193, 399

Nestor, D. B., Pettini, M., Hewett, P. C., Rao, S., & Wild, V. 2008, Monthly Notices of the RAS, 390, 1670

Nielsen, N. M., Churchill, C. W., Kacprzak, G. G., & Murphy, M. T. 2013, Astrophysical Journal, 776, 114

Nissen, P. E., Akerman, C., Asplund, M., Fabbian, D., Kerber, F., Kaufl, H. U., & Pettini, M. 2007, Astronomy and Astrophysics, 469, 319

Nissen, P. E., Chen, Y. Q., Asplund, M., & Pettini, M. 2004, Astronomy and Astrophysics, 415, 993

Nissen, P. E., Chen, Y. Q., Schuster, W. J., & Zhao, G. 2000, Astronomy and Astrophysics, 353, 722

Nissen, P. E., Primas, F., Asplund, M., & Lambert, D. L. 2002, Astronomy and Astrophysics, 390, 235

Nissen, P. E. & Schuster, W. J. 2010, Astronomy and Astrophysics, 511, L10

North, P. et al. 2012, Astronomy and Astrophysics, 541, A45

Noterdaeme, P. et al. 2012a, Astronomy and Astrophysics, 540, A63

Noterdaeme, P., Ledoux, C., Petitjean, P., Le Petit, F., Srianand, R., & Smette, A. 2007a, Astronomy and Astrophysics, 474, 393

Noterdaeme, P., Ledoux, C., Petitjean, P., & Srianand, R. 2008, Astronomy and Astrophysics, 481, 327

Noterdaeme, P., López, S., Dumont, V., Ledoux, C., Molaro, P., & Petitjean, P. 2012b, Astronomy and Astrophysics, 542, L33

Noterdaeme, P. et al. 2012c, Astronomy and Astrophysics, 547, L1

Noterdaeme, P., Petitjean, P., Ledoux, C., & Srianand, R. 2009, Astronomy and Astrophysics, 505, 1087

Noterdaeme, P., Petitjean, P., Srianand, R., Ledoux, C., & Le Petit, F. 2007b, Astronomy and Astrophysics, 469, 425

Outram, P. J., Chaffee, F. H., & Carswell, R. F. 1999, Monthly Notices of the RAS, 310, 289

Pagel, B. E. J. 2009, Nucleosynthesis and Chemical Evolution of Galaxies

Penprase, B. E., Prochaska, J. X., Sargent, W. L. W., Toro-Martinez, I., & Beeler, D. J. 2010, Astrophysical Journal, 721, 1

Péroux, C., Bouché, N., Kulkarni, V. P., York, D. G., & Vladilo, G. 2011, Monthly Notices of the RAS, 410, 2237

Péroux, C., Meiring, J. D., Kulkarni, V. P., Ferlet, R., Khare, P., Lauroesch, J. T., Vladilo, G., & York, D. G. 2006, Monthly Notices of the RAS, 372, 369

Péroux, C., Meiring, J. D., Kulkarni, V. P., Khare, P., Lauroesch, J. T., Vladilo, G., & York, D. G. 2008, Monthly Notices of the RAS, 386, 2209

Péroux, C., Petitjean, P., Aracil, B., & Srianand, R. 2002, New Astronomy, 7, 577

Péroux, C., Storrie-Lombardi, L. J., McMahon, R. G., Irwin, M., & Hook, I. M. 2001, Astronomical Journal, 121, 1799

Petitjean, P., Ledoux, C., & Srianand, R. 2008, Astronomy and Astrophysics, 480, 349

Petitjean, P., Srianand, R., & Ledoux, C. 2000, Astronomy and Astrophysics, 364, L26

— 2002, Monthly Notices of the RAS, 332, 383

Pettini, M., Boksenberg, A., & Hunstead, R. W. 1990, Astrophysical Journal, 348, 48

Pettini, M. & Cooke, R. 2012, Monthly Notices of the RAS, 425, 2477

Pettini, M., Ellison, S. L., Bergeron, J., & Petitjean, P. 2002, Astronomy and Astrophysics, 391, 21

Pettini, M., Ellison, S. L., Steidel, C. C., & Bowen, D. V. 1999, Astrophysical Journal, 510, 576

Pettini, M., Ellison, S. L., Steidel, C. C., Shapley, A. E., & Bowen, D. V. 2000, Astrophysical Journal, 532, 65

Pettini, M., Lipman, K., & Hunstead, R. W. 1995, Astrophysical Journal, 451, 100

Pettini, M., Smith, L. J., Hunstead, R. W., & King, D. L. 1994, Astrophysical Journal, 426, 79

Pettini, M., Smith, L. J., King, D. L., & Hunstead, R. W. 1997, Astrophysical Journal, 486, 665

Pettini, M., Zych, B. J., Steidel, C. C., & Chaffee, F. H. 2008, Monthly Notices of the RAS, 385, 2011

Pignatari, M. et al. 2013, ArXiv e-prints

Pompéia, L. et al. 2008, Astronomy and Astrophysics, 480, 379

Prantzos, N. 2012, Astronomy and Astrophysics, 542, A67

Preston, G. W., Sneden, C., Thompson, I. B., Shectman, S. A., & Burley, G. S. 2006, Astronomical Journal, 132, 85

Prochaska, J. X., Castro, S., & Djorgovski, S. G. 2003a, Astrophysical Journal, Supplement Series, 148, 317

Prochaska, J. X., Gawiser, E., & Wolfe, A. M. 2001a, Astrophysical Journal, 552, 99

Prochaska, J. X., Gawiser, E., Wolfe, A. M., Castro, S., & Djorgovski, S. G. 2003b, Astrophysical Journal, Letters to the Editor, 595, L9

Prochaska, J. X., Gawiser, E., Wolfe, A. M., Cooke, J., & Gelino, D. 2003c, Astrophysical Journal, Supplement Series, 147, 227

Prochaska, J. X., Henry, R. B. C., O'Meara, J. M., Tytler, D., Wolfe, A. M., Kirkman, D., Lubin, D., & Suzuki, N. 2002, Publications of the ASP, 114, 933

Prochaska, J. X. & Herbert-Fort, S. 2004, Publications of the ASP, 116, 622

Prochaska, J. X., Herbert-Fort, S., & Wolfe, A. M. 2005, Astrophysical Journal, 635, 123

Prochaska, J. X., Howk, J. C., & Wolfe, A. M. 2003d, Nature, 423, 57

Prochaska, J. X. & McWilliam, A. 2000, Astrophysical Journal, Letters to the Editor, 537, L57

Prochaska, J. X., Naumov, S. O., Carney, B. W., McWilliam, A., & Wolfe, A. M. 2000, Astronomical Journal, 120, 2513

Prochaska, J. X. & Wolfe, A. M. 1996, Astrophysical Journal, 470, 403

— 1997a, Astrophysical Journal, 474, 140

— 1997b, Astrophysical Journal, 474, 140

— 1997c, Astrophysical Journal, 487, 73

— 1999, Astrophysical Journal, Supplement Series, 121, 369

— 2000, Astrophysical Journal, Letters to the Editor, 533, L5

— 2002, Astrophysical Journal, 566, 68

— 2009, Astrophysical Journal, 696, 1543

Prochaska, J. X., Wolfe, A. M., Howk, J. C., Gawiser, E., Burles, S. M., & Cooke, J. 2007, Astrophysical Journal, Supplement Series, 171, 29

Prochaska, J. X. et al. 2001b, Astrophysical Journal, Supplement Series, 137, 21

Rafelski, M., Neeleman, M., Fumagalli, M., Wolfe, A. M., & Prochaska, J. X. 2013, ArXiv e-prints

Rafelski, M., Wolfe, A. M., Prochaska, J. X., Neeleman, M., & Mendez, A. J. 2012, Astrophysical Journal, 755, 89

Ramírez, I., Meléndez, J., & Chanamé, J. 2012, Astrophysical Journal, 757, 164

Rao, S. M., Belfort-Mihalyi, M., Turnshek, D. A., Monier, E. M., Nestor, D. B., & Quider, A. 2011, Monthly Notices of the RAS, 416, 1215

Rao, S. M., Prochaska, J. X., Howk, J. C., & Wolfe, A. M. 2005, Astronomical Journal, 129, 9

Rao, S. M. & Turnshek, D. A. 2000, Astrophysical Journal, Supplement Series, 130, 1

Reddy, B. E., Lambert, D. L., & Allende Prieto, C. 2006, Monthly Notices of the RAS, 367, 1329

Reddy, B. E., Tomkin, J., Lambert, D. L., & Allende Prieto, C. 2003, VizieR Online Data Catalog, 734, 304

Reeves, H., Fowler, W. A., & Hoyle, F. 1970, Nature, 226, 727

Renda, A. et al. 2004, Monthly Notices of the RAS, 354, 575

Rich, J. A. & Boesgaard, A. M. 2009, Astrophysical Journal, 701, 1519

Ritchey, A. M., Federman, S. R., Sheffer, Y., & Lambert, D. L. 2011, Astrophysical Journal, 728, 70

Rix, S. A., Pettini, M., Steidel, C. C., Reddy, N. A., Adelberger, K. L., Erb, D. K., & Shapley, A. E. 2007, Astrophysical Journal, 670, 15

Roth, K. C. & Blades, J. C. 1995, Astrophysical Journal, Letters to the Editor, 445, L95

Sadler, E. M., Rich, R. M., & Terndrup, D. M. 1996, Astronomical Journal, 112, 171

Salmon, S., Montalbán, J., Morel, T., Miglio, A., Dupret, M.-A., & Noels, A. 2012, Monthly Notices of the RAS, 422, 3460

Samland, M., Hensler, G., & Theis, C. 1997, Astrophysical Journal, 476, 544

Sargent, W. L. W., Steidel, C. C., & Boksenberg, A. 1988, Astrophysical Journal, 334, 22

— 1989, Astrophysical Journal, Supplement Series, 69, 703

Savage, B. D. & Sembach, K. R. 1991, Astrophysical Journal, 379, 245

— 1996, Annual Review of Astronomy and Astrophysics, 34, 279

Savaglio, S., D'Odorico, S., & Moller, P. 1994, Astronomy and Astrophysics, 281, 331

Sbordone, L., Bonifacio, P., Buonanno, R., Marconi, G., Monaco, L., & Zaggia, S. 2007, Astronomy and Astrophysics, 465, 815

Schmidt, M. 1963, Astrophysical Journal, 137, 758

Searle, L. & Zinn, R. 1978, Astrophysical Journal, 225, 357

Seitenzahl, I. R. et al. 2013, Monthly Notices of the RAS, 429, 1156

Sembach, K. R., Steidel, C. C., Macke, R. J., & Meyer, D. M. 1995, Astrophysical Journal, Letters to the Editor, 445, L27

Sheinis, A. I., Bolte, M., Epps, H. W., Kibrick, R. I., Miller, J. S., Radovan, M. V., Bigelow, B. C., & Sutin, B. M. 2002, Publications of the ASP, 114, 851

Shetrone, M., Venn, K. A., Tolstoy, E., Primas, F., Hill, V., & Kaufer, A. 2003, Astronomical Journal, 125, 684

Shi, J. R., Gehren, T., Mashonkina, L., & Zhao, G. 2009, Astronomy and Astrophysics, 503, 533

Shi, J. R., Takada-Hidai, M., Takeda, Y., Tan, K. F., Hu, S. M., Zhao, G., & Cao, C. 2012, Astrophysical Journal, 755, 36

Smiljanic, R., Pasquini, L., Bonifacio, P., Galli, D., Gratton, R. G., Randich, S., & Wolff, B. 2009, Astronomy and Astrophysics, 499, 103

Smith, V. V., Cunha, K., & King, J. R. 2001, Astronomical Journal, 122, 370

Sneden, C. 1973, Astrophysical Journal, 184, 839

Sneden, C. & Crocker, D. A. 1988, Astrophysical Journal, 335, 406

Sneden, C., Gratton, R. G., & Crocker, D. A. 1991, Astronomy and Astrophysics, 246, 354

Songaila, A. & Cowie, L. L. 2002, Astronomical Journal, 123, 2183

Spite, M. et al. 2011, Astronomy and Astrophysics, 528, A9

— 2005, Astronomy and Astrophysics, 430, 655

Sreekumar, P. et al. 1993, Physical Review Letters, 70, 127

Srianand, R., Gupta, N., Petitjean, P., Noterdaeme, P., Ledoux, C., Salter, C. J., & Saikia, D. J. 2012, Monthly Notices of the RAS, 421, 651

Srianand, R., Petitjean, P., & Ledoux, C. 2000, Nature, 408, 931

Srianand, R., Petitjean, P., Ledoux, C., Ferland, G., & Shaw, G. 2005, Monthly Notices of the RAS, 362, 549

Steidel, C. C., Dickinson, M., Meyer, D. M., Adelberger, K. L., & Sembach, K. R. 1997, Astrophysical Journal, 480, 568

Storrie-Lombardi, L. J. & Wolfe, A. M. 2000, Astrophysical Journal, 543, 552

Takada-Hidai, M. et al. 2002, Astrophysical Journal, 573, 614

Takeda, Y. 2007, Publications of the ASJ, 59, 335

Takeda, Y., Hashimoto, O., Taguchi, H., Yoshioka, K., Takada-Hidai, M., Saito, Y., & Honda, S. 2005, Publications of the ASJ, 57, 751

Tan, K., Shi, J., & Zhao, G. 2010, Astrophysical Journal, 713, 458

Terndrup, D. M., Sadler, E. M., & Rich, R. M. 1995, Astronomical Journal, 110, 1774

Thielemann, F.-K. et al. 2003, in From Twilight to Highlight: The Physics of Supernovae, ed. W. Hillebrandt & B. Leibundgut, 331

Timmes, F. X., Woosley, S. E., & Weaver, T. A. 1995, Astrophysical Journal, Supplement Series, 98, 617

Tinsley, B. M. 1979, Astrophysical Journal, 229, 1046

Tolstoy, E., Hill, V., & Tosi, M. 2009, Annual Review of Astronomy and Astrophysics, 47, 371

Travaglio, C., Hillebrandt, W., Reinecke, M., & Thielemann, F.-K. 2004, Astronomy and Astrophysics, 425, 1029

Turnshek, D. A., Rao, S. M., Nestor, D. B., Vanden Berk, D., Belfort-Mihalyi, M., & Monier, E. M. 2004, Astrophysical Journal, Letters to the Editor, 609, L53

van den Bergh, S. 1962, Astronomical Journal, 67, 486

Venn, K. A., Brooks, A. M., Lambert, D. L., Lemke, M., Langer, N., Lennon, D. J., & Keenan, F. P. 2002, Astrophysical Journal, 565, 571

Venn, K. A., Irwin, M., Shetrone, M. D., Tout, C. A., Hill, V., & Tolstoy, E. 2004, Astronomical Journal, 128, 1177

Venn, K. A. et al. 2012, Astrophysical Journal, 751, 102

Vernet, J. et al. 2011, Astronomy and Astrophysics, 536, A105

Vladilo, G. 2002a, Astrophysical Journal, 569, 295

— 2002b, Astronomy and Astrophysics, 391, 407

Vladilo, G., Abate, C., Yin, J., Cescutti, G., & Matteucci, F. 2011, Astronomy and Astrophysics, 530, A33

Vladilo, G., Centurión, M., Bonifacio, P., & Howk, J. C. 2001, Astrophysical Journal, 557, 1007

Vladilo, G., Centurión, M., D'Odorico, V., & Péroux, C. 2003, Astronomy and Astrophysics, 402, 487

Vogt, S. S. et al. 1994, in Society of Photo-Optical Instrumentation Engineers (SPIE) Conference Series, Vol. 2198, Instrumentation in Astronomy VIII, ed. D. L. Crawford & E. R. Craine, 362

Willis, J. 2011, Lecture 4: Big Bang Nucleosynthesis, University Lecture

Wolfe, A. M., Fan, X.-M., Tytler, D., Vogt, S. S., Keane, M. J., & Lanzetta, K. M. 1994, Astrophysical Journal, Letters to the Editor, 435, L101

Wolfe, A. M., Gawiser, E., & Prochaska, J. X. 2005, Annual Review of Astronomy and Astrophysics, 43, 861

Wolfe, A. M., Lanzetta, K. M., Foltz, C. B., & Chaffee, F. H. 1995, Astrophysical Journal, 454, 698

Wolfe, A. M., Prochaska, J. X., & Gawiser, E. 2003, Astrophysical Journal, 593, 215

Wolfe, A. M., Turnshek, D. A., Smith, H. E., & Cohen, R. D. 1986, Astrophysical Journal, Supplement Series, 61, 249

Woosley, S. E., Hartmann, D. H., Hoffman, R. D., & Haxton, W. C. 1990, Astrophysical Journal, 356, 272

Woosley, S. E. & Weaver, T. A. 1995, Astrophysical Journal, Supplement Series, 101, 181

Wyse, R. F. G. & Gilmore, G. 1992, Astronomical Journal, 104, 144

— 1995, Astronomical Journal, 110, 2771

Zafar, T. et al. 2011, Astronomy and Astrophysics, 532, A51

Zhang, L., Karlsson, T., Christlieb, N., Korn, A. J., Barklem, P. S., & Zhao, G. 2011, Astronomy and Astrophysics, 528, A92

Zoccali, M. et al. 2003, Astronomy and Astrophysics, 399, 931

Appendix A

Additional Information

A.1 DLA Literature Catalogue

Table A.1: DLA literature catalogue

QSO	z_{em}	z_{abs}	logN(HI)	logN(FeII)	logN(ZnII)	logN(SiII)	logN(MnII)	logN(CrII)	logN(NiII)	logN(SII)	logN(OI)	Reference
J0140−0839	3.716	3.696	20.75 ± 0.15	< 12.73	...	< 13.33	...	< 12.39	...	< 13.33	14.69 ± 0.01	80
B2314−409	2.448	1.857	20.90 ± 0.10	15.08 ± 0.10	12.52 ± 0.10	15.41 ± 0.10	...	13.38 ± 0.08	13.84 ± 0.08	15.10 ± 0.15	...	26
Q1759+75	3.050	2.625	20.76 ± 0.05	15.08 ± 0.02	> 11.65	15.53 ± 0.02	...	13.21 ± 0.06	13.80 ± 0.01	15.24 ± 0.01	> 16.26	13,23,65
TXS0311+430	2.870	2.289	20.30 ± 0.00	14.85 ± 0.20	< 12.50	...	12.50 ± 0.20	< 13.05	...	...	...	82
J1440+0637	3.386	2.518	21.00 ± 0.15	14.50 ± 0.00	...	14.20 ± 0.00	...	...	...	...	...	86
J0844+5153	3.200	2.775	21.45 ± 0.15	15.29 ± 0.06	...	15.97 ± 0.02	13.18 ± 0.10	13.80 ± 0.04	14.19 ± 0.04	...	...	55
Q0450−13	2.250	2.067	20.53 ± 0.08	14.29 ± 0.02	< 11.60	14.68 ± 0.04	...	12.50 ± 0.09	13.49 ± 0.13	14.29 ± 0.06	> 15.86	54
Q0948+433	1.892	1.233	21.62 ± 0.06	15.56 ± 0.01	13.15 ± 0.01	> 16.15	13.30 ± 0.01	13.90 ± 0.01	...	...	...	53
J0816+1446	3.840	3.288	22.00 ± 0.10	15.89 ± 0.00	13.53 ± 0.00	> 16.31	...	14.07 ± 0.00	14.54 ± 0.00	...	...	88
J1249−0233	2.120	1.781	21.45 ± 0.15	15.47 ± 0.02	13.10 ± 0.04	15.80 ± 0.03	13.19 ± 0.02	13.91 ± 0.02	14.23 ± 0.03	15.50 ± 0.16	< 18.20	55,84,85
TXS0229+230	3.420	2.620	20.30 ± 0.11	...	...	...	...	...	...	...	...	82
Q1224+0037	1.482	1.235	20.88 ± 0.05	> 15.11	< 11.89	15.10 ± 0.07	< 12.14	13.12 ± 0.09	...	...	...	67
PSS1802+5616	4.180	3.762	20.55 ± 0.15	...	...	> 14.37	...	...	< 13.33	...	...	44
Q1232+082	2.570	2.338	20.90 ± 0.10	14.68 ± 0.08	12.71 ± 0.11	15.24 ± 0.11	...	...	...	14.83 ± 0.10	...	19,25,40
J1101+0531	4.990	4.345	21.30 ± 0.10	15.19 ± 0.14	...	15.74 ± 0.06	...	...	13.95 ± 0.11	...	...	101
J1552+4910	2.040	1.960	...	15.41 ± 0.02	12.96 ± 0.02	15.98 ± 0.01	13.41 ± 0.04	13.76 ± 0.02	14.24 ± 0.01	15.34 ± 0.00	...	84,85
J1435+5359	2.636	2.343	21.05 ± 0.10	...	...	15.13 ± 0.02	...	...	...	14.78 ± 0.05	...	65
J2241+1225	2.630	2.418	21.15 ± 0.15	14.89 ± 0.10	...	...	13.39 ± 0.09	...	13.79 ± 0.06	14.94 ± 0.04	...	84,85
Q0551−366	2.318	1.962	20.50 ± 0.08	15.05 ± 0.05	13.02 ± 0.05	15.62 ± 0.06	13.11 ± 0.05	13.27 ± 0.06	14.08 ± 0.06	15.38 ± 0.11	...	32
AO0235+164	0.940	0.524	21.70 ± 0.10	15.30 ± 0.40	...	...	...	...	...	...	...	83
CTQ418	2.910	2.429	20.68 ± 0.07	13.91 ± 0.05	...	14.32 ± 0.03	...	...	...	13.97 ± 0.03	...	65
Q0951−04	4.370	4.203	20.40 ± 0.10	< 13.28	...	13.34 ± 0.03	...	...	< 12.59	...	> 14.60	13,23
PSS1535+2943	3.990	3.761	20.40 ± 0.15	...	...	13.94 ± 0.05	...	...	< 13.45	...	> 14.71	44
HS0741+4741	3.220	3.017	20.48 ± 0.10	14.05 ± 0.01	...	14.35 ± 0.01	...	...	12.76 ± 0.05	14.00 ± 0.02	...	23,35
Q0300−3152	2.370	2.179	20.80 ± 0.10	14.21 ± 0.02	...	...	...	...	...	14.20 ± 0.03	...	70
Q1127−145	1.184	0.313	21.70 ± 0.08	> 15.16	13.53 ± 0.13	...	13.26 ± 0.03	...	...	...	...	99
3C336	0.927	0.656	20.36 ± 0.10	14.59 ± 0.11	...	...	< 12.42	...	...	...	...	6,15,31
J1541+3153	2.550	2.443	20.95 ± 0.10	14.50 ± 0.11	12.03 ± 0.11	14.97 ± 0.04	...	12.61 ± 0.14	13.10 ± 0.08	...	> 14.92	101
Q1425+6039	3.170	2.827	20.30 ± 0.04	14.48 ± 0.01	12.18 ± 0.04	> 15.02	...	< 12.61	13.27 ± 0.03	...	> 16.04	3,24,35,64
Q1008+36	3.119	2.799	20.70 ± 0.05	< 15.11	...	14.46 ± 0.02	...	...	...	...	...	65
Q0151+0448	1.923	1.934	20.36 ± 0.10	13.70 ± 0.01	< 11.81	14.01 ± 0.05	...	< 12.45	...	< 13.47	> 14.84	80,98

Continued on next page

Table A.1 – continued from previous page

QSO	z_{em}	z_{abs}	logN(HI)	logN(FeII)	logN(ZnII)	logN(SiII)	logN(MnII)	logN(CrII)	logN(NiII)	logN(SII)	logN(OI)	Reference
Q0425−5214	2.250	2.224	20.30 ± 0.10	13.96 ± 0.03	...	...	...	...	...	14.07 ± 0.03	...	70
Q2344+12	2.760	2.538	20.36 ± 0.10	14.03 ± 0.03	...	14.18 ± 0.01	...	...	< 12.81	< 14.20	> 15.03	23,35
SBS1543+393	0.867	0.009	20.42 ± 0.04	...	...	> 15.10	...	...	< 13.83	15.19 ± 0.04	> 16.20	52
Q0027−1836	2.480	2.402	21.75 ± 0.10	14.97 ± 0.02	12.79 ± 0.02	15.67 ± 0.03	12.84 ± 0.03	13.37 ± 0.01	13.70 ± 0.02	15.23 ± 0.02	...	62,70
J0058+0115	2.490	2.010	21.10 ± 0.15	15.19 ± 0.02	...	< 15.54	...	13.53 ± 0.02	14.09 ± 0.01	15.41 ± 0.01	...	84,85
B0105008	1.374	1.371	21.70 ± 0.15	15.59 ± 0.03	12.93 ± 0.04	> 15.85	13.29 ± 0.04	13.92 ± 0.03	14.25 ± 0.04	...	...	93
FJ2334−0908	3.330	3.057	20.48 ± 0.05	14.39 ± 0.03	12.13 ± 0.02	14.82 ± 0.03	...	...	< 13.13	13.93 ± 0.03	16.19 ± 0.06	43,51,56,69
Q1225+0035	1.226	0.773	21.38 ± 0.11	15.69 ± 0.03	< 13.01	...	...	13.99 ± 0.11	...	...	...	60,78
J1048+3911	2.774	2.296	20.70 ± 0.10	13.70 ± 0.00	...	13.90 ± 0.00	...	...	...	...	> 14.46	86
Q1727+5302	1.444	1.031	21.41 ± 0.15	14.81 ± 0.01	12.76 ± 0.24	15.51 ± 0.01	13.05 ± 0.02	13.33 ± 0.11	...	...	...	48,78
J0127−00	4.060	3.727	21.15 ± 0.10	...	...	> 14.31	...	...	< 13.69	...	> 15.18	43
J1219+1603	3.148	3.003	20.35 ± 0.10	13.80 ± 0.10	...	13.88 ± 0.15	...	...	...	...	14.52 ± 0.34	86
Q1137+3907	1.023	0.720	21.10 ± 0.10	15.45 ± 0.05	13.43 ± 0.05	...	...	13.71 ± 0.20	...	...	...	60
J2321+1421	2.554	2.573	20.70 ± 0.05	14.18 ± 0.03	< 11.84	14.45 ± 0.04	...	< 12.57	...	< 13.60	> 15.10	80
J0928+0939	3.655	2.910	20.75 ± 0.15	14.10 ± 0.00	...	> 14.13	...	...	...	...	> 14.66	86
Q0102−190	3.037	2.370	21.00 ± 0.08	14.44 ± 0.02	...	...	...	...	...	14.30 ± 0.02	...	51,59,70
PKS1229−021	1.045	0.395	20.75 ± 0.07	< 14.95	12.92 ± 0.10	...	13.48 ± 0.10	...	13.70 ± 0.10	...	...	9
B1055−301	2.523	1.903	21.54 ± 0.10	...	12.91 ± 0.03	...	...	13.61 ± 0.02	...	...	...	50
J1340+1106	2.914	2.796	21.00 ± 0.06	14.32 ± 0.01	...	14.68 ± 0.02	...	12.62 ± 0.11	13.08 ± 0.03	14.30 ± 0.02	16.04 ± 0.04	75
Q1209+093	3.300	2.584	21.40 ± 0.10	15.36 ± 0.02	13.06 ± 0.02	15.91 ± 0.01	13.16 ± 0.05	13.61 ± 0.05	14.11 ± 0.02	...	...	43,59,64,70
Q1323−0021	1.388	0.716	20.54 ± 0.15	...	13.29 ± 0.21	...	...	13.70 ± 0.18	...	...	...	78
Q0010−002	2.145	2.025	20.95 ± 0.10	15.18 ± 0.03	12.19 ± 0.05	15.31 ± 0.04	...	...	...	14.96 ± 0.04	...	51,59,70
Q1715+4606	0.989	0.651	20.44 ± 0.10	14.94 ± 0.03	< 12.87	...	...	< 13.54	...	...	...	60
B0913+003	3.074	2.743	20.74 ± 0.10	14.60 ± 0.00	< 12.82	14.78 ± 0.00	...	< 13.46	...	...	...	50
Q1223+1753	2.940	2.466	21.50 ± 0.10	15.16 ± 0.02	12.55 ± 0.03	15.47 ± 0.01	...	13.49 ± 0.01	13.95 ± 0.01	15.14 ± 0.03	> 15.48	18,23,35,51
J1555+4800	3.300	2.391	21.50 ± 0.15	15.73 ± 0.02	< 13.93	> 16.52	...	14.17 ± 0.01	14.75 ± 0.01	> 15.88	...	84,85
J1325+1255	4.140	3.551	20.50 ± 0.15	< 13.69	...	13.50 ± 0.00	...	...	...	...	> 14.80	86
Q0454+039	1.343	0.859	20.69 ± 0.06	...	12.33 ± 0.08	15.45 ± 0.08	12.91 ± 0.06	13.49 ± 0.06	...	...	...	14
Q0449−1645	2.679	1.007	20.98 ± 0.07	15.09 ± 0.01	12.62 ± 0.07	15.86 ± 0.04	12.91 ± 0.03	13.47 ± 0.02	...	...	...	72
PSS1253−0228	4.010	2.783	21.85 ± 0.20	15.36 ± 0.04	12.77 ± 0.07	> 15.60	13.42 ± 0.07	13.63 ± 0.03	14.17 ± 0.04	...	> 15.35	43
J1042+3107	4.690	4.087	20.75 ± 0.10	14.22 ± 0.03	...	14.31 ± 0.01	...	...	< 13.26	...	...	101
B1230−101	2.394	1.931	20.48 ± 0.10	...	12.94 ± 0.05	...	...	13.67 ± 0.04	...	...	...	50
J1431+3952	1.215	0.602	21.20 ± 0.10	15.15 ± 0.11	13.03 ± 0.19	...	13.07 ± 0.14	13.53 ± 0.18	...	...	...	93

Continued on next page

Table A.1 – continued from previous page

QSO	z_{em}	z_{abs}	logN(HI)	logN(FeII)	logN(ZnII)	logN(SiII)	logN(MnII)	logN(CrII)	logN(NiII)	logN(SII)	logN(OI)	Reference
Q2343+12	2.510	2.431	20.34 ± 0.10	14.66 ± 0.03	12.24 ± 0.03	15.29 ± 0.04	12.27 ± 0.04	12.80 ± 0.03	...	...	...	24,30,46
J2059−0529	2.540	2.210	20.80 ± 0.20	15.00 ± 0.11	12.94 ± 0.11	15.36 ± 0.10	< 12.90	13.55 ± 0.12	13.88 ± 0.11	...	...	55
PSSJ2155+1358	4.260	3.316	20.50 ± 0.15	14.51 ± 0.13	12.05 ± 0.32	14.81 ± 0.20	...	< 12.60	< 12.90	...	...	27,43
Q2359−02	2.800	2.154	20.35 ± 0.10	13.86 ± 0.04	< 11.90	14.29 ± 0.04	...	< 12.95	< 13.21	14.17 ± 0.11	...	13,23,24,56
Q1354+258	2.006	1.420	21.54 ± 0.06	15.01 ± 0.04	12.59 ± 0.08	15.36 ± 0.08	12.75 ± 0.06	13.42 ± 0.06	13.11 ± 0.08	...	...	11
HE1104−1805	2.310	1.662	20.85 ± 0.01	14.77 ± 0.02	12.48 ± 0.01	15.38 ± 0.02	12.77 ± 0.14	13.07 ± 0.01	13.42 ± 0.03	...	16.80 ± 0.20	12
J2222−0946	2.927	2.354	20.50 ± 0.15	14.95 ± 0.02	< 12.78	15.56 ± 0.12	12.96 ± 0.05	...	14.13 ± 0.19	...	< 17.99	55,84,85,99
J1135−0010	2.890	2.207	22.05 ± 0.10	15.76 ± 0.03	13.62 ± 0.03	16.49 ± 0.03	13.62 ± 0.01	14.14 ± 0.01	14.67 ± 0.02	> 16.19	...	89,90
J0255+00	3.970	3.915	21.30 ± 0.05	14.75 ± 0.09	...	> 14.19	...	...	13.27 ± 0.04	14.72 ± 0.01	> 15.17	23
PSS1715+3809	4.520	3.341	21.05 ± 0.12	13.74 ± 0.04	< 12.11	< 14.49	...	< 12.77	< 13.29	...	...	44
Q1210+17	2.540	1.892	20.63 ± 0.08	15.01 ± 0.03	12.40 ± 0.05	15.33 ± 0.03	12.72 ± 0.01	13.28 ± 0.03	13.67 ± 0.06	14.96 ± 0.02	...	23,54,66
J0035−0918	2.419	2.340	20.55 ± 0.10	12.98 ± 0.07	...	13.41 ± 0.04	...	...	...	< 13.08	14.96 ± 0.00	76
Q2230+025	2.150	1.864	20.83 ± 0.05	15.24 ± 0.03	12.72 ± 0.05	15.70 ± 0.03	13.03 ± 0.03	13.44 ± 0.04	14.09 ± 0.04	15.29 ± 0.06	< 18.52	13,23,24,54
–												66,84,85
Q0930+28	3.420	3.235	20.35 ± 0.10	13.49 ± 0.03	...	13.79 ± 0.02	...	...	...	...	> 14.20	35,43
J1031+4055	3.006	2.569	20.55 ± 0.10	13.80 ± 0.00	...	< 14.43	...	...	...	...	< 15.03	86
Q0528−2505	2.779	2.141	20.95 ± 0.05	14.85 ± 0.09	12.25 ± 0.03	15.22 ± 0.05	12.38 ± 0.10	13.10 ± 0.04	13.22 ± 0.06	14.83 ± 0.04	...	3,40
Q0405−443	3.020	2.622	20.47 ± 0.10	...	...	...	...	...	...	...	...	92,95
PSS0209+0517	4.170	3.864	20.55 ± 0.10	< 13.34	...	13.46 ± 0.03	...	...	< 13.12	...	> 14.37	43
Q1328+307	0.849	0.692	21.25 ± 0.10	14.98 ± 0.10	12.72 ± 0.10	...	< 12.59	13.30 ± 0.10	...	...	...	7,9,31
PSSJ1248+31	4.350	3.696	20.60 ± 0.10	...	...	...	...	...	...	...	...	101
Q2059−360	3.090	3.083	20.98 ± 0.08	14.52 ± 0.07	...	14.80 ± 0.05	...	...	...	14.41 ± 0.04	16.09 ± 0.04	18,51,69
JJ1558+4053	2.635	2.553	20.30 ± 0.04	13.07 ± 0.06	...	13.32 ± 0.02	...	...	...	...	14.54 ± 0.04	71
PSS1535+2943	3.990	3.202	20.65 ± 0.15	> 14.60	< 12.53	> 14.74	...	< 13.19	< 13.97	...	...	44
Q1451+123	3.250	2.469	20.39 ± 0.10	13.36 ± 0.07	...	14.00 ± 0.12	...	...	...	< 13.55	...	18,51
J0817+1351	4.390	4.258	21.30 ± 0.15	15.45 ± 0.06	...	> 14.93	...	...	14.35 ± 0.04	15.30 ± 0.02	> 15.41	101
JJ1009+0713	0.456	0.114	20.68 ± 0.10	15.29 ± 0.17	...	> 15.00	...	...	13.93 ± 0.18	15.25 ± 0.00	> 16.00	73
J2328+0022	1.308	0.652	20.32 ± 0.07	14.84 ± 0.01	12.43 ± 0.15	...	12.84 ± 0.02	13.35 ± 0.19	...	...	...	61
Q0952+179	1.476	0.238	21.32 ± 0.05	...	< 12.93	...	...	13.32 ± 0.15	...	...	...	81,99
Q1215+33	2.610	1.999	20.95 ± 0.07	14.75 ± 0.05	12.33 ± 0.05	15.03 ± 0.03	...	13.13 ± 0.03	13.59 ± 0.03	< 15.36	> 15.13	13,20,23,24
J1604+3951	3.154	3.163	21.75 ± 0.20	15.40 ± 0.15	13.00 ± 0.10	16.10 ± 0.01	...	...	14.30 ± 0.01	15.70 ± 0.02	< 17.66	80,84,85
PSS1443+2724	4.410	4.224	20.95 ± 0.10	15.33 ± 0.03	...	> 15.43	...	...	14.09 ± 0.02	15.52 ± 0.01	...	22,23,57
Q2222−3939	2.180	2.154	20.85 ± 0.10	14.42 ± 0.03	...	...	...	...	...	14.08 ± 0.02	...	70

Continued on next page

Table A.1 – continued from previous page

QSO	z_{em}	z_{abs}	logN(HI)	logN(FeII)	logN(ZnII)	logN(SiII)	logN(MnII)	logN(CrII)	logN(NiII)	logN(SII)	logN(OI)	Reference
J1155+3510	2.840	2.758	21.00 ± 0.10	< 14.73	...	15.14 ± 0.03	...	...	13.69 ± 0.04	14.77 ± 0.01	> 15.05	101
TXS1239+376	3.810	3.411	20.40 ± 0.05	...	...	...	...	...	...	...	...	82
Q0841+12	2.500	2.476	20.78 ± 0.08	14.50 ± 0.03	11.69 ± 0.10	14.99 ± 0.03	12.33 ± 0.15	12.89 ± 0.06	13.19 ± 0.09	14.48 ± 0.10	16.15 ± 0.10	13,18,23,24
–												40,54,66,69
Q2318−1107	2.960	1.989	20.68 ± 0.05	14.91 ± 0.01	12.50 ± 0.03	15.34 ± 0.01	...	13.13 ± 0.06	13.82 ± 0.03	15.09 ± 0.02	...	62,70
J1709+3417	3.309	2.530	20.45 ± 0.15	14.30 ± 0.00	...	14.50 ± 0.00	...	...	...	...	...	86
J1626+2751	5.190	4.311	21.34 ± 0.15	15.33 ± 0.06	...	> 16.09	...	...	14.00 ± 0.06	...	...	101
Q0100+13	2.690	2.309	21.37 ± 0.08	15.09 ± 0.01	12.47 ± 0.01	> 14.72	...	13.37 ± 0.01	13.87 ± 0.01	15.09 ± 0.06	...	13,30,46
J2100−0641	3.140	3.092	21.05 ± 0.15	15.36 ± 0.03	< 13.14	15.89 ± 0.02	...	13.53 ± 0.13	14.20 ± 0.02	15.64 ± 0.03	> 15.77	55,84,85
HS1132+2243	2.885	2.783	21.00 ± 0.07	14.02 ± 0.01	< 11.99	14.49 ± 0.12	< 12.46	12.83 ± 0.10	< 13.16	14.07 ± 0.06	> 14.99	43
J1200+4618	4.730	4.476	20.50 ± 0.15	14.27 ± 0.02	...	> 14.55	...	...	< 13.44	...	> 15.23	101
J1607+1604	4.800	4.474	20.30 ± 0.15	14.03 ± 0.06	...	14.10 ± 0.01	...	...	13.71 ± 0.10	...	> 14.85	101
J0834+2140	4.500	4.390	21.00 ± 0.20	14.76 ± 0.02	...	> 15.14	...	...	< 13.77	14.85 ± 0.04	> 15.73	101
FJ0747+2739	4.110	3.900	20.50 ± 0.10	< 13.80	< 12.40	14.03 ± 0.01	...	...	< 13.11	< 14.36	> 14.81	43
J1003+5520	3.068	2.502	20.35 ± 0.15	12.90 ± 0.00	...	13.80 ± 0.00	...	...	...	...	< 14.83	86
Q0335−1213	3.442	3.180	20.78 ± 0.10	13.70 ± 0.12	...	13.77 ± 0.10	...	...	...	...	...	50,70
J0853+2431	3.617	2.790	20.70 ± 0.20	...	...	...	...	...	...	...	...	95
J1419+0829	3.030	3.050	20.40 ± 0.03	13.54 ± 0.03	...	13.83 ± 0.01	...	...	...	...	15.17 ± 0.02	75,91
Q1409+095	2.838	2.456	20.53 ± 0.08	13.74 ± 0.02	...	14.03 ± 0.02	...	...	...	...	15.33 ± 0.02	39,69
Q1755+578	2.110	1.971	21.40 ± 0.15	15.81 ± 0.01	< 13.82	> 16.42	< 13.55	...	14.77 ± 0.01	> 15.97	...	84,85
J1241+4617	2.770	2.667	20.70 ± 0.10	14.02 ± 0.04	...	14.03 ± 0.01	...	...	...	14.01 ± 0.11	> 14.62	101
J1037+0139	3.059	2.705	20.50 ± 0.08	13.53 ± 0.02	...	13.97 ± 0.03	...	...	...	...	15.06 ± 0.04	75,86
J1353+5328	2.920	2.835	20.80 ± 0.10	> 14.46	...	14.81 ± 0.07	...	12.76 ± 0.13	13.36 ± 0.05	14.57 ± 0.02	> 15.06	101
J0759+3129	3.167	3.035	20.60 ± 0.10	13.80 ± 0.00	...	14.10 ± 0.00	...	...	...	...	> 14.56	86
J1242+3720	3.839	3.413	20.50 ± 0.30	...	...	...	...	...	...	...	...	95
BR1117−1329	3.960	3.350	20.84 ± 0.12	14.83 ± 0.03	12.26 ± 0.03	15.13 ± 0.05	...	13.15 ± 0.03	13.52 ± 0.03	...	...	36,51
PC0953+4749	4.460	3.404	21.15 ± 0.15	> 14.47	...	> 14.62	...	...	< 13.90	...	...	43
Q1501+0019	1.930	1.483	20.85 ± 0.13	...	12.93 ± 0.06	15.71 ± 0.02	...	13.40 ± 0.09	...	...	...	60
J0924+0951	3.430	3.338	20.85 ± 0.10	> 14.25	...	> 14.63	...	...	...	...	> 14.83	86
Q0405−443	3.020	2.595	21.09 ± 0.10	...	...	...	...	...	...	...	...	95
B1228−113	3.528	2.193	20.60 ± 0.10	...	13.01 ± 0.03	...	...	13.45 ± 0.03	...	...	...	50
J0834+2140	4.500	3.710	20.85 ± 0.10	14.44 ± 0.02	...	< 14.67	...	...	< 13.68	...	...	101
J1310+5424	1.930	1.801	21.45 ± 0.15	15.63 ± 0.02	13.57 ± 0.01	> 16.22	...	14.00 ± 0.03	14.47 ± 0.01	> 15.97	...	84,85

Continued on next page

Table A.1 – continued from previous page

QSO	z_{em}	z_{abs}	logN(HI)	logN(FeII)	logN(ZnII)	logN(SiII)	logN(MnII)	logN(CrII)	logN(NiII)	logN(SII)	logN(OI)	Reference
PC0953+4749	4.460	3.891	21.20 ± 0.10	15.09 ± 0.10	...	> 15.16	...	...	13.75 ± 0.06	...	...	37,43
Q0421−2624	2.280	2.157	20.65 ± 0.10	13.97 ± 0.01	...	14.35 ± 0.01	...	...	...	...	...	70
Q2359−02	2.800	2.095	20.70 ± 0.10	14.56 ± 0.02	12.55 ± 0.04	15.45 ± 0.05	...	12.75 ± 0.09	13.14 ± 0.05	15.02 ± 0.06	...	13,23,24,56
Q0405−443	3.020	2.595	21.09 ± 0.10	15.15 ± 0.02	12.68 ± 0.02	15.59 ± 0.03	12.87 ± 0.01	13.37 ± 0.04	13.86 ± 0.31	15.19 ± 0.05	...	41,51,95
J1051+3107	4.250	4.139	20.70 ± 0.20	13.95 ± 0.03	...	14.21 ± 0.02	...	...	...	13.86 ± 0.08	> 15.04	101
Q2348−1444	2.940	2.279	20.59 ± 0.08	13.84 ± 0.05	< 11.28	14.18 ± 0.06	11.66 ± 0.15	12.30 ± 0.09	< 12.30	13.75 ± 0.06	> 15.04	1,13,24,35
–												54,66
J1654+2227	4.680	4.002	20.60 ± 0.15	14.09 ± 0.03	...	< 14.54	...	...	< 13.11	...	...	101
FJ0812+32	2.701	2.626	21.35 ± 0.10	15.09 ± 0.01	13.15 ± 0.02	15.98 ± 0.05	< 13.00	13.36 ± 0.03	13.89 ± 0.01	15.63 ± 0.08	17.49 ± 0.09	43,64,84,85
Q1733+5533	1.074	0.998	20.70 ± 0.10	...	< 12.11	15.48 ± 0.06	...	< 12.79	...	...	...	60,78
Q0021+0104A	1.829	1.576	20.48 ± 0.15	14.61 ± 0.00	< 11.95	14.88 ± 0.03	< 11.90	< 12.58	...	...	...	74
Q1111−152	3.370	3.266	21.30 ± 0.05	14.81 ± 0.01	12.32 ± 0.10	...	...	...	...	...	...	59,70
Q2237−0608	4.560	4.080	20.52 ± 0.11	13.88 ± 0.12	...	14.21 ± 0.02	...	...	< 13.17	...	...	3,37,65
Q0918+1636	3.070	2.583	20.96 ± 0.05	15.43 ± 0.01	13.40 ± 0.01	16.01 ± 0.01	13.47 ± 0.01	13.72 ± 0.01	14.40 ± 0.01	15.82 ± 0.01	...	79
J1116+4118A	2.982	2.662	20.48 ± 0.10	14.36 ± 0.10	12.40 ± 0.20	15.05 ± 0.11	...	< 12.70	13.35 ± 0.20	...	...	68
Q2311−3721	2.476	2.182	20.55 ± 0.07	14.22 ± 0.03	< 11.82	14.54 ± 0.04	...	< 12.53	...	...	...	50,64
B0438−436	2.863	2.347	20.78 ± 0.10	14.93 ± 0.00	12.72 ± 0.02	...	...	13.08 ± 0.05	...	...	...	50
Q0458−0203	2.290	2.040	21.65 ± 0.09	15.51 ± 0.05	13.13 ± 0.02	> 15.89	...	13.80 ± 0.01	14.18 ± 0.02	...	< 18.49	13,23,24,84
–												85
Q0302−223	1.409	1.009	20.36 ± 0.11	14.67 ± 0.05	12.45 ± 0.06	15.18 ± 0.06	12.57 ± 0.06	13.08 ± 0.06	13.57 ± 0.06	...	...	14
Q0642−5038	3.090	2.659	20.95 ± 0.08	14.20 ± 0.03	11.67 ± 0.04	...	...	...	...	...	...	70
B2355106	1.639	1.173	21.00 ± 0.10	15.08 ± 0.10	12.76 ± 0.17	15.42 ± 0.13	12.91 ± 0.10	< 13.20	14.17 ± 0.12	...	...	93
BRI1013+0035	4.405	3.104	21.10 ± 0.10	15.18 ± 0.05	13.33 ± 0.02	15.78 ± 0.02	...	> 13.21	13.89 ± 0.05	...	...	64
J0927+1543	1.800	1.731	...	> 15.00	13.72 ± 0.03	15.98 ± 0.01	...	13.79 ± 0.03	14.16 ± 0.03	< 15.86	...	84,85
Q0049−2820	2.260	2.071	20.45 ± 0.10	14.50 ± 0.02	...	14.70 ± 0.05	...	...	...	...	...	70
Q1010+0003	1.398	1.265	21.52 ± 0.07	15.44 ± 0.10	12.96 ± 0.06	15.87 ± 0.06	13.23 ± 0.11	13.78 ± 0.09	14.20 ± 0.07	...	< 20.00	60,78,84,85
PSS1723+2243	4.520	3.695	20.50 ± 0.15	> 14.57	> 12.51	> 14.86	...	< 13.21	< 13.95	...	...	43
J1435+0420	1.950	1.656	21.25 ± 0.15	15.70 ± 0.07	< 13.21	15.92 ± 0.07	13.49 ± 0.03	13.72 ± 0.13	< 14.22	...	...	55
J1610+4724	3.216	2.508	21.15 ± 0.15	15.57 ± 0.04	13.53 ± 0.02	16.16 ± 0.10	13.78 ± 0.01	13.87 ± 0.04	14.54 ± 0.02	> 16.01	< 18.32	55,84,85
HE0512m3329B	1.569	0.931	20.47 ± 0.08	> 14.65	...	...	13.02 ± 0.01	...	...	...	...	49
J0814+5029	3.708	3.708	21.25 ± 0.15	> 13.76	...	> 13.87	...	...	...	...	> 14.44	86
J1402+5909	4.135	3.775	21.35 ± 0.10	> 14.47	...	> 14.43	...	...	...	...	> 14.87	86
J1417+4132	2.020	1.951	21.45 ± 0.25	15.63 ± 0.01	13.54 ± 0.01	> 16.28	...	14.04 ± 0.01	14.54 ± 0.00	> 15.80	...	84,85

Continued on next page

Table A.1 – continued from previous page

QSO	z_{em}	z_{abs}	logN(HI)	logN(FeII)	logN(ZnII)	logN(SiII)	logN(MnII)	logN(CrII)	logN(NiII)	logN(SII)	logN(OI)	Reference
Q1021+30	3.120	2.949	20.70 ± 0.10	14.04 ± 0.01	< 12.23	14.32 ± 0.02	...	< 12.89	< 13.04	13.87 ± 0.07	> 15.09	43,64
Q0841+12	2.500	2.375	20.99 ± 0.08	14.76 ± 0.01	12.10 ± 0.02	15.21 ± 0.04	12.50 ± 0.02	13.07 ± 0.02	13.53 ± 0.05	14.69 ± 0.05	> 16.05	18,23,40,54
–												66
BR0951−04	4.370	3.857	20.60 ± 0.10	14.06 ± 0.06	...	14.65 ± 0.03	...	...	< 12.98	...	...	13,23
HE0515−4414	1.713	1.150	20.45 ± 0.15	14.31 ± 0.20	12.11 ± 0.04	14.74 ± 0.18	11.93 ± 0.11	...	< 12.52	...	...	16
PSS1802+5616	4.180	3.554	20.50 ± 0.10	14.08 ± 0.06	< 12.63	> 14.24	...	...	< 13.30	...	...	44
BRI1346−03	3.990	3.736	20.72 ± 0.10	< 14.13	...	13.95 ± 0.01	...	...	< 12.76	...	> 15.02	13,23
Q0112−306	2.985	2.418	20.50 ± 0.08	13.42 ± 0.03	...	13.64 ± 0.02	...	...	...	< 14.14	14.95 ± 0.08	51,59,69,70
J1358+6522	3.197	3.067	20.47 ± 0.07	13.10 ± 0.03	...	13.40 ± 0.03	...	...	...	13.11 ± 0.09	14.94 ± 0.05	94
J0307−4945	4.780	4.466	20.67 ± 0.09	14.21 ± 0.17	...	14.68 ± 0.07	...	...	< 12.60	< 15.46	15.91 ± 0.17	28
J1201+2117	4.580	3.797	21.35 ± 0.15	15.56 ± 0.04	...	16.11 ± 0.01	...	...	14.66 ± 0.02	...	...	101
PSSJ2344+0342	4.240	3.220	21.25 ± 0.08	15.06 ± 0.15	12.23 ± 0.30	< 15.81	...	13.34 ± 0.10	13.59 ± 0.11	...	...	27,43
Q0135−273	3.210	2.107	20.30 ± 0.15	...	...	...	...	...	...	14.38 ± 0.06	...	59
J1043+6151	3.055	2.787	20.60 ± 0.15	14.00 ± 0.00	...	14.10 ± 0.00	...	...	...	...	> 14.83	86
Q0149+33	2.430	2.141	20.50 ± 0.10	14.20 ± 0.02	11.50 ± 0.10	14.57 ± 0.05	...	12.72 ± 0.04	13.17 ± 0.04	< 14.80	...	13,20,23
Q2138−444	3.170	2.383	20.60 ± 0.05	...	12.12 ± 0.09	...	...	...	...	...	...	59
J1435+5436	3.811	3.303	20.30 ± 0.20	...	...	...	...	...	...	...	...	95
J0747+4434	4.430	4.020	20.95 ± 0.15	> 14.32	...	< 14.55	...	...	12.67 ± 0.13	...	...	101
J0834+2140	4.500	4.461	20.30 ± 0.15	13.71 ± 0.07	...	13.95 ± 0.04	...	...	< 13.57	< 14.13	> 15.14	101
J0825+5127	3.510	3.318	20.85 ± 0.10	14.22 ± 0.01	...	14.69 ± 0.10	...	...	< 13.22	...	...	101
Q0935+417	1.935	1.373	20.52 ± 0.10	14.82 ± 0.10	12.26 ± 0.02	...	12.45 ± 0.08	13.18 ± 0.05	...	...	...	2,7,17
FJ0812+32	2.701	2.067	21.00 ± 0.10	14.89 ± 0.02	12.21 ± 0.02	15.18 ± 0.01	12.65 ± 0.03	13.24 ± 0.01	13.62 ± 0.01	...	...	64,65
TXS2039+187	3.050	2.192	20.70 ± 0.10	...	...	...	...	...	...	...	...	82
J1240+1455	3.109	3.108	21.30 ± 0.20	14.60 ± 0.03	12.90 ± 0.07	15.93 ± 0.03	...	< 13.02	...	15.56 ± 0.02	> 15.24	80
PSS2241+1352	4.440	4.282	21.15 ± 0.10	> 14.65	...	> 15.01	...	...	< 13.22	14.58 ± 0.03	...	43
Q2348−01	3.010	2.615	21.30 ± 0.10	14.57 ± 0.09	< 11.87	14.89 ± 0.07	...	12.67 ± 0.06	13.19 ± 0.07	...	...	23
Q1418−0630	3.689	3.448	20.40 ± 0.10	14.18 ± 0.02	< 11.98	14.63 ± 0.09	...	< 12.71	...	...	...	50,70
TXS0620+389	3.460	2.031	20.30 ± 0.04	...	...	...	...	...	...	...	...	82
Q0019−15	4.530	3.439	20.92 ± 0.10	> 14.79	...	15.42 ± 0.05	...	...	13.68 ± 0.04	...	...	13,23
Q0112+030	2.810	2.423	20.90 ± 0.10	14.85 ± 0.01	...	15.23 ± 0.06	...	...	...	14.79 ± 0.05	...	51,59,70
J0751+4516	3.761	3.046	20.35 ± 0.15	> 13.72	...	> 13.52	...	...	...	...	< 14.94	86
JJ1619+3342	0.471	0.096	20.55 ± 0.10	14.38 ± 0.15	...	> 13.93	...	...	< 13.53	15.08 ± 0.09	> 14.80	96
Q0933+733	2.525	1.479	21.62 ± 0.10	15.19 ± 0.01	12.71 ± 0.02	> 15.56	12.96 ± 0.01	13.56 ± 0.01	13.92 ± 0.01	...	...	53

Continued on next page

Table A.1 – continued from previous page

QSO	z_{em}	z_{abs}	logN(HI)	logN(FeII)	logN(ZnII)	logN(SiII)	logN(MnII)	logN(CrII)	logN(NiII)	logN(SII)	logN(OI)	Reference
J2144−0632	4.236	4.126	20.40 ± 0.15	< 13.51	...	13.23 ± 0.13	...	...	...	...	14.72 ± 0.45	86
J0801+4725	3.276	3.224	20.80 ± 0.10	...	...	...	...	...	...	...	...	95
Q2231−00	3.020	2.066	20.53 ± 0.08	14.83 ± 0.03	12.30 ± 0.05	15.29 ± 0.04	12.59 ± 0.04	13.00 ± 0.04	13.54 ± 0.06	15.10 ± 0.15	...	13,23,30,46
Q2206−199	2.559	2.076	20.43 ± 0.04	13.33 ± 0.01	< 11.20	13.65 ± 0.01	...	< 11.91	< 12.59	...	15.05 ± 0.03	8,23,24,39
–												71,88
PSS0007+2417	4.050	3.496	21.10 ± 0.10	> 14.63	< 12.39	15.08 ± 0.04	...	...	13.53 ± 0.04	...	...	44
Q1502+4837	3.200	2.570	20.30 ± 0.15	14.15 ± 0.12	...	14.24 ± 0.09	...	...	...	...	> 15.34	43
Q0405−443	3.020	2.622	20.47 ± 0.10	13.60 ± 0.02	...	13.99 ± 0.06	...	...	...	< 14.34	15.19 ± 0.02	41,51,92,95
TXS2039+187	3.050	2.752	20.70 ± 0.10	...	...	...	...	...	...	...	...	82
J1056+1208	1.920	1.610	21.45 ± 0.15	15.81 ± 0.01	13.76 ± 0.01	> 16.34	...	14.06 ± 0.01	14.61 ± 0.00	> 15.66	...	84,85
Q0836+11	2.700	2.465	20.58 ± 0.10	14.68 ± 0.01	< 12.12	14.99 ± 0.05	...	< 12.90	13.39 ± 0.07	< 14.66	> 15.48	23,35
J0040−0915	4.980	4.739	20.30 ± 0.15	14.05 ± 0.06	...	> 14.18	...	...	...	...	> 14.91	101
Q0432−4401	2.649	2.302	20.95 ± 0.10	14.87 ± 0.10	< 12.20	15.28 ± 0.06	...	13.11 ± 0.07	...	...	...	50,70
J1358+0349	2.889	2.853	20.50 ± 0.10	13.01 ± 0.05	...	13.30 ± 0.17	...	...	...	...	14.38 ± 0.25	86
J1737+5828	4.850	4.742	20.65 ± 0.10	13.30 ± 0.10	...	...	...	...	...	...	...	37
J1251+4120	3.173	2.730	21.10 ± 0.10	14.20 ± 0.00	...	13.90 ± 0.00	...	...	...	...	> 14.87	86
J0255+00	3.970	3.253	20.70 ± 0.10	14.76 ± 0.01	...	15.32 ± 0.04	...	...	13.61 ± 0.07	...	...	23
HE1122−1649	2.400	0.680	20.45 ± 0.05	14.55 ± 0.01	< 11.76	15.36 ± 0.12	11.92 ± 0.14	...	< 13.65	...	< 17.00	16,31
Q0405−443	3.020	2.550	21.13 ± 0.10	14.95 ± 0.06	12.44 ± 0.05	15.32 ± 0.04	12.86 ± 0.02	13.20 ± 0.03	13.94 ± 0.02	14.82 ± 0.06	...	41,51
Q1451+123	3.250	2.255	20.30 ± 0.15	14.33 ± 0.07	11.85 ± 0.11	> 15.46	...	12.88 ± 0.14	...	...	...	45
J1412+0624	4.420	4.109	20.40 ± 0.15	13.83 ± 0.08	...	> 14.11	...	...	< 13.37	...	> 14.64	101
J1304+1202	2.980	2.913	20.55 ± 0.15	13.72 ± 0.04	< 11.83	< 14.55	...	< 12.81	< 13.16	14.05 ± 0.05	...	101
BR0952−0115	4.430	4.024	20.55 ± 0.10	14.19 ± 0.08	...	...	...	...	< 13.44	...	...	22,23,37
PSSJ1248+31	4.350	3.696	20.63 ± 0.07	13.89 ± 0.05	< 12.62	14.39 ± 0.02	...	< 13.24	< 13.49	...	...	24,43,101
Q0201+1120	3.610	3.386	21.26 ± 0.10	15.35 ± 0.10	...	> 14.00	...	...	13.84 ± 0.10	15.21 ± 0.10	...	29
J1712+5755	3.007	2.253	20.60 ± 0.10	14.49 ± 0.02	...	14.92 ± 0.06	...	...	...	...	...	65
Q0013−004	2.084	1.973	20.83 ± 0.05	14.81 ± 0.03	12.74 ± 0.05	15.43 ± 0.02	12.36 ± 0.05	12.99 ± 0.03	13.16 ± 0.06	15.28 ± 0.04	...	1,20,33,51
–												55
J1107+0048	1.391	0.740	21.00 ± 0.05	15.53 ± 0.02	13.06 ± 0.15	...	13.27 ± 0.03	13.84 ± 0.06	...	...	...	61,78
J0927+5823	1.910	1.635	20.40 ± 0.25	15.28 ± 0.04	13.27 ± 0.01	15.74 ± 0.01	...	13.54 ± 0.02	14.34 ± 0.01	15.79 ± 0.14	...	84,85
BRJ0426−2202	4.320	2.983	21.50 ± 0.15	14.15 ± 0.07	< 12.17	< 15.00	...	< 12.90	< 13.37	...	...	43
J0831+4046	4.890	4.344	20.75 ± 0.15	13.79 ± 0.07	...	13.90 ± 0.03	...	...	< 13.54	...	...	101
PSS1802+5616	4.180	3.391	20.30 ± 0.10	14.26 ± 0.04	< 12.41	> 14.31	...	...	< 13.65	...	...	44

Continued on next page

Table A.1 – continued from previous page

QSO	z_{em}	z_{abs}	logN(HI)	logN(FeII)	logN(ZnII)	logN(SiII)	logN(MnII)	logN(CrII)	logN(NiII)	logN(SII)	logN(OI)	Reference
Q0039−3354	2.480	2.224	20.60 ± 0.10	14.41 ± 0.04	...	14.85 ± 0.04	...	...	...	...	...	70
Q1354−1046	3.007	2.501	20.44 ± 0.05	14.35 ± 0.08	< 11.70	...	...	12.87 ± 0.05	...	14.13 ± 0.09	...	50,70
Q1727+5302	1.444	0.945	21.16 ± 0.10	15.29 ± 0.01	13.25 ± 0.11	15.91 ± 0.08	13.51 ± 0.01	13.59 ± 0.11	...	...	...	48,78
Q1036−2257	3.130	2.778	20.93 ± 0.05	14.76 ± 0.01	< 12.36	> 14.97	12.66 ± 0.05	13.01 ± 0.05	13.59 ± 0.02	14.77 ± 0.01	> 15.56	43,59,70
B0537−286	3.110	2.975	20.30 ± 0.10	...	< 12.53	...	...	< 13.30	...	...	...	50
J2036−0553	2.578	2.280	21.20 ± 0.15	14.68 ± 0.11	...	15.04 ± 0.05	...	...	...	...	...	65
Q0253+0107	1.034	0.632	20.78 ± 0.10	...	< 13.06	...	...	< 13.69	...	...	...	78
J1507+4406	3.110	3.064	20.75 ± 0.10	14.03 ± 0.03	...	< 14.68	...	...	< 13.33	13.97 ± 0.10	> 14.82	101
Q2353−0028	0.764	0.604	21.54 ± 0.15	...	13.25 ± 0.29	...	...	13.40 ± 0.17	...	...	...	78
FJ0747+2739	4.110	3.423	20.85 ± 0.05	> 14.43	...	> 14.54	...	...	< 13.27	...	...	43
J1131+6044	2.907	2.875	20.50 ± 0.15	13.76 ± 0.03	...	14.49 ± 0.13	...	...	...	< 13.29	> 14.82	80
J0844+4624	3.785	3.336	20.70 ± 0.15	> 13.92	...	> 14.03	...	...	...	...	...	86
PSS1802+5616	4.180	3.811	20.35 ± 0.20	13.67 ± 0.10	...	13.87 ± 0.10	...	...	< 13.08	...	...	44
Q2228−3954	2.210	2.095	21.20 ± 0.10	15.17 ± 0.02	12.51 ± 0.06	...	...	...	...	...	...	70
J0825+3544	3.850	3.207	20.30 ± 0.10	13.77 ± 0.03	...	> 13.98	...	< 12.59	< 13.07	...	...	101
B0347−211	2.944	1.947	20.30 ± 0.10	...	< 12.38	...	...	< 12.87	...	...	...	50
J0811+2838	2.953	2.434	20.50 ± 0.10	> 13.12	...	...	...	...	...	...	...	86
J1709+3417	3.309	3.010	20.40 ± 0.10	13.90 ± 0.00	...	> 14.03	...	...	...	...	...	86
J1108+1209	3.672	3.396	20.55 ± 0.15	< 13.72	...	> 13.63	...	...	...	...	< 14.63	86
J0008−0958	1.950	1.768	20.85 ± 0.15	15.62 ± 0.02	13.32 ± 0.01	16.05 ± 0.01	< 13.44	13.92 ± 0.01	14.47 ± 0.01	15.83 ± 0.02	< 17.99	84,85
HE0512−3329A	1.569	0.931	20.49 ± 0.08	14.47 ± 0.06	...	...	12.58 ± 0.03	...	...	...	...	49
Q0000−262	4.110	3.390	21.41 ± 0.08	14.87 ± 0.03	12.01 ± 0.05	15.06 ± 0.02	...	13.09 ± 0.03	13.39 ± 0.03	...	16.45 ± 0.06	21,23
Q0336−01	3.200	3.062	21.20 ± 0.10	14.90 ± 0.03	...	15.20 ± 0.00	...	...	13.47 ± 0.06	14.99 ± 0.01	...	23,35
PSS0209+0517	4.170	3.667	20.45 ± 0.10	13.64 ± 0.05	...	> 14.11	...	< 13.08	< 13.25	...	> 14.77	43
CTQ418	2.910	2.514	20.50 ± 0.07	14.07 ± 0.03	...	14.52 ± 0.03	...	...	...	13.99 ± 0.06	...	65
Q1354−1046	3.007	2.967	20.80 ± 0.10	14.63 ± 0.04	< 12.93	14.97 ± 0.02	...	< 12.78	...	...	...	50,70
Q1331+17	2.080	1.776	21.14 ± 0.08	14.63 ± 0.03	12.54 ± 0.02	15.30 ± 0.01	12.50 ± 0.03	12.95 ± 0.03	13.44 ± 0.08	15.08 ± 0.11	...	13,23,30,46
Q0139−0023	1.379	0.682	20.60 ± 0.10	...	< 13.15	...	...	< 13.66	...	...	...	78
Q0933−3319	2.906	2.682	20.50 ± 0.10	14.45 ± 0.08	< 11.99	14.79 ± 0.10	...	< 12.94	...	...	...	50,70
J0825+3544	3.850	3.657	21.25 ± 0.10	< 14.62	...	14.93 ± 0.08	...	< 13.16	13.60 ± 0.04	...	> 15.35	101
Q0201+365	2.490	2.463	20.38 ± 0.05	15.01 ± 0.01	12.47 ± 0.05	15.53 ± 0.01	...	13.25 ± 0.03	14.02 ± 0.01	15.29 ± 0.01	...	5,7,23,35
–												84
Q0135−273	3.210	2.800	21.00 ± 0.10	14.77 ± 0.03	...	15.07 ± 0.16	...	...	...	14.80 ± 0.02	...	51,59,70

Continued on next page

Table A.1 – continued from previous page

QSO	z_{em}	z_{abs}	logN(HI)	logN(FeII)	logN(ZnII)	logN(SiII)	logN(MnII)	logN(CrII)	logN(NiII)	logN(SII)	logN(OI)	Reference
Q0242−2917	3.270	2.560	20.90 ± 0.10	14.36 ± 0.03	...	...	...	...	...	14.11 ± 0.02	...	70
J1456+0407	2.876	2.674	20.35 ± 0.10	13.00 ± 0.10	...	13.49 ± 0.07	...	...	...	...	14.55 ± 0.28	86
PSS0007+2417	4.050	3.705	20.55 ± 0.15	> 14.21	...	> 14.37	...	...	< 13.20	...	> 14.85	44
Q1337+113	2.917	2.796	21.00 ± 0.08	14.33 ± 0.01	< 12.25	14.70 ± 0.04	< 12.58	< 12.95	13.27 ± 0.08	14.33 ± 0.02	15.74 ± 0.07	43,51,59,64
–												69,70
J1637+2901	3.643	3.496	20.70 ± 0.10	13.84 ± 0.10	...	13.41 ± 0.14	...	...	...	...	14.29 ± 0.20	86
J1100+1122	4.710	4.395	21.74 ± 0.10	15.21 ± 0.09	...	> 16.09	...	...	13.96 ± 0.02	...	...	101
J1558−0031	2.830	2.703	20.67 ± 0.05	14.11 ± 0.03	...	14.24 ± 0.02	...	...	...	14.07 ± 0.02	...	65
J0311−1722	4.039	3.734	20.30 ± 0.06	< 13.76	...	13.31 ± 0.07	...	...	...	...	14.70 ± 0.08	75
J1200+4015	3.360	3.220	20.65 ± 0.15	15.39 ± 0.02	...	...	...	...	14.21 ± 0.01	15.37 ± 0.01	...	84,85,101
J1238+3437	2.570	2.471	20.80 ± 0.10	14.06 ± 0.03	...	> 14.28	...	...	< 13.49	13.91 ± 0.11	...	101
PSSJ0808+52	4.450	3.114	20.65 ± 0.07	14.17 ± 0.04	< 12.13	14.60 ± 0.12	...	< 12.74	< 13.24	...	> 14.94	24,43
PSS0133+0400	4.130	3.693	20.70 ± 0.10	13.57 ± 0.04	...	> 14.26	...	...	...	< 13.35	...	43,69
J1524+1030	2.060	1.941	...	15.25 ± 0.03	> 13.32	> 16.00	...	...	14.23 ± 0.02	> 15.53	...	84,85
Q0216+0803	2.990	2.293	20.40 ± 0.08	14.87 ± 0.05	12.43 ± 0.05	15.45 ± 0.04	...	< 13.39	13.60 ± 0.07	14.99 ± 0.03	...	3,56
J1155+0530	3.480	3.326	21.05 ± 0.10	15.36 ± 0.03	12.75 ± 0.04	15.95 ± 0.02	...	13.58 ± 0.04	14.18 ± 0.01	15.35 ± 0.00	...	84,85
Q1409+095	2.838	2.019	20.65 ± 0.10	...	11.70 ± 0.12	...	...	...	...	...	...	59
Q1157+014	1.990	1.944	21.70 ± 0.10	15.46 ± 0.02	12.99 ± 0.05	15.97 ± 0.01	13.25 ± 0.02	13.76 ± 0.02	14.21 ± 0.02	> 15.16	< 17.97	18,54,66,84
–												85
HE2243−6031	3.010	2.330	20.67 ± 0.02	14.92 ± 0.01	12.22 ± 0.03	15.36 ± 0.02	< 11.60	13.24 ± 0.02	13.86 ± 0.03	14.88 ± 0.01	16.21 ± 0.19	38
PSSJ0957+33	4.250	3.279	20.45 ± 0.08	14.37 ± 0.02	< 12.13	14.88 ± 0.05	...	< 12.89	13.32 ± 0.07	< 14.58	...	23,43
Q0918+1636	3.070	2.412	21.26 ± 0.06	15.51 ± 0.23	13.23 ± 0.18	16.00 ± 0.20	13.34 ± 0.21	13.70 ± 0.21	...	...	...	102
J1017+6116	2.810	2.768	20.60 ± 0.10	13.76 ± 0.05	...	13.94 ± 0.03	...	...	13.44 ± 0.13	...	14.58 ± 0.02	101
PSS1432+39	4.280	3.272	21.25 ± 0.10	> 14.93	< 12.65	15.67 ± 0.05	...	< 13.16	13.75 ± 0.10	...	...	43
Q0913+072	2.785	2.618	20.34 ± 0.04	12.99 ± 0.01	< 11.90	13.30 ± 0.01	< 12.27	< 12.53	< 12.17	< 13.92	14.63 ± 0.01	10,58,69,71
J1017+6116	2.805	2.768	20.60 ± 0.15	...	...	...	...	...	...	...	...	95
J1557+2320	4.130	3.538	20.65 ± 0.10	13.50 ± 0.00	...	14.10 ± 0.00	...	...	...	...	15.10 ± 0.00	86
J1350+5952	2.963	2.756	20.65 ± 0.10	13.50 ± 0.00	...	> 13.71	...	...	...	...	> 14.81	86
Q0738+313	0.630	0.221	20.90 ± 0.09	...	< 12.83	...	...	13.11 ± 0.24	...	...	...	60,81,99
Q0058−292	3.090	2.671	21.10 ± 0.10	14.75 ± 0.02	12.24 ± 0.02	15.23 ± 0.06	...	...	...	14.92 ± 0.01	...	51,59,70
J1626+2751	5.190	4.497	21.39 ± 0.15	14.08 ± 0.02	...	> 14.31	...	...	...	...	...	101
J2340−00	2.090	2.054	20.35 ± 0.15	14.96 ± 0.20	12.63 ± 0.08	15.17 ± 0.04	...	< 12.90	13.78 ± 0.03	14.95 ± 0.04	> 15.45	64,84,85
J1042+0117	2.440	2.267	20.75 ± 0.15	15.08 ± 0.13	< 12.74	15.47 ± 0.09	< 12.89	13.48 ± 0.09	13.99 ± 0.12	...	> 15.46	55

Continued on next page

Table A.1 – continued from previous page

QSO	z_{em}	z_{abs}	logN(HI)	logN(FeII)	logN(ZnII)	logN(SiII)	logN(MnII)	logN(CrII)	logN(NiII)	logN(SII)	logN(OI)	Reference
J1623+0718	1.648	1.336	21.35 ± 0.10	15.28 ± 0.05	12.91 ± 0.09	15.78 ± 0.05	13.06 ± 0.06	13.55 ± 0.06	14.11 ± 0.07	...	...	93
PSS2323+2758	4.180	3.684	20.95 ± 0.10	13.32 ± 0.13	...	13.92 ± 0.03	...	...	...	...	> 15.61	43
Q0405−443	3.020	1.913	20.80 ± 0.10	...	12.44 ± 0.02	...	...	...	...	...	...	59
Q2342+34	3.010	2.908	21.10 ± 0.10	15.02 ± 0.06	< 12.47	15.62 ± 0.02	...	13.36 ± 0.08	13.82 ± 0.03	15.19 ± 0.01	> 17.96	43,64,84,85
Q1055+46	4.130	3.317	20.34 ± 0.10	13.94 ± 0.06	...	14.25 ± 0.11	...	...	...	...	...	24,65
Q0347−38	3.230	3.025	20.63 ± 0.01	14.43 ± 0.01	11.79 ± 0.04	15.24 ± 0.01	...	12.44 ± 0.04	13.38 ± 0.03	14.76 ± 0.04	16.64 ± 0.01	23,34,35,69
BR1202−0725	4.690	4.383	20.55 ± 0.03	13.88 ± 0.11	...	14.39 ± 0.05	...	...	< 12.50	...	15.75 ± 0.06	4,37,47
J1337+3153	3.174	3.175	21.36 ± 0.10	...	...	...	...	...	...	...	...	95
Q2206−199	2.559	1.920	20.65 ± 0.07	15.30 ± 0.02	12.91 ± 0.01	15.80 ± 0.01	...	13.64 ± 0.01	14.23 ± 0.01	...	...	8,23,24,100
J1253+1046	4.910	4.600	20.30 ± 0.15	14.09 ± 0.03	...	> 14.22	...	...	...	...	> 15.23	101
Q2138−444	3.170	2.852	20.98 ± 0.05	14.63 ± 0.02	11.91 ± 0.02	14.86 ± 0.02	...	...	...	14.50 ± 0.02	...	51,59,70
PKS1354−17	3.150	2.780	20.30 ± 0.15	13.37 ± 0.08	...	13.98 ± 0.06	...	...	...	...	...	43
Q2149+212	1.538	0.911	20.70 ± 0.10	...	< 12.40	...	...	< 12.78	...	...	...	78
Q0528−2505	2.779	2.812	21.20 ± 0.04	15.47 ± 0.02	13.27 ± 0.03	16.01 ± 0.03	...	13.65 ± 0.12	13.89 ± 0.03	15.56 ± 0.02	...	3,40
BR1108−0747	3.920	3.608	20.37 ± 0.07	13.88 ± 0.01	...	14.26 ± 0.01	...	...	< 13.14	...	15.37 ± 0.03	22,23,69
J1201+2117	4.580	4.158	20.60 ± 0.15	13.76 ± 0.03	...	13.73 ± 0.02	...	...	< 13.13	...	...	101
J0759+1800	4.860	4.658	20.85 ± 0.15	< 15.16	...	> 14.68	...	...	< 13.61	14.26 ± 0.05	> 15.28	101
J0909+3303	3.780	3.658	20.55 ± 0.10	14.43 ± 0.01	...	14.89 ± 0.09	...	...	13.55 ± 0.13	14.51 ± 0.04	> 15.34	101
Q0112−306	2.985	2.702	20.30 ± 0.10	14.80 ± 0.06	...	15.37 ± 0.05	...	...	...	...	...	51,59,70
JJ1616+4154	0.440	0.321	20.60 ± 0.20	15.02 ± 0.05	...	> 15.08	...	...	...	15.37 ± 0.11	> 15.45	96
J0900+42	3.290	3.246	20.30 ± 0.10	14.54 ± 0.01	...	> 14.95	...	...	13.30 ± 0.02	14.65 ± 0.01	...	64,65
PSS0007+2417	4.050	3.838	20.85 ± 0.15	13.91 ± 0.03	...	> 14.01	...	...	< 13.04	...	> 14.64	44
Q0841+129	2.500	1.864	21.00 ± 0.10	...	...	...	...	...	...	14.69 ± 0.05	...	59
Q1712+5559	1.356	1.210	20.72 ± 0.10	> 14.54	< 12.19	...	...	< 12.86	...	...	...	60
PSS2315+0921	4.520	3.425	21.10 ± 0.20	> 14.63	...	15.15 ± 0.05	...	...	< 13.36	...	...	44
Q1007+0042	1.676	1.037	21.15 ± 0.20	...	13.27 ± 0.04	...	...	13.55 ± 0.08	...	...	...	78
J0256+0110	1.346	0.725	20.70 ± 0.16	15.13 ± 0.30	13.19 ± 0.04	...	13.24 ± 0.02	13.81 ± 0.05	...	...	...	61
B0405−331	2.570	2.569	20.60 ± 0.10	14.31 ± 0.00	< 12.74	14.71 ± 0.00	...	< 13.32	...	...	...	50
PSS0134+3317	4.520	3.761	20.85 ± 0.08	...	...	> 13.89	...	...	...	...	...	43
J0839+3524	4.780	4.280	20.30 ± 0.15	14.30 ± 0.04	...	> 14.39	...	...	...	...	...	101
J0142+0023	3.373	3.348	20.38 ± 0.05	13.70 ± 0.10	< 11.50	14.15 ± 0.03	...	< 12.17	...	13.26 ± 0.06	> 15.01	80
J0225+0054	2.970	2.714	21.00 ± 0.15	15.30 ± 0.08	12.89 ± 0.11	15.61 ± 0.07	...	13.78 ± 0.10	14.17 ± 0.11	...	> 15.69	55
QXO0001	3.119	3.000	20.70 ± 0.05	< 15.09	...	14.45 ± 0.01	...	...	...	...	15.77 ± 0.02	35

Continued on next page

Table A.1 – continued from previous page

QSO	z_{em}	z_{abs}	logN(HI)	logN(FeII)	logN(ZnII)	logN(SiII)	logN(MnII)	logN(CrII)	logN(NiII)	logN(SII)	logN(OI)	Reference
Q2223+20	3.561	3.119	20.30 ± 0.10	13.32 ± 0.06	...	13.64 ± 0.04	...	...	...	...	> 14.84	43
J1049−0110	2.120	1.658	20.35 ± 0.15	15.20 ± 0.02	13.15 ± 0.02	15.78 ± 0.01	...	13.35 ± 0.03	14.10 ± 0.03	15.47 ± 0.01	...	84,85
PSS1506+5220	4.180	3.224	20.67 ± 0.07	13.71 ± 0.03	< 12.11	13.88 ± 0.02	...	< 12.78	< 13.41	...	> 14.66	43
J1313+1441	1.880	1.795	...	15.51 ± 0.02	13.22 ± 0.01	...	...	13.55 ± 0.03	14.18 ± 0.01	15.71 ± 0.01	...	84,85
PC0953+4749	4.460	4.243	20.90 ± 0.15	13.90 ± 0.07	...	14.23 ± 0.03	...	...	< 13.61	...	> 15.16	37,43
PSS2315+0921	4.520	3.219	21.35 ± 0.15	> 14.56	< 11.95	...	...	< 13.19	...	...	...	44
Q0254−4025	2.280	2.046	20.45 ± 0.08	14.17 ± 0.01	...	...	...	...	...	14.10 ± 0.04	...	70
Q0827+243	0.941	0.525	20.30 ± 0.05	14.59 ± 0.02	< 12.80	...	...	< 13.42	...	...	...	60,99
PSS0133+0400	4.130	3.774	20.60 ± 0.10	> 14.87	< 13.10	15.46 ± 0.02	...	< 13.24	13.98 ± 0.03	...	...	43,70
TXS0229+230	3.420	2.683	20.70 ± 0.10	...	...	...	...	...	...	...	...	82
J1358+6522	3.197	3.067	20.35 ± 0.15	< 12.80	...	13.29 ± 0.25	...	...	...	...	14.03 ± 0.08	86,94
J1200+4015	3.360	3.220	20.85 ± 0.10	15.31 ± 0.04	12.86 ± 0.04	> 15.21	...	13.53 ± 0.03	...	...	> 15.52	101
J1013+5615	3.610	2.284	...	> 15.17	...	16.14 ± 0.01	...	...	...	...	...	84,85
PSSJ0957+33	4.250	4.178	20.70 ± 0.10	14.13 ± 0.05	...	14.56 ± 0.01	...	...	< 12.91	14.39 ± 0.06	> 14.97	23,43
Q0738+313	0.630	0.091	21.18 ± 0.06	15.02 ± 0.15	< 12.66	...	...	13.28 ± 0.22	...	...	...	60,81
J1257−0111	4.110	4.021	20.30 ± 0.10	13.65 ± 0.07	...	14.25 ± 0.02	...	...	...	< 13.90	> 14.57	101
UM673A	2.719	1.626	20.70 ± 0.10	14.59 ± 0.03	11.43 ± 0.15	14.75 ± 0.03	...	12.78 ± 0.04	12.99 ± 0.04	14.53 ± 0.00	...	77
Q2348−01	3.010	2.426	20.50 ± 0.10	14.61 ± 0.01	...	15.37 ± 0.02	...	< 12.71	13.35 ± 0.10	15.01 ± 0.00	...	23,63

References–

(1) Pettini et al. (1994). (2) Meyer et al. (1995). (3) Lu et al. (1996a). (4) Lu et al. (1996b). (5) Prochaska & Wolfe (1996). (6) Steidel et al. (1997). (7) Pettini et al. (1997). (8) Prochaska & Wolfe (1997b). (9) Boisse et al. (1998). (10) Ledoux et al. (1998). (11) Pettini et al. (1995). (12) Lopez et al. (1999). (13) Prochaska & Wolfe (1999). (14) Pettini et al. (2000). (15) Churchill et al. (2000). (16) de la Varga et al. (2000). (17) Rao & Turnshek (2000). (18) Petitjean et al. (2000). (19) Srianand et al. (2000). (20) Centurión et al. (2000). (21) Molaro et al. (2000). (22) Prochaska & Wolfe (2000). (23) Prochaska et al. (2001b). (24) Prochaska et al. (2001a). (25) Ge et al. (2001). (26) Ellison & Lopez (2001). (27) Dessauges-Zavadsky (unpublished).(28) Dessauges-Zavadsky et al. (2001). (29) Ellison et al. (2001a). (30) Dessauges-Zavadsky et al. (2002). (31) Ledoux et al. (2002a). (32) Ledoux et al. (2002b). (33) Petitjean et al. (2002). (34) Levshakov et al. (2002). (35) Prochaska et al. (2002). (36) Péroux et al. (2002). (37) Songaila & Cowie (2002). (38) Lopez et al. (2002). (39) Pettini et al. (2002). (40) Centurión et al. (2003). (41) Lopez & Ellison (2003). (42) Prochaska et al. (2003d). (43) Prochaska et al. (2003c). (44) Prochaska et al. (2003a). (45) Dessauges-Zavadsky et al. (2003). (46) Dessauges-Zavadsky et al. (2004). (47) D'Odorico & Molaro (2004). (48) Turnshek et al. (2004). (49) Lopez et al. (2005b). (50) Akerman et al. (2005). (51) Srianand et al. (2005). (52) Bowen et al. (2005). (53) Rao et al. (2005). (54) Dessauges-Zavadsky et al. (2006). (55) Herbert-Fort et al. (2006). (56) Dessauges-Zavadsky et al (unpublished).(57) Ledoux et al. (2006b). (58) Erni et al. (2006). (59) Ledoux et al. (2006a). (60) Meiring et al. (2006). (61) Péroux et al. (2006). (62) Noterdaeme et al. (2007a). (63) Noterdaeme et al. (2007b). (64) Prochaska et al. (2007). (65) Henry & Prochaska (2007). (66) Dessauges-Zavadsky et al. (2007). (67) Meiring et al. (2007). (68) Ellison et al. (2007). (69) Petitjean et al. (2008). (70) Noterdaeme et al. (2008). (71) Pettini et al. (2008). (72) Péroux et al. (2008). (73) Meiring et al. (2011). (74) Meiring et al. (2009). (75) Cooke et al. (2011b). (76) Cooke et al. (2011a). (77) Cooke et al. (2010). (78) Nestor et al. (2008). (79) Fynbo et al. (2011). (80) Ellison et al. (2010). (81) Kulkarni et al. (2005).

(82) Ellison et al. (2008). (83) Chen et al. (2005). (84) Berg et al. (2013). (85) This work. (86) Penprase et al. (2010). (87) Ellison et al. (2008). (88) Guimarães et al. (2012). (89) Carswell et al. (2012). (90) Kulkarni et al. (2012). (91) Noterdaeme et al. (2012a). (92) Pettini & Cooke (2012). (93) Noterdaeme et al. (2012b). (94) Ellison et al. (2012). (95) Cooke et al. (2012). (96) Srianand et al. (2012). (97) Battisti et al. (2012). (98) Meiring et al. (2011). (99) Zafar et al. (2011). (100) Kanekar et al. (2014). (101) Krogager et al. (2013). (102) Vladilo et al. (2011). (103) Rafelski et al. (2012). (104) Fynbo et al. (2013).

A.2 Thesis Sample Profiles

Figures A.1–A.30 show a selection of absorption lines for commonly observed elements in each Thesis Sample DLA. The horizontal dashed lines represents the continuum of the spectrum.

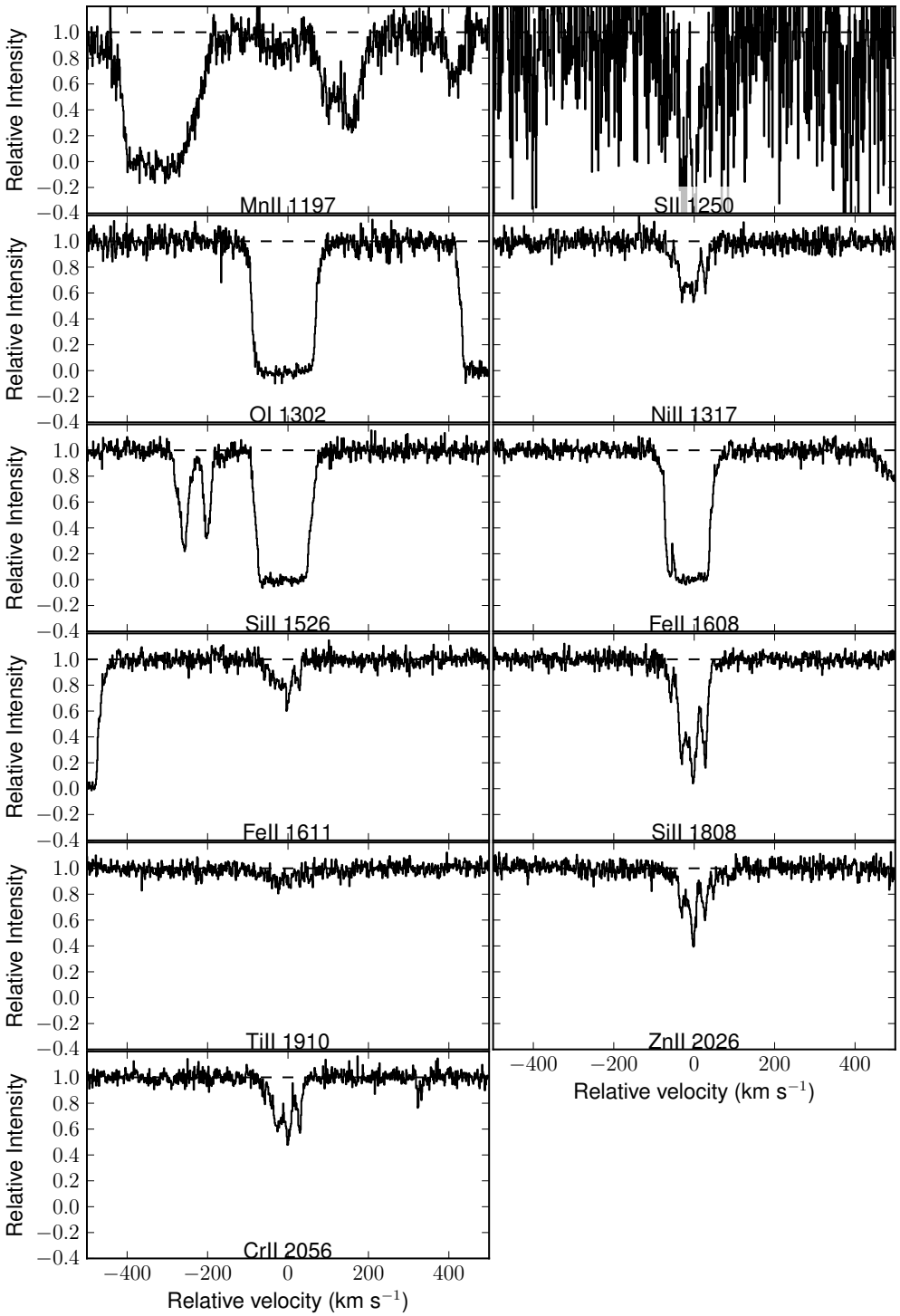

Figure A.1 Absorption line profiles for J1159+0112.

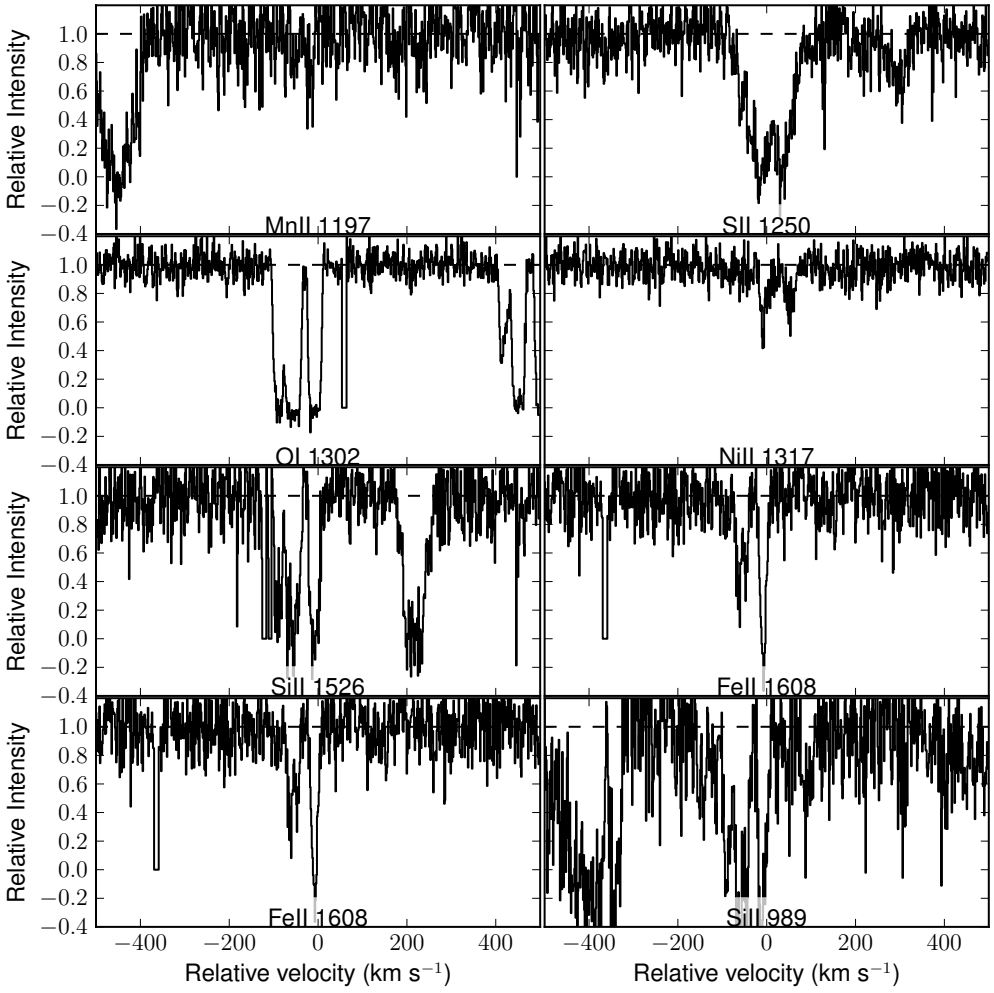

Figure A.2 Absorption line profiles for J2241+1225.

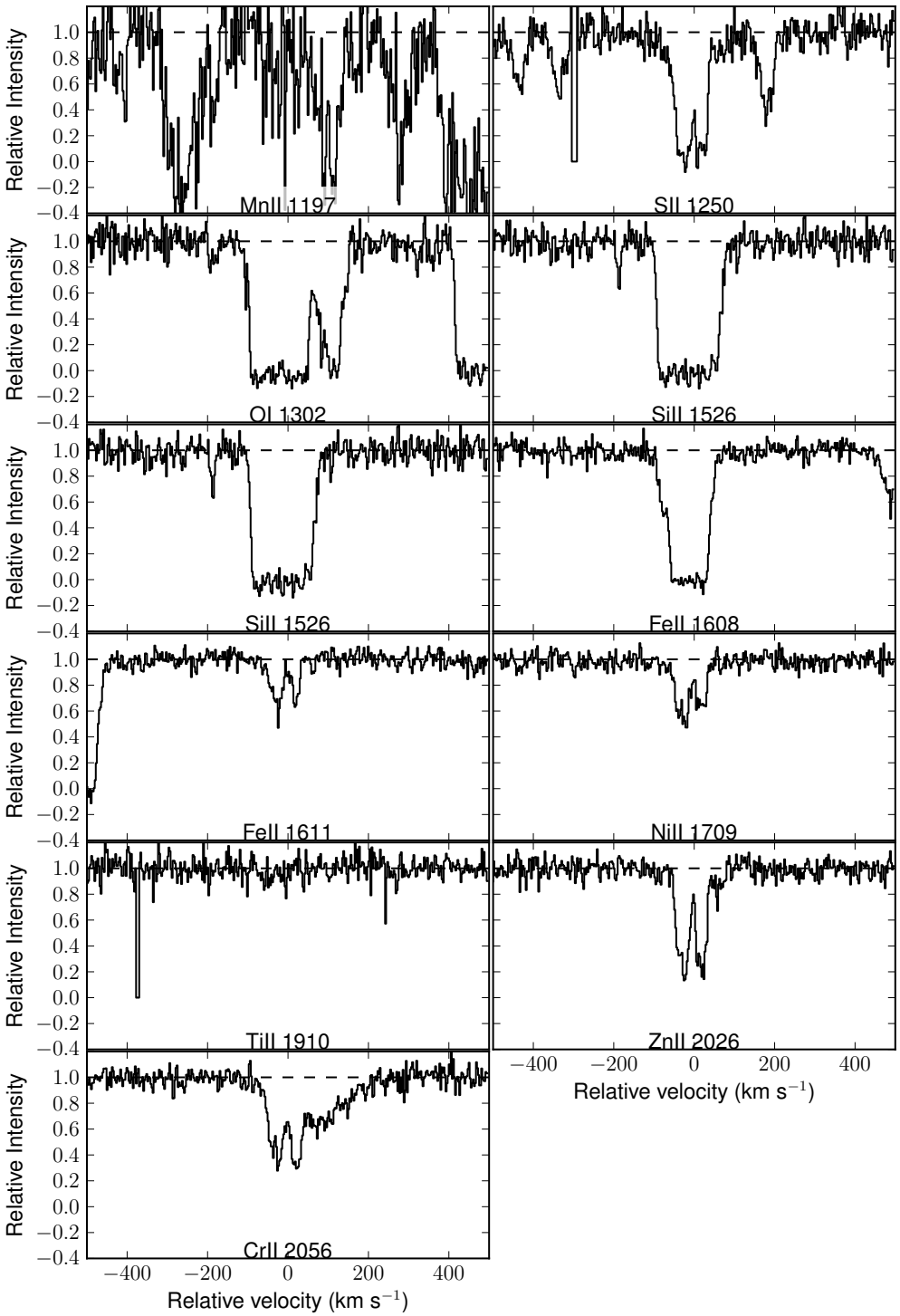

Figure A.3 Absorption line profiles for J1310+5424.

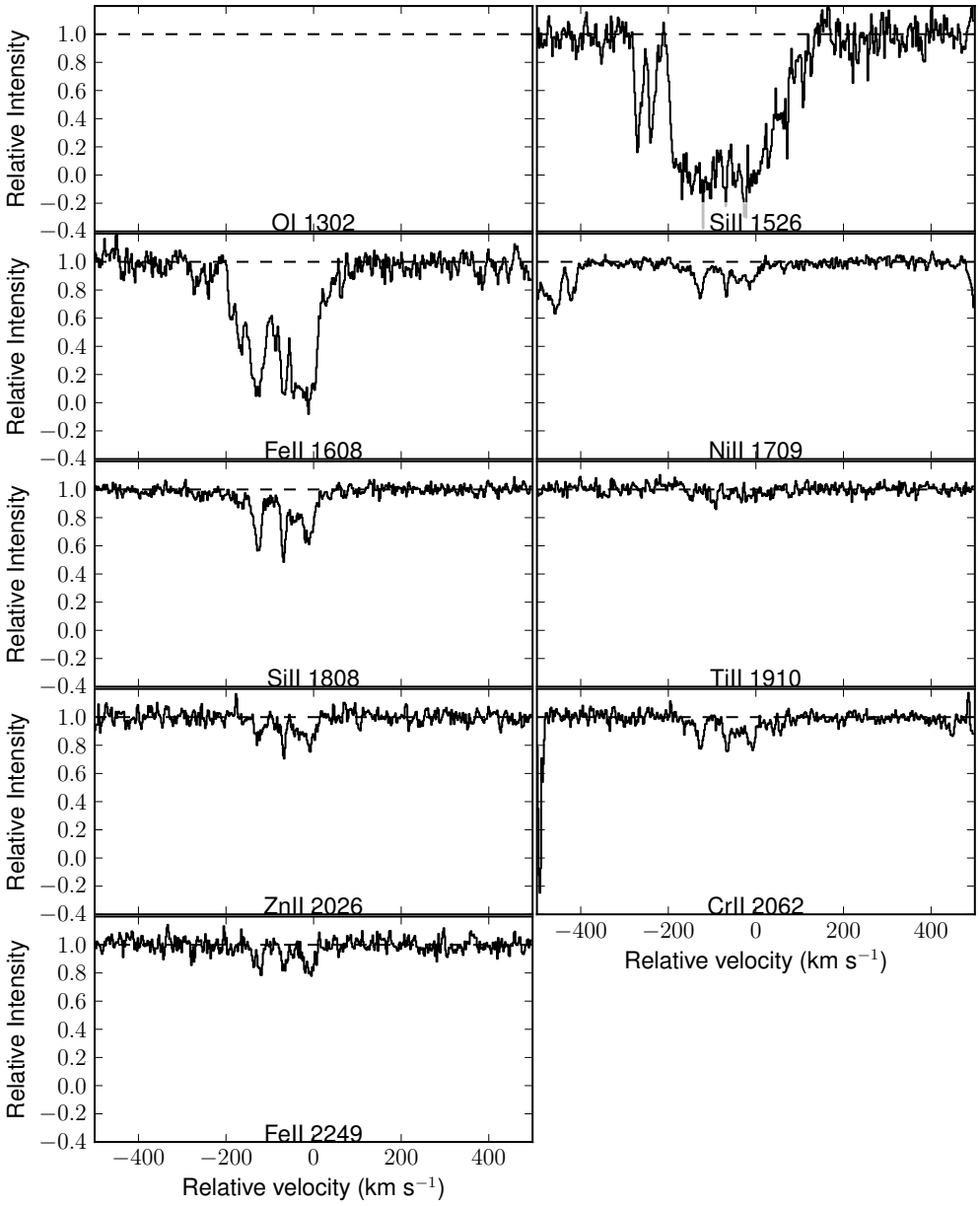

Figure A.4 Absorption line profiles for Q2230+02.

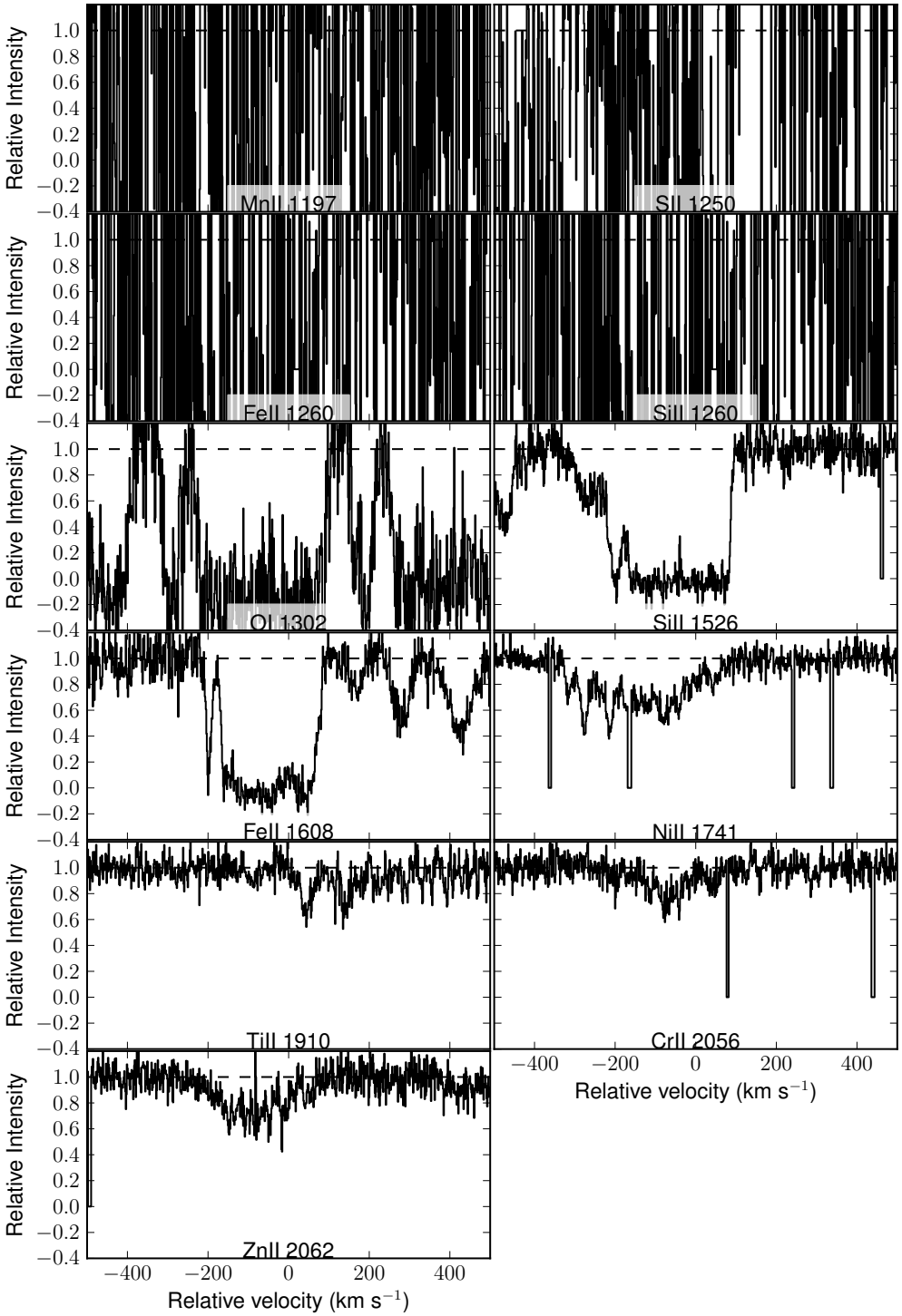

Figure A.5 Absorption line profiles for J1013+5615.

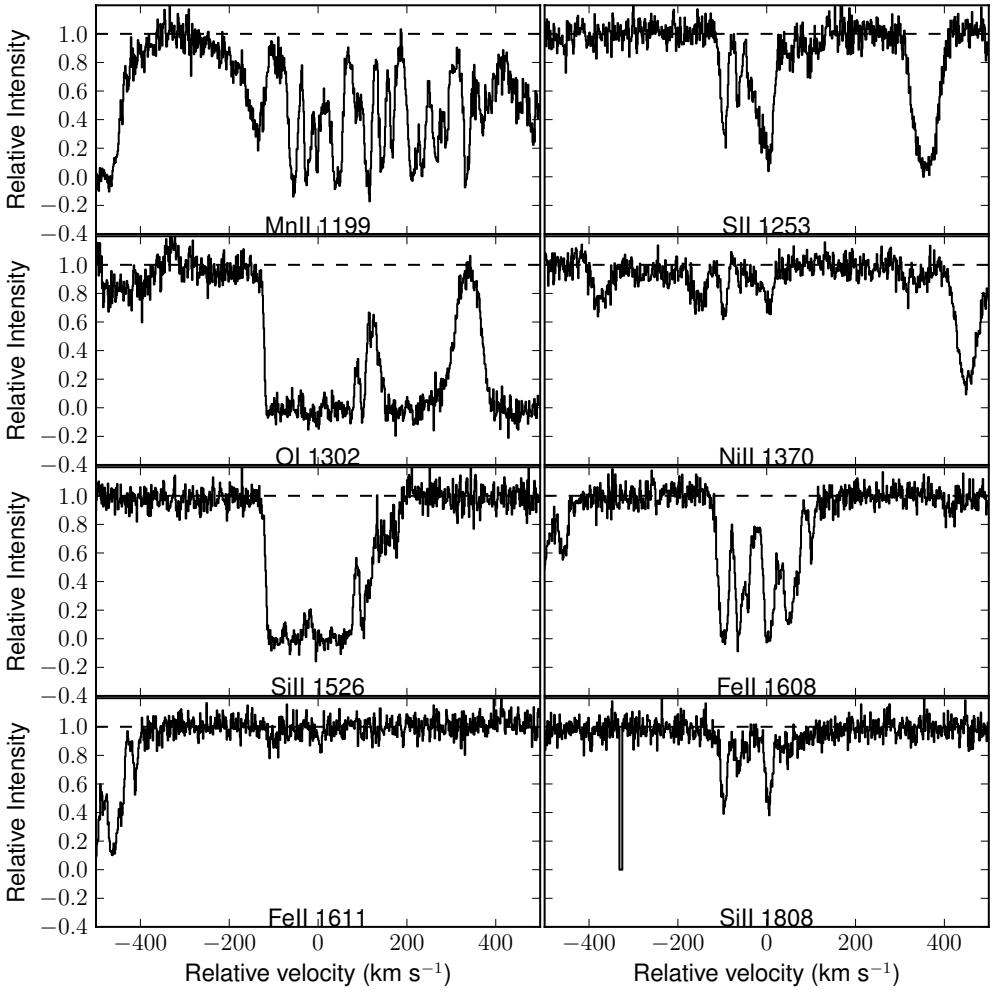

Figure A.6 Absorption line profiles for J2222-0945.

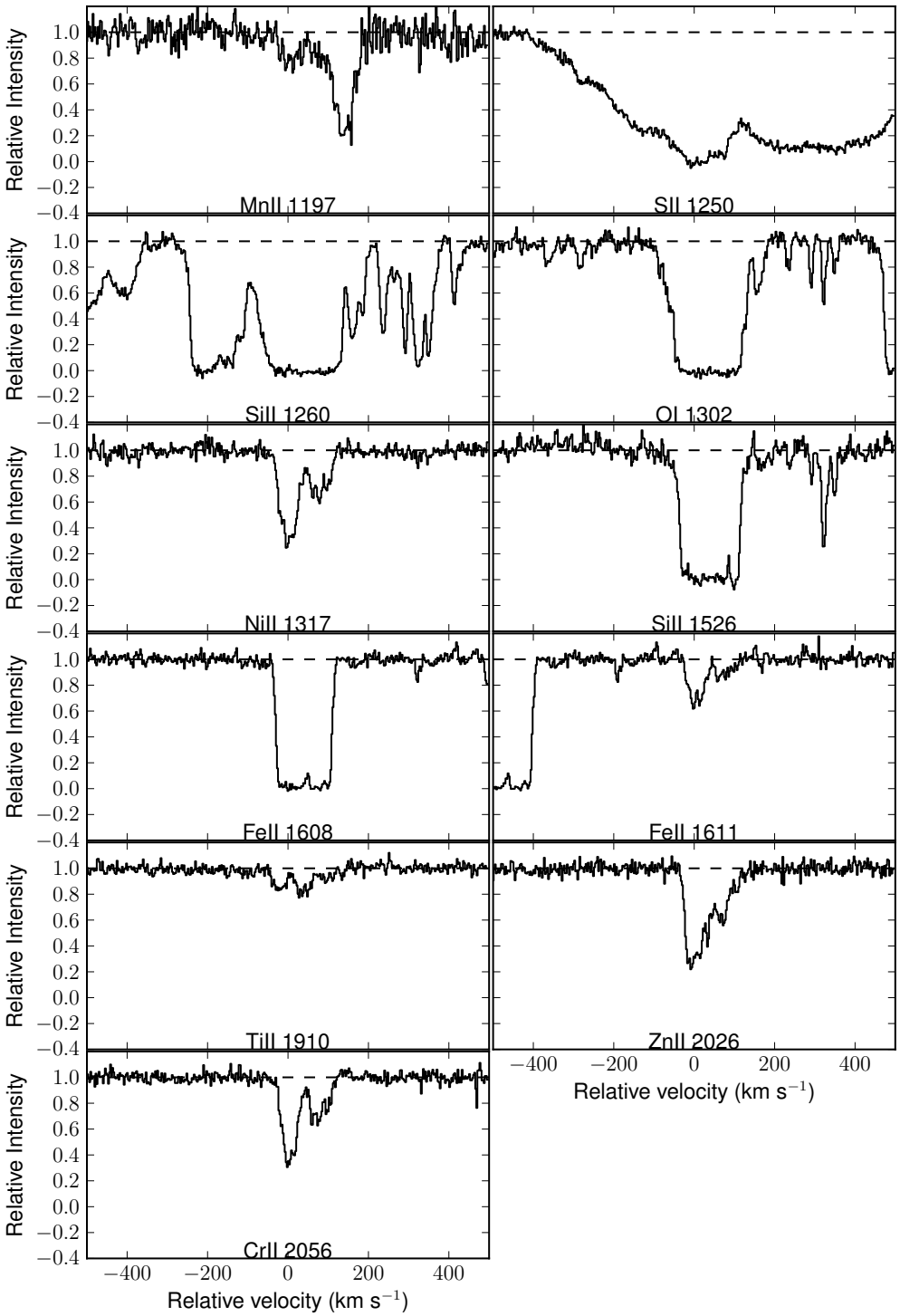

Figure A.7 Absorption line profiles for J1417+4132.

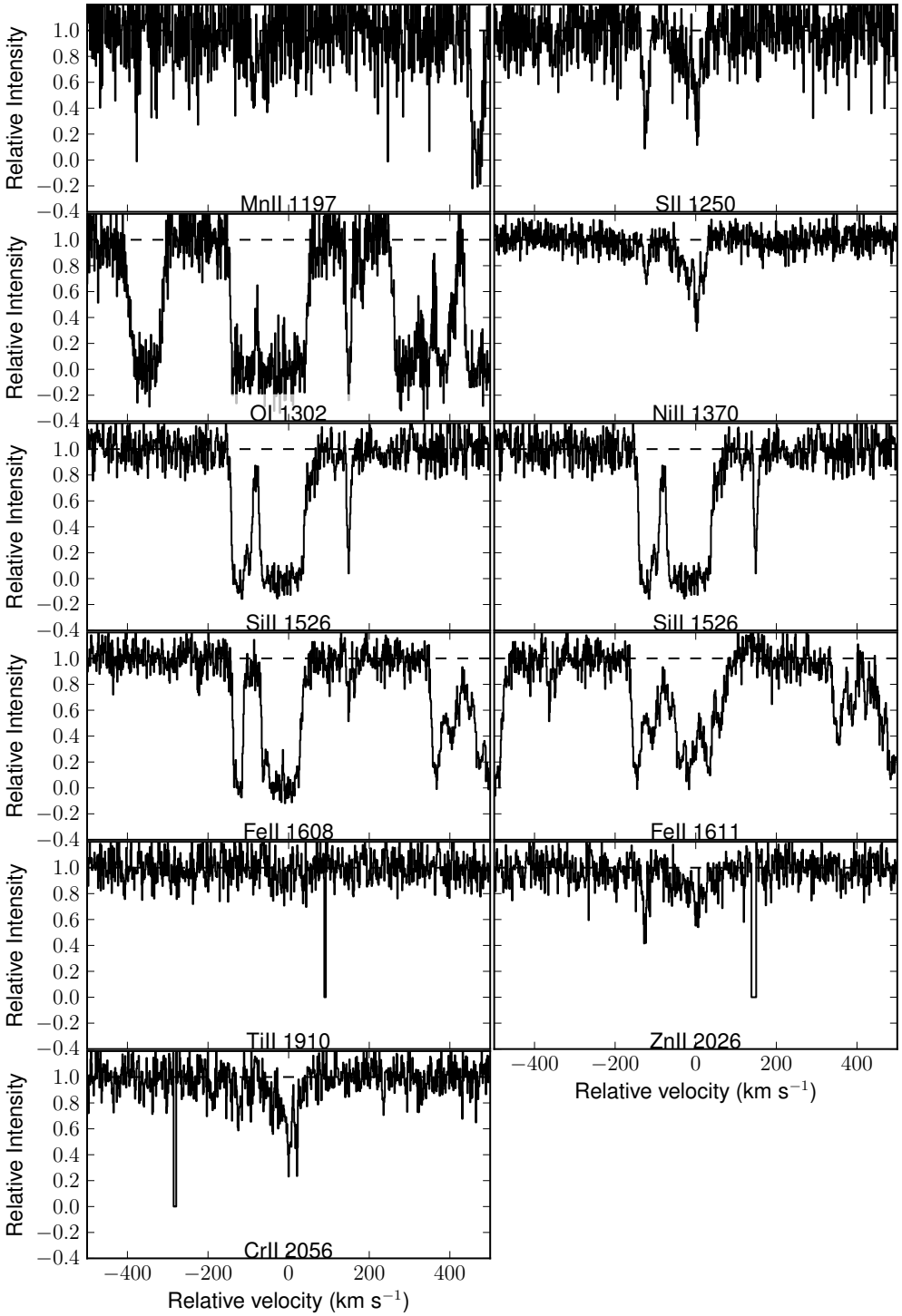

Figure A.8 Absorption line profiles for J1249-0233.

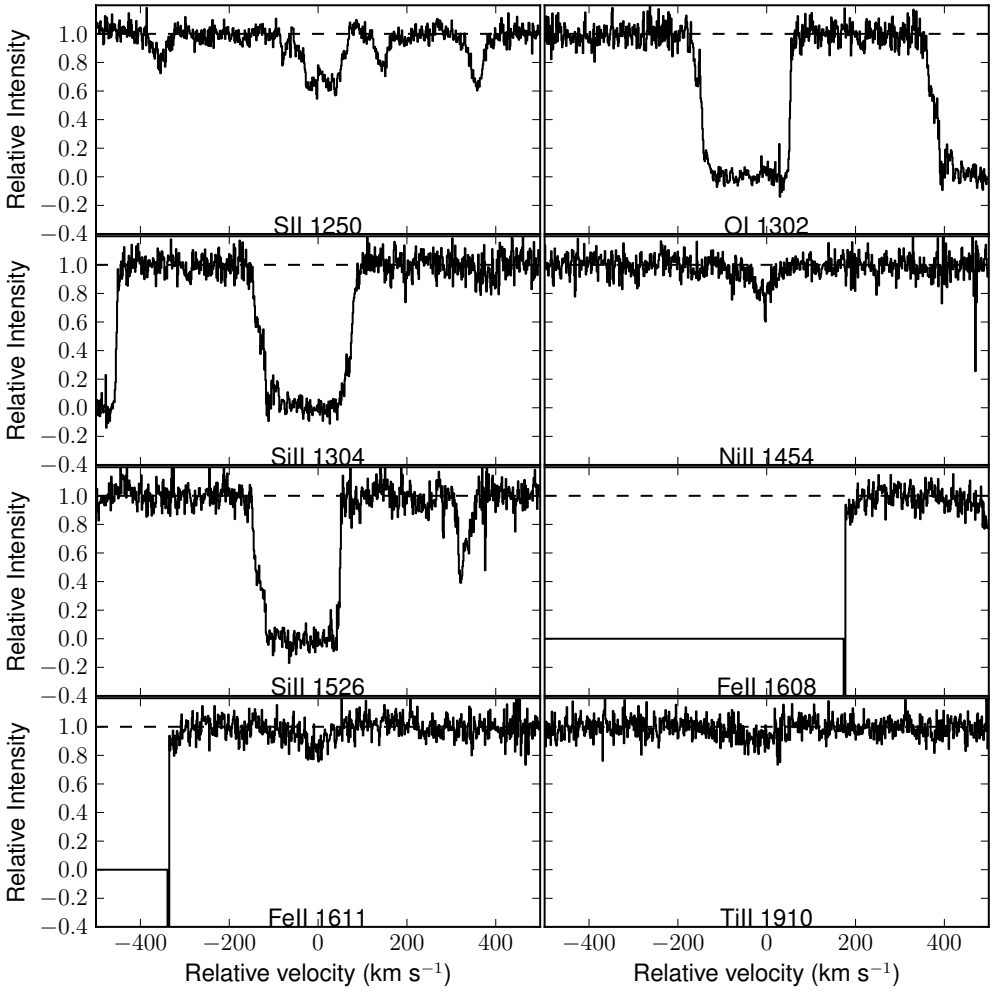

Figure A.9 Absorption line profiles for J1200+4015.

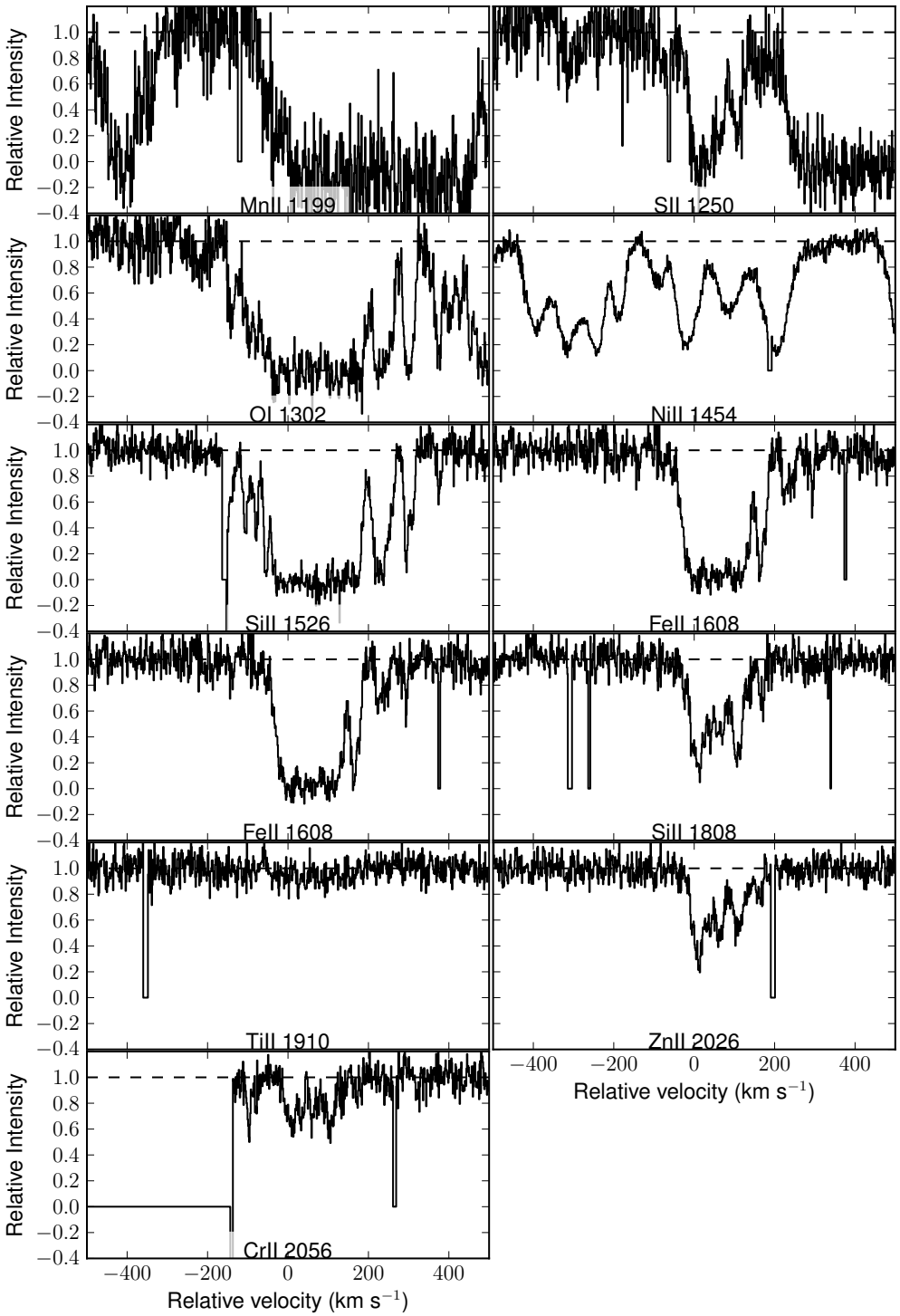

Figure A.10 Absorption line profiles for J1610+4724.

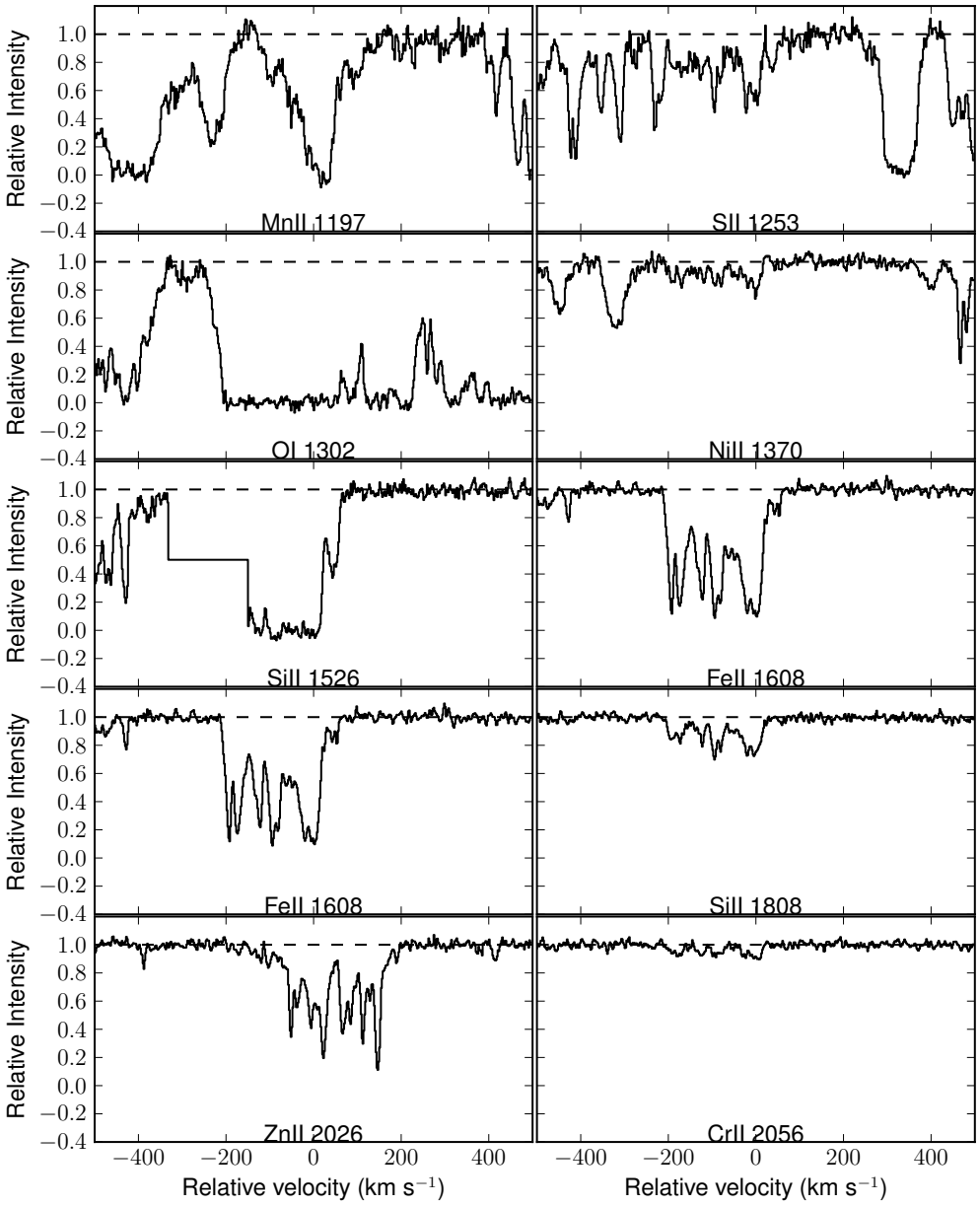

Figure A.11 Absorption line profiles for Q0201+36.

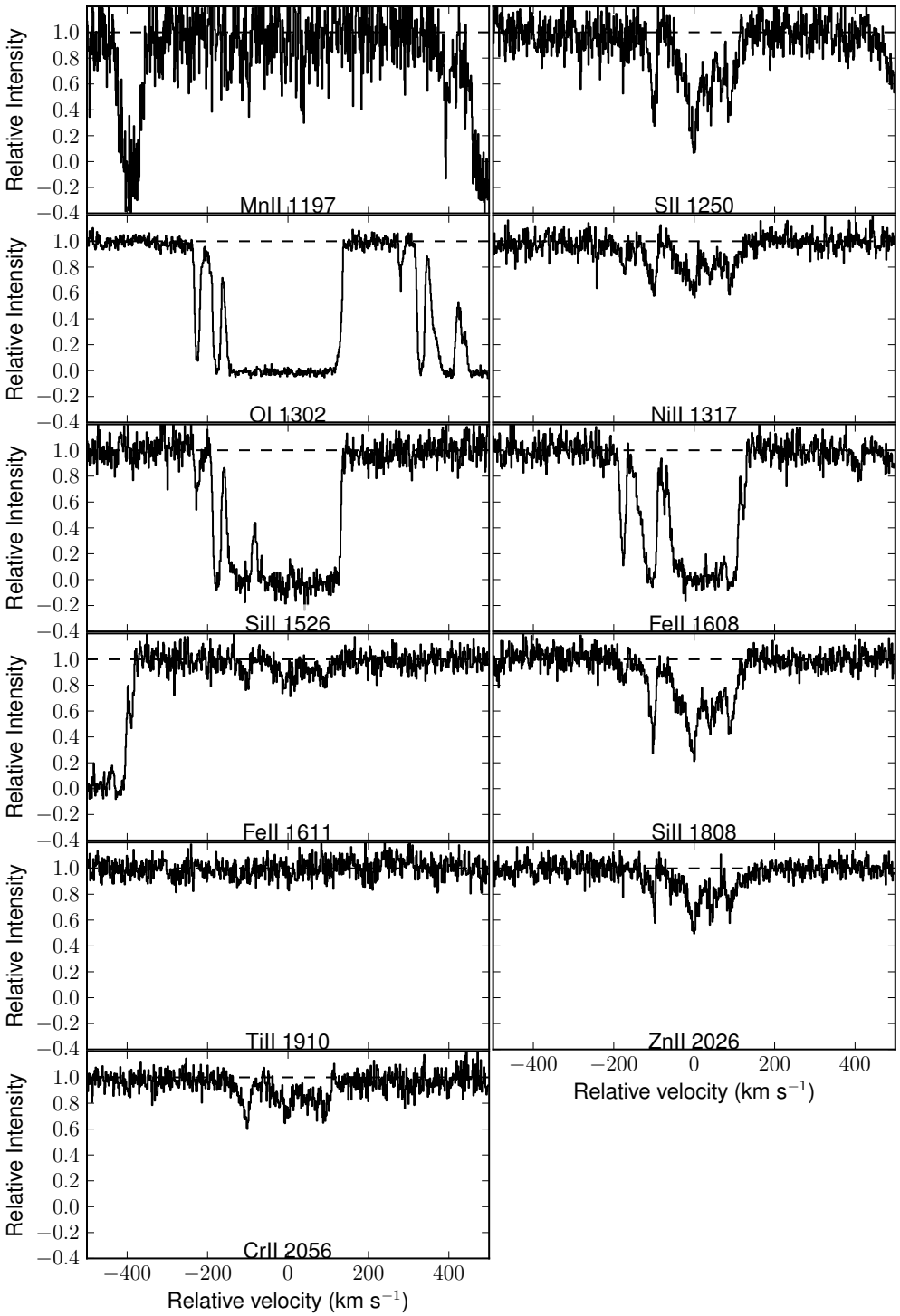

Figure A.12 Absorption line profiles for J0008-0958.

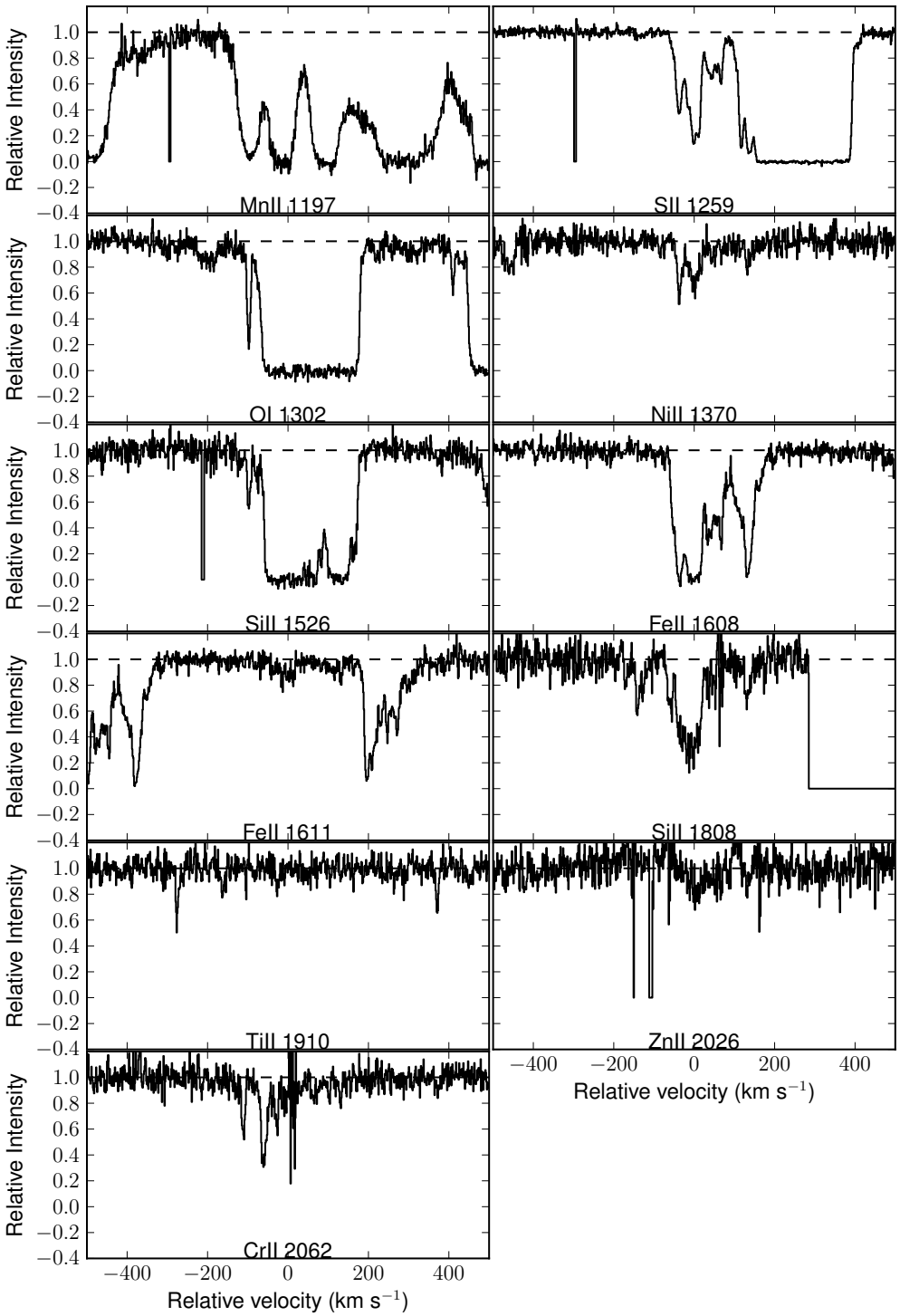

Figure A.13 Absorption line profiles for J1155+0530.

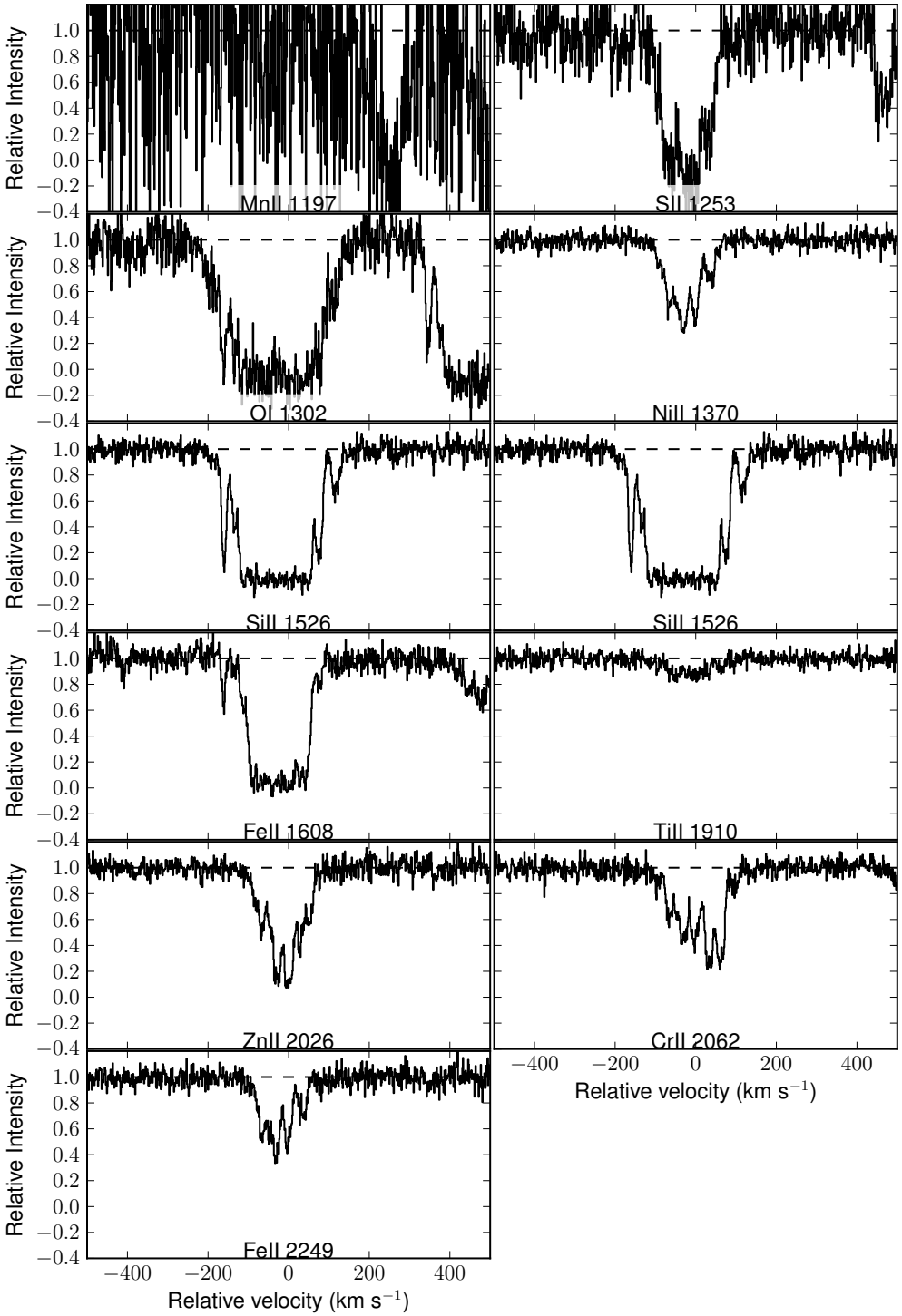

Figure A.14 Absorption line profiles for J1056+1208.

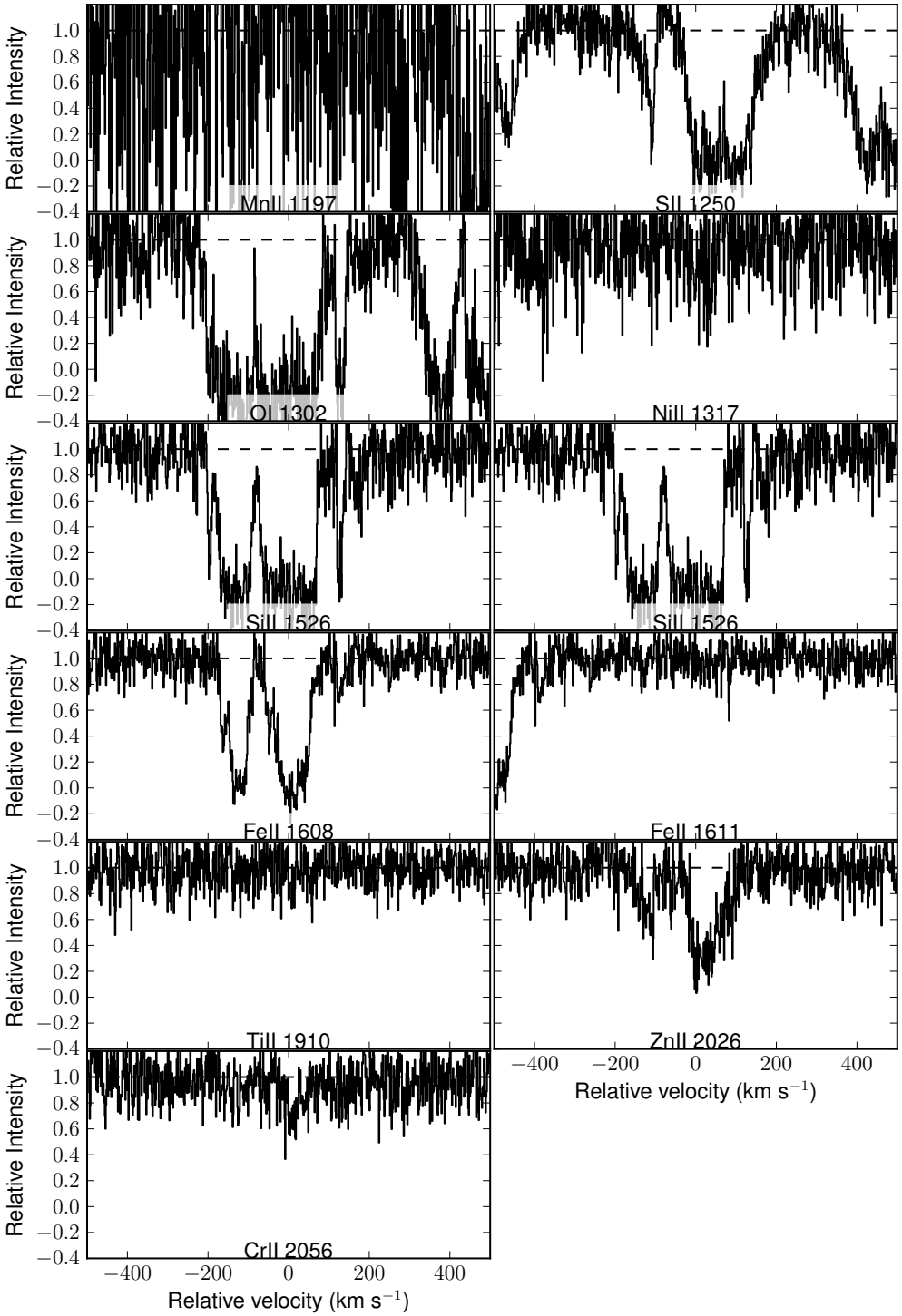

Figure A.15 Absorption line profiles for J0927+1543.

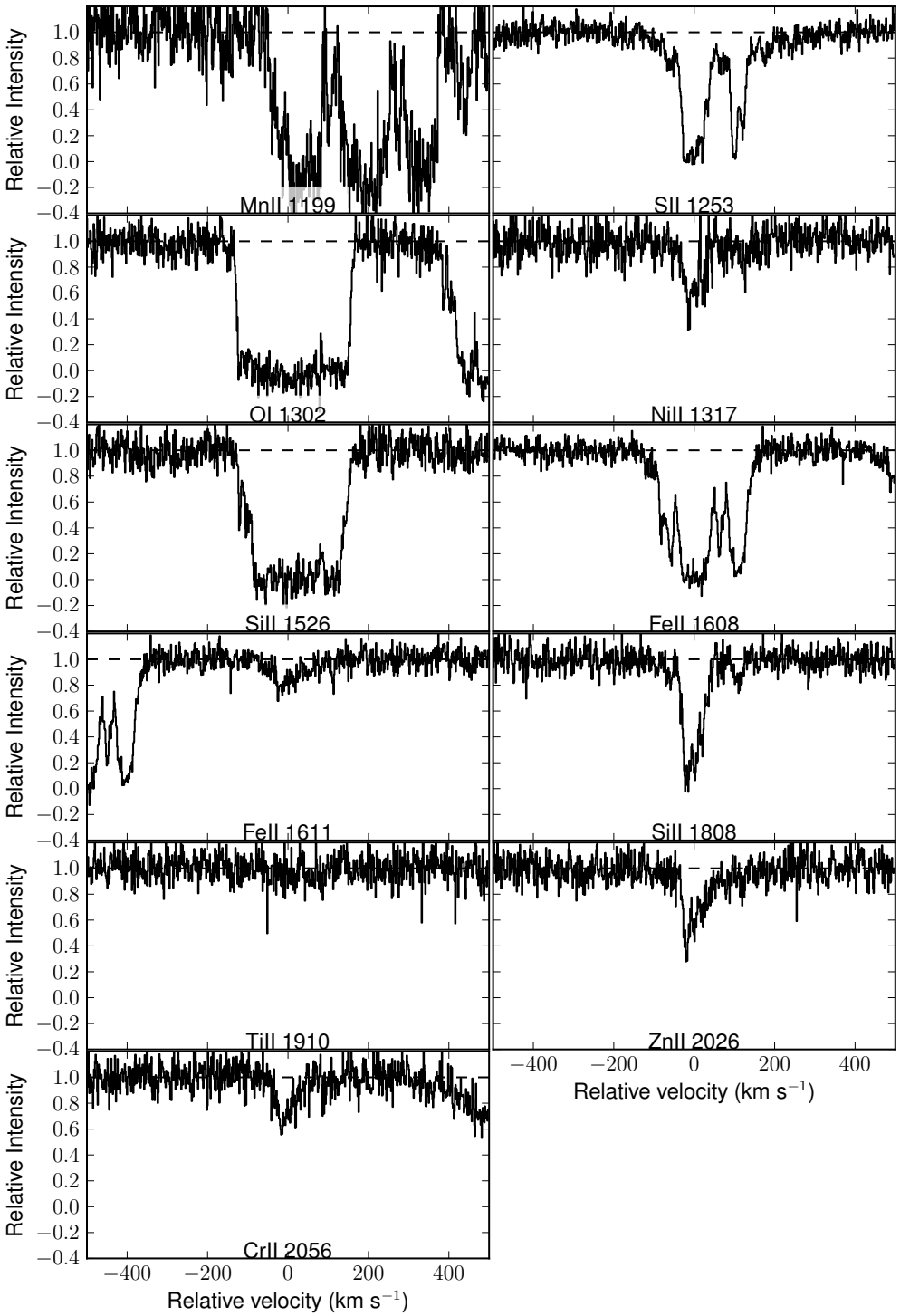

Figure A.16 Absorption line profiles for J1313+1441.

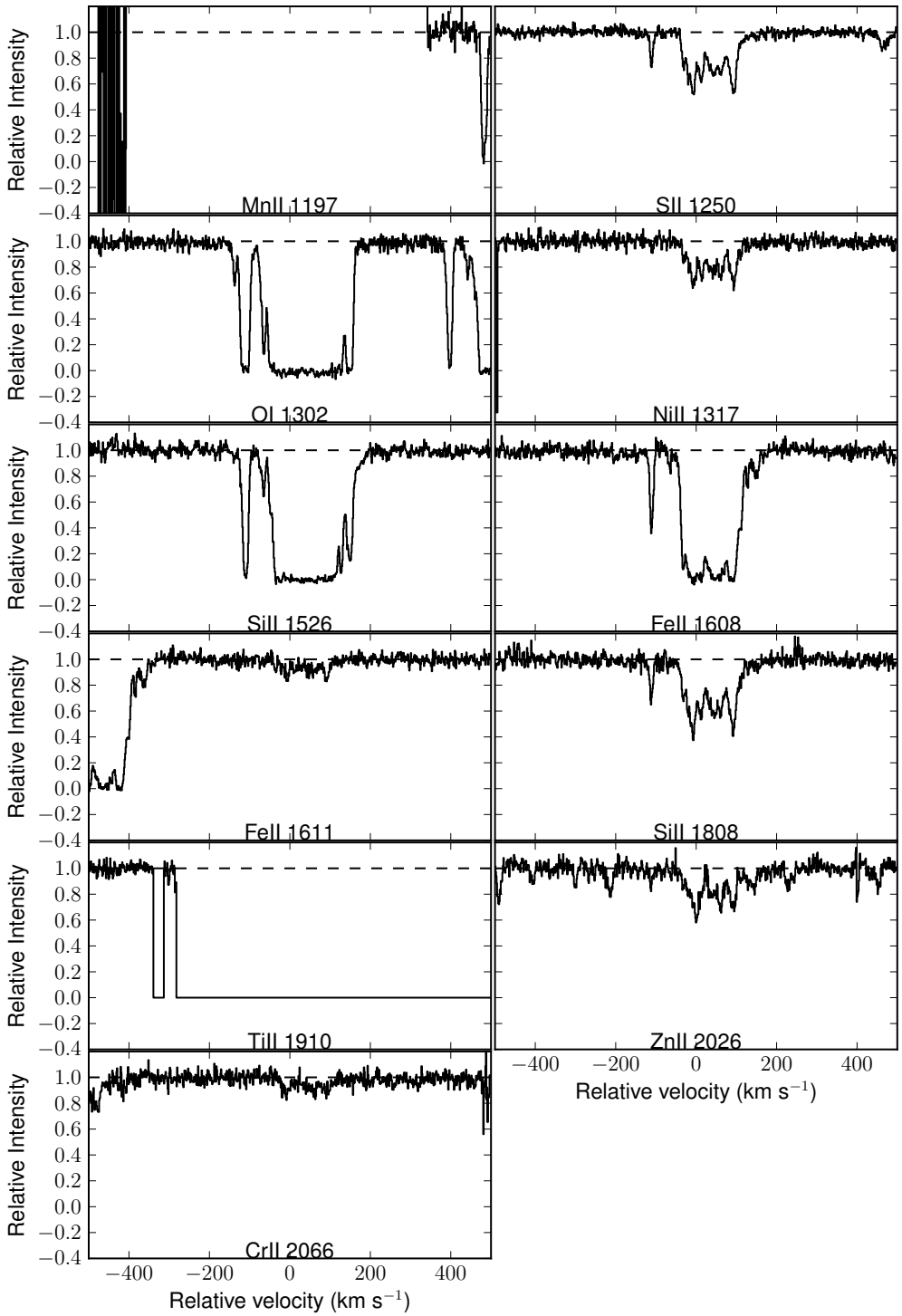

Figure A.17 Absorption line profiles for J2100-0641.

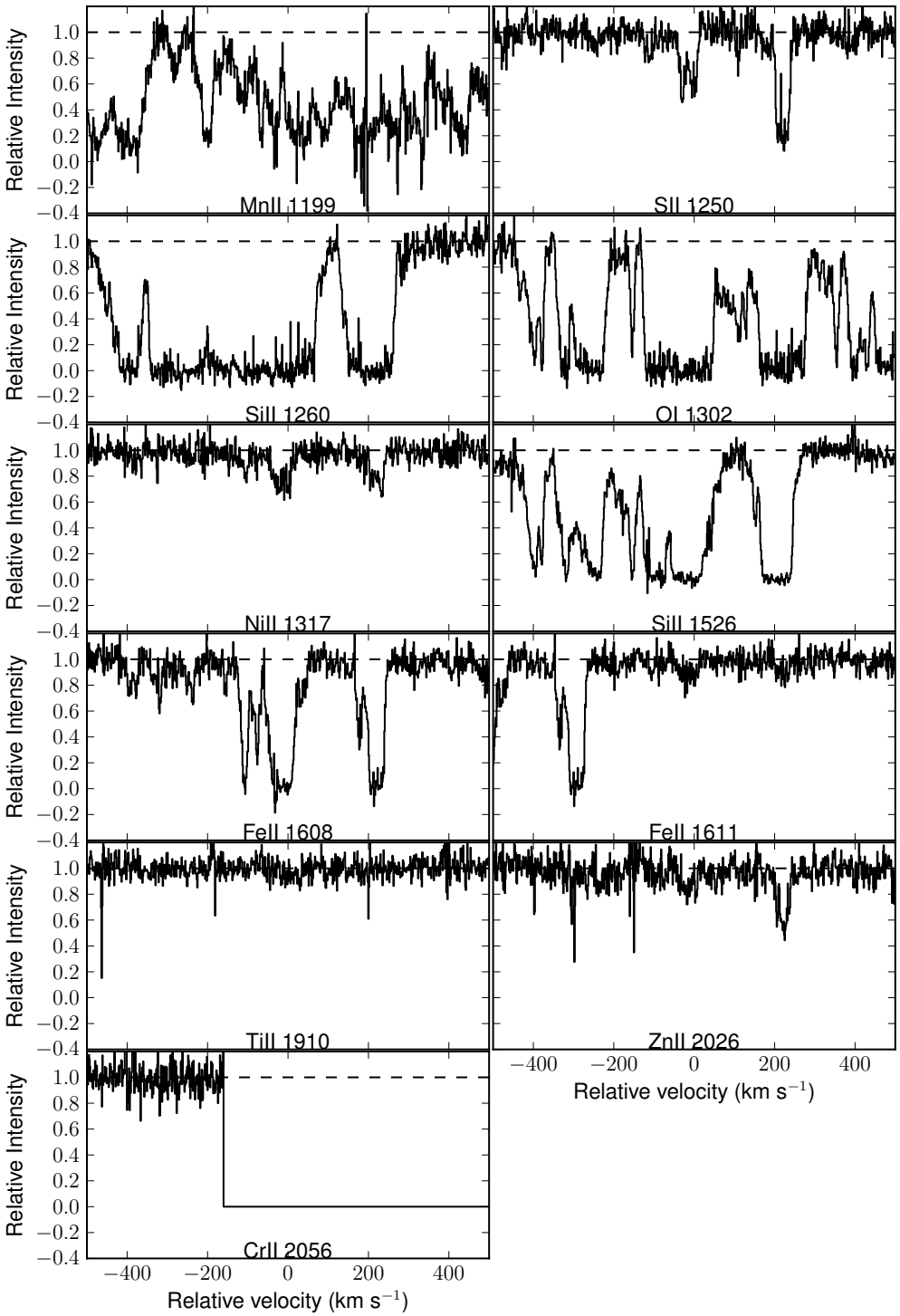

Figure A.18 Absorption line profiles for J1604+3951.

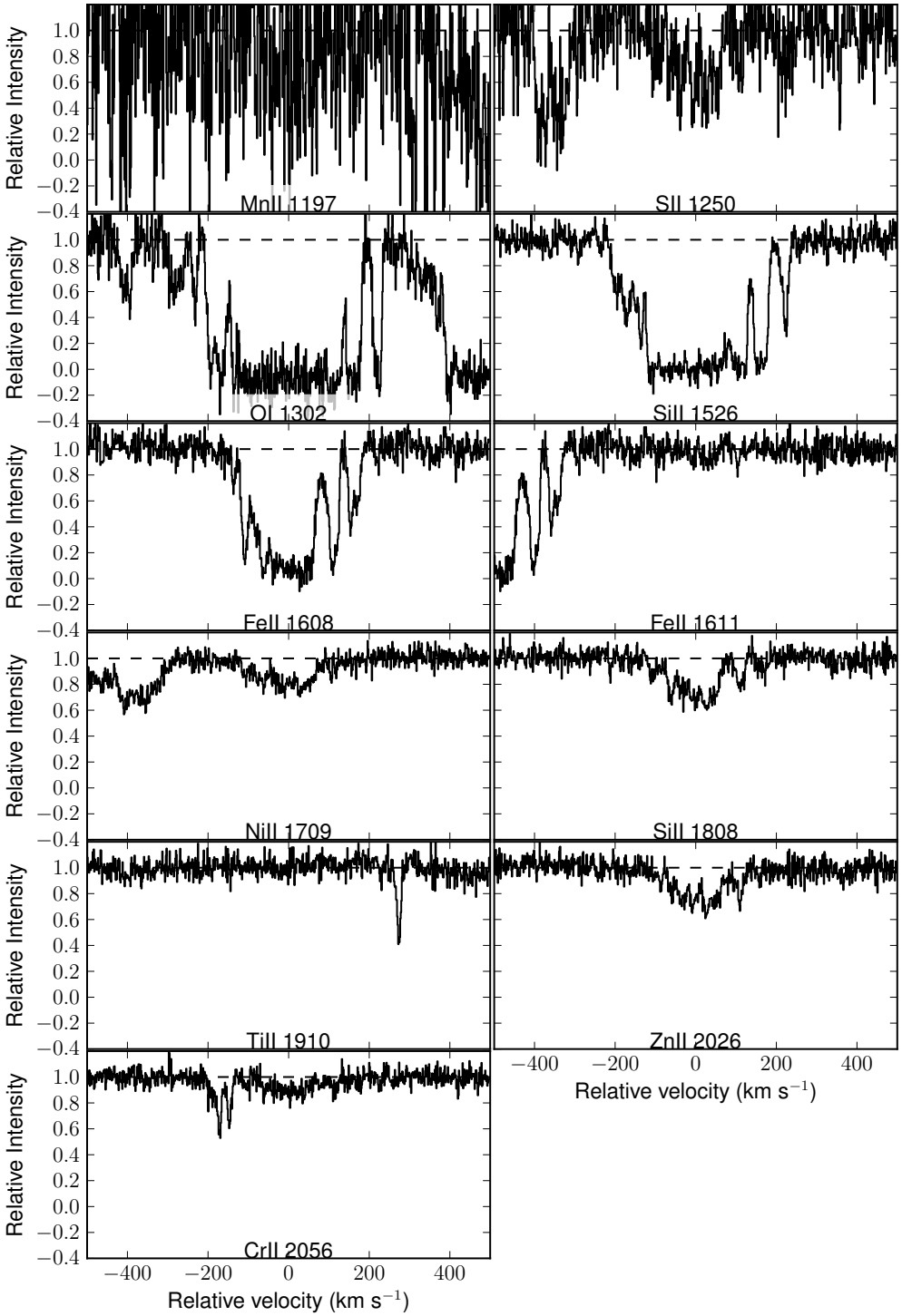

Figure A.19 Absorption line profiles for J0927+5823.

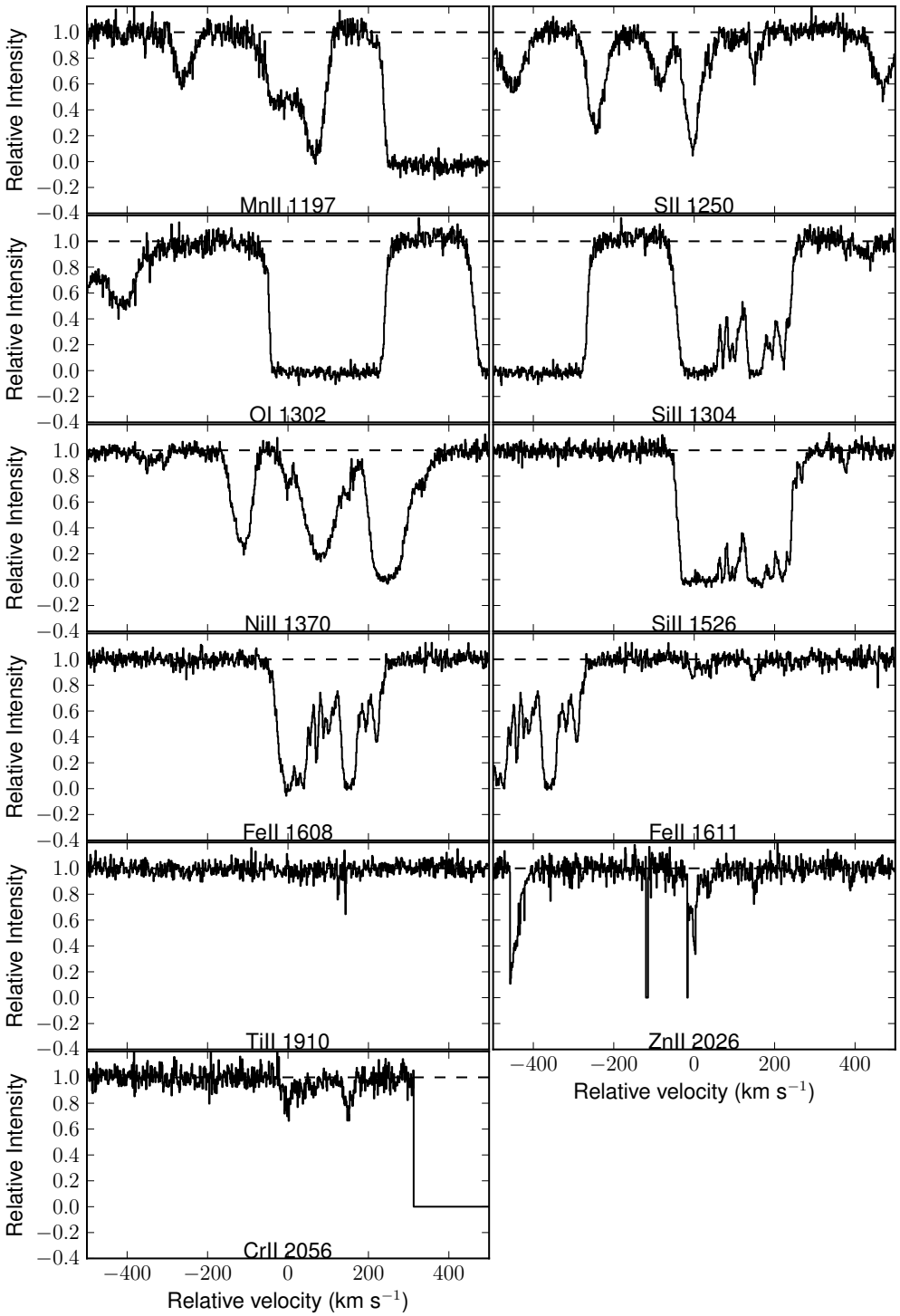

Figure A.20 Absorption line profiles for J0058+0115.

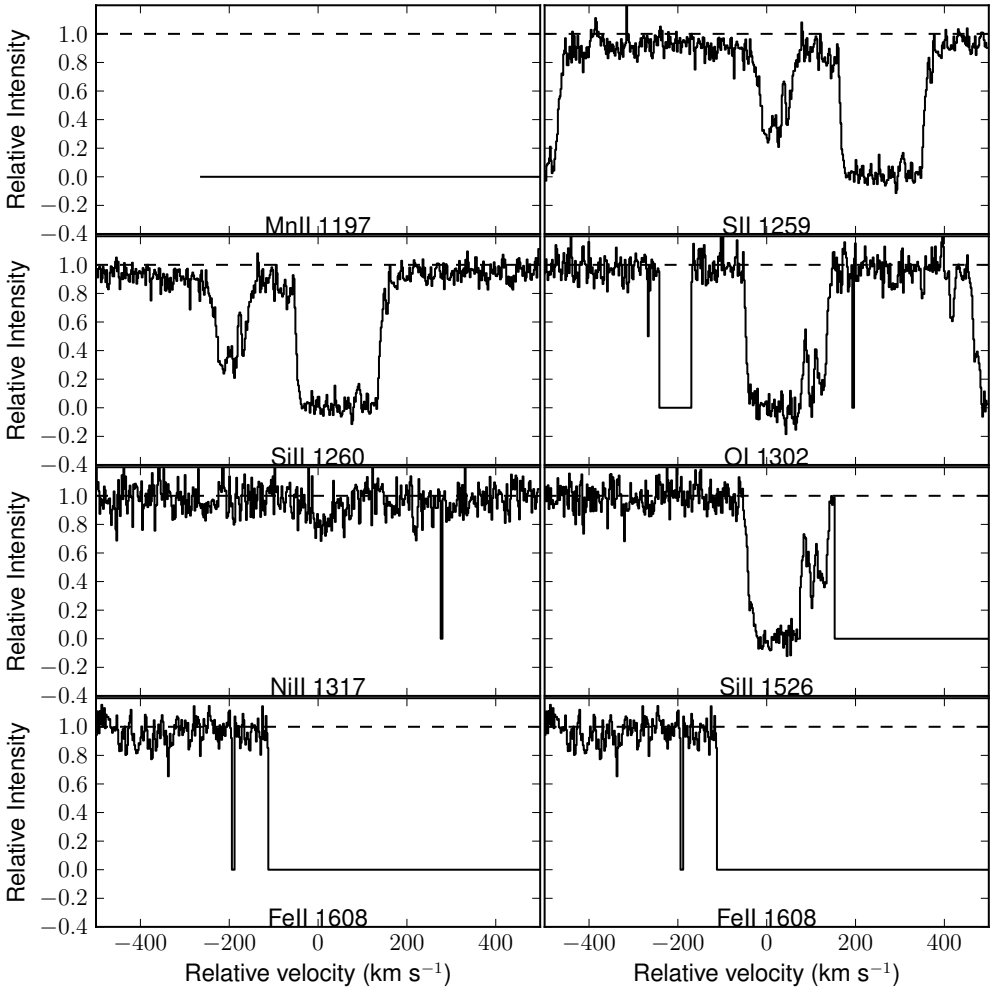

Figure A.21 Absorption line profiles for Q2342+34.

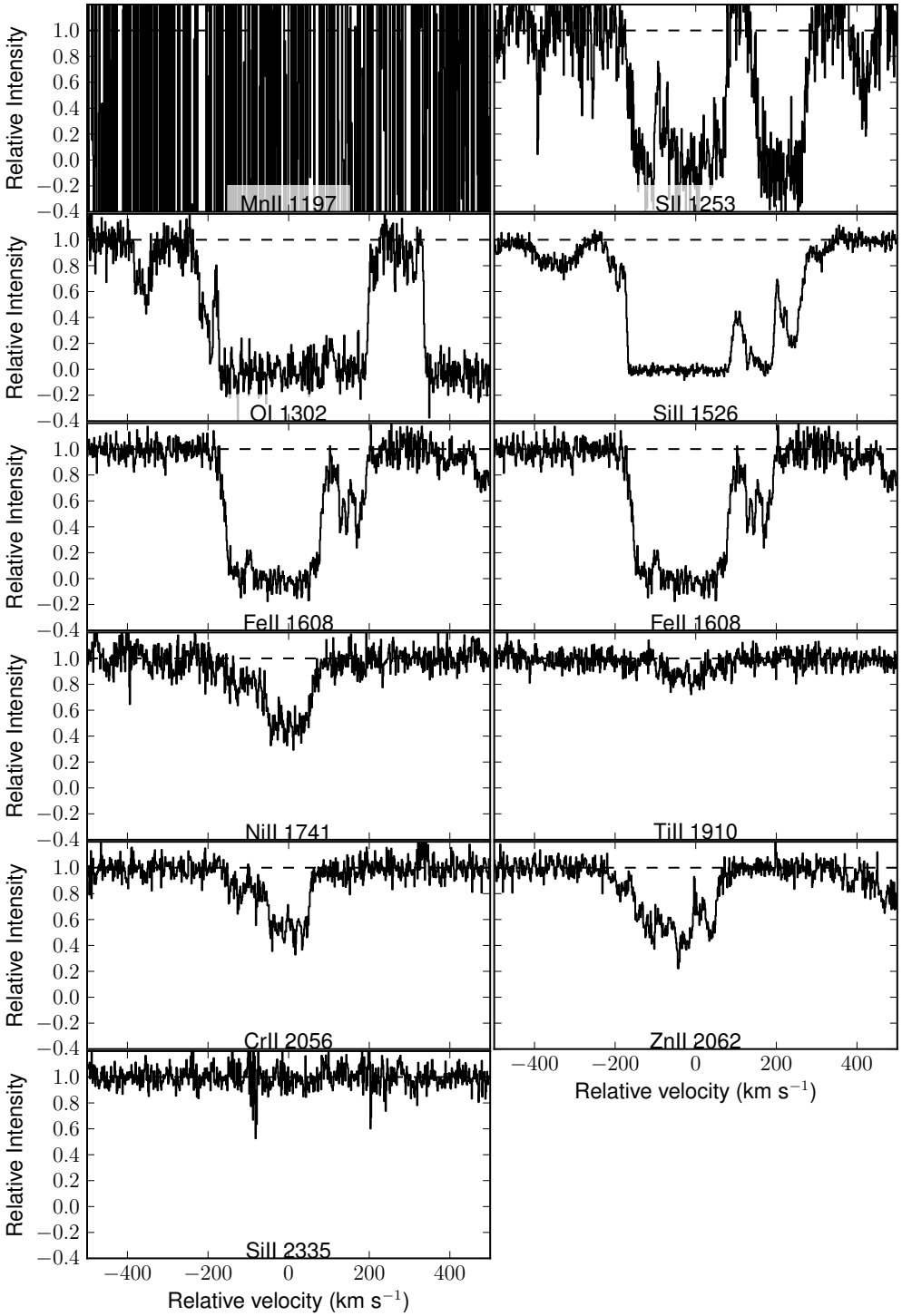

Figure A.22 Absorption line profiles for J1555+4800.

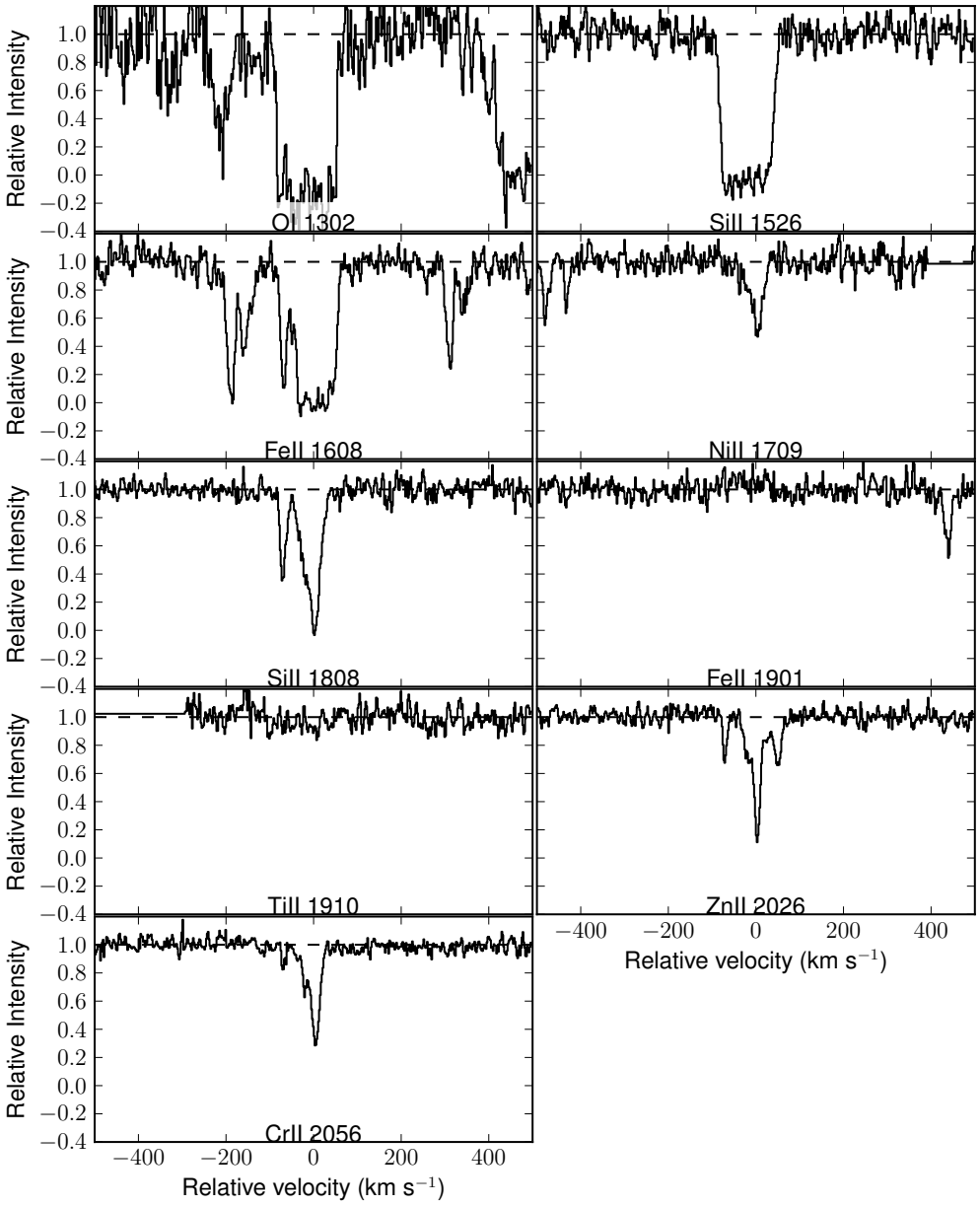

Figure A.23 Absorption line profiles for Q0458-02.

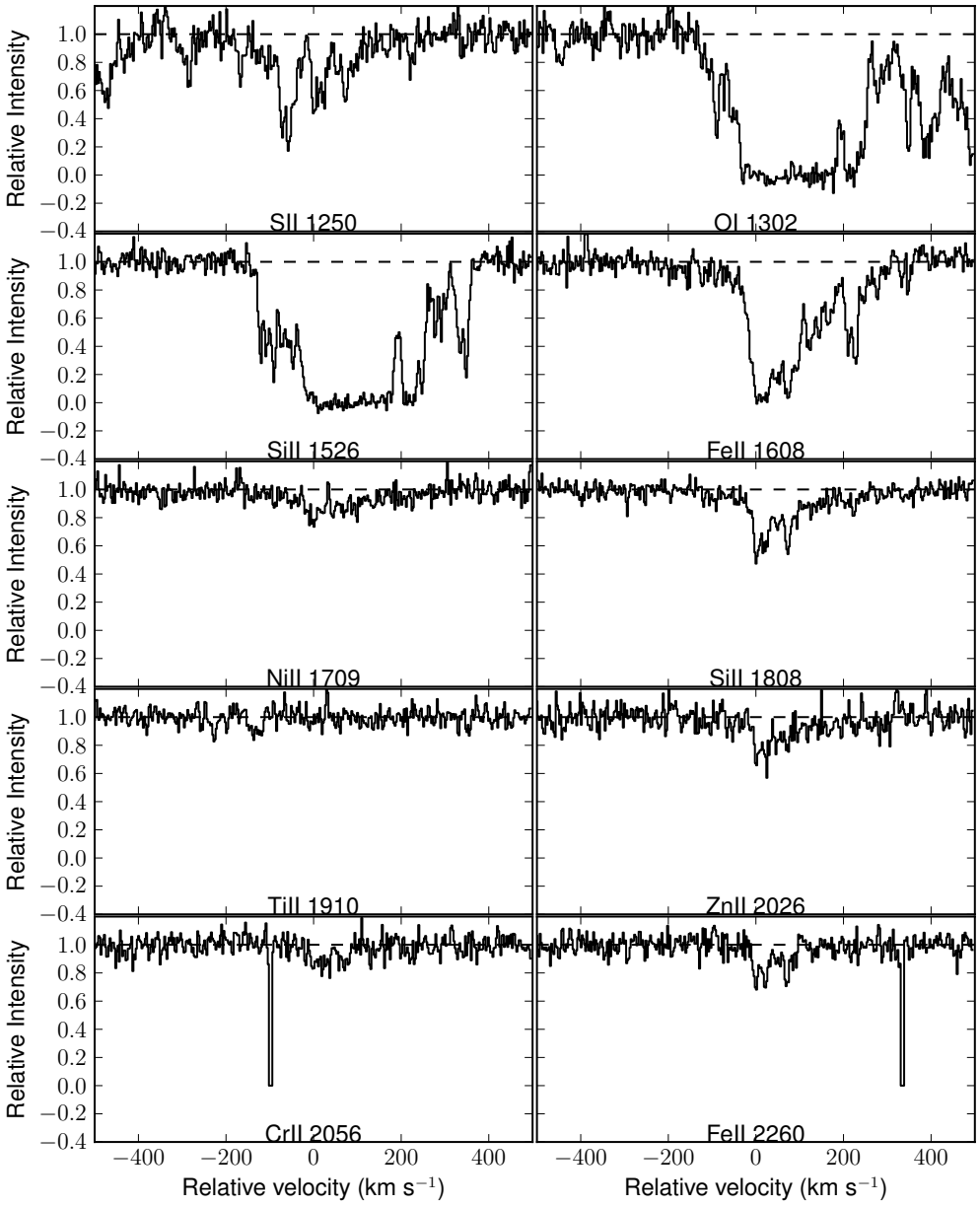

Figure A.24 Absorption line profiles for J1049-0110.

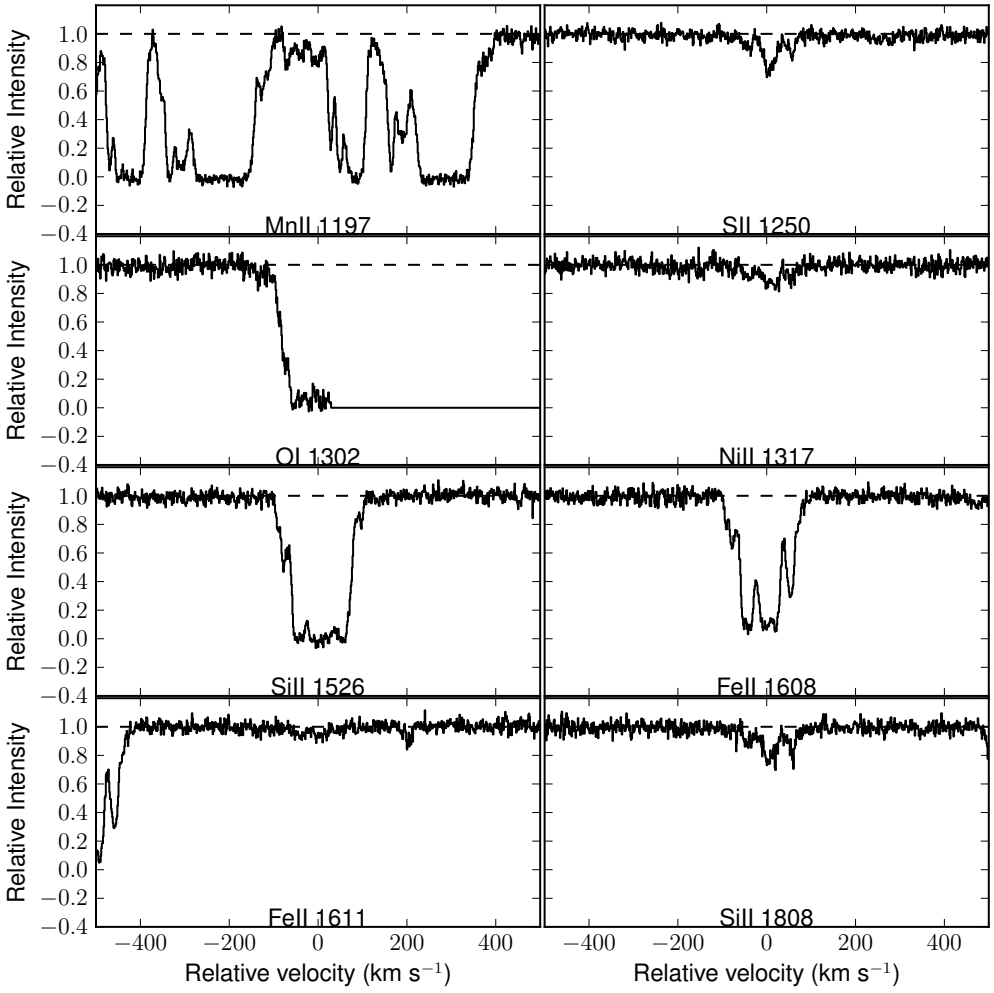

Figure A.25 Absorption line profiles for J2340-0053.

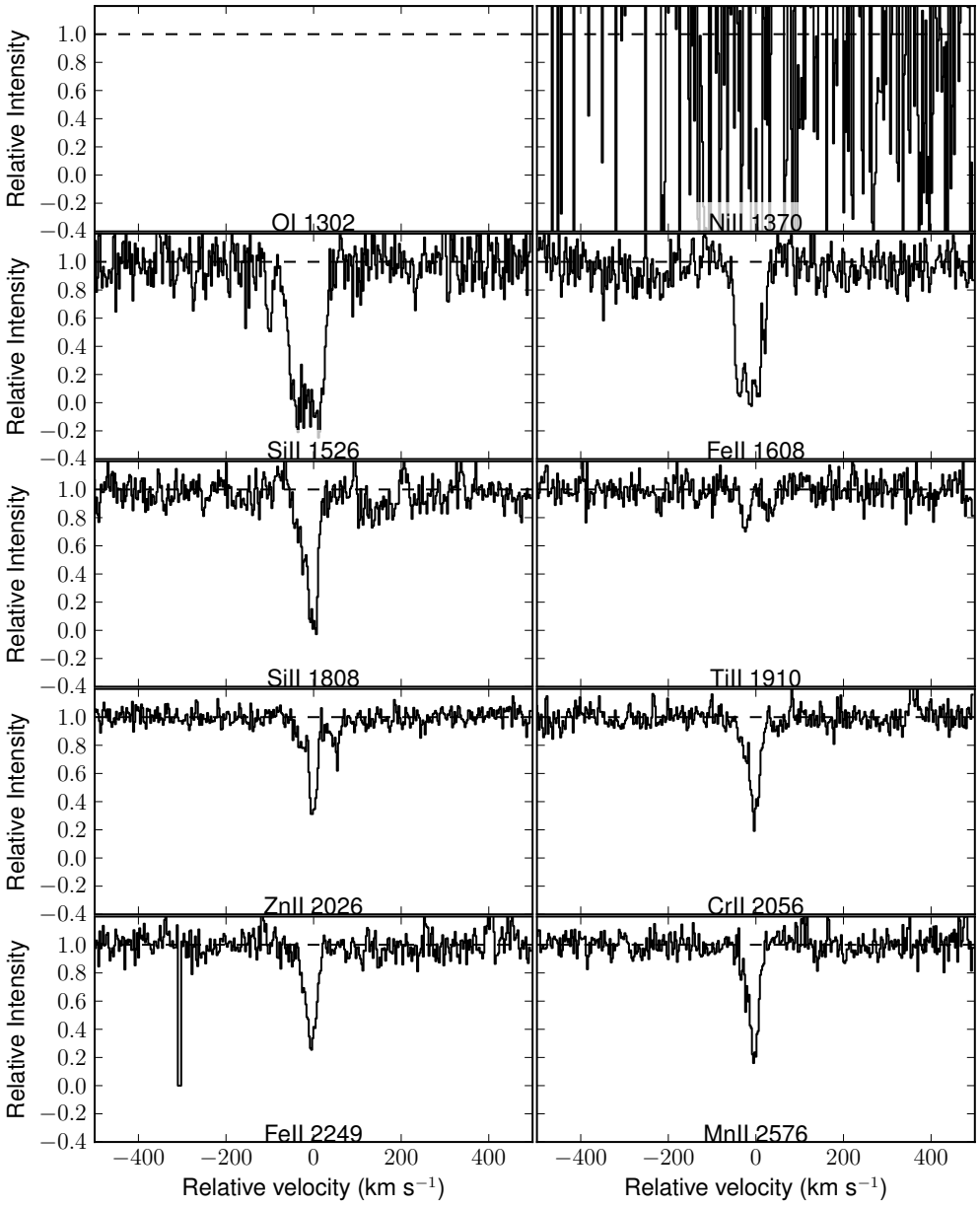

Figure A.26 Absorption line profiles for J1010+0003.

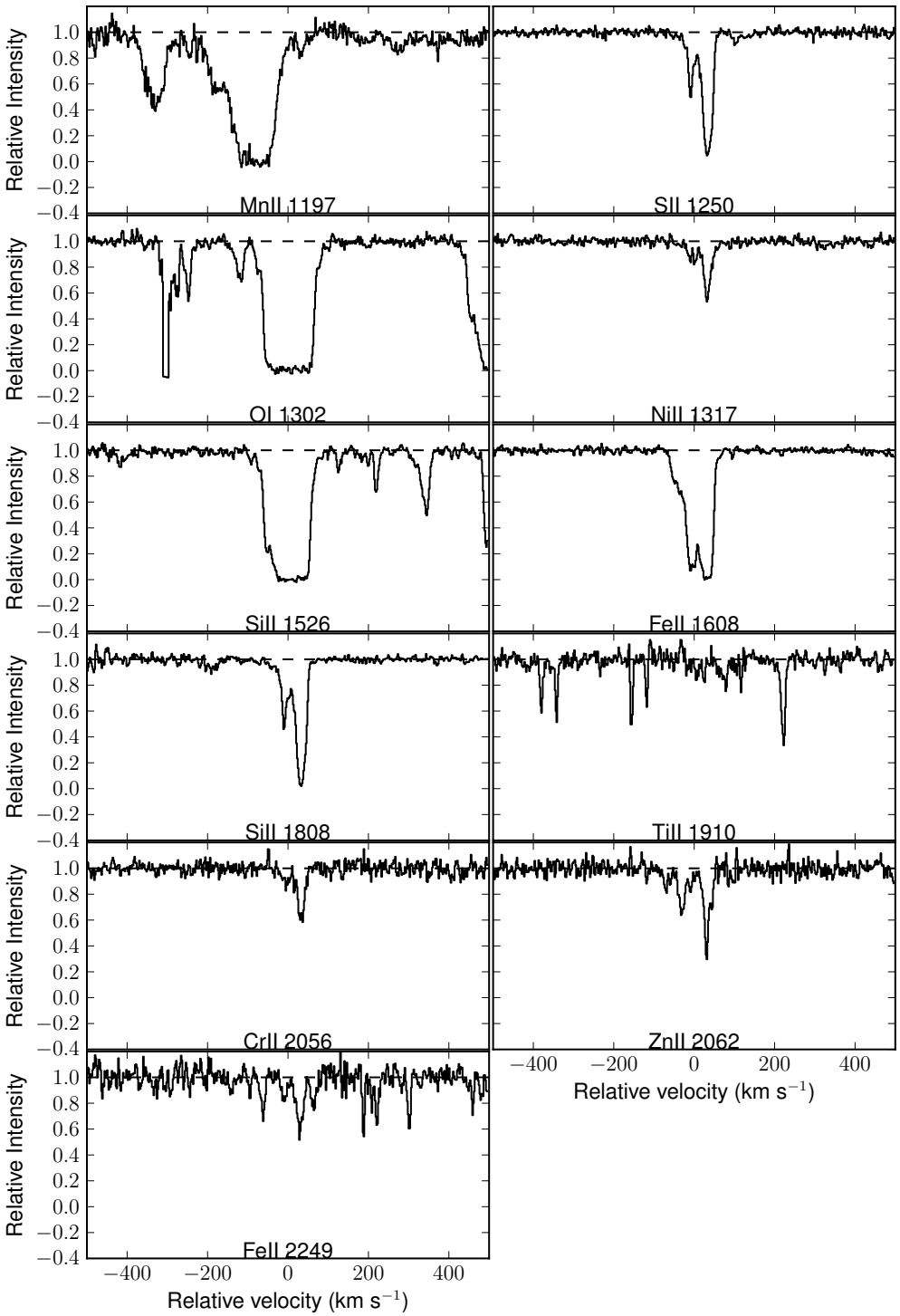

Figure A.27 Absorption line profiles for FJ0812+3208.

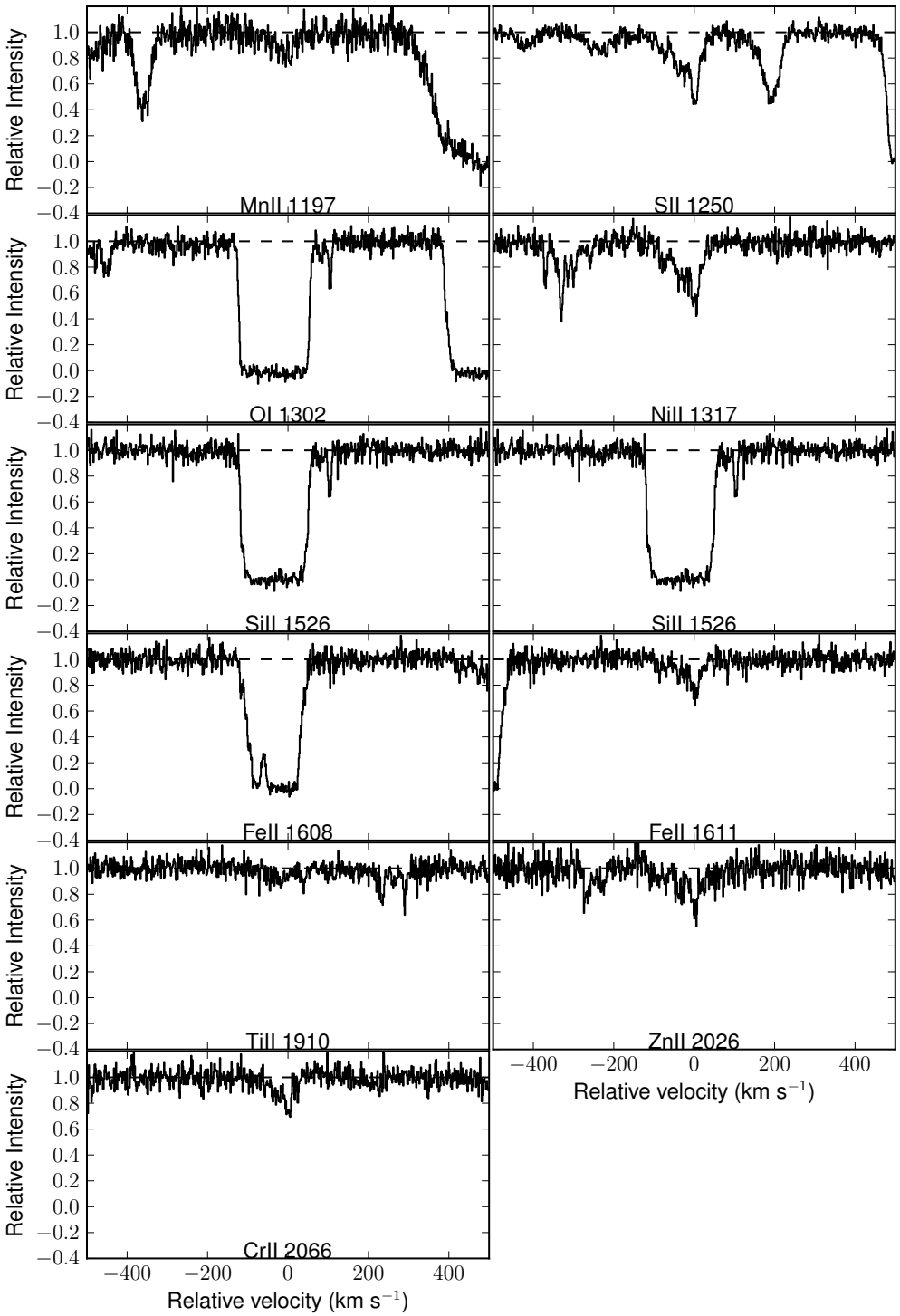

Figure A.28 Absorption line profiles for J1552+4910.

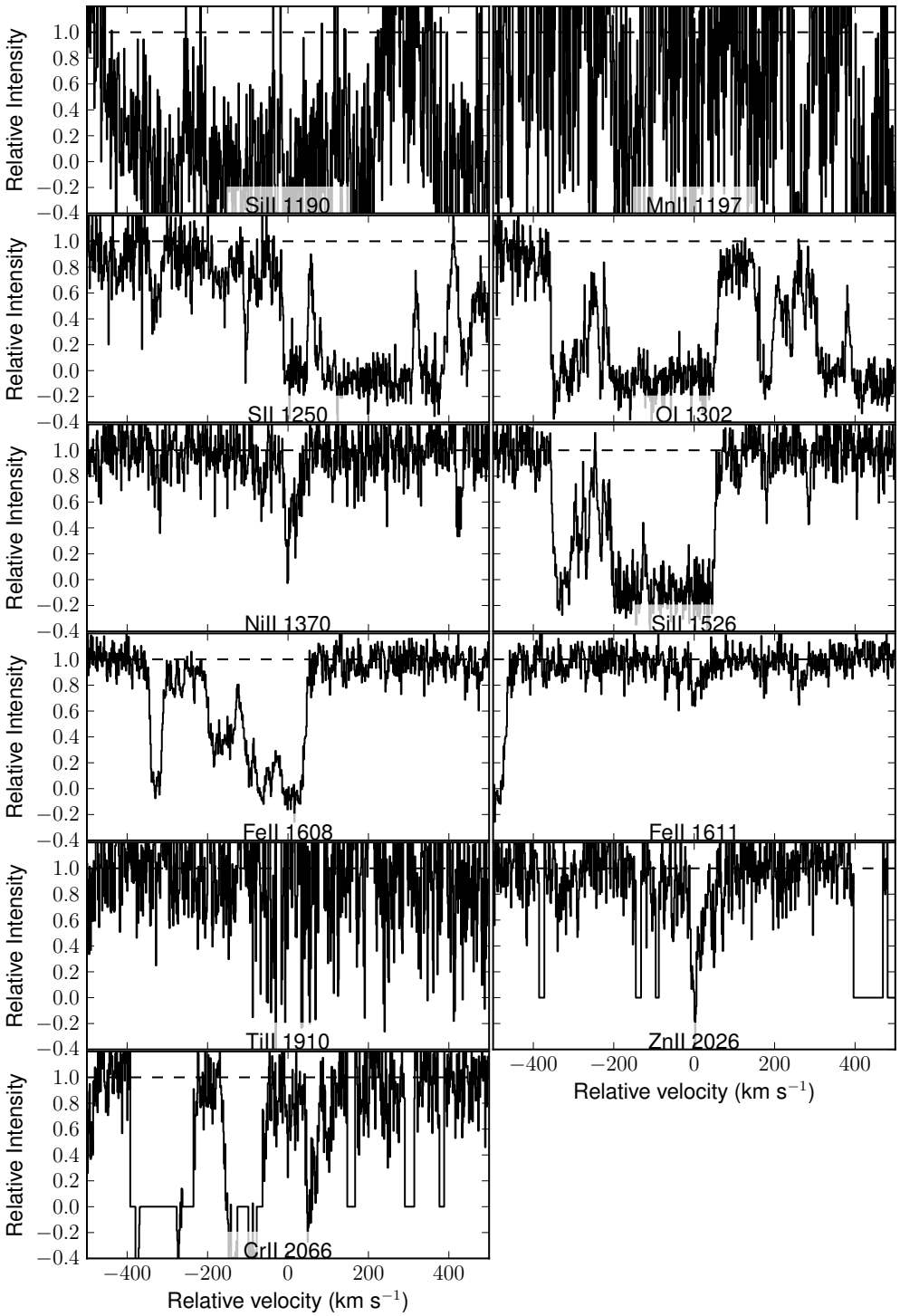

Figure A.29 Absorption line profiles for J1524+1030.

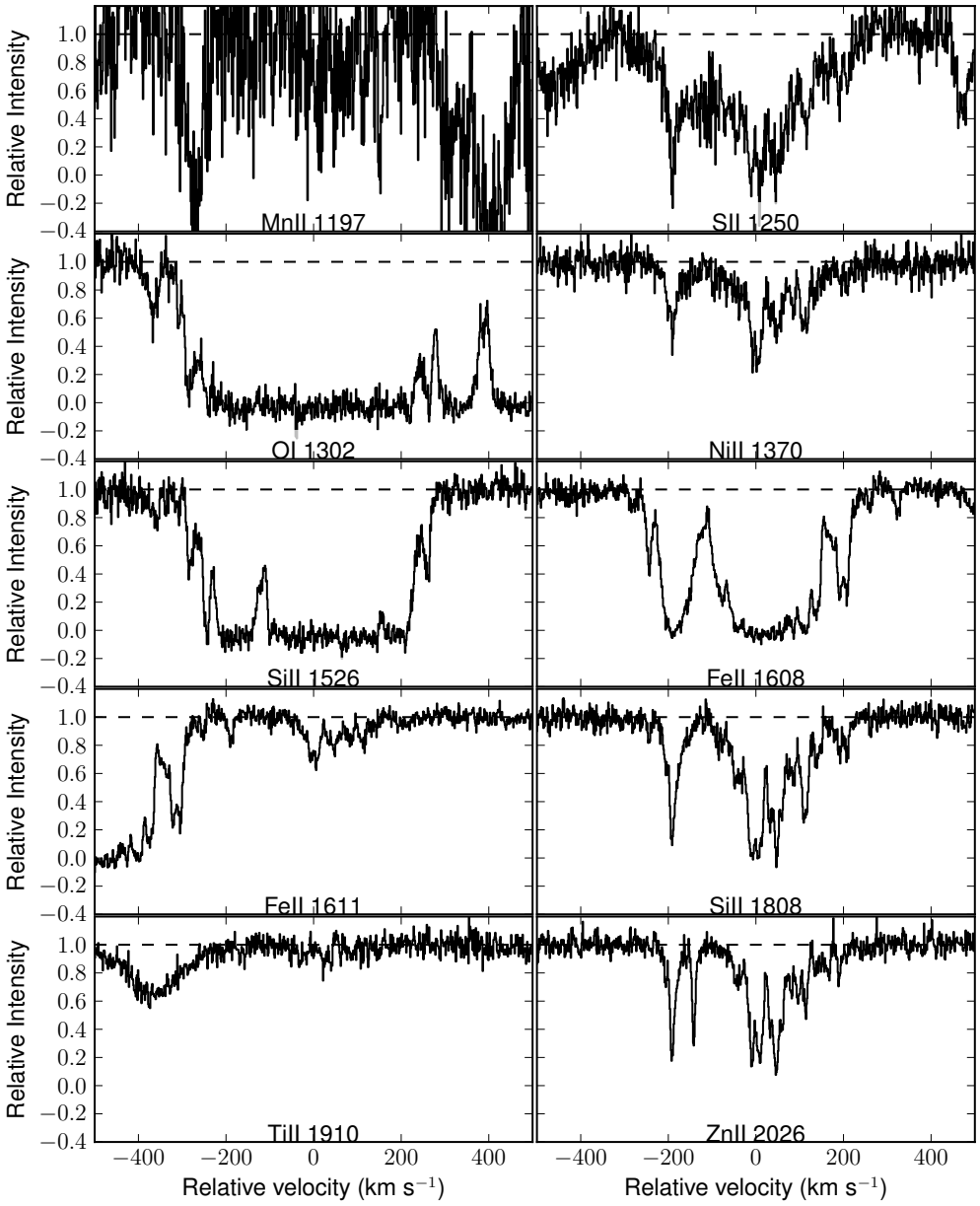

Figure A.30 Absorption line profiles for Q1755+578.

A.3 Thesis Sample AODM Measurements

Figures A.31 – A.60 show the absorption profiles used for the derivation of the column densities (Table 2.5). The vertical dotted lines represent the AODM bounds in velocity space. The horizontal dashed lines represents the continuum.

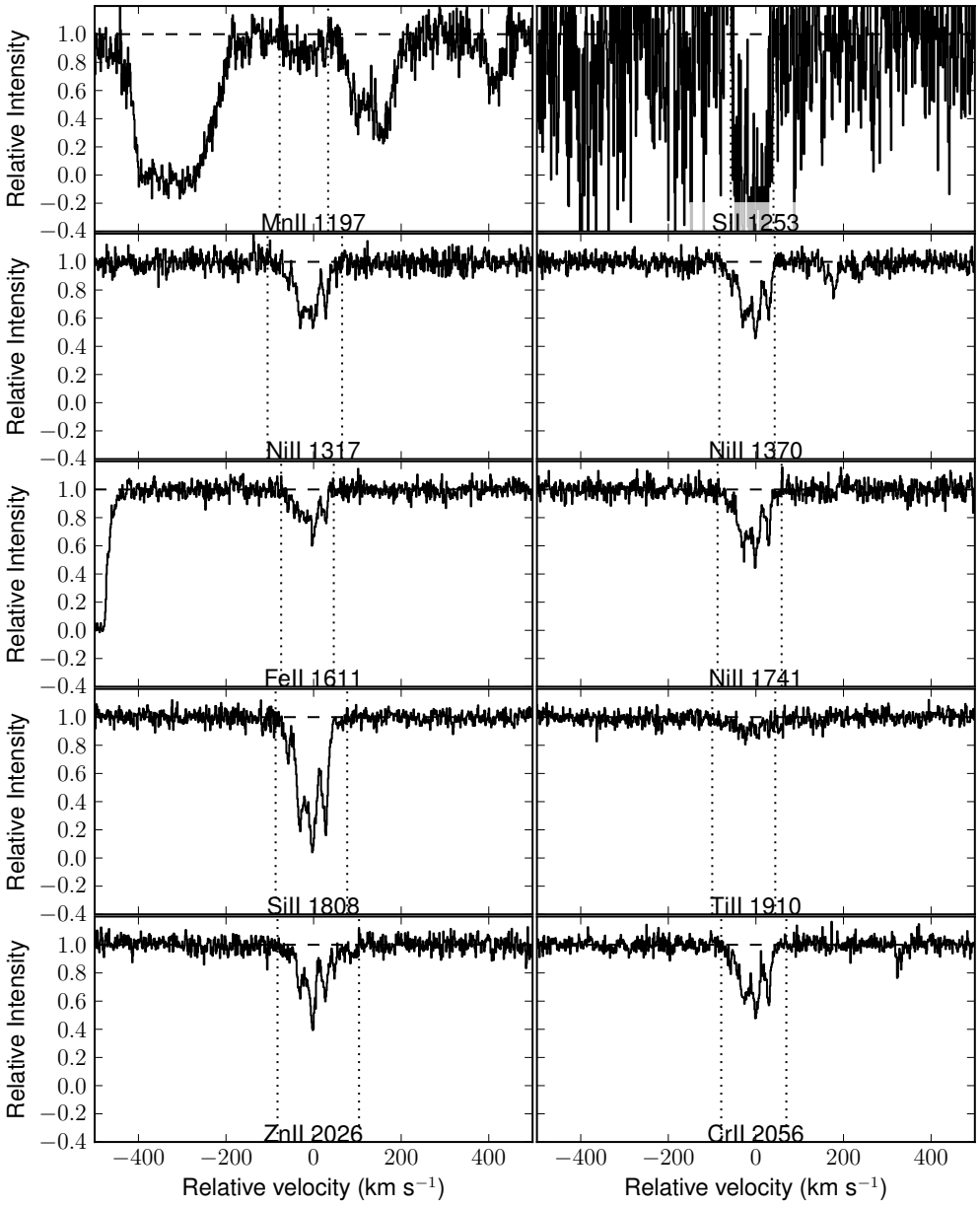

Figure A.31 Absorption line profiles for J1159+0112.

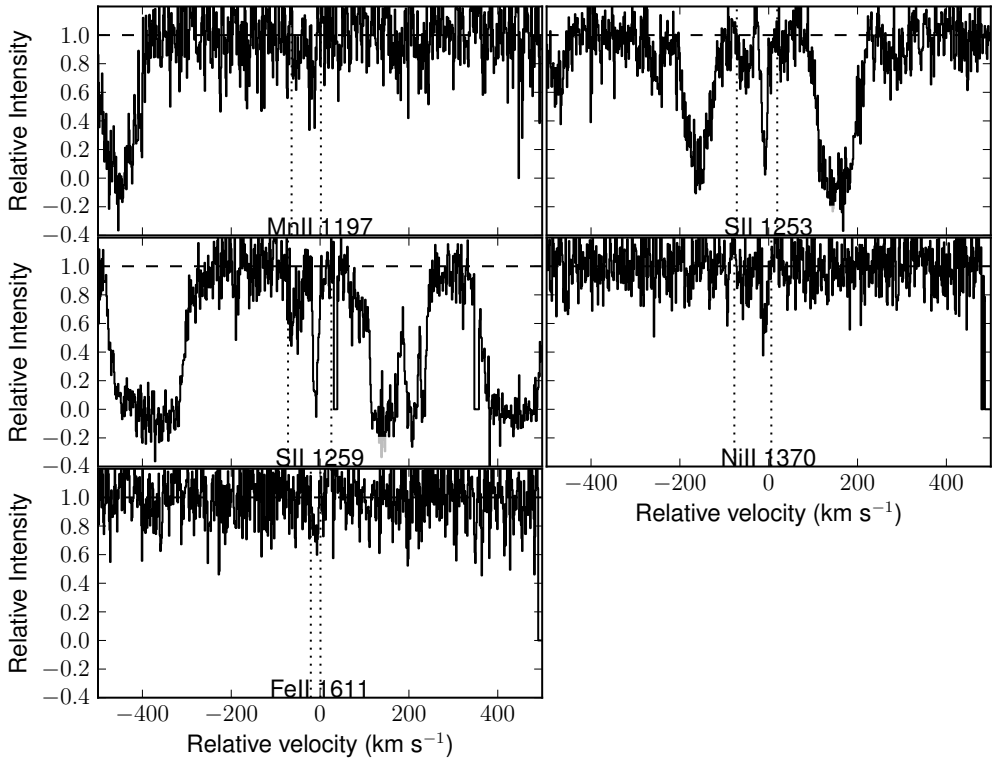

Figure A.32 Absorption line profiles for J2241+1225.

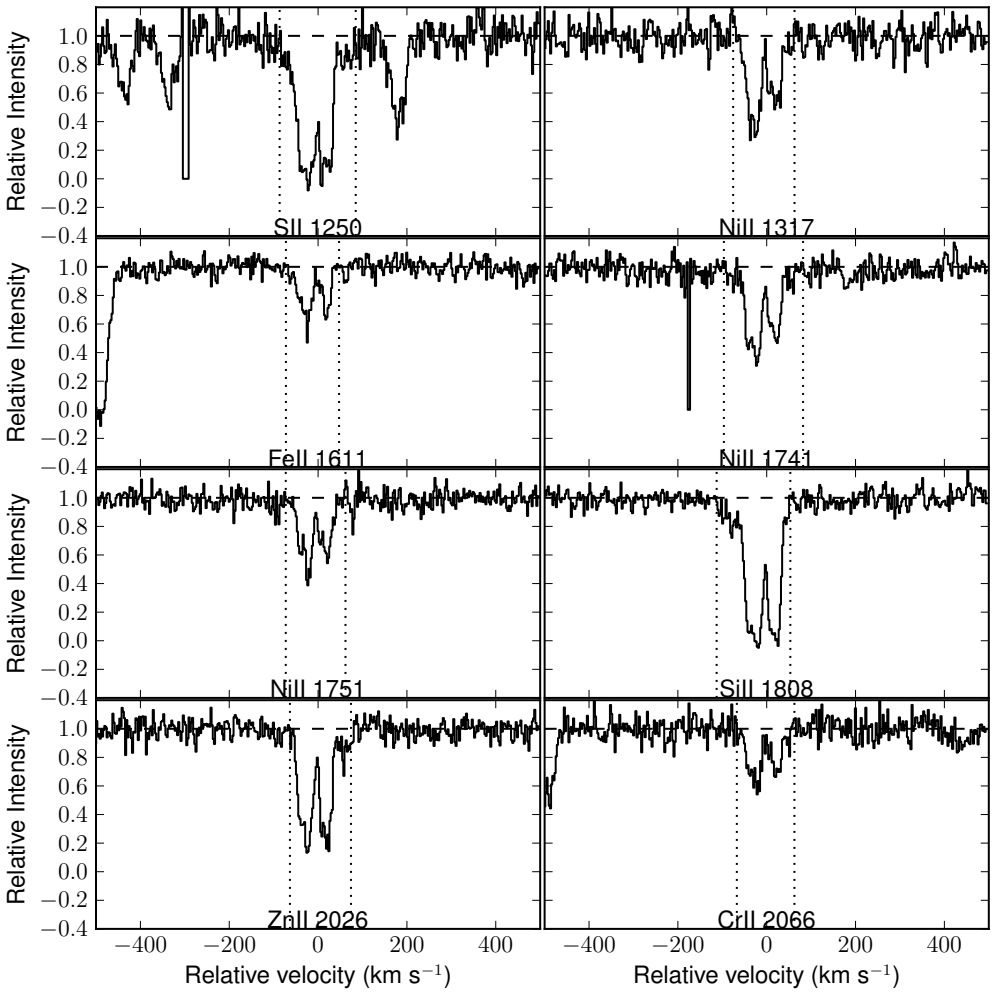

Figure A.33 Absorption line profiles for J1310+5424.

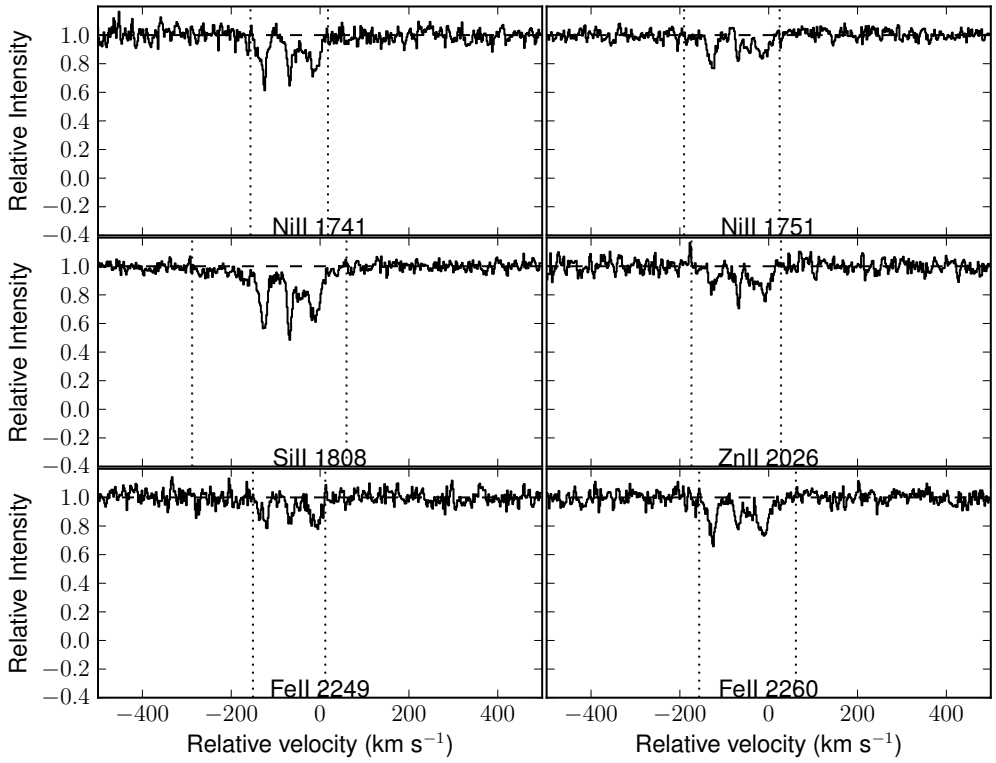

Figure A.34 Absorption line profiles for Q2230+02.

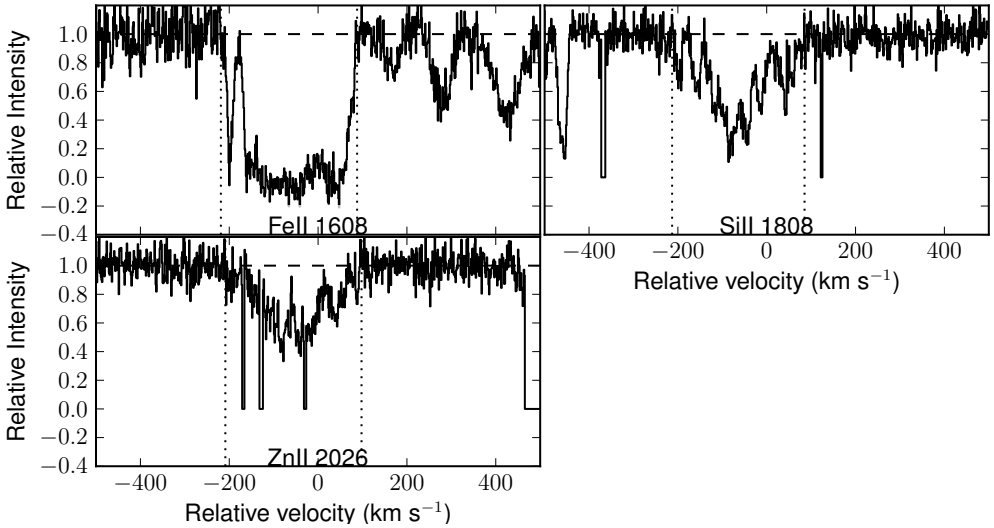

Figure A.35 Absorption line profiles for J1013+5615.

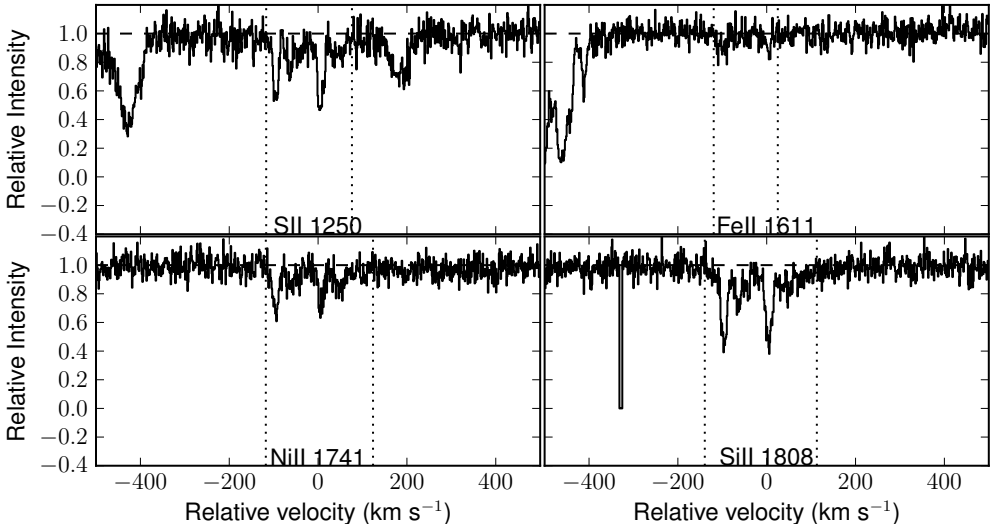

Figure A.36 Absorption line profiles for J2222-0945.

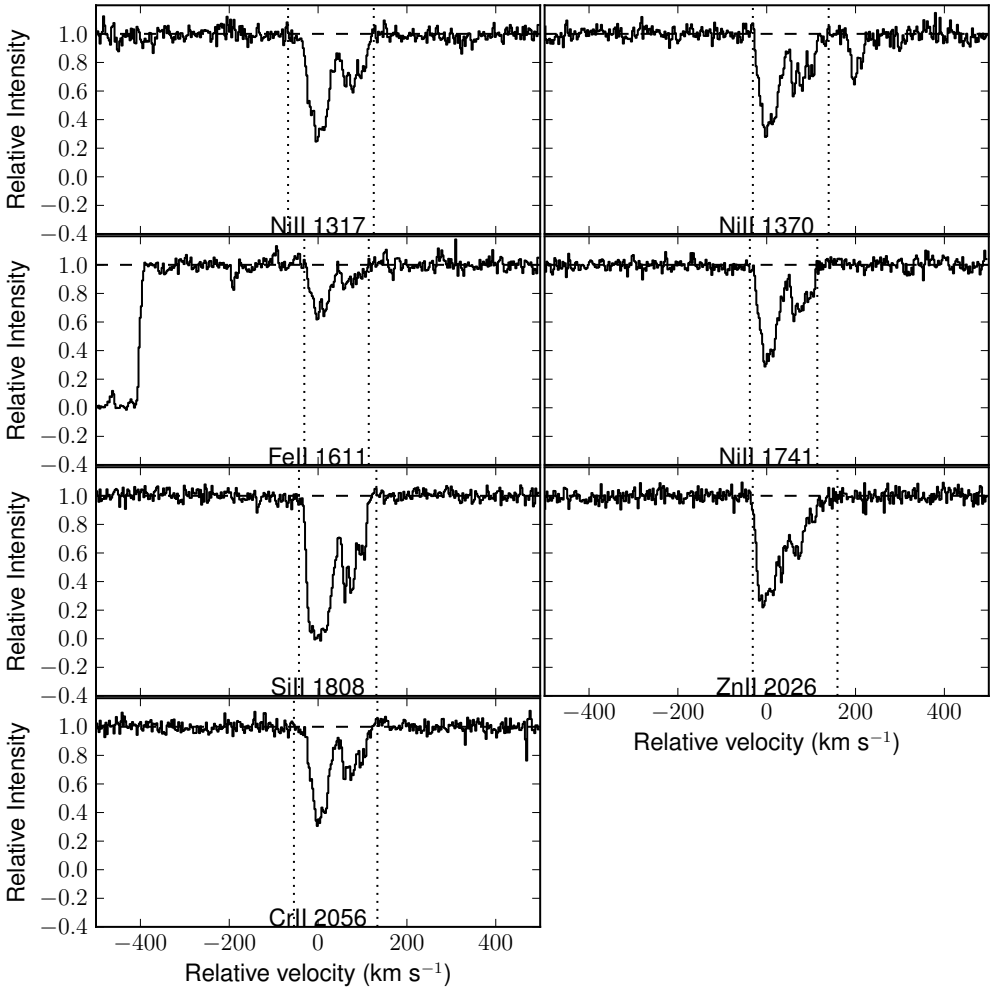

Figure A.37 Absorption line profiles for J1417+4132.

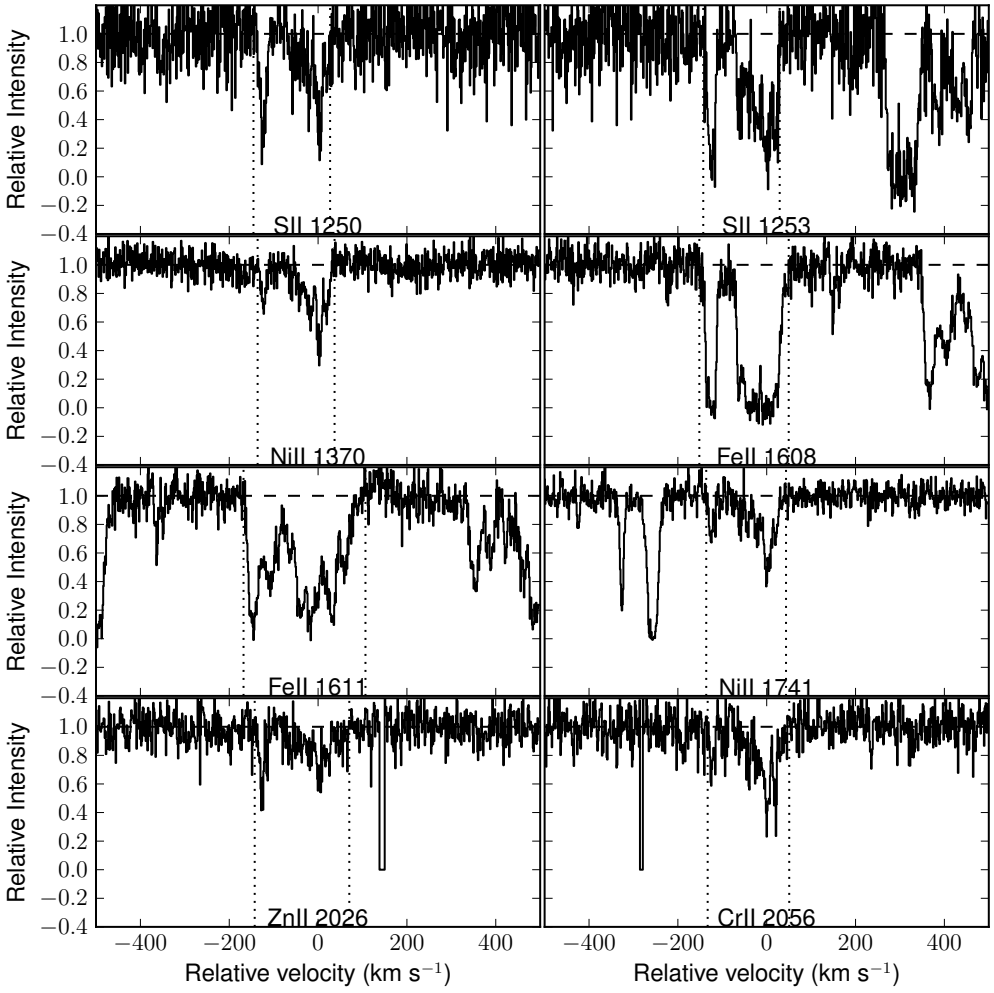

Figure A.38 Absorption line profiles for J1249-0233.

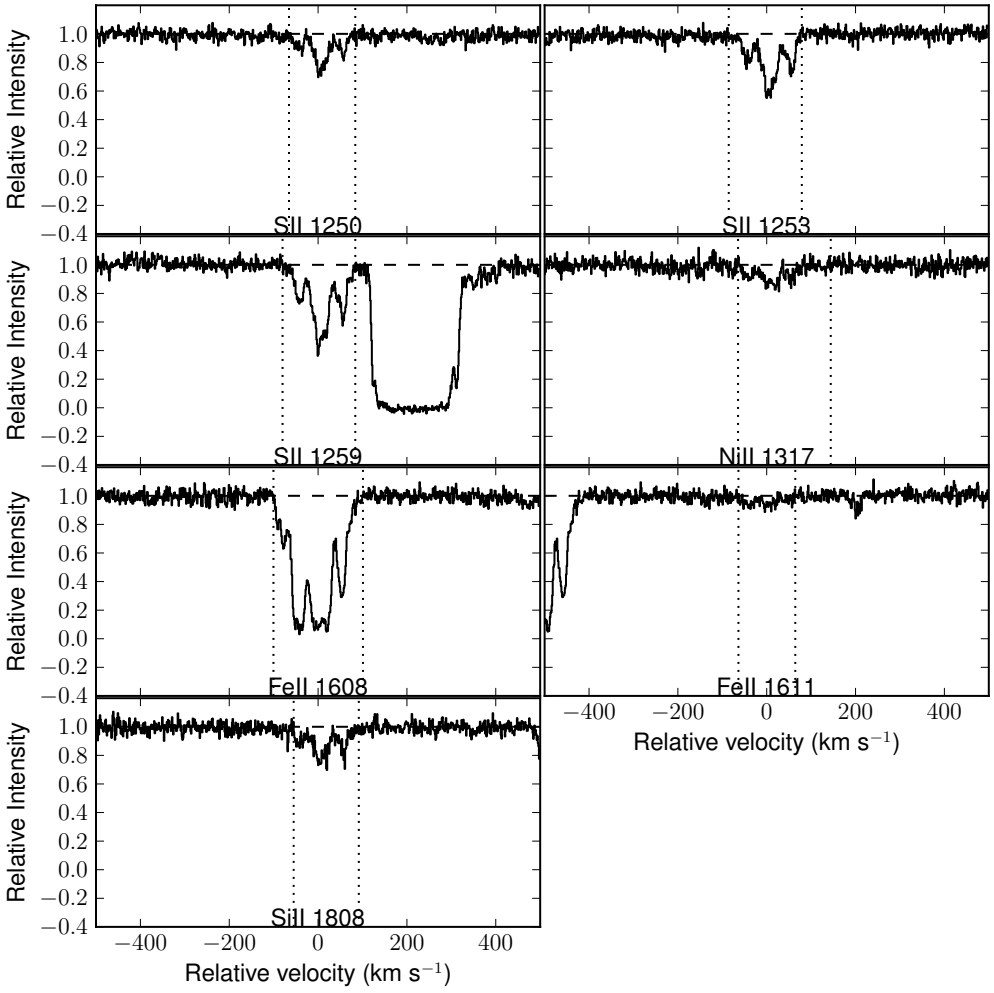

Figure A.39 Absorption line profiles for J2340-0053.

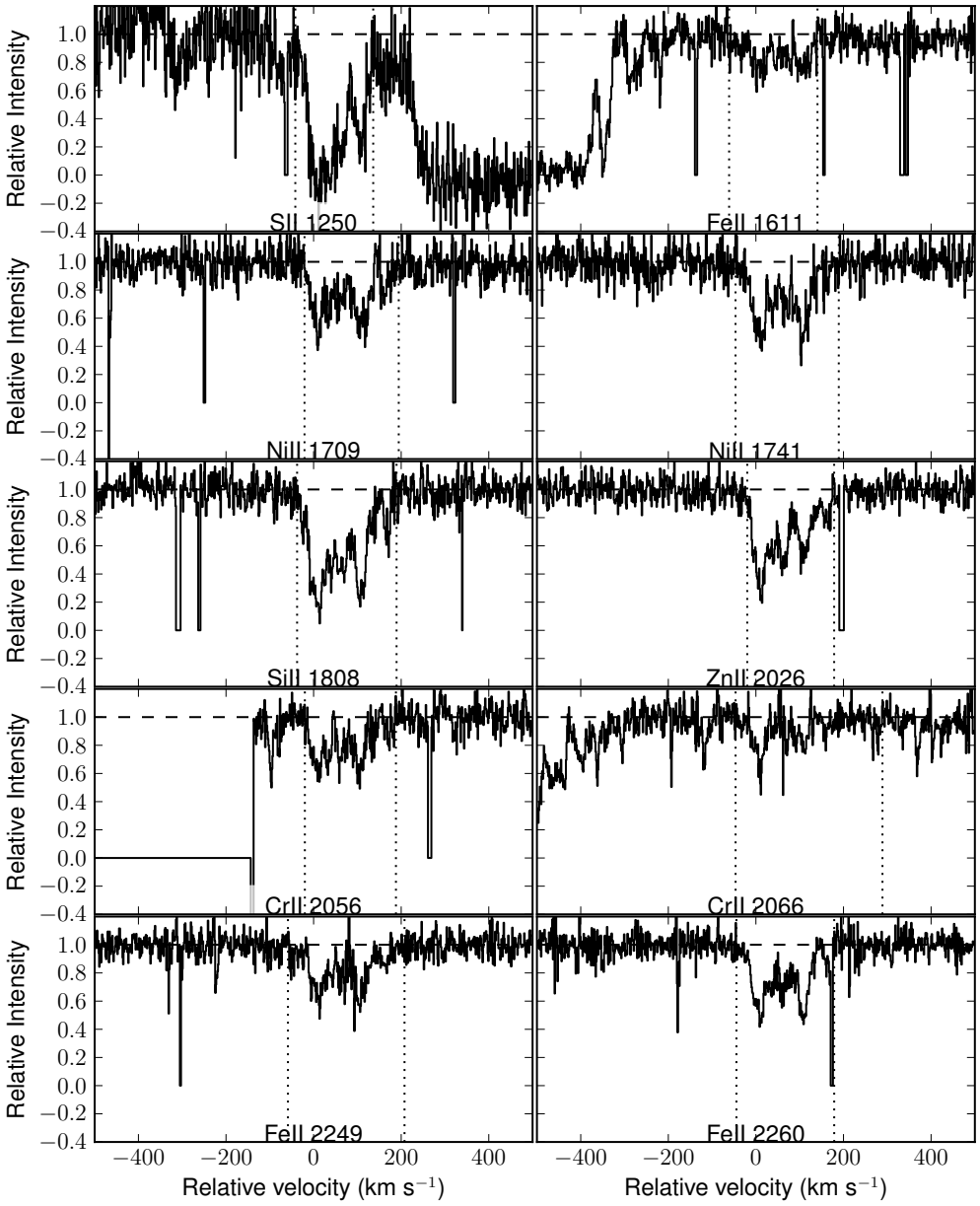

Figure A.40 Absorption line profiles for J1610+4724.

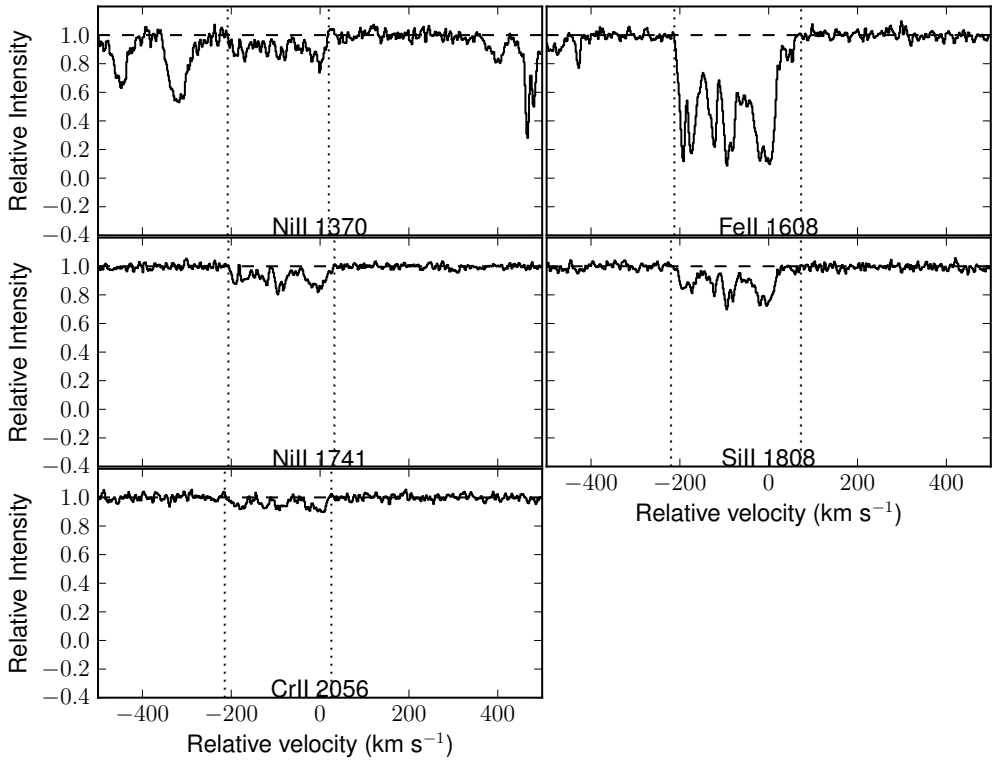

Figure A.41 Absorption line profiles for Q0201+36.

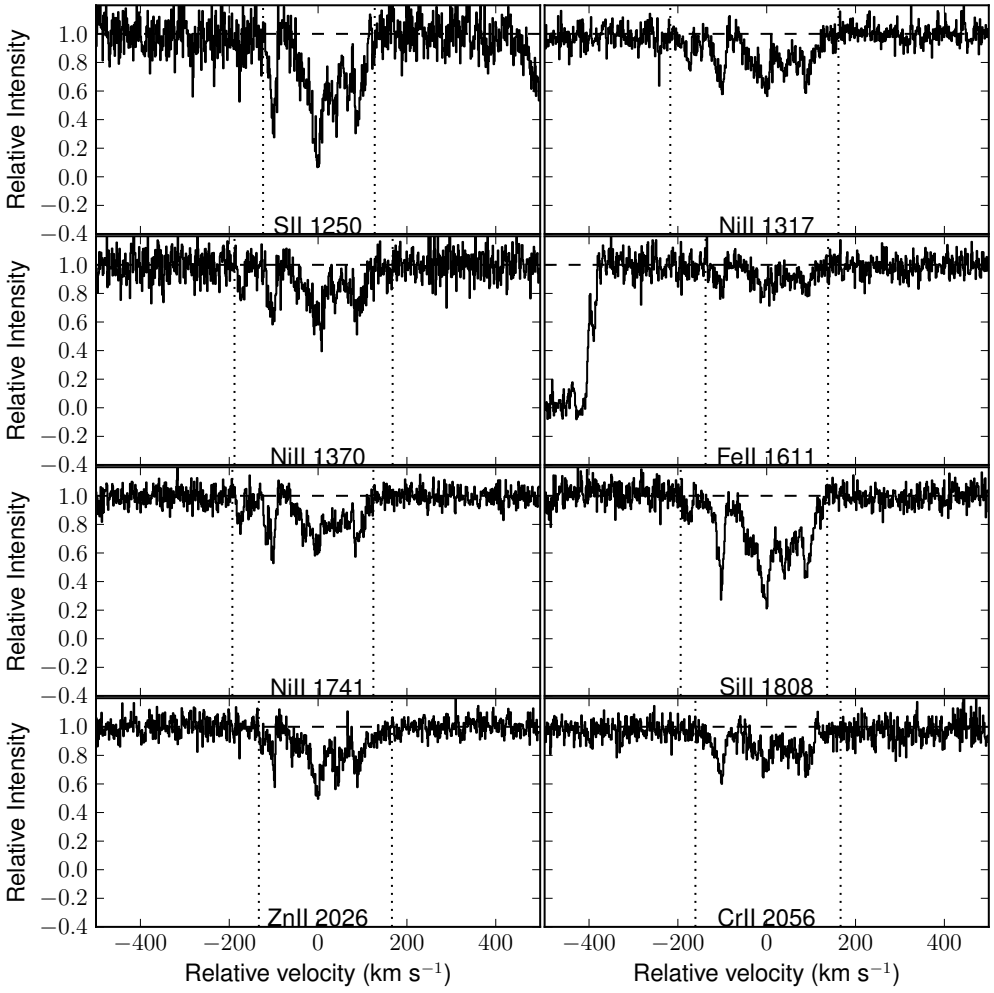

Figure A.42 Absorption line profiles for J0008-0958.

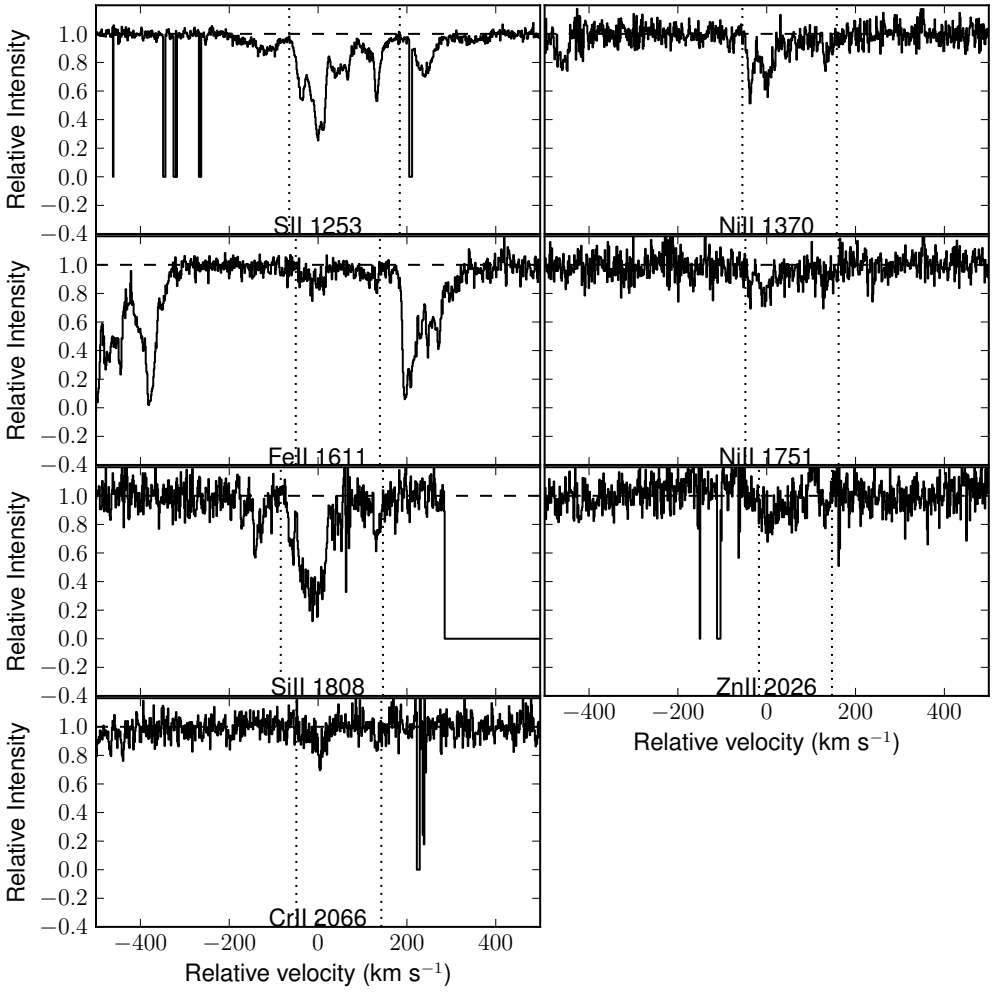

Figure A.43 Absorption line profiles for J1155+0530.

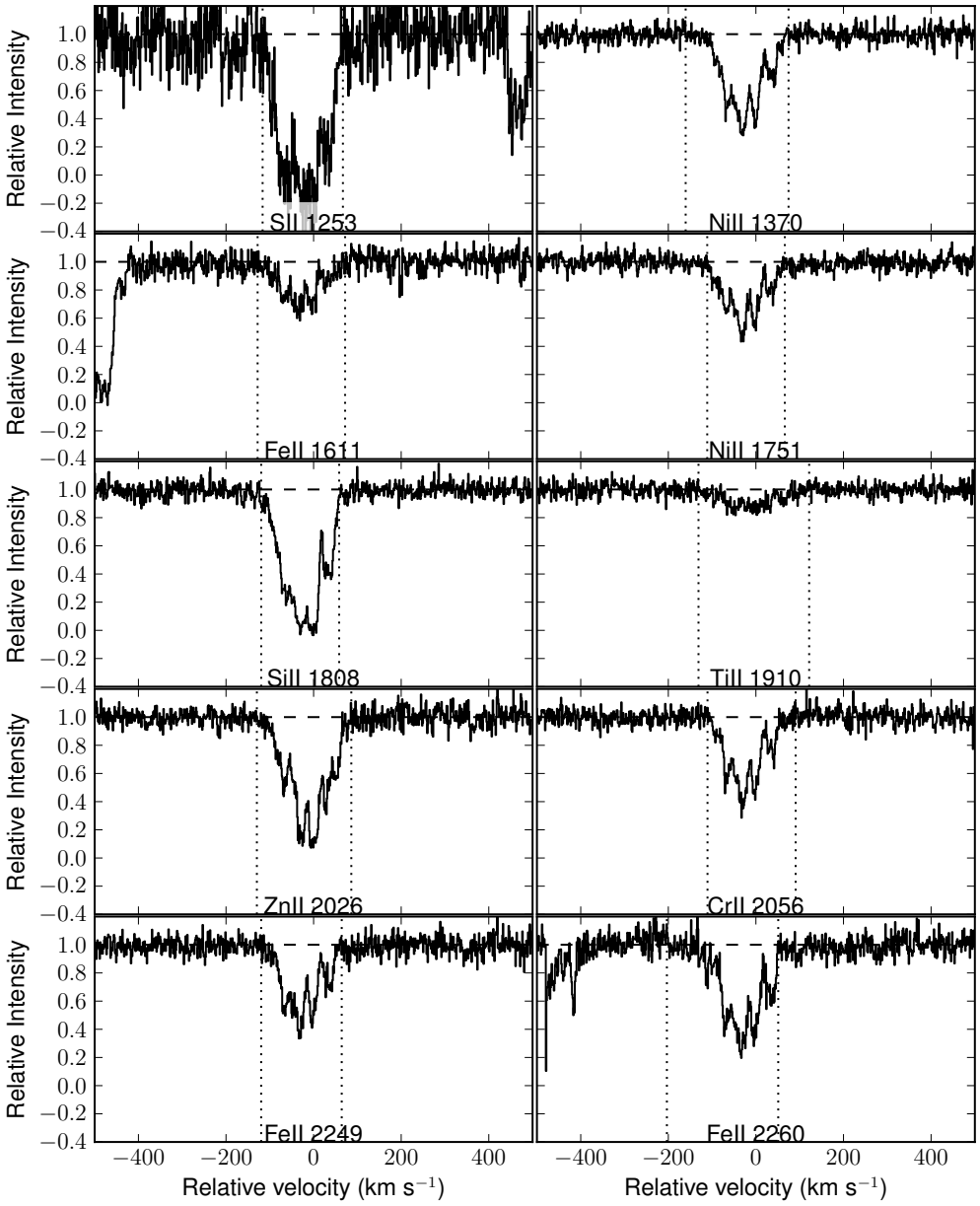

Figure A.44 Absorption line profiles for J1056+1208.

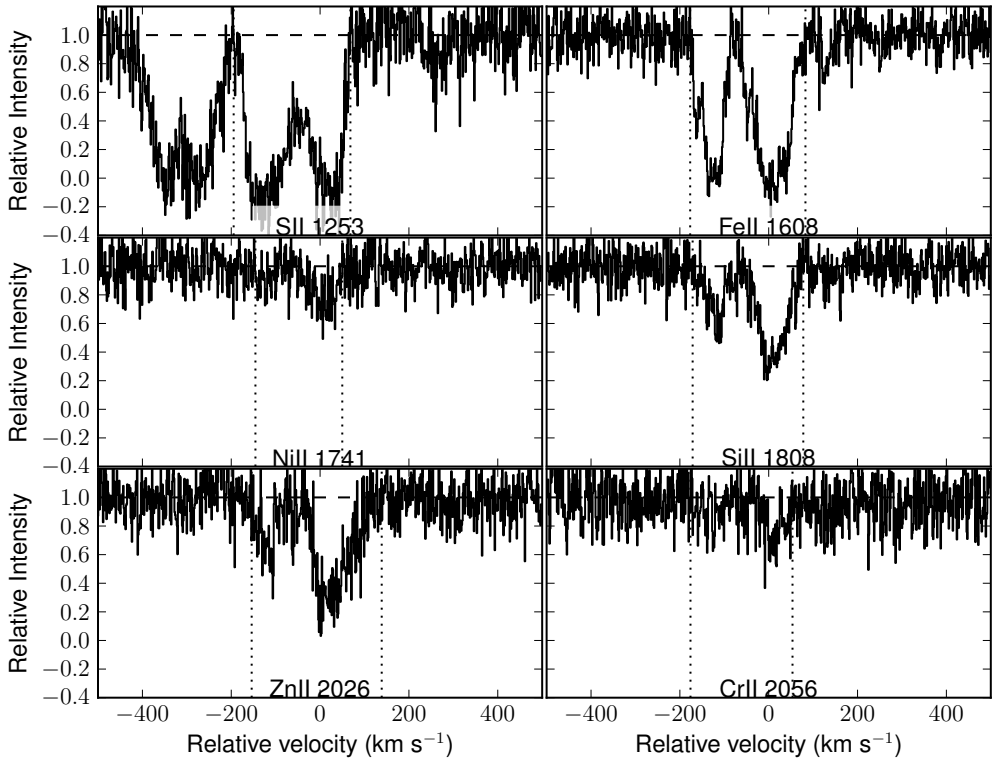

Figure A.45 Absorption line profiles for J0927+1543.

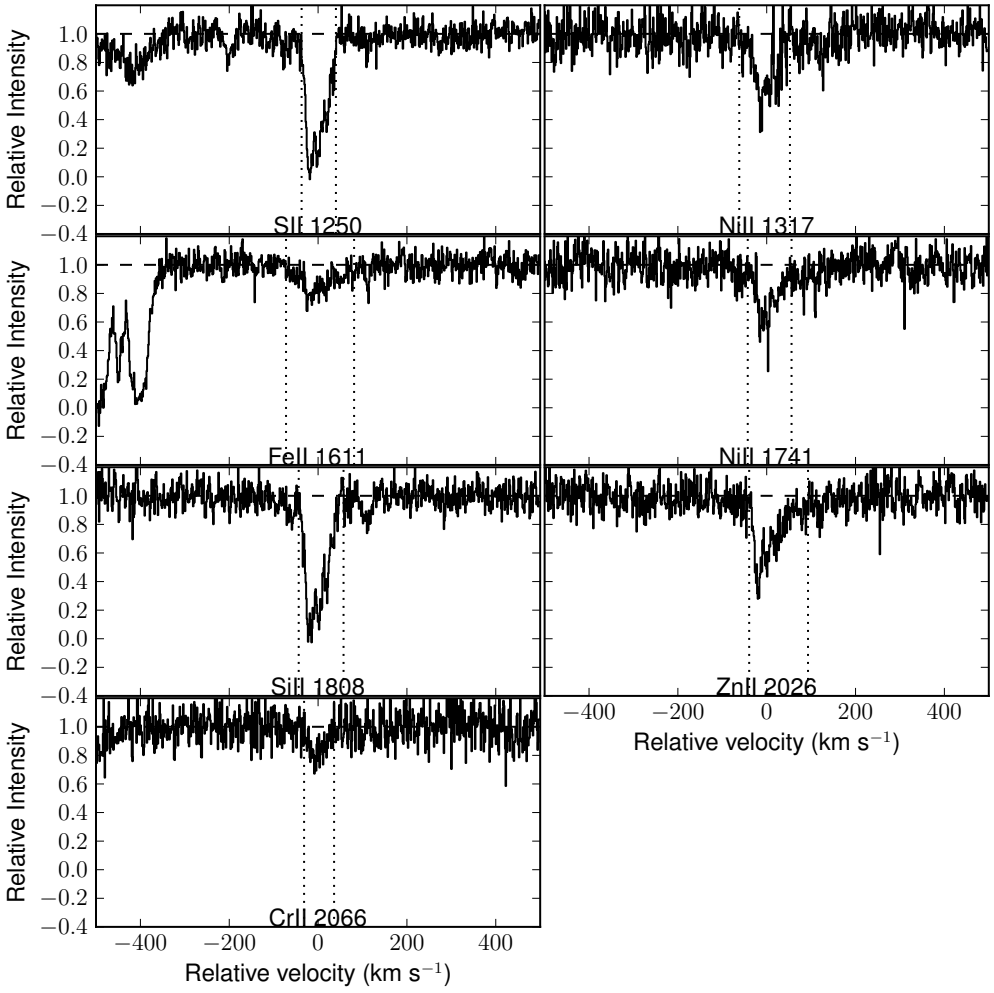

Figure A.46 Absorption line profiles for J1313+1441.

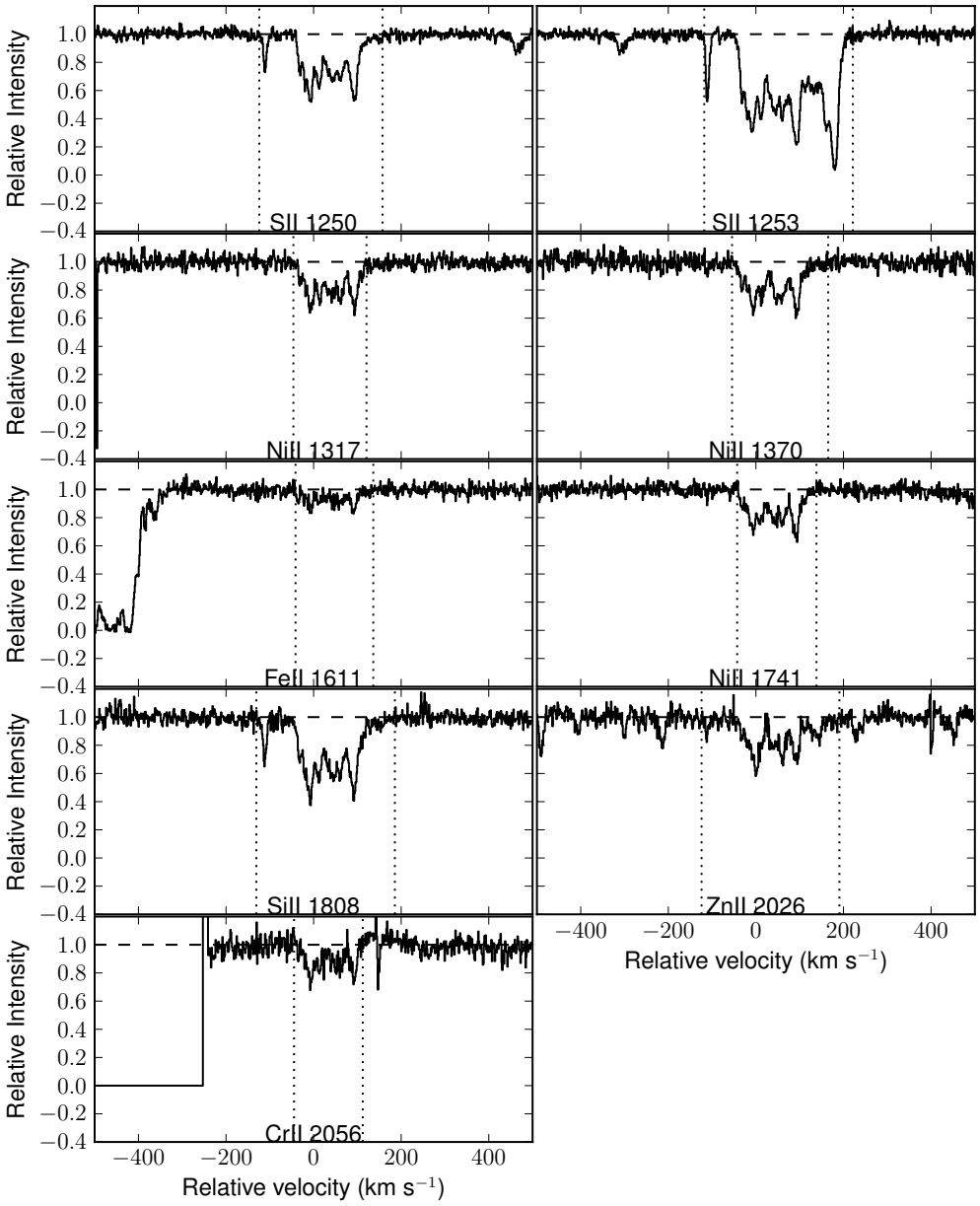

Figure A.47 Absorption line profiles for J2100-0641.

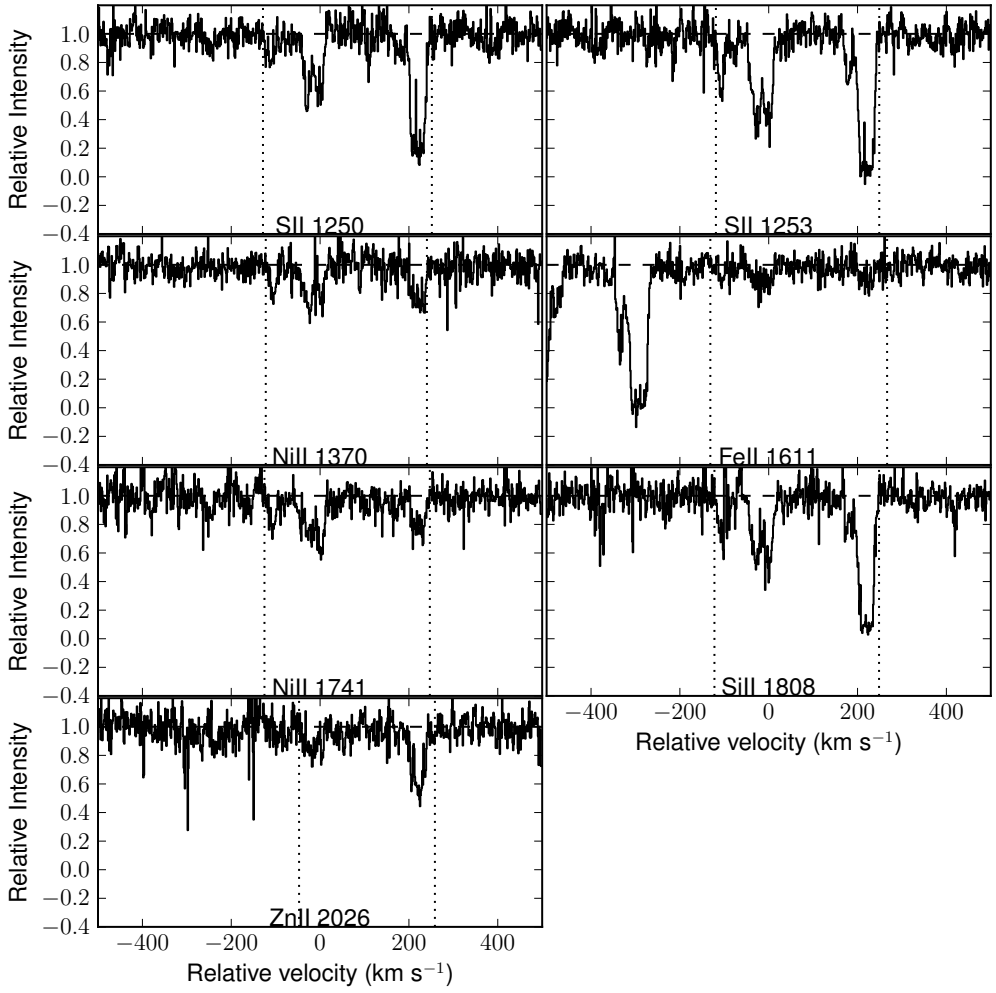

Figure A.48 Absorption line profiles for J1604+3951.

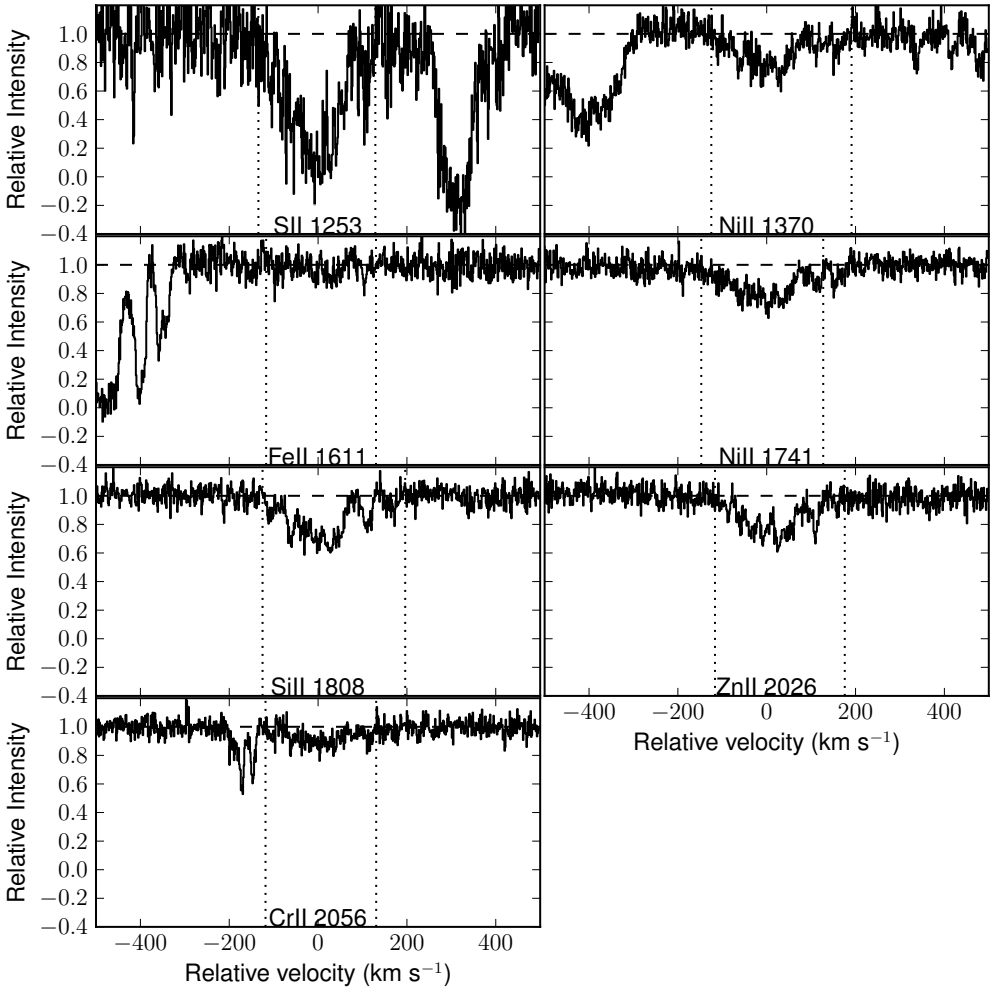

Figure A.49 Absorption line profiles for J0927+5823.

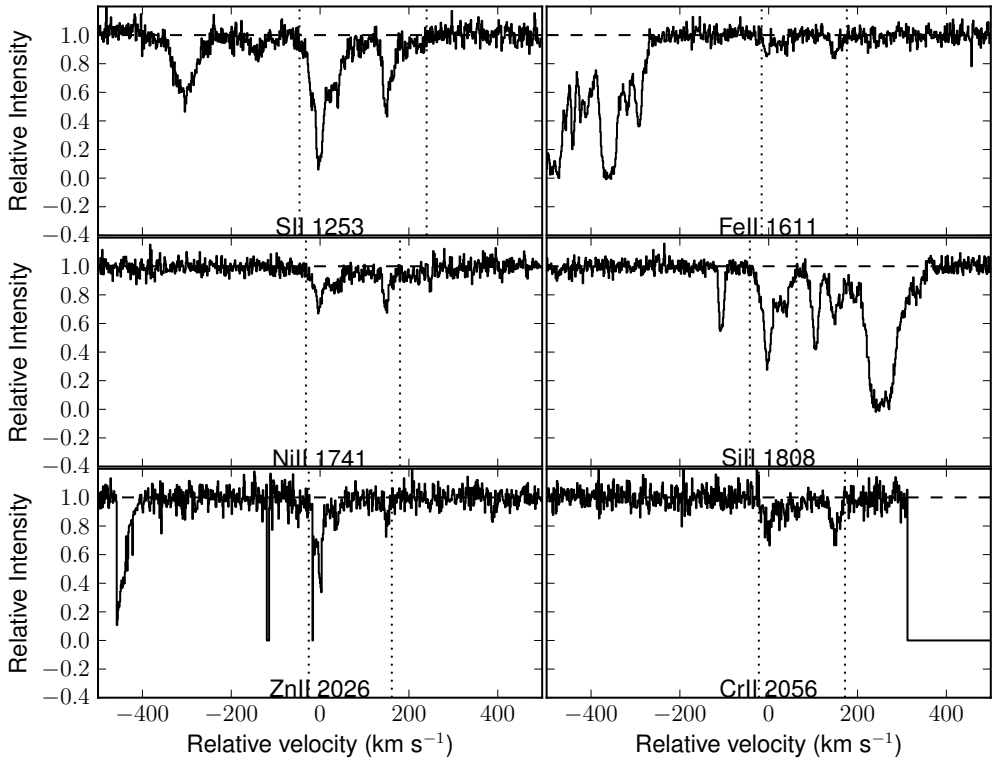

Figure A.50 Absorption line profiles for J0058+0115.

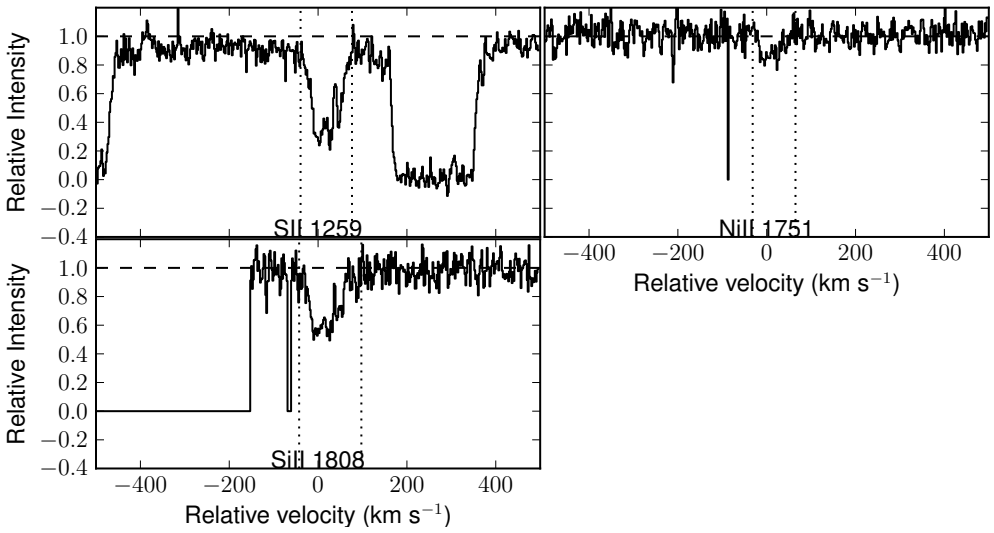

Figure A.51 Absorption line profiles for Q2342+34.

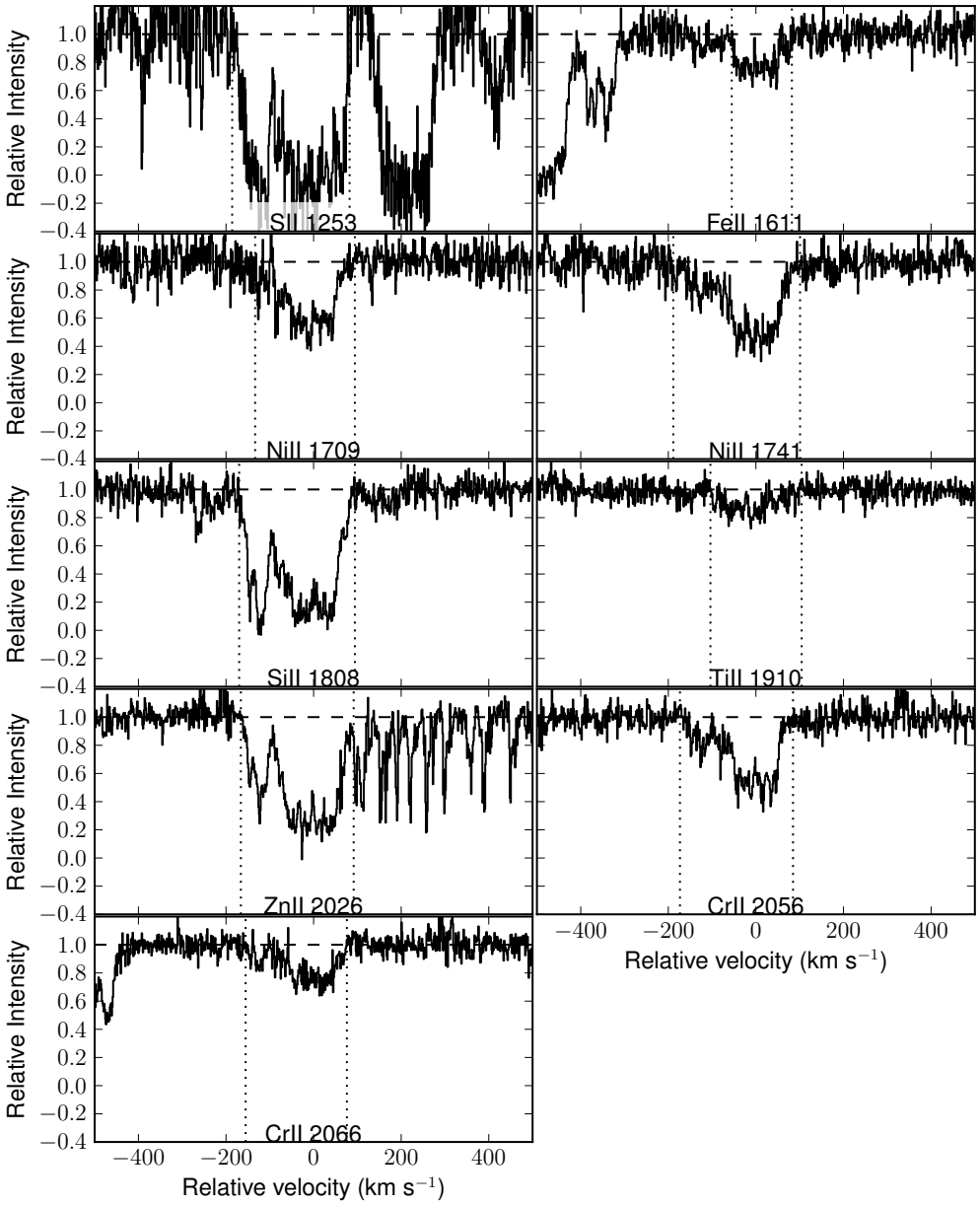

Figure A.52 Absorption line profiles for J1555+4800.

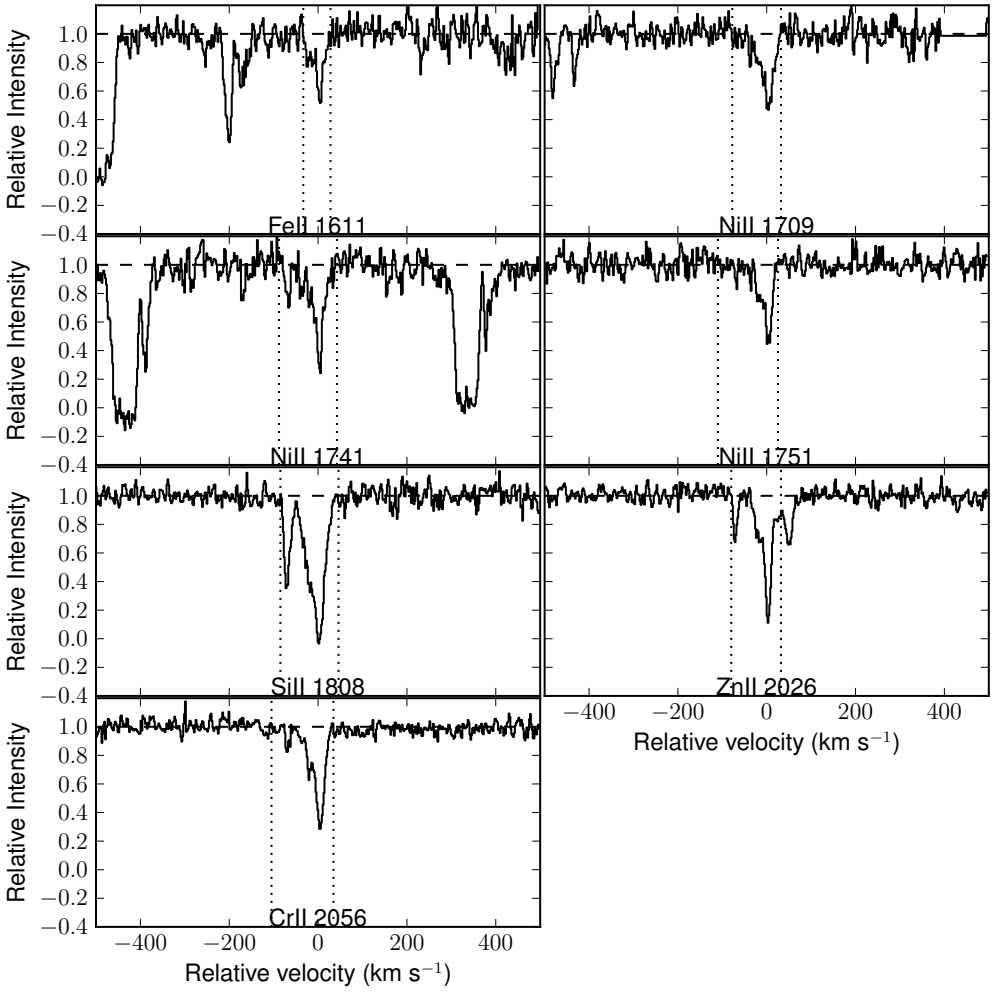

Figure A.53 Absorption line profiles for Q0458-02.

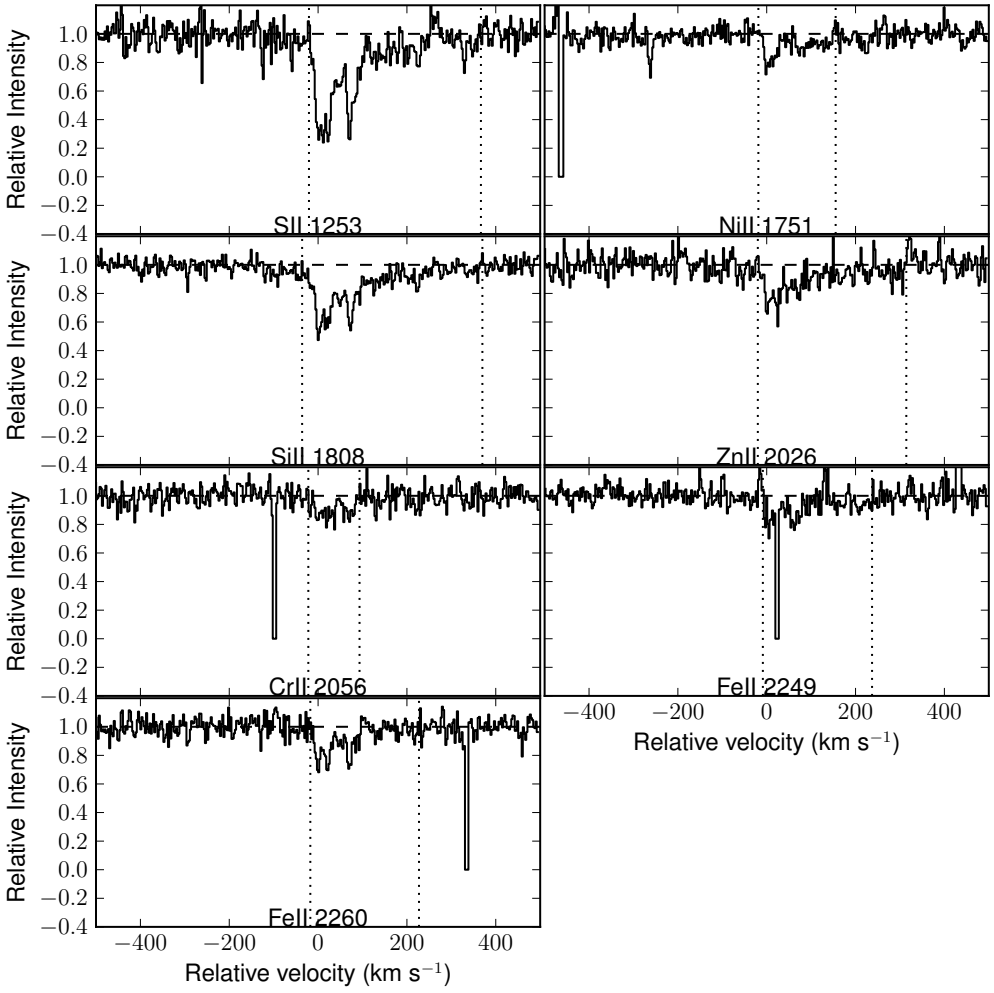

Figure A.54 Absorption line profiles for J1049-0110.

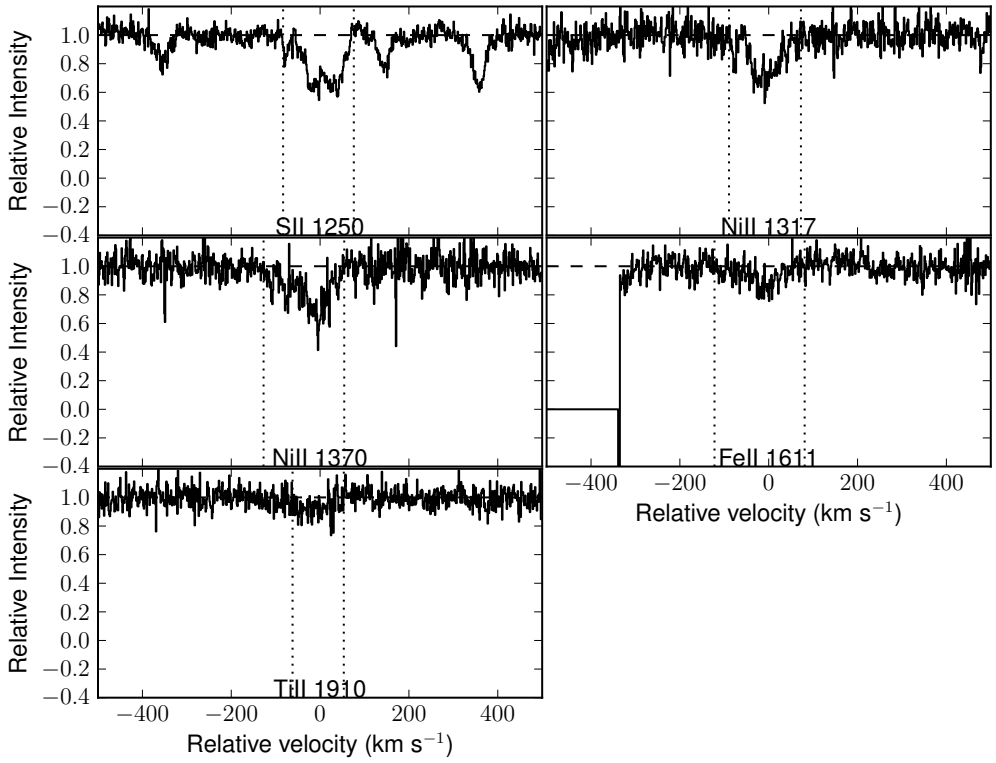

Figure A.55 Absorption line profiles for J1200+4015.

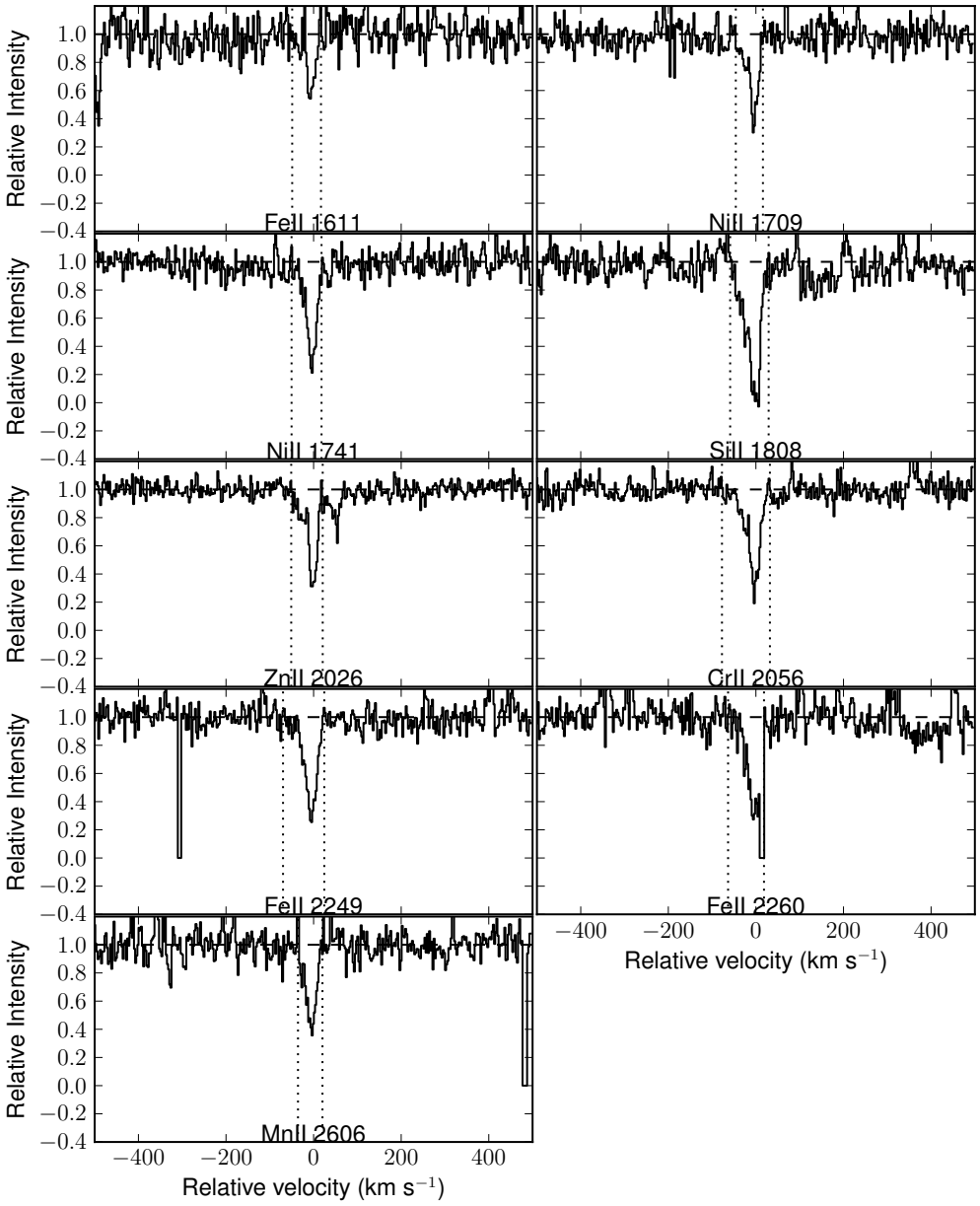

Figure A.56 Absorption line profiles for J1010+0003.

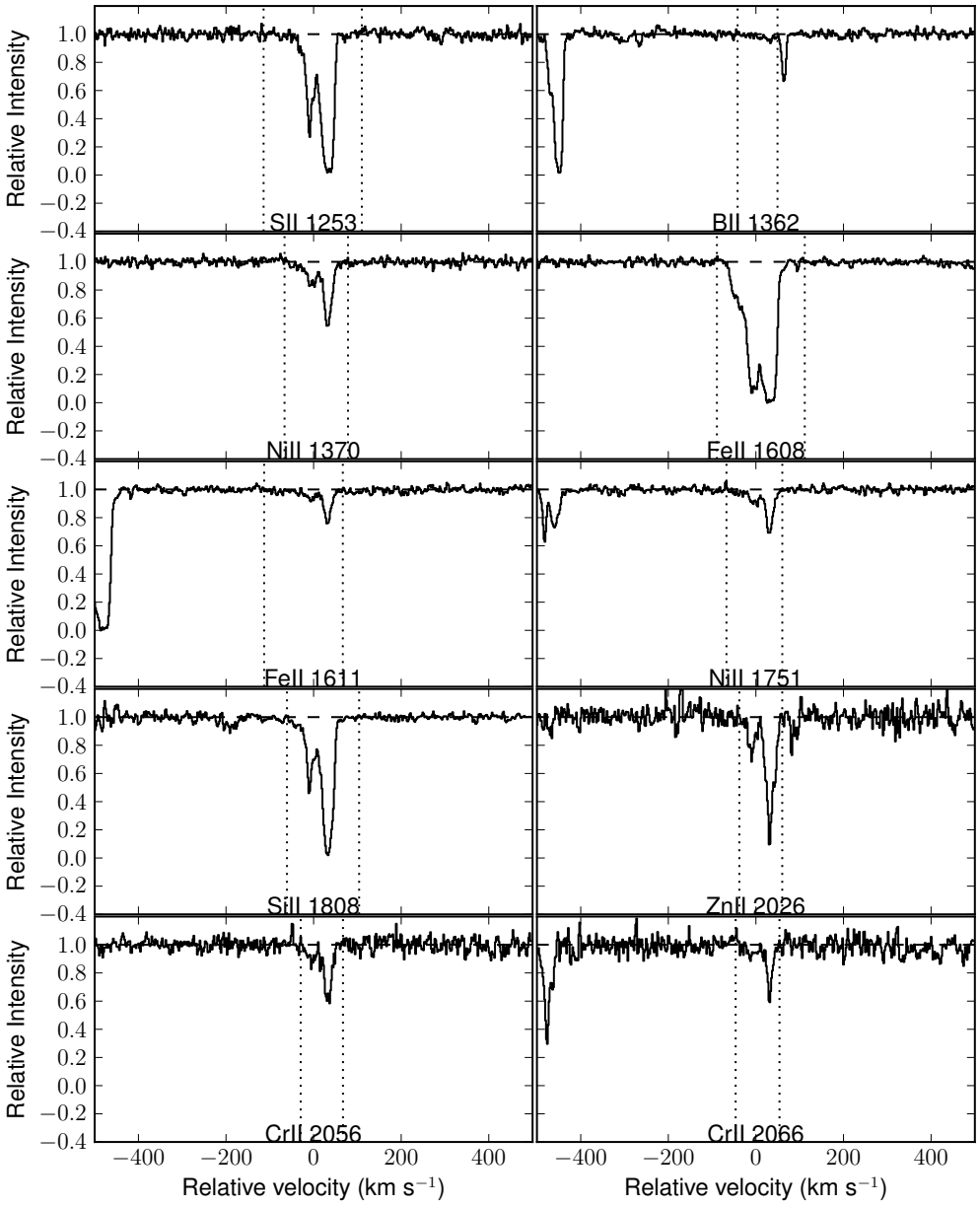

Figure A.57 Absorption line profiles for FJ0812+3208.

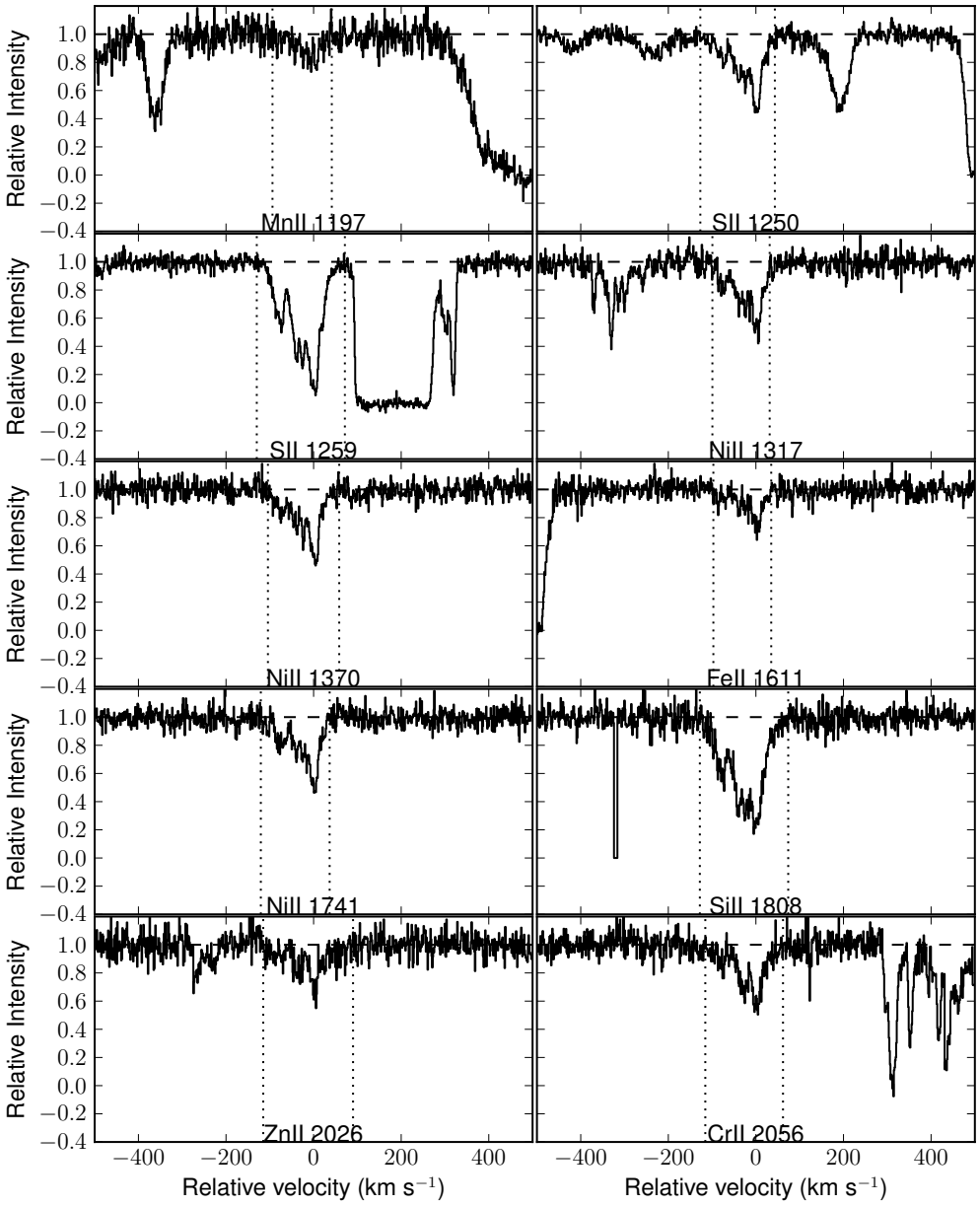

Figure A.58 Absorption line profiles for J1552+4910.

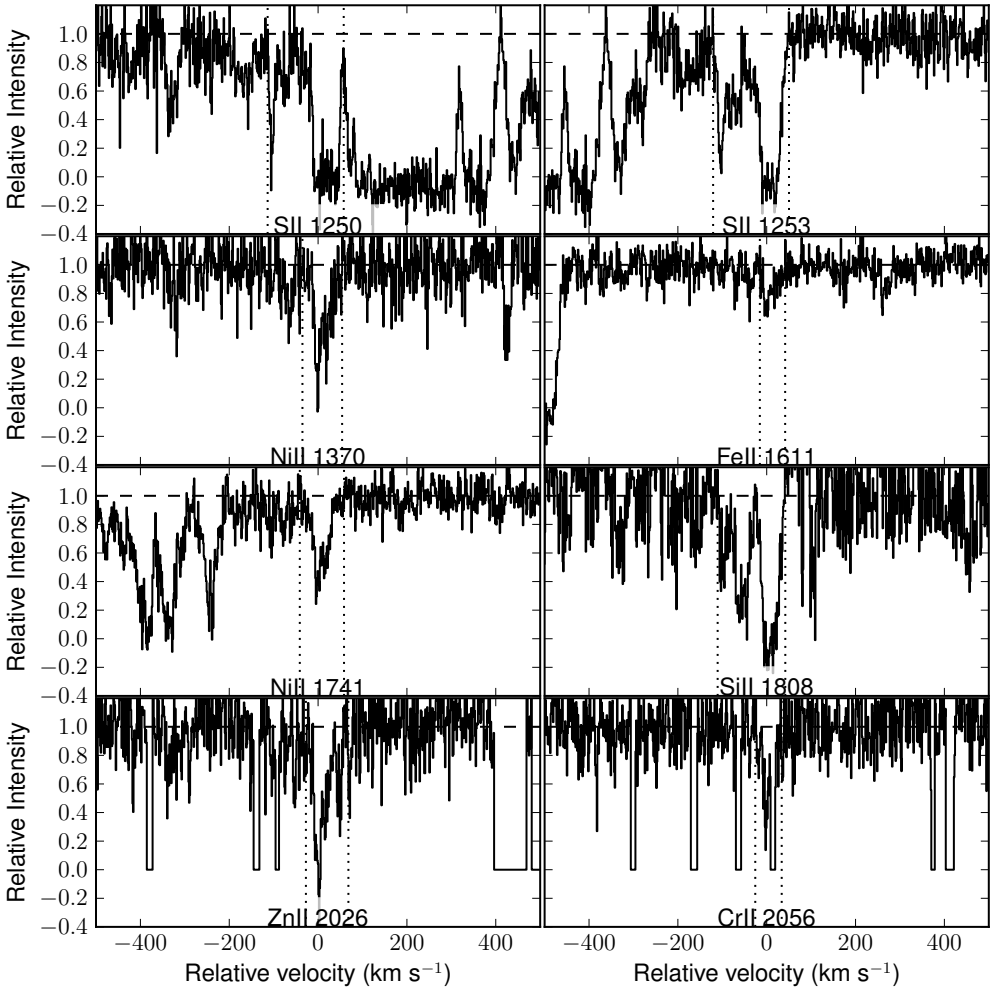

Figure A.59 Absorption line profiles for J1524+1030.

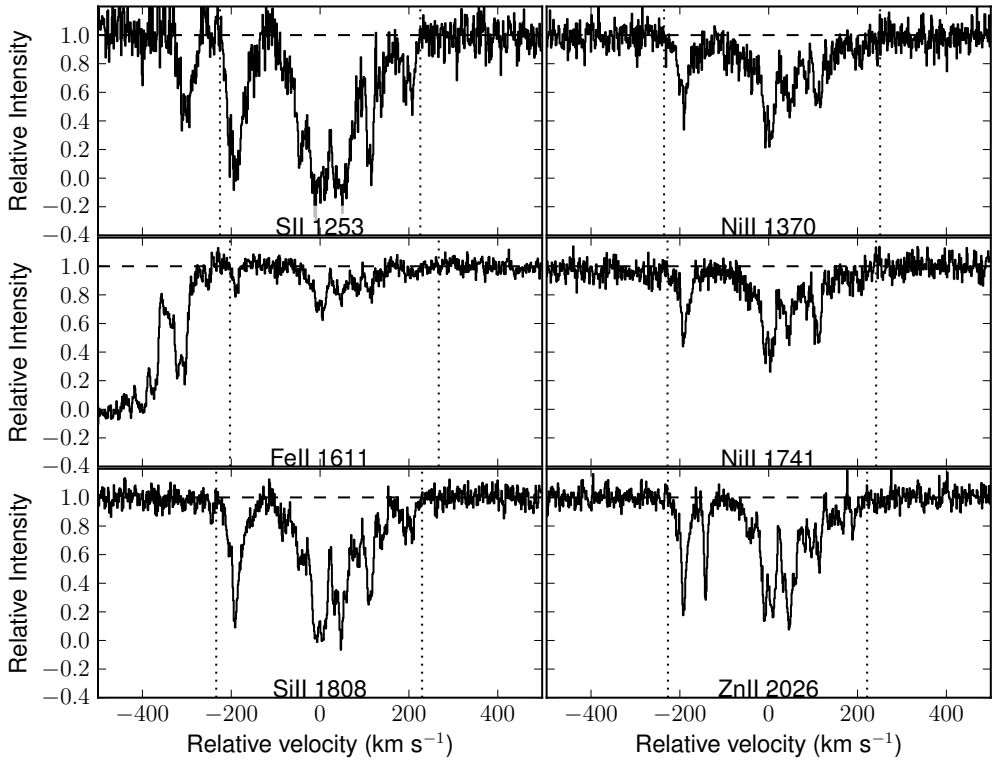

Figure A.60 Absorption line profiles for Q1755+578.

A.4 Literature Boron, Oxygen, and Sulphur Abundances

Table A.2: Literature boron, oxygen, and sulphur abundances

ID	[O/H]	[S/H]	[B/H]	References
		Stars		
HD19994	0.25 ± 0.06	0.11 ± 0.10	0.01 ± 0.20	1,2
HD159332	-0.07 ± 0.06	. . .	-0.39 ± 0.20	1,2
HD5015	0.07 ± 0.06	-0.01 ± 0.10	-0.29 ± 0.20	1,2
HD216385	0.04 ± 0.06	-0.14 ± 0.10	-0.39 ± 0.20	1,2
HD185395	0.07 ± 0.06	-0.19 ± 0.10	-0.19 ± 0.20	1,2
HD184499	-0.15 ± 0.06	. . .	-0.69 ± 0.20	1,2
HD210027	-0.04 ± 0.06	. . .	-0.19 ± 0.20	1,2
HD128167	-0.06 ± 0.06	-0.33 ± 0.10	-0.49 ± 0.20	1,2
HD82328	0.07 ± 0.06	-0.25 ± 0.10	-0.19 ± 0.20	1,2
HD4813	0.09 ± 0.06	-0.08 ± 0.10	-0.09 ± 0.20	1,2
HD28033	0.20 ± 0.06	. . .	-0.19 ± 0.20	1,2
NGC346−637	-0.69 ± 0.2	. . .	< -1.19	3
AV304	-0.49 ± 0.2	. . .	< -1.19	3
HD194598	-0.69 ± 0.10	-0.76 ± 0.15	-1.36 ± 0.14	4,5
HD94028	-0.87 ± 0.10	-1.22 ± 0.15	-1.48 ± 0.16	4,5
BD+23°3130	-1.58 ± 0.10	. . .	-2.88 ± 0.25	4
HD76932	-0.35 ± 0.10	-0.68 ± 0.15	-0.72 ± 0.14	4,5
HD201891	-0.56 ± 0.10	-0.81 ± 0.15	-1.03 ± 0.15	4,5
HD19445	-1.32 ± 0.10	-1.42 ± 0.15	-2.12 ± 0.19	4,5
HD84937	-1.61 ± 0.10	-1.68 ± 0.15	< -2.15	4,5
BD+26°3578	-1.65 ± 0.10	. . .	< -2.35	4
HD160617	-1.30 ± 0.10	-1.35 ± 0.15	-2.18 ± 0.20	4,5
HD184499	-0.19 ± 0.10	. . .	-0.56 ± 0.17	4
HD64090	-1.00 ± 0.10	. . .	-1.50 ± 0.13	4
BD+03°740	-2.08 ± 0.10	. . .	< -2.13	4
BD−13°3442	-2.14 ± 0.10	-2.26 ± 0.15	< -2.35	4,5
HD106516	-0.22 ± 0.10	-0.34 ± 0.15	-1.36 ± 0.15	4,5
HD140283	-1.69 ± 0.10	-2.06 ± 0.15	-2.60 ± 0.22	4,5
HD221377	-0.55 ± 0.10	. . .	-1.30 ± 0.19	4
HD37744	-0.23 ± 0.20	. . .	-0.29 ± 0.10	6
HD44743	0.09 ± 0.20	. . .	0.01 ± 0.10	6
HD36959	-0.08 ± 0.20	0.01 ± 0.14	-0.29 ± 0.10	6,7
HD36629	-0.37 ± 0.20	. . .	-0.29 ± 0.10	6
HD36351	-0.17 ± 0.20	. . .	-0.19 ± 0.10	6
HD214993	0.14 ± 0.20	. . .	-0.49 ± 0.10	6
HD216916	-0.08 ± 0.20	. . .	-0.48 ± 0.10	6
HD35337	-0.14 ± 0.20	. . .	-0.69 ± 0.10	6
HD37356	-0.25 ± 0.20	-0.02 ± 0.14	-0.29 ± 0.10	6,7
HD35039	-0.35 ± 0.20	0.03 ± 0.15	0.13 ± 0.10	6,7
HD29248	-0.02 ± 0.20	. . .	-0.29 ± 0.10	6
BD+56°576	-0.35 ± 0.20	. . .	-0.54 ± 0.10	6
HD34816	-0.02 ± 0.20	. . .	-0.49 ± 0.10	6

Continued on next page

Table A.2 – continued from previous page

ID	[O/H]	[S/H]	[B/H]	References
LP815−43	-1.86 ± 0.15	-2.49 ± 0.22	. . .	8,9
CS22873−055	-2.42 ± 0.25	-2.53 ± 0.10	. . .	10,11
CS30325−094	-2.53 ± 0.25	-2.90 ± 0.18	. . .	10,11
HD179626	-0.46 ± 0.03	-0.90 ± 0.22	. . .	8,12
CS22948−066	-2.20 ± 0.25	-2.83 ± 0.14	. . .	10,11
G64−12	-2.24 ± 0.15	-3.00 ± 0.22	. . .	8,9
G18-39	-0.87 ± 0.04	-1.15 ± 0.22	. . .	8,12
HD148816	-0.24 ± 0.03	-0.44 ± 0.15	. . .	5,12
CS29518−051	-1.84 ± 0.25	-2.58 ± 0.10	. . .	10,11
CS22186−025	-2.36 ± 0.25	-2.66 ± 0.10	. . .	10,11
LP635−14	-2.00 ± 0.12	-2.20 ± 0.22	. . .	8,9
CS22896−154	-1.70 ± 0.25	-2.52 ± 0.08	. . .	10,11
HD2796	-1.92 ± 0.25	-2.11 ± 0.10	. . .	10,11
G11−44	-1.63 ± 0.15	-1.71 ± 0.22	. . .	8,9
HD106516	-0.16 ± 0.03	-0.34 ± 0.15	. . .	5,12
HD76932	-0.37 ± 0.03	-0.68 ± 0.15	. . .	5,12
CS29491−053	-2.23 ± 0.25	-2.65 ± 0.10	. . .	10,11
CS22891−209	-2.47 ± 0.25	-2.88 ± 0.15	. . .	10,11
G53−41	-0.99 ± 0.05	-1.04 ± 0.22	. . .	8,12
HD194598	-0.67 ± 0.03	-0.97 ± 0.22	. . .	8,12
LP651−4	-2.04 ± 0.14	-2.47 ± 0.22	. . .	8,9
CS22966−057	-1.58 ± 0.25	-2.45 ± 0.10	. . .	10,11
G64−37	-2.32 ± 0.14	-2.93 ± 0.22	. . .	8,9
BD−13°3442	-2.15 ± 0.15	-2.41 ± 0.22	. . .	8,9
BD+17°3248	-1.33 ± 0.25	-1.94 ± 0.10	. . .	10,11
CS31082−001	-2.26 ± 0.25	-2.54 ± 0.10	. . .	10,11
BD−18°5550	-2.59 ± 0.25	-2.67 ± 0.12	. . .	10,11
HD122563	-2.15 ± 0.25	-2.39 ± 0.10	. . .	10,11
HD186478	-1.79 ± 0.25	-2.25 ± 0.08	. . .	10,11
CS22953−003	-2.04 ± 0.25	-2.68 ± 0.10	. . .	10,11
HD193901	-0.64 ± 0.03	-0.88 ± 0.22	. . .	8,12
CS22956−050	-2.16 ± 0.25	-2.91 ± 0.20	. . .	10,11
CS22892−052	-2.51 ± 0.25	-2.81 ± 0.10	. . .	10,11
HD9091	-0.04 ± 0.15	-0.32 ± 0.15	. . .	13
HD20427	-0.12 ± 0.15	-0.39 ± 0.15	. . .	13
HD112887	0.02 ± 0.15	-0.26 ± 0.15	. . .	13
HD2663	-0.11 ± 0.15	-0.37 ± 0.15	. . .	13
HD209858	0.00 ± 0.15	-0.23 ± 0.15	. . .	13
HD7228	0.13 ± 0.15	-0.07 ± 0.15	. . .	13
HD157467	0.30 ± 0.15	0.21 ± 0.15	. . .	13
HD218172	0.07 ± 0.15	-0.15 ± 0.15	. . .	13
HD133641	-0.06 ± 0.15	-0.34 ± 0.15	. . .	13
HD210457	0.04 ± 0.15	-0.22 ± 0.15	. . .	13
HD222155	0.09 ± 0.15	-0.18 ± 0.15	. . .	13
HD103891	-0.06 ± 0.15	-0.21 ± 0.15	. . .	13
HD42618	0.02 ± 0.15	-0.15 ± 0.15	. . .	13
HD80218	0.10 ± 0.15	-0.19 ± 0.15	. . .	13
HD109303	0.11 ± 0.15	-0.36 ± 0.15	. . .	13
HD198390	0.02 ± 0.15	-0.30 ± 0.15	. . .	13
HD59360	0.13 ± 0.15	-0.16 ± 0.15	. . .	13

Continued on next page

Table A.2 – continued from previous page

ID	[O/H]	[S/H]	[B/H]	References
HD110989	0.11 ± 0.15	-0.25 ± 0.15	. . .	13
HD171620	-0.16 ± 0.15	-0.39 ± 0.15	. . .	13
HD121560	-0.13 ± 0.15	-0.38 ± 0.15	. . .	13
HD5065	0.12 ± 0.15	-0.12 ± 0.15	. . .	13
HD155646	0.27 ± 0.15	-0.03 ± 0.15	. . .	13
HD11007	-0.09 ± 0.15	-0.29 ± 0.15	. . .	13
HD153240	0.15 ± 0.15	-0.05 ± 0.15	. . .	13
HD191672	-0.16 ± 0.15	-0.38 ± 0.15	. . .	13
HD73400	0.00 ± 0.15	-0.17 ± 0.15	. . .	13
HD63333	-0.06 ± 0.15	-0.33 ± 0.15	. . .	13
HD15398	0.23 ± 0.15	0.02 ± 0.15	. . .	13
HD214576	-0.18 ± 0.15	-0.44 ± 0.15	. . .	13
HD107038	-0.21 ± 0.15	-0.33 ± 0.15	. . .	13
HD22718	0.15 ± 0.15	-0.13 ± 0.15	. . .	13
HD182758	-0.14 ± 0.15	-0.49 ± 0.15	. . .	13
HD186379	-0.11 ± 0.15	-0.33 ± 0.15	. . .	13
HD201444	-0.10 ± 0.15	-0.50 ± 0.15	. . .	13
HD216106	0.10 ± 0.15	-0.24 ± 0.15	. . .	13
HD159333	0.12 ± 0.15	-0.18 ± 0.15	. . .	13
HD153668	0.04 ± 0.15	-0.17 ± 0.15	. . .	13
HD153627	-0.04 ± 0.15	-0.30 ± 0.15	. . .	13
HD76349	-0.16 ± 0.15	-0.39 ± 0.15	. . .	13
HD77408	-0.09 ± 0.15	-0.21 ± 0.15	. . .	13
HD26421	-0.03 ± 0.15	-0.32 ± 0.15	. . .	13
HD330	0.08 ± 0.15	-0.20 ± 0.15	. . .	13
HD210985	-0.21 ± 0.15	-0.46 ± 0.15	. . .	13
HD200580	-0.37 ± 0.15	-0.53 ± 0.15	. . .	13
HD22255	-0.01 ± 0.15	-0.22 ± 0.15	. . .	13
HD63332	0.21 ± 0.15	0.06 ± 0.15	. . .	13
HD88446	0.06 ± 0.15	-0.26 ± 0.15	. . .	13
HD69897	-0.05 ± 0.15	-0.20 ± 0.15	. . .	13
HD199085	0.03 ± 0.15	-0.10 ± 0.15	. . .	13
HD140750	0.14 ± 0.15	-0.26 ± 0.15	. . .	13
HD100446	-0.16 ± 0.15	-0.43 ± 0.15	. . .	13
HD149576	0.16 ± 0.15	-0.14 ± 0.15	. . .	13
HD126053	-0.16 ± 0.15	-0.34 ± 0.15	. . .	13
HD87838	-0.21 ± 0.15	-0.35 ± 0.15	. . .	13
HD219497	-0.07 ± 0.15	-0.42 ± 0.15	. . .	13
HD52711	0.05 ± 0.15	-0.16 ± 0.15	. . .	13
HD210718	-0.16 ± 0.15	-0.27 ± 0.15	. . .	13
HD140324	-0.01 ± 0.15	-0.28 ± 0.15	. . .	13
HD24421	-0.07 ± 0.15	-0.35 ± 0.15	. . .	13
HD136925	0.11 ± 0.15	-0.18 ± 0.15	. . .	13
HD101	-0.05 ± 0.15	-0.24 ± 0.15	. . .	13
HD218059	-0.02 ± 0.15	-0.24 ± 0.15	. . .	13
HD152986	0.06 ± 0.15	-0.12 ± 0.15	. . .	13
HD22521	0.03 ± 0.15	-0.21 ± 0.15	. . .	13
HD45067	0.07 ± 0.15	-0.09 ± 0.15	. . .	13
HD41640	-0.30 ± 0.15	-0.50 ± 0.15	. . .	13
HD204712	-0.04 ± 0.15	-0.38 ± 0.15	. . .	13

Continued on next page

Table A.2 – continued from previous page

ID	[O/H]	[S/H]	[B/H]	References
HD224233	0.07 ± 0.15	-0.12 ± 0.15	. . .	13
HD9670	-0.07 ± 0.15	-0.24 ± 0.15	. . .	13
HD108134	-0.06 ± 0.15	-0.32 ± 0.15	. . .	13
HD131599	-0.07 ± 0.15	-0.40 ± 0.15	. . .	13
HD127667	-0.13 ± 0.15	-0.34 ± 0.15	. . .	13
HD6840	-0.10 ± 0.15	-0.34 ± 0.15	. . .	13
HD167588	-0.08 ± 0.15	-0.33 ± 0.15	. . .	13
HD198089	0.00 ± 0.15	-0.24 ± 0.15	. . .	13
HD5750	-0.19 ± 0.15	-0.31 ± 0.15	. . .	13
HD193664	-0.02 ± 0.15	-0.17 ± 0.15	. . .	13
HD218637	-0.13 ± 0.15	-0.22 ± 0.15	. . .	13
HD221356	-0.15 ± 0.15	-0.25 ± 0.15	. . .	13
HD3454	-0.22 ± 0.15	-0.51 ± 0.15	. . .	13
HD16067	0.23 ± 0.15	-0.04 ± 0.15	. . .	13
HD91638	-0.03 ± 0.15	-0.24 ± 0.15	. . .	13
HD146946	-0.07 ± 0.15	-0.33 ± 0.15	. . .	13
HD204559	-0.04 ± 0.15	-0.32 ± 0.15	. . .	13
HD94835	0.24 ± 0.15	0.12 ± 0.15	. . .	13
HD198109	-0.15 ± 0.15	-0.41 ± 0.15	. . .	13
HD131039	0.18 ± 0.15	-0.14 ± 0.15	. . .	13
HD36066	0.16 ± 0.15	0.01 ± 0.15	. . .	13
HD5494	0.18 ± 0.15	-0.06 ± 0.15	. . .	13
HD210923	0.12 ± 0.15	-0.17 ± 0.15	. . .	13
HD212858	-0.10 ± 0.15	-0.39 ± 0.15	. . .	13
HD157466	-0.17 ± 0.15	-0.39 ± 0.15	. . .	13
HD220908	0.15 ± 0.15	-0.10 ± 0.15	. . .	13
HD3532	0.02 ± 0.15	-0.28 ± 0.15	. . .	13
HD109154	0.01 ± 0.15	-0.32 ± 0.15	. . .	13
HD174160	0.12 ± 0.15	-0.06 ± 0.15	. . .	13
HD102618	0.03 ± 0.15	-0.26 ± 0.15	. . .	13
HD86884	-0.01 ± 0.15	-0.24 ± 0.15	. . .	13
HD223436	0.21 ± 0.15	0.03 ± 0.15	. . .	13
HD15029	-0.10 ± 0.15	-0.28 ± 0.15	. . .	13
HD6312	-0.04 ± 0.15	-0.28 ± 0.15	. . .	13
HD3440	-0.03 ± 0.15	-0.30 ± 0.15	. . .	13
HD214111	0.20 ± 0.15	-0.05 ± 0.15	. . .	13
HD100067	-0.11 ± 0.15	-0.27 ± 0.15	. . .	13
HD118687	-0.11 ± 0.15	-0.38 ± 0.15	. . .	13
HD218470	0.23 ± 0.15	-0.07 ± 0.15	. . .	13
HD102080	-0.14 ± 0.15	-0.32 ± 0.15	. . .	13
HD11592	-0.05 ± 0.15	-0.27 ± 0.15	. . .	13
HD220842	0.09 ± 0.15	-0.24 ± 0.15	. . .	13
HD11045	0.07 ± 0.15	-0.25 ± 0.15	. . .	13
HD106510	-0.16 ± 0.15	-0.39 ± 0.15	. . .	13
HD186408	0.21 ± 0.15	0.06 ± 0.15	. . .	13
HD204306	-0.13 ± 0.15	-0.52 ± 0.15	. . .	13
HD201835	-0.04 ± 0.15	-0.28 ± 0.15	. . .	13
HD3079	0.08 ± 0.15	-0.16 ± 0.15	. . .	13
HD210640	0.01 ± 0.15	-0.28 ± 0.15	. . .	13
HD163363	0.17 ± 0.15	0.01 ± 0.15	. . .	13

Continued on next page

Table A.2 – continued from previous page

ID	[O/H]	[S/H]	[B/H]	References
HD152449	0.16 ± 0.15	-0.03 ± 0.15	. . .	13
HD86560	-0.08 ± 0.15	-0.37 ± 0.15	. . .	13
HD101716	0.20 ± 0.15	-0.11 ± 0.15	. . .	13
HD216385	0.02 ± 0.15	-0.15 ± 0.15	. . .	13
HD89010	0.23 ± 0.15	0.02 ± 0.15	. . .	13
HD101676	-0.12 ± 0.15	-0.37 ± 0.15	. . .	13
HD139457	-0.11 ± 0.15	-0.41 ± 0.15	. . .	13
HD190681	0.17 ± 0.15	-0.02 ± 0.15	. . .	13
HD21922	-0.07 ± 0.15	-0.41 ± 0.15	. . .	13
HD99126	0.07 ± 0.15	-0.10 ± 0.15	. . .	13
HD20717	-0.11 ± 0.15	-0.27 ± 0.15	. . .	13
HD6250	0.06 ± 0.15	-0.13 ± 0.15	. . .	13
HD77134	-0.08 ± 0.15	-0.26 ± 0.15	. . .	13
HD97037	0.03 ± 0.15	-0.12 ± 0.15	. . .	13
HD130253	0.06 ± 0.15	-0.16 ± 0.15	. . .	13
HD124819	0.08 ± 0.15	-0.22 ± 0.15	. . .	13
HD70	-0.06 ± 0.15	-0.27 ± 0.15	. . .	13
HD85902	-0.17 ± 0.15	-0.50 ± 0.15	. . .	13
HD219476	-0.17 ± 0.15	-0.46 ± 0.15	. . .	13
HD217877	0.04 ± 0.15	-0.14 ± 0.15	. . .	13
HD223854	-0.24 ± 0.15	-0.47 ± 0.15	. . .	13
HD171886	0.00 ± 0.15	-0.28 ± 0.15	. . .	13
HD153	0.29 ± 0.15	0.00 ± 0.15	. . .	13
HD3894	-0.20 ± 0.15	-0.35 ± 0.15	. . .	13
HD214435	-0.07 ± 0.15	-0.28 ± 0.15	. . .	13
HD202884	-0.03 ± 0.15	-0.22 ± 0.15	. . .	13
HD54182	0.18 ± 0.15	-0.16 ± 0.15	. . .	13
HD112756	-0.13 ± 0.15	-0.31 ± 0.15	. . .	13
HD169359	-0.01 ± 0.15	-0.23 ± 0.15	. . .	13
HD225239	-0.10 ± 0.15	-0.44 ± 0.15	. . .	13
HD219983	0.02 ± 0.15	-0.17 ± 0.15	. . .	13
HD76272	-0.09 ± 0.15	-0.35 ± 0.15	. . .	13
HD219306	-0.01 ± 0.15	-0.25 ± 0.15	. . .	13
HD14877	-0.12 ± 0.15	-0.36 ± 0.15	. . .	13
HD201490	-0.04 ± 0.15	-0.20 ± 0.15	. . .	13
HD216631	-0.14 ± 0.15	-0.41 ± 0.15	. . .	13
HD148049	-0.08 ± 0.15	-0.31 ± 0.15	. . .	13
HD214557	0.21 ± 0.15	0.02 ± 0.15	. . .	13
HD201639	-0.32 ± 0.15	-0.45 ± 0.15	. . .	13
HD176796	0.00 ± 0.15	-0.32 ± 0.15	. . .	13
HD195200	0.05 ± 0.15	-0.19 ± 0.15	. . .	13
HD23438	-0.02 ± 0.15	-0.29 ± 0.15	. . .	13
HD90878	0.15 ± 0.15	-0.19 ± 0.15	. . .	13
HD94012	-0.14 ± 0.15	-0.43 ± 0.15	. . .	13
HD27816	-0.25 ± 0.15	-0.47 ± 0.15	. . .	13
HD191649	0.06 ± 0.15	-0.18 ± 0.15	. . .	13
HD215442	0.28 ± 0.15	-0.11 ± 0.15	. . .	13
HD101472	0.11 ± 0.15	-0.15 ± 0.15	. . .	13
HD71148	0.07 ± 0.15	-0.07 ± 0.15	. . .	13
HD223583	-0.14 ± 0.15	-0.41 ± 0.15	. . .	13

Continued on next page

Table A.2 – continued from previous page

ID	[O/H]	[S/H]	[B/H]	References
HD8671	0.10 ± 0.15	-0.15 ± 0.15	. . .	13
HD6834	-0.30 ± 0.15	-0.53 ± 0.15	. . .	13
HD36909	0.08 ± 0.15	-0.18 ± 0.15	. . .	13
HD99984	-0.03 ± 0.15	-0.30 ± 0.15	. . .	13
HD912	0.17 ± 0.15	-0.18 ± 0.15	. . .	13
HD209320	0.16 ± 0.15	-0.10 ± 0.15	. . .	13
HD36667	-0.06 ± 0.15	-0.35 ± 0.15	. . .	13
HD156635	0.16 ± 0.15	-0.03 ± 0.15	. . .	13
HD194497	-0.07 ± 0.15	-0.26 ± 0.15	. . .	13
HD192145	-0.04 ± 0.15	-0.28 ± 0.15	. . .	13
HD160078	0.36 ± 0.15	-0.03 ± 0.15	. . .	13
HD99233	-0.24 ± 0.15	-0.54 ± 0.15	. . .	13
HD206860	0.10 ± 0.15	-0.10 ± 0.15	. . .	13
HD145937	-0.11 ± 0.15	-0.52 ± 0.15	. . .	13
		DLAs		
J1340+1106	-1.65 ± 0.09	-1.85 ± 0.07	. . .	14
Q2059−360	-1.58 ± 0.10	-1.72 ± 0.09	. . .	15,16
Q0841+12	-1.32 ± 0.14	-1.45 ± 0.13	. . .	16,17
HE2243−6031	-1.15 ± 0.20	-0.94 ± 0.03	. . .	18
Q1337+113	-1.95 ± 0.12	-1.82 ± 0.08	. . .	16,19
		ISM		
HD88115	0.03 ± 0.16	. . .	-0.28 ± 0.18	20
HD92554	0.03 ± 0.14	. . .	-0.35 ± 0.16	20
HD99890	0.25 ± 0.17	. . .	-0.41 ± 0.25	20
HD104705	0.01 ± 0.08	. . .	-0.42 ± 0.10	20
HD121968	0.02 ± 0.11	. . .	-0.51 ± 0.21	20
HD177989	0.05 ± 0.09	. . .	-0.53 ± 0.12	20

References – (1) Smith et al. (2001). (2) Takeda (2007). (3) Brooks et al. (2002) and references therein. (4) Tan et al. (2010). (5) Caffau et al. (2005). (6) Venn et al. (2002) and references therein. (7) Daflon et al. (2009). (8) Nissen et al. (2007). (9) Rich & Boesgaard (2009). (10) Spite et al. (2005). (11) Spite et al. (2011). (12) Ramírez et al. (2012). (13) Reddy et al. (2003) (14) Cooke et al. (2011b). (15) Srianand et al. (2005). (16) Petitjean et al. (2008). (17) Dessauges-Zavadsky et al. (2007). (18) Lopez et al. (2002). (19) Prochaska et al. (2007). (20) Ritchey et al. (2011).